

# THÈSE

UNIVERSITE DE PAU ET DES PAYS DE L'ADOUR

Doctoral School of Exact Sciences and their Applications (ED 211)

Presentée et soutenue le 15 décembre 2017  
par **Ezequiel DE SOUZA FREIRE ORLANDI**

Pour obtenir le grade de docteur  
de l'Université de Pau et des Pays de l'Adour  
**Spécialité: Génie Pétrolier**

## FOLLOWING ASPHALTENES DESTABILIZATION AND DEPOSITION BY QUARTZ CRYSTAL RESONATOR

### MEMBRES DU JURY

#### RAPPORTEURS

- Simon IVAR ANDERSEN
- Loïc BARRE

Scientific Advisor, PhD/ Technical University of Denmark  
Engineer, PhD / IFPEN

#### EXAMINATEURS

- Johan SJØBLOM
- Isabelle BARAILLE

Professor / Norwegian University of Science and Technology  
Professor / University of Pau and Pays de l'Adour

#### DIRECTEURS

- Hervé CARRIER
- Jean-Luc DARIDON

Professor / University of Pau and Pays de l'Adour  
Professor / University of Pau and Pays de l'Adour





## Acknowledgments

I would like to express my gratitude towards my family which supported me throughout my doctoral studies.

I would also like to acknowledge the professors, doctors and fellow scientists that helped me on my trajectory from the beginning of my studies to the end, for I am sure their positive influences will accompany me in my work long into the future.

I acknowledge **Agnes de Paula Scheer** who accepted me during my graduation studies at her laboratory at the Federal University of Parana to develop research on crude oil emulsions. It was my first experience with crude oil research and it was very captivating for me.

One year before finishing my Master Degree in Brazil I had the opportunity to spend a period of time in Norway, working at the Ugelstad Laboratory hosted by Norwegian University of Science and Technology. The work was on the application of Isothermal Titration Calorimetry to the study of asphaltene aggregation and interaction with tetrameric acids. I greatly acknowledge **Johan Sjøblom** and **Sébastien Simon** for the guidance throughout this work, which ultimately served to increase my interest for crude oil research.

After finishing my Master in Brazil I moved to Pau to start the PhD in the Laboratory of Complex Fluids and their Reservoirs (LFCR) which is a part of the Physics department at the University of Pau and Pays de l'Adour. It is always exciting for chemical engineers to start a PhD in the Physics department. I would like to acknowledge **Jean-Luc Daridon** and **Hervé Carrier**.

I thoroughly enjoyed my time in France and had a very enriching experience at the LFCR. I also had the privilege to have many discussions about the research topics with Patrick Bouriat and Daniel Broseta. I greatly acknowledge Patrick Bouriat for the trials of studying asphaltene deposits with the Ellipsometry. We shared some good days of exchanging ideas and looking forward to making new discoveries on the subject. So important to the work was also Guillaume Galliero. I appreciate the many discussions we had.

At the end of the PhD I had the pleasure of working with Sadia Radji for performing the Atomic Force Microscopy analysis. I greatly acknowledge her for the time she dedicated to helping me perform such important experiments. The work yielded a project on the use of AFM and QCM.

The thesis was undertaken as a part of a JIP program\* funded by the Norwegian Research Council and many enterprises from the crude oil sector† and having academic partners‡. The work progress was presented in meetings in which I had the pleasure of meeting some scientists which I would like to acknowledge. Their expert opinions were greatly appreciated and were essential for the conclusion of the developed work. For this I acknowledge Zhengue Xu, Hans Oskarsson, Per-Erik Hellberg, Ben Smith, Hans Oschmann, Ingvild Andersen Johnsen, Hans Petter Rønningsen, Arve Erga, Nicolas Passade-Boupat, Honggang Zhou and Thierry Palermo.

At the end of my PhD, I also had the pleasure of meeting Francis Rondelez whose insights on some aspects on crude oil research were essential for developing the work.

So important at the final stages of the PhD were the highly appreciated critical evaluations from the manuscript examiners, **Simon Ivar Andersen** and **Loic Barré**. I greatly acknowledge the time they placed at my disposal to perform the examination. Together with them I would like to acknowledge Isabelle Barraille and Johan Sjøblom for accepting being the reporters of the work. I greatly acknowledge their fruitful questions and comments during the PhD defense.

Also greatly important for the work progress and motivation were the participation in the Petroleum Phase Behavior and Fouling conferences (PetroPhase), where I had the great opportunity of meeting great names on Petroleum research, learning and sharing the work progress. Among them I would like to acknowledge Watson Loh and Juan Carlos Pereira for the good discussions during the conference held in Le Havre.

I would like to acknowledge Djamel Nasri and Jean-Patrick Bazile for assisting me with the technical support in the “everyday life” in the laboratory and the fellow PhDs “in the same boat”: Abdoul Wahid, Deneb Peredo, Fouad Oulebsir, Hafid Touil, Ingrid Velázquez, Henry Delroise,

---

\* Joint Industrial Project “Improved Mechanisms of Asphaltene Deposition and Precipitation to Minimize Irregularities in Production and Transport – A Cost Effective and Environmentally Friendly Approach”.

† AkzoNobel, British Petroleum, Canada Natural Resources, Nalco Champion, Petrobras, Statoil and Total.

‡ Norwegian University of Science and Technology, University of Alberta and Federal University of Parana.

Leticia Ligiero, Romouald Coupain and Victor Manuel Perez. It was also a pleasure working besides the fellow post-doc Hai Hoang. It was very good also to get to know professors Peter Moonen and Hannelore Derluyn.

I also would like to acknowledge the “friday morning coffee and croissants group”, with the following members Djamel Nasri, Catherine Urrea, Jean-Patrick Bazile, Jean-Phillippe Torr , Val rie Rouch, Bertrand Guatarbes and Eric Normandin for the good moments together.

I would also like to express my gratitude to V ronique Giancola and Blandine Gaio for the support during my time at the LFCR.

## **Following asphaltenes destabilization and deposition by quartz crystal resonator**

Asphaltenes and other heavy petroleum constituents, like resins and high molecular weight alkanes, pose significant challenges in all segments from the petroleum production chain. Among the many problems, asphaltene destabilization and deposition within upstream operations has rendered tons of research time and is still not completely understood. Part of the difficulty in capturing the real physics behind such phenomena is the widespread use of model systems and extracted molecules, greatly altering the complex fluid organization of crude oils, and thus bypassing real processes. To date two extremes of asphaltene organizational structure can be drawn, as a part of an aggregate, with simple pi-pi attractions and alkane chains repulsion, controlling aggregation; and as a part of a macromolecular structure, with significant participation of other crude components. The last structure being way more difficult to model, and captures its physics and being poorly reproducible with the use of model systems. Another important aspect when researching asphaltene deposition is the way asphaltene destabilization occurs. When using extracted asphaltenes in model systems, the former affirmation has virtually no mean, as the many asphaltene fractions were beforehand mixed. However, when dealing with the whole crude oil, the path of destabilization matters and is still greatly bypassed within the scientific community. Summing up to the exposed topics, there is the rather non-specificity from the majority of experimental techniques used on the research of asphaltene destabilization and deposition in relation to the depositing particles size scales.

Spectroscopy techniques, capable of sweeping interfacial physical parameters are good candidates for improving the deleterious exposed points. In the present thesis quartz crystal

resonator, connected to a vector network analyzer is used is shown to present the potential of revealing many aspects on asphaltene destabilization and deposition directly from crude oils (live, recombined or dead oils) as well as model systems. Crude oil equilibrium is disturbed by solubility changes in a continuous or step gradient mimicking production processes. The interpretation of the quartz crystal resonance parameters, frequency and energy dissipation, is performed in a qualitative and to some extent quantitative way. The study innovates in the sense of extending the use of the quartz crystal to interpret process, not only detecting phase changes, as it is the case of the majority of the former studies. The evaluation of production chemicals is undergone once the methodology is thoroughly discussed. The potential of the proposed analysis is credited by atomic force microscopy which opens the horizon for more research and potential applications of the methodology. Among the possible application is the development of flow assurance sensors capable of detecting phase changes and evaluate deposition *in situ*.

## **Suivi de la déstabilisation et du dépôt des asphaltènes par un résonateur à quartz**

Les asphaltènes et autres constituants lourds du pétrole, comme les résines et les alcanes de haut poids moléculaire, posent des défis importants dans tous les segments de la chaîne de production pétrolière. Parmi les nombreux problèmes, la déstabilisation et le dépôt des asphaltènes dans les opérations en amont ont fait perdre beaucoup de temps à la recherche et ne sont pas encore complètement compris. Une partie de la difficulté à saisir la véritable physique derrière de tels phénomènes est l'utilisation répandue des systèmes modèles et des molécules extraites, modifiant considérablement l'organisation fluide complexe des pétroles bruts, et donc en contournant les processus réels. À ce jour, deux extrêmes de la structure organisationnelle asphaltènes peuvent être dessinés, en tant que partie d'un agrégat, avec des attractions pi-pi simples et des répulsions chaînes d'alcane, contrôlant l'agrégation; et dans le cadre d'une structure macromoléculaire, avec une participation significative d'autres composants bruts. La dernière structure étant beaucoup plus difficile à modéliser, elle capture sa physique et est difficilement reproductible à l'aide de systèmes modèles. Un autre aspect important de la recherche des dépôts d'asphaltènes est la manière dont se produit la déstabilisation des asphaltènes. Lorsque l'on utilise des asphaltènes extraits dans des systèmes modèles, l'affirmation précédente n'a pratiquement aucune moyenne, car les nombreuses fractions d'asphaltènes ont été préalablement mélangées. Cependant, lorsqu'il s'agit de tout le pétrole brut, la voie de la déstabilisation est importante et est encore largement dépassée au sein de la communauté scientifique. Pour résumer les sujets exposés, il y a plutôt la non-spécificité de la majorité des techniques expérimentales utilisées sur la recherche de la déstabilisation et du dépôt des asphaltènes en relation avec les dépôts d'échelle des particules.

Les techniques de spectroscopie, capables de balayer les paramètres physiques interfaciaux, sont de bons candidats pour améliorer les points exposés délétères. Dans la présente thèse, le résonateur à quartz connecté à un analyseur de réseau vectoriel présente le potentiel de révéler de nombreux aspects sur la déstabilisation et le dépôt des asphaltènes directement à partir de pétrole brut (huiles vivantes, recombinaées ou mortes) et de systèmes modèles. L'équilibre du pétrole brut est perturbé par les changements de solubilité dans un processus continu ou en gradin imitant les processus de production. L'interprétation des paramètres de résonance des cristaux de quartz, de la fréquence et de la dissipation d'énergie, est effectuée de manière qualitative et, dans une certaine mesure, quantitative. L'étude innove dans le sens d'étendre l'utilisation du cristal de quartz pour interpréter le processus, non seulement en détectant les changements de phase, comme c'est le cas de la majorité des études précédentes. L'évaluation des produits chimiques de production est effectuée une fois que la méthodologie a fait l'objet d'une discussion approfondie. Le potentiel de l'analyse proposée est crédité par la microscopie à force atomique qui ouvre l'horizon pour plus de recherche et d'applications potentielles de la méthodologie. Parmi les applications possibles figure le développement de capteurs d'assurance de débit capables de détecter les changements de phase et d'évaluer les dépôts in situ.

# Table of Contents

Introduction .....	1
1. Literature review .....	5
1.1 Crude oil origin and composition .....	5
1.1.1 The SARA fractions.....	11
1.1.1.1 Saturates .....	12
1.1.1.2 Aromatics .....	12
1.1.1.3 Resins.....	12
1.1.1.4 Asphaltenes.....	15
1.2 Flow assurance issues.....	15
1.2.1 Asphaltenes.....	19
1.2.1.1 The physical nature of asphaltenes.....	19
1.2.1.2 Asphaltene molecules .....	28
1.2.1.3 Asphaltene Fractions.....	33
1.2.2 Asphaltene destabilization.....	34
1.2.3 Asphaltene adsorption.....	34
1.2.4 The onset of asphaltene destabilization and the asphaltene yield .....	35
1.2.5 Methods of detection of asphaltene destabilization.....	38
1.2.6 Methods of studying asphaltene deposition .....	39
1.3 Phase separations and organic deposits .....	40

1.3.1 Interpretations of the process of asphaltene destabilization and deposition .....	41
2. Quartz crystal resonator and flow assurance .....	43
2.1 Introduction to the QCR technique .....	43
2.1.1 Effect of roughness .....	49
2.1.2 Effect of pressure and pressurized liquid .....	50
2.2 Quartz crystal applied to crude oil research .....	51
2.2.1 Observations concerning the researched systems and experimental schematics.....	56
2.3 New approach on the utilization of QCM to access heavy organics destabilization and deposition from crude oils (live or dead) .....	58
2.4 Modeling.....	62
3. Materials and Methods .....	65
3.1 Dead crude oils .....	65
3.2 Live crude oils .....	66
3.3 Asphaltenes extraction .....	67
3.4 Quartz crystal.....	67
3.5 Atmospheric pressure experimental apparatus.....	67
3.6 Asphaltene destabilization procedures .....	68
3.7 Acquisition Method .....	69
3.8 High pressure experimental apparatus .....	71
3.8.1 Constant mass expansion test .....	72
3.9 The asphaltene onset of asphaltene destabilization determination .....	74
4. Results .....	76
4.1 Crude oil titration with an asphaltene solvent .....	76
4.1.1 $\Delta f_n$ and $\Delta \Gamma_n$ as a function of toluene or cyclohexane mass fraction .....	76
4.1.2 Model application: density-viscosity and <i>hinterface</i> determination.....	79

4.2 Crude oil Titration with an asphaltene nonsolvent .....	83
4.2.1 $\Delta f_n$ and $\Delta \Gamma_n$ as a function of n-heptane mass fraction ( $x_{C7}$ ) .....	83
4.2.2 $\Delta F_n$ and $\Delta \Gamma_n$ as a function of experimental run time .....	90
4.2.3 The analysis of the deposit energy dissipation .....	93
4.2.4 The onset of asphaltene destabilization .....	96
4.2.5 Observation concerning the onset of asphaltene destabilization by quartz crystal resonator .....	103
4.2.6 Model application .....	104
4.2.7 Discretization of regions within the titration .....	110
4.2.8 Recording of more overtones of resonance .....	114
4.2.9 Other experiments probing various asphaltene deposition aspects .....	121
4.2.10 Crude oil titration with an asphaltene non solvent at higher temperatures: $\Delta \Gamma$ interpretation .....	147
4.2.11 Diluted crude oil and extracted asphaltenes destabilization and deposition .....	154
4.2.12 Bandwidth profiles obtained from crude oils and extracted asphaltenes .....	160
4.3 The use of production chemicals: onset and deposition assessment. ....	163
4.3.1 Crude oil plus proprietary chemical .....	164
4.3.2 Crude oil plus Dodecylbenzenesulfonic acid (DBSA).....	168
4.3.3 Crude oil plus dodecanoic acid.....	171

4.4 Interpretation of occurring physical phenomena from $\Delta\Gamma\eta$ , $\Delta F\eta$ and $\Delta Fm$ data: whole crude oils and extracted asphaltenes in toluene.....	179
4.5 Macroscopic and microscopic experimental aspects .....	186
4.6 An AFM study of a deposit obtained at asphaltenes continuous destabilization .....	192
4.7 Crude oil with injected nitrogen and the onset of asphaltene destabilization .....	203
Conclusions .....	206
Bibliography.....	209

# List of Figures

Figure 1. Three main systems which are to be studied by the quartz crystal technique to understand asphaltene destabilization and deposition as well as other or other phase separations processes. ....	2
Figure 2. Stages of organic matter transformation to hydrocarbons (adapted from Tissot and Welte, 1984) .....	6
Figure 3. Hypothetical kerogen molecular structure (after Tissot <sup>10</sup> ) .....	7
Figure 4. Van Krevelen diagram with the evolution of different kerogen types (After Speight, 1982) .....	8
Figure 5. Reservoir, production tubing and surface facilities in a crude oil production site. Two wells are represented one with mechanical pump recovery and the other producing by natural reservoir pressure reduction. X-tree, three phase separator and stocking units are also shown. (Photo taken at the stand of the China Petroleum Technology Development Corporation, CPTDC at Rio Oil and Gas 2014). ....	9
Figure 6. Crude oil SARA fractionation. Asphaltenes are precipitated from crude oils with excess n-alkane and separated from the maltenes by filtration. The maltenes are then percolated through a chromatographic column and the saturates, aromatics and resins are eluted with solvents of increasing polarity. ....	11
Figure 7. Resin model molecules proposed by Murgich <sup>36</sup> . Reprinted with permission from Murgich, J.; Rodríguez, J. M.; Aray, Y. Molecular recognition and molecular mechanics of micelles	

of some models asphaltenes and resin. *Energy & Fuels* **1996**, 10 (7), 68–76. Copyright 1996 American Chemical Society. ....14

Figure 8. Schematics of micelles proposed by Pfeiffer and Saal<sup>57</sup> in 1939. (I) Fully peptized asphaltene cores and (II) micelles deficient in resins giving rise to a gel structure and non-Newtonian behavior. Reprinted with permission from Pfeiffer, J. P.; Saal, R. N. J. J. *Asphaltic bitumen as Colloid System*. *Phys. Chem.* 1940, 44 (2), 139–149. Copyright 1940 American Chemical Society. ....20

Figure 9. Proposed asphaltene aggregate structure by Teh Fu Yen and co workers<sup>66,67</sup>. Reprinted with permission from Yen, T. F.; Erdman, J. G.; Pollack, S. S. *Investigation of the Structure of Petroleum Asphaltenes by X-Ray Diffraction Anal. Chem.* **1961**, 33 (11), 1587–1594; and Dickie, J. P.; Yen, T. F. *Macrostructures of the asphaltic fractions by various instrumental methods*. *Anal. Chem.* **1967**, 39 (14), 1847–1852. Copyrights 1961 and 1967 American Chemical Society. ....22

Figure 10. Asphaltene hierarchical structures proposed by Mullins<sup>68</sup>. Reprinted with permission from Mullins, O. C. *The modified Yen Model*. *Energy & Fuels* **2010**, 24 (4), 2179–2207. Copyright 2010 American Chemical Society. ....23

Figure 11. Supramolecular models for heavy organic fractions in crude oil. (A) Organization proposed by Dickie<sup>74</sup> in 1967 and (B) by Gray<sup>83</sup>, in 2011, defying the increasingly acceptance of asphaltenes nanoaggregates as proposed by Mullins<sup>68</sup>. Reprinted with permission from Gray, M. R.; Tykwinski, R. R.; Stryker, J. M.; Tan, X. *Supramolecular assembly model for aggregation of petroleum asphaltenes*. *Energy and Fuels* **2011**, 25 (7), 3125–3134; and Dickie, J. P.; Yen, T. F. *Macrostructures of the asphaltic fractions by various instrumental methods*. *Anal. Chem.* **1967**, 39 (14), 1847–1852. Copyrights 2011 and 1967 American Chemical Society. ....26

Figure 12. Physical model of petroleum according to Wiehe<sup>11,85</sup>. Reprinted with permission from Wiehe, I. A.; Kennedy, R. J. The Oil Compatibility Model and Crude Oil Incompatibility Energy and Fuels **2000**, 14 (1), 56–59. Copyrigh 2000 American Chemical Society.....27

Figure 13. Atomic Force Microscopy images from petroleum (PA) and coal (CA) asphaltenes. Reprinted with permission from Schuler, B.; Meyer, G.; Peña, D.; Mullins, O. C.; Gross, L. J. Unraveling the molecular structure of asphaltenes by Atomic Force Microscopy. Am. Chem. Soc. **2015**, 137 (31), 9870–9876. Copyrigh 2000 American Chemical Society.....30

Figure 14. Coal and petroleum asphaltene molecules after Schuler<sup>100</sup>. Reprinted with permission from Schuler, B.; Meyer, G.; Peña, D.; Mullins, O. C.; Gross, L. J. Unraveling the molecular structure of asphaltenes by Atomic Force Microscopy. Am. Chem. Soc. **2015**, 137 (31), 9870–9876. Copyrigh 2015 American Chemical Society. ....31

Figure 15. Asphaltene structures from different origins as hypothesized by Schuler<sup>101</sup>. Reprinted with permission from Schuler, B.; Meyer, G.; Peña, D.; Mullins, O. C.; Gross, L. J. Heavy oil based mixtures of different origins and treatments studied by Atomic Force Microscopy. Am. Chem. Soc. **2015**, 137 (31), 9870–9876. Copyrigh 2017 American Chemical Society.....32

Figure 16. Sorbent active sites and asphaltene active groups involved on asphaltenes adsorption processes. Reprinted with permission from Adams, J. J. Asphaltene adsorption, a literature review. Energy & Fuels **2014**, 28 (5), 2831–2856. Copyrigh 2014 American Chemical Society...35

Figure 17. Onset of asphaltene flocculation variation according to the utilized nonsolvent. Reprinted with permission from Wiehe, I. A.; Yarranton, H. W.; Akbarzadeh, K.; Rahimi, P. M.; Teclemariam, A. The paradox of asphaltene precipitation with normal paraffins. Energy & Fuels **2005**, 19 (4), 1261–1267. Copyrigh 2005 American Chemical Society.....36

Figure 18. Amount of precipitated asphaltenes as a function of paraffin hydrocarbon. Reprinted with permission from Mitchell, D. L.; Speight, J. G. The solubility of asphaltenes in hydrocarbon solvents. *Fuel* **1973**, 52 (2), 149–152. Copyright 1973 Elsevier. ....37

Figure 19. Classical experimental assembly for detecting asphaltene destabilization at high pressure conditions. (A) System with stable asphaltenes and (B) system with destabilized asphaltenes presenting a reduction in the light transmission due to light scattering caused by the presence of particles. ....38

Figure 20. Classical experimental assembly for detecting asphaltene deposition. Crude oil and an asphaltene precipitant are mixed prior to be flown through a capillary tube. The capillary inlet and outlet pressure ( $P_1$  and  $P_2$ ) are constantly measured. Asphaltene deposition is estimated by calculating the decrease of the capillary radius, with the Hagen-Poiseuille law, taken into account the pressure drop ( $P_2 - P_1$ )<sup>132</sup>. ....39

Figure 21. Size scale on asphaltene particles inducing deposition. ....40

Figure 22. Occurring processes once asphaltenes are destabilized according to Vargas<sup>142</sup>. ....42

Figure 23. AT-cut quartz crystal and the temperature sensitivity of different quartz crystals cuts. ....44

Figure 24. Admittance analysis of a 3 MHz quartz crystal resonating at its 3<sup>rd</sup> overtone ( $n=3$ ). The real (Conductance-G) and imaginary parts (Susceptance-B) of admittance is shown. At quartz resonance conductance is at its maxima and susceptance is zero.  $2\Gamma n$  is obtained directly from the frequency window between maximum and minimum susceptance. These points are equivalent to the half width at half band of the conductance spectra. ....49

Figure 25. Two different experimental schematics when using quartz crystals to research on crude oil adsorption/deposition processes. (A) Mostly used experimental assembly. A stable or unstable solution of extracted asphaltenes or diluted crude oil is injected into a flow cell in fairly low flow rates ( $\mu\text{L}/\text{min}$ ). Normally one quartz side is exposed to the analyte. (B) Experimental assembly utilized in the present work. The quartz is totally immersed in crude oil, diluted crude oils, or solutions of extracted asphaltenes in toluene. The asphaltenes are destabilized in situ by the injection of n asphaltene nonsolvent. An asphaltene good solvent may also be used to study changes in crude oil viscosity due to dilution. ....57

Figure 26. Schematics from the possible yielding asphaltenes deposits on the gold electrodes. One electrode is shown for clarity. (A) One side of the quartz exposed to a crude oil with stable asphaltenes. (B) and (C) one side of the quartz crystal exposed to crude oil with destabilized asphaltenes forming a smooth and elastic deposit as exposed in (B) or a rough and viscoelastic deposit as shown in (C). ....59

Figure 27. Various deposit and liquid loads on the quartz crystal surface. Only one quartz side is shown for simplicity. The parameters influencing frequency and bandwidth data is shown in each case.....61

Figure 28. Schematics on the model application and definition of  $\Delta F_m$ ,  $\Delta F_\eta$  and  $\Delta\Gamma_\eta$ . ....64

Figure 29. Schematics of the experimental assembly for experiments at atmospheric pressure.68

Figure 30. Experimental run time and achieved n-heptane mass fractions during continuous crude oil titration. N-heptane was injected at a constant mass flow rate as is shown by the second y-axis. A baseline collection of frequency and bandwidth is done with the n-heptane injection starting at (1). The n-heptane injection from (1) to (2) is performed at lower mass flow rate to

assure good mixing from the viscous crude oil with n-heptane. At (2) the n-heptane mass flow rate is adjusted to the desired experimental flow rate ( $\sim 9$  mg/s).....69

Figure 31. (A) High pressure experimental apparatus. (1) High pressure PVT cell with the quartz crystal resonator. (2) Network analyzer and (3) high pressure syringe pump. (B) An image of the high pressure cell thermo-stabilized by a build in jacket (a); step motor (b); magnetic stirrer (c); temperature sound (d); coaxial cable and connector (e); high pressure cap (f) and connected needle valves for injecting asphaltenes destabilizers or cleaning procedures (g). .....72

Figure 32. Crude oil C diluted with toluene, response in resonance frequency and bandwidth as a function of toluene mass fraction ( $x_{\text{toluene}}$ ). .....76

Figure 33. Change in resonance frequency and bandwidth due to cyclohexane continuous injection into crude oil C.  $x_{\text{cyclohexane}}$ = cyclohexane mass fraction.....76

Figure 34. Inter-harmonic spreading from the normalized frequency and bandwidths as a function of toluene mass fraction (Crude oil C) .....78

Figure 35. Variations in system composition with toluene injection for each cycle of measurement of complex resonance frequency data by the network analyzer (from the 3<sup>rd</sup> to 7<sup>th</sup> overtone). .78

Figure 36. Resonance frequency and bandwidth changes for toluene injection into crude oil C as a function of time.....78

Figure 37.  $\Delta Fm$ ,  $\Delta F\eta$  and  $\Delta \Gamma\eta$  determination for the continuous dilution of crude oil C with toluene at 25 °C and atmospheric pressure.....79

Figure 38. Density-viscosity product and thickness of the interfacial layer as determined from the viscous and mass contributions to change in resonance frequency and bandwidth. Crude oil C continuously injected with toluene at 25 °C and atmospheric pressure.....80

Figure 39. Density-viscosity product and  $h_{interface}$  for the dilution of crude oil D with toluene at 25 °C and atmospheric pressure. ....81

Figure 40. Ratio between the model calculated density-viscosity products from change in resonance frequency and bandwidth data for the dilution of crude oil D with toluene.....81

Figure 41. Comparison between model calculated thicknesses for the interfacial layer in the case of the continuous injection of toluene and n-heptane in crude oil A. *h<sub>interface</sub>* becomes *h<sub>deposit</sub>* for the case of crude oil titration with an asphaltene nonsolvent. 25 °C and atmospheric pressure.....82

Figure 42.  $h_{interface}$  for the dilution of crude oils A, C, D and E with toluene at 25 °C and atmospheric pressure.....83

Figure 43. Change in resonance frequency and bandwidth for the continuous n-heptane injection in crude oil C at 25 °C. Circles, squares and crosses standing for 3<sup>rd</sup>, 5<sup>th</sup> and 7<sup>th</sup> overtones of resonance. Full blue lines obtained from the crude oil dilution with toluene. Number 1, 2 and 3 indicates the different regimes occurring within the change in resonance frequency above asphaltene onset of destabilization. ....84

Figure 44. Bandwidth change profile for the n-heptane injection into crude oil C at 25 °C and atmospheric pressure. Circles, squares and crosses standing for 3<sup>rd</sup>, 5<sup>th</sup> and 7<sup>th</sup> overtones of resonance. Full blue lines obtained from the crude oil dilution with toluene. ....86

Figure 45. N-heptane or toluene injection into crude oil B at 25 °C and atmospheric pressure. Circles, squares and crosses standing for 3<sup>rd</sup>, 5<sup>th</sup> and 7<sup>th</sup> overtones of resonance. Full blue lines are obtained from the crude oil dilution with toluene. ....86

Figure 46. N-heptane injection into crude oil A at 25 °C and atmospheric pressure. Circles, squares and crosses standing for 3<sup>rd</sup>, 5<sup>th</sup> and 7<sup>th</sup> overtones of resonance. Full blue lines are obtained from the crude oil dilution with toluene. ....87

Figure 47. Change in Frequency and bandwidth for the continuous n-C7 injection in crude oil D at 25 °C and atmospheric pressure. Circles, squares and crosses standing for 3<sup>rd</sup>, 5<sup>th</sup> and 7<sup>th</sup> overtones of resonance.....88

Figure 48. Change in Frequency and bandwidth for the continuous n-C7 injection in crude oil E at 25 °C and atmospheric pressure. Circles, squares and crosses standing for 3<sup>rd</sup>, 5<sup>th</sup> and 7<sup>th</sup> overtones of resonance respectively. ....88

Figure 49. Change in Frequency and bandwidth for the continuous n-C7 injection in crude oil F at 25 °C and atmospheric pressure. Circles, squares and crosses standing for 3<sup>rd</sup>, 5<sup>th</sup> and 7<sup>th</sup> overtones of resonance respectively. ....89

Figure 50. Change in Frequency and bandwidth for the continuous n-C7 injection in crude oil G at 25 °C and atmospheric pressure. Circles, squares and crosses standing for 3<sup>rd</sup>, 5<sup>th</sup> and 7<sup>th</sup> overtones of resonance respectively. ....89

Figure 51. Change in Frequency and bandwidth for the continuous n-C7 injection in crude oil H at 25 °C and atmospheric pressure. Circles, squares and crosses standing for 3<sup>rd</sup>, 5<sup>th</sup> and 7<sup>th</sup> overtones of resonance respectively. ....90

Figure 52. Quartz impedance analysis as a function of time for the continuous injection of n-heptane into crude oil B. Dilution with toluene is also added for comparison as depicted by the full line. The diamond indicates the end of the n-heptane injection. The inset enlarges the bandwidth profile as a function of time for the region in which bandwidth starts to increase.

Circles, squares and crosses standing for 3<sup>rd</sup>, 5<sup>th</sup> and 7<sup>th</sup> overtones of resonance respectively.—3<sup>rd</sup> harmonic for toluene injection. ....91

Figure 53. Bandwidth profile ( $\Delta\Gamma n/n12$ ) as a function of time for the n-heptane continuous injection into crude oil A. The vertical dashed line indicates the onset of asphaltene destabilization and the diamond (◆) the end of the n-heptane injection. The bandwidth minima is shown to appear much before the end of the n-heptane injection. The spreading between harmonics augments after the bandwidth minima. The augmentation of the bandwidth appears to be independent on the n-heptane injection as no discontinuities or curve inflections are observed at the end of the injection (see inset). ....92

Figure 54. Change bandwidth and dissipation factor due to deposition on one electrode surface for the seventh harmonic obtained by applying a Grunberg—Nissan-type mixing rule with one adjustable parameter to the crude oil/n-heptane mixture <sup>178</sup>. The values are for one electrode side. ....95

Figure 55. Asphaltene onset of destabilization by analysis of derivatives of changes in resonance frequency relative to the asphaltene solvent or nonsolvent mass fraction. Two asphaltene solvents were used: toluene and cyclohexane. Asphaltene precipitation performed by n-hexane. The inset shows the n-heptane mass fraction points in which the derivative of the asphaltene destabilization experiment diverges from the pure dilution. The 3<sup>rd</sup>, 5<sup>th</sup> and 7<sup>th</sup> harmonics of resonance are shown for the n-heptane titration. Only the third harmonic is shown for the dilution experiments (cyclohexane and toluene). Crude oil C, all the experiments were performed at 25 °C and atmospheric pressure.....98

Figure 56. Onset of asphaltene destabilization determination by the fitting of a mixing rule to the dilution region and extrapolating to the case of  $x_{C7}=1$ . (1) Onset of asphaltene destabilization obtained by the deviation from the experimental points to the mixing rule and (2) onset of asphaltene destabilization obtained by the derivative method. Crude oil C at 25 °C and atmospheric pressure.....99

Figure 57. Asphaltene onset of destabilization by fitting a mixing rule to the third overtone of resonance for the continuous asphaltene destabilization from crude oil C at 45 °C and atmospheric pressure.....100

Figure 58. Inter-harmonic spreading analysis for detecting onset of asphaltene destabilization. Blue stripe represents onset conditions. ....102

Figure 59. Asphaltene onset of destabilization determined by the analysis of *hinterface* and *hdeposit*. Crude oil C at 25 °C and atmospheric pressure. ....103

Figure 60. Impedance analysis and model application for the n-heptane continuous injection into crude oil A.....105

Figure 61. Impedance analysis and model application for the n-heptane continuous injection into crude oil B.....105

Figure 62. Impedance analysis and model application for the n-heptane continuous injection into crude oil C.....106

Figure 63. Impedance analysis and model application for the n-heptane continuous injection into crude oil D. ....106

Figure 64. Impedance analysis and model application for the n-heptane continuous injection into crude oil E.....107

Figure 65. Density-viscosity ( $\rho\eta$ ) product from the resonance frequency and bandwidth changes due to viscous effects ( $\Delta\Gamma\eta$  and  $\Delta F\eta$ ) obtained by the model application (Equations 21 and 22). Experimental  $\rho\eta$  values are added for crude oil C. Triangles:  $\rho\eta\Delta\Gamma\eta$ , squares:  $\rho\eta\Delta F\eta$  and crosses:  $\rho\eta_{exp}$ .) .....108

Figure 66. Deposit thicknesses obtained during the n-heptane continuous injection into the five studied crude oils. ....109

Figure 67. Discretized regions during asphaltene destabilization and deposition by n-heptane into crude oil A. Upper panel:  $\Delta\Gamma_n$ ; middle panel: derivatives of frequency change in relation to n-heptane mass fractions (black) and toluene mass fractions (red); Lower panel: Normalized frequency changes ( $\Delta F_n/n$ ) and model calculated  $\Delta F_m$  and  $\Delta F_n$ . Numbers 1 to 5 indicates different regions appearing titration of the studied crude oils with n-heptane. ....111

Figure 68. Model calculated change in frequency and bandwidth as a function of time for the continuous injection of n-heptane into crude oil A. ....113

Figure 69. Change in resonance frequency and bandwidth up to the 15<sup>th</sup> overtone of resonance. Crude oil C at 25 °C and atmospheric pressure.....115

Figure 70. Bandwidth profile for the n-heptane injection into crude oil C at 25 °C, recording of seven overtones of resonance. The red dashed line indicates the earlier appearance of the bandwidth minima with higher overtones of resonance.....116

Figure 71. Comparison between the model calculated density-viscosity product using the three and seven overtones of resonance. Crude oil C at 25 °C and atmospheric pressure. ....116

Figure 72. Comparative of deposit thicknesses obtained with the continuous n-heptane injection in 20 g of crude oil (blue) and in 40 g (black squares). Crude oil C at 25 °C and atmospheric pressure. ....117

Figure 73. Comparative of  $h_{\text{deposit}}$  obtained from the experiment with initial mass of 20 g (3<sup>rd</sup>, 5<sup>th</sup> and 7<sup>th</sup> utilized overtones – blue), and 40 g (3<sup>rd</sup>, 5<sup>th</sup>, and 7<sup>th</sup> overtones – red; and all the overtones – black squares). Crude oil C at 25 °C and atmospheric pressure.....118

Figure 74. Model application for different n-heptane mass fractions. Continuous n-heptane injection into crude oil C. (1) .....119

Figure 75. Model application for different n-heptane mass fractions. Continuous n-heptane injection into crude oil C. (2) .....120

Figure 76. Model application for different n-heptane mass fractions. Continuous n-heptane injection into crude oil C. (3) .....121

Figure 77. N-heptane mass fraction as a function of experimental run time for an intermittent n-heptane injection into crude oil C at 25 °C and atmospheric pressure. ....122

Figure 78. Intermittent n-heptane injection into crude oil C at 25 °C and atmospheric pressure. Circles, squares and crosses standing for 3<sup>rd</sup>, 5<sup>th</sup> and 7<sup>th</sup> overtones of resonance.....123

Figure 79. Frequency and bandwidth profiles when the n-heptane injection is stopped at the dilution plus destabilization region. Circles, squares and crosses standing for 3<sup>rd</sup>, 5<sup>th</sup> and 7<sup>th</sup> overtones of resonance.....125

Figure 80. Comparison between bandwidth profiles from the continuous n-heptane injection into crude oil with continuous and intermittent n-heptane injection. ....126

Figure 81. Frequency and bandwidth profiles for the continuous and intermittent (i) n-heptane injection into crude oil C as a function of n-heptane mass fraction.....127

Figure 82. Comparative of deposit profiles obtained from the n-heptane injection into crude oil C at 3 mg/s; 8 mg/s and 8 mg/s with intermittent n-heptane injection.....128

Figure 83. (I) Bandwidth profiles for the continuous n-heptane injection into crude oil at 3 mg/s; 8 mg/s; 8 mg/s (intermittent injection) and at 8 mg/s with dodecanoic acid at 2 wt%. (II) Model calculated deposit thickness for the exposed experiments.....129

Figure 84. Quartz activity evaluation on the frequency and bandwidth changes. (I) The quartz crystal was shut off and turned on after 2 hours (II). The n-heptane mass flow rate was kept constant during the entire experiment.....130

Figure 85. Evaluation of the influence of the first deposited asphaltene layer on deposit build up. (I) Changes in resonance frequency as a function of time. The time of the cleaning procedure is not shown. (II) Changes in resonance frequency as a function of n-heptane mass fraction ( $x_{C7}$ ). During the cleaning the n-heptane injection was stopped. Red arrows indicate the lag on the detection of deposition after the quartz was cleaned. Circles, squares and crosses standing for 3<sup>rd</sup>, 5<sup>th</sup> and 7<sup>th</sup> overtones of resonance respectively.....131

Figure 86. Deposition profile after the quartz crystal was cleaned with toluene and re-submerged in the crude oil/n-heptane solution. The inset magnifies the changes in bandwidth highlighting its imperceptible variation despite the fact that a deposit yielding 1000 Hz in frequency change is created on the gold electrodes. Circles, squares and crosses standing for 3<sup>rd</sup>, 5<sup>th</sup> and 7<sup>th</sup> overtones of resonance respectively. ....132

Figure 87. Bandwidth (I) and resonance frequency (II) profiles for the continuous n-heptane injection into crude oil which was or not submitted to heat treatment at 60 °C. The experiment with the heat treated crude oil is indicated by the arrows. Crude oil C at 25 °C and atmospheric pressure.....134

Figure 88. Effect of temperature treatment on bandwidth changes induced by asphaltene deposition.  $x_{C7}$  stands for n-heptane mass fraction .....136

Figure 89. Density-viscosity products as obtained from the change in frequency and bandwidth data for crude oil C with heat treatment before experiment. Circles, squares and crosses standing for 3<sup>rd</sup>, 5<sup>th</sup> and 7<sup>th</sup> overtones of resonance. Big blue crosses are experimental density-viscosity values.....137

Figure 90. Density-viscosity profile for crude oil C with no heat treatment (I) and with 2 hours heat treatment and 2 hours at 25 °C (II).  $x_{C7}$  stands for n-heptane mass fraction.....138

Figure 91. Bandwidth profile for crude oil A with heat treatment (I) and without heat treatment (II).  $x_{C7}$  stands for n-heptane mass fraction. ....139

Figure 92. Differences in bandwidth profile when the crude oil is submitted to heat treatment before the n-heptane injection to crude oil A. Both experiments were done at 25 °C.  $x_{C7}$  stands for n-heptane mass fraction.....139

Figure 93.  $\Delta F$  and  $\Delta \Gamma$  as a function of n-heptane mass fraction ( $x_{C7}$ ) for the continuous n-heptane injection into crude oil C at 25 °C and atmospheric pressure.....141

Figure 94.  $\Delta F$  and  $\Delta \Gamma$  as a function of time for the continuous n-heptane injection into crude oil C at 25 °C and atmospheric pressure. ....141

Figure 95.  $\Delta F$  and  $\Delta\Gamma$  as a function of time for the quartz crystal with asphaltenic deposit obtained at the end of the experiments exposed in Figures 93 and 94. The system was kept at 25 °C during the entire experiment. ....142

Figure 96. Comparison of the model calculated deposit thicknesses for the crude oil C titrated with n-heptane (I) and the thickness obtained when washing the deposit and immersing it in pure n-heptane (II). The experiments were done at 25 °C and atmospheric pressure.....143

Figure 97. Model calculated density-viscosity profile from changes in frequency and bandwidth as a function of time for the asphaltenic deposit in pure n-heptane. The red line is the density-viscosity product obtained when the clean quartz crystal (with no asphaltenic deposit) is immersed in pure n-heptane. ....144

Figure 98. Quartz crystal resonance frequency change and estimated deposit thickness for the asphaltenic deposit in air at 25 °C.....145

Figure 99. Changes in frequency and bandwidth, as a function of toluene mass fraction, for the asphaltenic deposit dissolution by continuous toluene injection into pure n-heptane. Circles, squares and crosses standing for 3<sup>rd</sup>, 5<sup>th</sup> and 7<sup>th</sup> overtones of resonance.  $X_{C_7H_8}$  stands for toluene mass fraction. ....146

Figure 100. Changes in frequency and bandwidth, as a function experimental run time, for the asphaltenic deposit dissolution by continuous toluene injection into pure n-heptane. Circles (black), squares and crosses (light gray) standing for 3<sup>rd</sup>, 5<sup>th</sup> and 7<sup>th</sup> overtones of resonance...147

Figure 101. Bandwidth changes for the crude oil C titration with n-heptane at different temperatures. Circles (black), squares and crosses (light gray) standing for 3<sup>rd</sup>, 5<sup>th</sup> and 7<sup>th</sup> overtones of resonance respectively. ....149

Figure 102. Bandwidths profiles as a function of experimental run time for the titration of crude oil C with heptane at different temperatures. Arrows: (1) n-heptane stop injection; (2) n-heptane injection re-start; (3) and (4) n-heptane injection and system agitation are stopped. Circles (black), squares and crosses (light gray) standing for 3<sup>rd</sup>, 5<sup>th</sup> and 7<sup>th</sup> overtones of resonance respectively.

.....150

Figure 103. Change in bandwidth as a function of experimental run time for crude oil D titrated with n-heptane at various temperatures. Circles (black), squares and crosses (light gray) standing for 3<sup>rd</sup>, 5<sup>th</sup> and 7<sup>th</sup> overtones of resonance. Red diamonds: n-heptane injection stop. ....152

Figure 104.  $\Delta F$  and  $\Delta \Gamma$  for a clean quartz crystal immersed in precipitated asphaltenes at 45 °C. Circles (black), squares and crosses (light gray) standing for 3<sup>rd</sup>, 5<sup>th</sup> and 7<sup>th</sup> overtones of resonance.

.....154

Figure 105. Comparison between changes in resonance frequency (I) and bandwidth (II) for the asphaltene precipitation from a diluted crude oil C and a solution of extracted asphaltenes (from crude oil C) in toluene. The asphaltene concentration in both experiments was 10 g/L.....155

Figure 106. Onset determination for the case of diluted crude oil (I) and extracted asphaltenes (II) by the fitting and optimizing a dilution mixing rule to the same n-heptane mass fraction range (from  $x_{hep}=0.02$  to  $x_{hep} = 0.28$ ).....156

Figure 107. Derivative of frequency as a function of n-heptane mass fraction for the continuous destabilization of asphaltenes from diluted crude oil (oil C) and from a solution of extracted asphaltenes in toluene. Initial asphaltene concentrations: 10 g/L. Experiments performed at 25 °C.....156

Figure 108. Bandwidths profiles for the asphaltene destabilization from diluted and extracted asphaltenes, both solutions were utilized with 10 g/L of asphaltenes. The onset of destabilization is observed to be occurring from  $x_{C7} = 0.3$  to  $x_{C7} = 0.4$  (from  $\Delta F$  data) and is hardly accused by the bandwidth profile, despite the low system viscosities.....157

Figure 109. Response in the change in resonance frequency (I) and bandwidth (II) as a function of n-heptane mass fraction for the destabilization of extracted asphaltenes (crude oil A) in toluene (asphaltene concentration: 10 g/L). Circles (black), squares and crosses (light gray) standing for 3<sup>rd</sup>, 5<sup>th</sup> and 7<sup>th</sup> overtones of resonance respectively. ....158

Figure 110. Response in the change in resonance frequency (I) and bandwidth (II) as a function of experimental run time for the destabilization of extracted asphaltenes (crude oil A) in toluene (asphaltene concentration: 10 g/L). Circles (black), squares and crosses (light gray) standing for 3<sup>rd</sup>, 5<sup>th</sup> and 7<sup>th</sup> overtones of resonance respectively. Red diamond: n-heptane injection stop. .158

Figure 111. Freshly prepared and aged asphaltene solution effect on bandwidth profile. Circles, squares and crosses standing for 3<sup>rd</sup>, 5<sup>th</sup> and 7<sup>th</sup> overtones of resonance respectively. Blue rectangle: asphaltene onset of destabilization region.....159

Figure 112. Comparison between bandwidth profiles for the asphaltene destabilization from crude oil A ( $C_{asp} = 116$  g/L) and from extracted asphaltenes (crude oil A) in toluene ( $C_{asp} = 10$  g/L). Circles, squares and crosses standing for 3<sup>rd</sup>, 5<sup>th</sup> and 7<sup>th</sup> overtones of resonance respectively. Initial masses of crude oil and asphaltene solution: 20 g. ....160

Figure 113. Comparison between bandwidth profiles from de continuous destabilization of crude oil and extracted asphaltenes with n-heptane injection. Blue rectangle: asphaltene destabilization region. Crude oil C and asphaltenes from crude oil C. 25 °C and atmospheric pressure. ....161

Figure 114. Extracted asphaltenes in toluene destabilization by continuous n-heptane injection at 25 °C. I.  $C_{asp}= 31$  g/L and II.  $C_{asp}=10$  g/L. Crude oil C. ....163

Figure 115.  $\Delta F/n$  and  $\Delta\Gamma/n^{1/2}$  profiles for the continuous titration of crude oil C with different concentration of commercial inhibitor. I (I) 0.5 wt %; (II) 1 wt % and (III) 2 wt % (colored point). The crude oil without inhibitor is shown as the blank experiment. Experiments performed at 25 °C and atmospheric conditions. ....165

Figure 116. Derivative of frequency versus n-heptane mass fraction for the continuous n-heptane injection into crude oil C treated or not with proprietary inhibitor. The derivatives from the dilution experiments (with cyclohexane and toluene) are also added. The horizontal arrow indicates the increase in the delay of the first steep decrease in resonance frequency change which is higher the higher the inhibitor concentration. Blue rectangle: onset of asphaltene destabilization region. ....166

Figure 117. Deposit thicknesses obtained by the continuous n-heptane injection into crude oil C, with or without proprietary chemical inhibitor. The thicknesses obtained with the dilution (toluene and cyclohexane) experiments are also added. Horizontal arrows in (I) indicates the decrease in the thickness of the deposited layer. (II) Magnification of the region where the precipitation experiments diverges from the dilution experiments. ....167

Figure 118.  $\Delta F/n$  and  $\Delta\Gamma/n^{1/2}$  profiles for the continuous titration of crude oil C with different concentration of DBSA (colored points). I. 0.5 wt %; II. 1 wt % and III. 2.5 wt %. The crude oil without DBSA is indicated as the blank experiment. ....168

Figure 119. Derivative of frequency versus n-heptane mass fraction for the cases of crude oil C dilution and precipitation with the addition of DBSA at different concentrations. ....169

Figure 120. Deposit thicknesses obtained when crude oil C doped with different concentrations of DBSA is continuously titrated with n-heptane at 25 °C. Blank experiment is indicated as without in the legend on the graph.....170

Figure 121. Change in resonance frequency and dissipation profile for the destabilization of asphaltenes from crude oil C doped with dodecanoic acid (2 wt %) (colored symbols) and the blank experiment. ....171

Figure 122. Derivative of frequency versus n-heptane mass fraction for the continuous injection of n-heptane into crude oil C doped with dodecanoic acid (2 wt %). ....172

Figure 123. Model calculated deposit thickness for the destabilization of crude oil doped with dodecanoic acid (full diamonds) and for the crude oil C with no chemical (squares). The high bandwidth yielded by the crude oil destabilization in the presence of dodecanoic acid yield an estimated deposit thickness much greater than the ones obtained with the crude oil without the chemical. ....173

Figure 124. Step n-heptane injection into crude oil C to an n-heptane mass fraction of 0.86. Circles (black), squares and crosses (light gray) standing for 3<sup>rd</sup>, 5<sup>th</sup> and 7<sup>th</sup> overtones of resonance...174

Figure 125. Zoom in the change in frequency and bandwidth data after the step n-heptane addition. Circles (black), squares and crosses (light gray) standing for 3<sup>rd</sup>, 5<sup>th</sup> and 7<sup>th</sup> overtones of resonance respectively.....175

Figure 126. Model calculated density-viscosity and deposit thickness profile for the step n-heptane injection into crude oil C above onset of asphaltene destabilization conditions.....176

Figure 127. Step n-heptane injection into crude oil A to an n-heptane mass fraction of 0.87. Circles (black), squares and crosses (light gray) standing for 3<sup>rd</sup>, 5<sup>th</sup> and 7<sup>th</sup> overtones of resonance...177

Figure 128. Model calculated density-viscosity and deposit thickness profile for the step n-heptane injection into crude oil A above onset of asphaltene destabilization conditions ( $x_{hep}=0.87$  wt %). .....178

Figure 129. Schematics of the proposed physical processes occurring within the continuous destabilization of asphaltenes by n-heptane injection. Different colors standing for different asphaltenes solubility classes. ....180

Figure 130. General perceived effect when asphaltenes are destabilized by a step solubility change. Particles deposition are truncated in a very early stage of asphaltene particle aggregation. ....183

Figure 131. (A) Proposed mechanisms of ordered aggregation obtained for the first destabilized particles by a continuous solubility gradient which induce severe deposition by inducing particles aggregation in an ordered way. (B) Disordered aggregation of the first destabilized particles occurring with the step solubility gradient yielding aggregates with low propensity to deposit due to steric hindrances. (1) nanoaggregate (2) asphaltene monomer (3) nanoaggregate (4) paraffin (5) two nanoaggregates orderly aggregated (6 and 7) two nanoaggregates disorderly aggregated. ....184

Figure 132. Hypothesis on the occurring processes when extracted asphaltenes in toluene are continuously destabilized by n-heptane injection. Different colors standing for different asphaltenes solubility classes. ....185

Figure 133. Macroscopic and Microscopic aspects on the precipitated asphaltenes by the step and continuous n-heptane injection. (I) and (III): Optical microscopy images from the asphaltenes flocs, in the bulk media, destabilized by a step or continuous n-heptane injection. (II) and (IV):

aspect of the wall of the mixing vessel after a step (II) or continuous (IV) n-heptane injection is performed. A thick deposit layer on the glass surface is observed when the asphaltenes are destabilized continuously. In (IV) it can be observed a thick and easily removable (by agitation) asphaltene deposit and a rigidly attached film on the glass surface. Such film is not observed in the case when the asphaltene destabilization is proceeded at once (step destabilization).....186

Figure 134. Quartz crystal resonator after two experiments in which n-heptane was continuously added to crude oil. (I) An asphaltene deposit is observed on the quartz and electrode surfaces. In the top of the image a region which was cleaned with toluene can be observed. (II) Asphaltene film on the metal surface inducing a change in the surface color by birefringence. ....187

Figure 135. Micrographs of some asphaltene deposits on the gold electrode surface after the continuous destabilization procedure. (I) And (II): deposits obtained after the continuous destabilization of crude oil C at 25 °C; (III) and (IV), deposits obtained after the continuous destabilization of crude oil A with 11.9 wt % asphaltenes at 25 °C; (V), asphaltene deposit from crude oil C (continuous destabilization at 25 °C) dissolved by toluene; (VI) asphaltene deposit formed after the onset of flocculation in a clean gold surface and its frontier with toluene dissolution; (VII), asphaltene deposit formed after the continuous asphaltene destabilization of crude oil D by continuous n-heptane injection at 55 °C; (VIII), asphaltene deposit after continuous destabilization of crude oil D with n-pentane at 25 °C. ....188

Figure 136. Micrographs from the bulk fluid (crude oil/n-heptane mixture) during the n-heptane injection into crude oil C (25 °C and atmospheric pressure). ....190

Figure 137. Quantification of the precipitated material by the continuous and step asphaltenes destabilization. (I) n-C7 asphaltenes masses in each crude oil (red) and the obtained precipitated

masses after each destabilization procedure (step-s or continuous-c). (II) Ratio between the mass of precipitated materials obtained in the step n-heptane injection and continuous n-heptane injection.....191

Figure 138. Experimental assembly utilized for collecting asphaltene deposit samples at different n-heptane mass fractions. (I) Mixing vessel with the quartz and the silica plates dipped in the crude oil/n-heptane mixture. The mixing vessel is inside an oven to maintain constant temperature during the experiment and is posed above a magnetic stirrer. The n-heptane injection is performed with the aid of a peristaltic pump subbing inserted in the bulk fluid. (II) and (III) quartz crystal with the surrounding silica coupons for collecting asphaltene deposits. ....193

Figure 139. Changes in resonance frequency and bandwidth for the continuous n-heptane injection into crude oil C for sampling asphaltenic deposits with the aid of silica coupons. Red vertical dashed lines indicate the system composition in n-heptane when the samples were withdrawn from the mixing vessel.....193

Figure 140. Model calculated crude oil/n-heptane density-viscosity product (I) and asphaltene deposit thicknesses (II) for the experiment shown in Figure 137. Vertical dashed lines indicate the system composition at which the coupons were withdrawn from the system. ....194

Figure 141. 2D AFM height profile (I) and the 3D representation (II) from the asphaltenic deposit sample taken at  $x_{C7}=0.48$ , above onset conditions and before the deep decrease in resonance frequency arising in region 3 as discretized in Figure 72. The vertical and horizontal cross sections of deposit grains represented by 1, 2 and 3 are shown in Figure 140.....195

Figure 142. Horizontal and vertical cross sections from three deposit nuclei as shown in Figure 139. The deposit “grains” are observed to be round shaped with diameters much greater than their height.....196

Figure 143. Height profile and the correspondent 3D representation for the nucleus or grain number “1” in Figure 139 at a much greater magnification (200 x 100 nm).....196

Figure 144. 2D height profile (I), 3D representation (II) and mean square roughness (III) for the asphaltenic deposit sample taken at  $x_{C7}=0.52$ . .....197

Figure 145. (I) 2D AFM image after the scratching of the deposit and (II) the thickness profile obtained from point “a” to point “b” in the 2D height image. Sample taken at  $x_{C7}=0.52$ . The arrow indicates the area without asphaltenic deposit obtained by scratching the silica surface with the AFM tip. ....198

Figure 146. 2D height profile, 3D representation and mean square roughness of one vertical and one horizontal deposit sections. Sample taken at  $x_{C7}=0.67$ . The arrow indicates the presence of cavities within the deposit. ....199

Figure 147. (I) 2D AFM image after the scratching of the deposit and (II) the thickness profile obtained from point “a” to point “b” in the 2D height image. Sample taken at  $x_{C7}=0.67$ . The arrow indicates the area without asphaltenic deposit obtained by scratching the silica surface with the AFM tip. ....200

Figure 148. 2D height profile, 3D representation and mean square roughness of one vertical and one horizontal deposit sections. Sample taken at  $x_{C7}=0.79$ . The arrow indicates the presence of cavities within the deposit. ....200

Figure 149. (I) 2D AFM image after the scratching of the deposit and (II) the thickness profile obtained from point “a” to point “b” in the 2D height image. Sample taken at  $x_{C7}=0.79$ . The arrow indicates the area without asphaltenic deposit obtained by scratching the silica surface with the AFM tip. ....201

Figure 150. Comparison between the deposit thicknesses obtained by Quartz Crystal Resonator (squares) and Atomic Force Microscopy (crosses).....202

Figure 151. Change in dissipation (half-band-half-width) measured by a quartz crystal resonator immersed in various mixtures of  $N_2$  + live oil 1 during a constant mass expansion experiment at  $T = 347.87$  K. 0% (✕); 10% (◆); 20% (●) and 30% (▲) of  $N_2$  in mol%. ....203

Figure 152. Change in dissipation (half-band-half-width) measured by a Quartz Crystal Resonator immersed in various mixtures of  $N_2$  + live oil 2 during a constant mass expansion experiment at  $T = 367.65$  K. 0% (✕); 10% (◆); 20% (●);30% (▲) and 40% (■) of  $N_2$  in mol%. ....204

Figure 153. Constant mass expansion test and the PV profile normally used to determine live oil bubble point pressure. Referent to live oil 1 (Figure 151). ....205

# List of Tables

Table 1. Division of organic material (adapted from Speight, 1982) .....	9
Table 2. Physical properties and SARA analysis of the utilized fluids. Viscosities and densities were evaluated at 25 °C and atmospheric pressure. The colloidal index of each oil is also added (see page 11 for details).....	65
Table 3. Live crude oils composition. ....	66
Table 4. Normalized frequency and dissipation factor for due to asphaltenic deposit load at $x_{C7}=0.85$ . Changes in resonance frequency within one electrode and penetration depth estimations from the predictions of density and viscosity (see section V, sub-section 3) are shown. The shear wave penetration depths ( $\delta n$ ) estimations for each harmonic are: 3 <sup>rd</sup> = 145 nm; 5 <sup>th</sup> = 110 nm and 7 <sup>th</sup> = 90 nm. The dissipation factor for the bare quartz in pure heptane for the three harmonics are as follows: 3 <sup>rd</sup> = $1.5 \times 10^{-6}$ ; 5 <sup>th</sup> = $1.1 \times 10^{-6}$ and 7 <sup>th</sup> = $0.9 \times 10^{-6}$ .....	94

## List of Abbreviations

<b>AD</b>	<b>Anno Domini</b>
<b>AFM</b>	<b>Atomic Force Microscope</b>
<b>ASCI</b>	<b>Asphaltene Solubility Class Index</b>
<b>CMC</b>	<b>Critical Micellar Concentration</b>
<b>CDC</b>	<b>Critical Dimer Concentration</b>
<b>COC</b>	<b>Critical Oligomer Concentration</b>
<b>CNAC</b>	<b>Critical Nanoaggregate Concentration</b>
<b>CNR</b>	<b>Critical Nanoaggregation Region</b>
<b>CCC</b>	<b>Critical Cluster Concentration</b>
<b>DLS</b>	<b>Dynamic Light Scattering</b>
<b>DDA</b>	<b>Difficult to Dissolve Asphaltenes</b>
<b>DBSA</b>	<b>Dodecylbenzenesulfonic Acid</b>
<b>EDA</b>	<b>Easy to Dissolve Asphaltenes</b>
<b>FEM</b>	<b>Finite Element Method</b>
<b>IF</b>	<b>Intermediate Frequency</b>
<b>MEG</b>	<b>Monoethylene Glycol</b>
<b>NIR</b>	<b>Near-Infra red</b>
<b>PTL</b>	<b>Power of Transmitted Light</b>
<b>QCR / QCM / QCM-D / RQCM / EQCM-D</b>	<b>Quartz Crystal Resonator / Quartz Crystal Microbalance / Quartz Crystal Microbalance</b>

	with <b>Dissipation</b> / <b>Research Quartz Crystal Microbalance</b> / <b>Electrochemical Quartz Crystal Microbalance with Dissipation</b>
<b>RF</b>	<b>Radio Frequency</b>
<b>SARA</b>	<b>Saturates Aromatics Resins Asphaltenes</b>
<b>SPR</b>	<b>Surface Plasmon Resonance</b>
<b>SEM</b>	<b>Scanning Electron Microscopy</b>
<b>SANS / SAXS</b>	<b>Small Angle Neutron / X-ray Scattering</b>
<b>TEG</b>	<b>Triethylene glycol</b>
<b>VPO</b>	<b>Vapor Pressure Osmometry</b>
<b>XRD</b>	<b>X-Ray Diffraction</b>
<b>XPS</b>	<b>X-Ray Photon Spectroscopy</b>

## List of symbols

$Q$	Quality factor
$D$	Dissipation factor ( $D = \frac{1}{Q} = \frac{2\Gamma_n}{F_n}$ )
$F_0$	Resonance frequency from the first harmonic ( $F_0 = \frac{v}{2h}$ ) at the reference state
$F_{n,0}$	Resonance frequency from the harmonic $n$ at the reference state
$F_n$	Resonance frequency from the harmonic $n$ when the quartz crystal is submitted to loads
$\Delta F_n = F_n - F_{n,0}$	Change in resonance frequency relative to a reference state when the quartz is submitted to loads
$\Gamma_{n,0}$	Half-band-half-width <sup>5</sup> for the harmonic $n$ at the reference state
$\Gamma_n$	Half-band-half-width for the harmonic $n$ for the quartz crystal submitted to loads (Hz)
$\Delta\Gamma_n = \Gamma_n - \Gamma_{n,0}$	Change in Half-band-half-width relative to a reference state when the quartz is submitted to loads (Hz)
$h_q$	Thickness of the quartz crystal
$v$	Velocity of a shear wave traveling though the quartz crystal
$A$	Electrode area (active area)
$m_q$	Quartz crystal mass

<sup>5</sup> The Half-band-half-width is referred along the present work as bandwidth for short.

$\rho_q$	Density of the quartz crystal ( $2.6485 \times 10^3 \text{ kgm}^{-3}$ )**
$\mu_q$	Quartz crystal shear modulus ( $2.92109 \times 10^{10} \text{ Nm}^{-2}$ )
$\rho_l$	Liquid density
$\eta_l$	Liquid viscosity
$\Delta\tilde{F}$	Complex change in resonance frequency ( $\Delta\tilde{F} = \Delta F + i\Delta\Gamma$ )
$Z_q$	Quartz crystal impedance
$\tilde{Z}_L$	Complex load impedance ( $\tilde{Z}_L = \frac{\hat{\sigma}_S}{\hat{v}_S}$ )
$\tilde{Z}_l$	Complex liquid impedance
$\tilde{Z}_d$	Complex deposit impedance
$\gamma_d$	Wave propagation constant
$C_m$	Sauerbrey coefficient ( $C_m = 2 F_0^2 / \sqrt{\rho_q \mu_q}$ )
$R_{interface}$	Model parameter taking into account surface inhomogeneity to the determination of liquid viscosities with the quartz crystal resonator.
$\hat{\sigma}_S, \hat{v}_S$	Tangential stress and velocity for relative to a shear wave propagating through the quartz crystal resonator
$\tilde{Z}_{el}$	Complex electrical impedance ( $\tilde{Z}_{el} = 1/\tilde{Y}_{el}$ )
$\tilde{Y}_{el}$	Electrical admittance ( $\tilde{Y}_{el} = G_{el} + iB_{el}$ )
$G_{el}$	Electrical conductance (Siemens – S)
$B_{el}$	Electrical susceptance (Siemens – S)
$G_{max.}$	Maximum electrical conductance achieved at quartz crystal resonance conditions (Siemens – S)

\*\* Quartz crystal physical constants at 25 °C.

$\kappa_v, \kappa_h$	Quartz crystal volumetric and linear compressibility factors $\kappa_v = 2.6939 \times 10^{-5} \text{ MPa}^{-1}$ $\kappa_h = 8.9803 \times 10^{-5} \text{ MPa}^{-1}$
$\omega$	Angular velocity
$h_r$	Vertical roughness
$l_r$	Lateral roughness
$\delta_n$	Shear wave penetration depth from the quartz surface into a liquid $\delta_n = \left( \frac{\eta_l}{\pi n F_0 \rho_l} \right)^{1/2}$
$\Delta F_p$	Change in frequency due to hydrostatic pressure
$\Delta P$	Pressure change
$h_{interface}$	Thickness of virtual rough layer used to determine liquid viscosity
$h_{deposit}$ or $h$	Thickness of a deposit in one electrode as calculated by the Sauerbrey approach
$D_f$	Diffusion coefficient
$\Gamma_{surface}$	Surface coverage concentration [M/L <sup>2</sup> ]
$t$	time
$C$	Mass concentration
$G'_d, G''_d$	Deposit elastic and viscous bulk shear modulus
$\Delta F_m$	Model calculated change in resonance frequency due to Sauerbrey mass load
$\Delta F_\eta$	Model calculated change in resonance frequency due to “Gordon and Kanazawa” liquid load (Newtonian liquid load).

$\Delta\Gamma_\eta$	Model calculated change in half-band-half-width for Newtonian liquid loads.
---------------------	---

# Introduction

The asphaltenes and more general heavy organic<sup>††</sup> fractions of petroleum onset of destabilization and deposition is already characterized by numerous methods. At high pressure asphaltene destabilization is normally detected by the power of transmitted light (PTL)<sup>1</sup>, with some speculations about the reliability of the method according to the constraints on particle size limitations. Less abundant are methods for to study of physical properties from the organic deposits under high pressure, with filtration and optical techniques normally employed. Filtration techniques have the drawback of risking bypassing the depositing fractions as well as disintegrating deposits. Optical techniques normally returns only a very qualitative aspect of deposition.

Quartz crystal resonator (QCR)<sup>††</sup> technique when applied in liquid environment is capable of probing the physical parameters of interfaces in the nanometer-micrometer range, thus potentially characterizing *in situ* heavy organic deposition. Despite the great potentialities of the technique its fully exploration has been greatly overlooked. The majority of the experimental reports follow similar procedures yielding similar information (particle sizes, diffusion coefficients, Sauerbrey adsorbed layer thicknesses) mainly on asphaltenes and resins adsorption from model systems. Some of the studies present on phase changes evaluated by the quartz crystal resonator completely immersed in live oil. Live oil lower and upper onset pressure of asphaltene destabilization, bubble point and wax appearance temperature (WAT) are to date

---

<sup>††</sup> Term employed to refer to the heaviest fractions of crude oil: high molecular weight paraffin, resins and asphaltenes.

<sup>††</sup> Normally known as quartz crystal microbalance (QCM) since Sauerbrey pioneer presentation in 1957 and publication in 1959.

completely characterized by quartz crystal resonator technique. Among the studies, reports on heavy organics destabilization and more importantly deposition characterization from the whole crude oil is almost inexistent exposing the knowledge gap which may be potentially developed in favor to the flow assurance science. The knowledge gap is put in evidence by recent studies taking advantage of the quartz crystal resonator technique to study micelles and other discrete particles (proteins, lipid bilayers, viruses<sup>2</sup> and latex<sup>3</sup>) adsorption and deposition, cell<sup>4</sup> and crystal growth<sup>5</sup>, as well as electrode usage<sup>6</sup>.

This thesis is therefore a step forward on the characterization of heavy organic deposition processes by using the Quartz Crystal Resonator totally immersed in crude oil. The asphaltenes are destabilized by a continuous or a step solubility change to trigger heavy organic compounds to phase separate, i. e., precipitate and deposit. The thesis has opened the perspective of the interpretation of deposition at high pressure<sup>7</sup>. It is inserted in an effort of comprehending autochthonous processes of asphaltenes and heavy organics destabilization, by analyzing the complex change in resonance frequency of quartz crystals totally immersed in crude oil, dead, recombined or live oils, as it is shown in Figure 1.

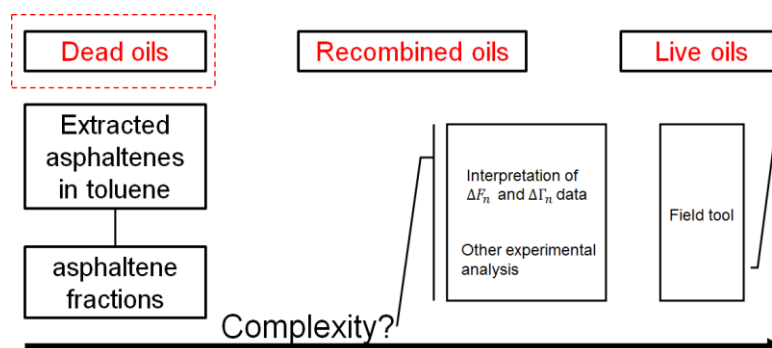


Figure 1. Three main systems which are to be studied by the quartz crystal technique to understand asphaltene destabilization and deposition as well as other or other phase separations processes.

Within the present thesis, dead oils as well as diluted dead oils and extracted asphaltenes in model oil system were researched. Some data on live oil is also shown.

## Thesis structure

The research presented here is divided into 4 Chapters. An introduction to crude oil and flow assurance related problems with an emphasis on asphaltenes is done in Chapter 1. Chapter 2 presents an introduction to the Quartz Crystal Resonator (QCR) technique, reviews the applied studies on crude oil systems and introduces a new proposition on the application of quartz crystal resonator technique to qualify and quantify heavy organics destabilization and deposition. Chapter 3 describes the experimental apparatus utilized for the experiments at atmospheric and high pressure as well as furnishes information on the utilized crude oils and experimental methods.

In the fourth and final chapter the experimental results are exposed and discussed. An emphasis is done within the context of crude oil smooth solubility change, with analysis of the onset of asphaltene destabilization and deposition from dead oils, diluted oils and extracted asphaltenes in toluene. Quartz crystal complex resonance frequency is critically analyzed within each context with the aim of understanding and categorizing phenomena. Hypothesis are posed on the probable processes of asphaltenes destabilization and deposition for the studied systems.

The abrupt crude oil solubility change (step n-heptane injection) was analyzed for two oils, yielding strongly different complex resonance frequency profiles when compared to the smooth and continuous asphaltenes destabilization.

The technique and interpretations are applied to evaluate production chemicals (asphaltenes inhibitors/dispersants) efficiency on asphaltene onset of destabilization delaying and deposition inhibition.

With the aim of providing more support to the complex resonance frequency interpretations, Atomic Force Microscopy was utilized to characterize asphaltene deposition. The data was then correlated with the results obtained by the QCR.

At the end of the thesis, high pressure experiments are analyzed. Live oils, with injected nitrogen, are probed by isothermal depressurization with a continuous recording of bandwidth data to research on the possible nitrogen induced asphaltene destabilization.

# Chapter 1

## 1. Literature review

### 1.1 Crude oil origin and composition

Although there are theories on the origin of crude oil from inorganic materials it is generally accepted that most hydrocarbon reserves come from once living organisms. Hydrocarbon reserves are derived from the massive burial of organic matter coming from a diversity of living organisms. Such theory is the most accepted given the great complexity of molecules within the crude oil and the presence of biomarkers as porphyrins, and submitted to different conditions of temperature and pressure<sup>8</sup>.

From the organic debris burial to the ultimate yield on hydrocarbons three stages of mineral and organic transformations are discretized: diagenesis, catagenesis and metagenesis. Within diagenesis the organic debris suffers mostly from aerobic and anaerobic bacterial activity which transforms the primary organic matter constituents (proteins, carbohydrates and lipids) into fulvic and humic acids, humin and kerogen by three main stages: biochemical degradation; polycondensation and insolubilization. During the diagenesis stage methane is produced. With increasing sediments burial depth and the consequent temperature increase the catagenesis stage of transformation of sediments is reached. The catagenesis is characterized by no more biological activity within the organic sediments and the massive thermal degradation from the organic matter to oil, wet gas and condensate. At the end of catagenesis the organic matrix is depleted of aliphatic hydrocarbons. Maceral particles in the kerogen assume some degree of ordering. At the last stage of sediment maturation, with the high overburden pressure and high

temperatures the organic matter produces some methane and is mostly transformed to carbon residue. The described processes are summarized in Figure 2<sup>9</sup>.

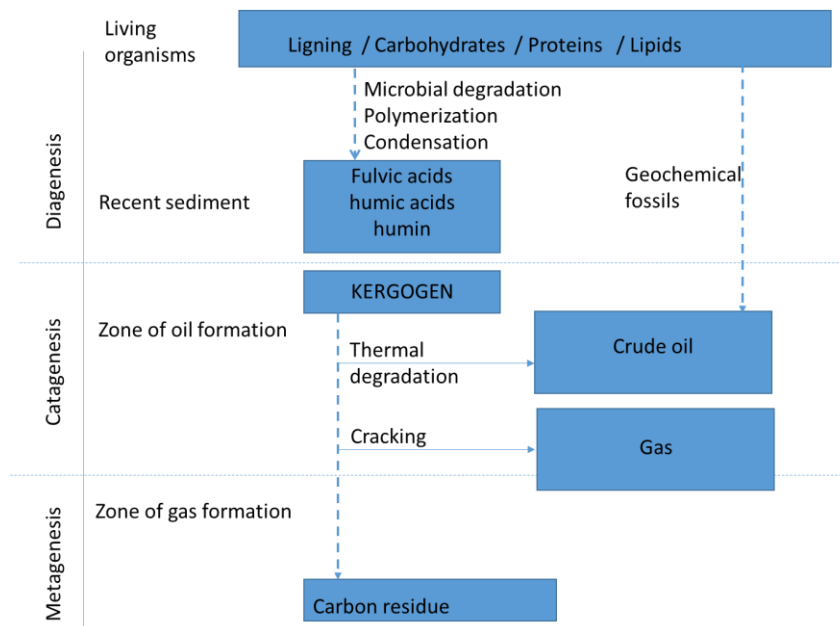


Figure 2. Stages of organic matter transformation to hydrocarbons (adapted from Tissot and Welte, 1984)

Kerogen, defined by the organic matter insoluble in organic solvents and alkaline solution and presenting no hydrolysable fraction is theorized by some scientists to be the precursor for crude oil although the formation conditions of crude oil from kerogen is not yet well defined: kerogen yields petroleum when heated to temperatures that are not naturally occurring within the catagenesis processes. Others theories portray kerogen and crude oil as coming from a common precursor or a *protopetroleum*. An attempt to capture the molecular structure of kerogen is shown in Figure 3. Tissot<sup>9,10</sup> pointed out the similarity of kerogen and asphaltenes, as the latter being analogous of small kerogen units.

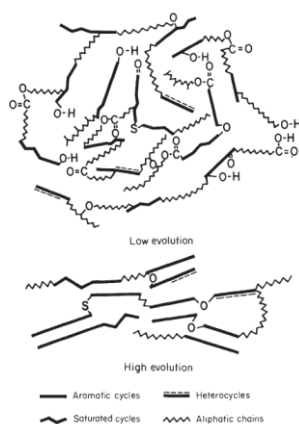


Figure 3. Hypothetical kerogen molecular structure (after Tissot <sup>10</sup>)

There are three main types of kerogen which are associated to the formation of different crude oils. Type I, the least abundant on earth is mostly originated from algae rich in lipids. Type II kerogen is mainly originated from microorganisms which were mostly deposited in reducing environment. Type III kerogen comes mostly from the deposition of higher continental plants. In such environments with the rapid burial of sediments limited biodegradation of the organic matter. The different types of kerogen are well analyzed within the van Krevelen diagram which was published in 1961 to describe the coalification path of coals from peat to anthracite. The diagram reproduced in Figure 4 shows the path of different organic material forming each type of kerogen. The arrows indicate an increase in the depth of overburden, with the three types of kerogens approximating to the state of pure carbon (Graphite). The frontiers of diagenetic, catagenetic and metagenetic processes are indicated within the dashed lines.

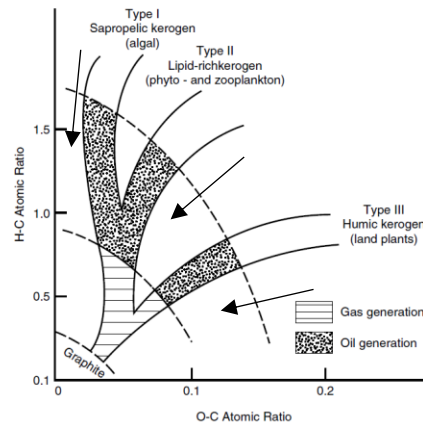


Figure 4. Van Krevelen diagram with the evolution of different kerogen types (After Speight, 1982)

The physical and chemical characteristics of crude oils produced in the catagenesis are rather dependent upon the nature of the organic sediments biological and physicochemical processes they undergo in the first centimeters and meters of burial. Particularly important is the biological activity within the first meter from the surface in which aerobic or anaerobic bacterial processes will greatly influence the organic and to some extent the inorganic matrix of the deposit. Kerogen Type I is the rarest and generates oil; Type II is the most frequent in petroleum source rocks and mostly generates waxy oil and kerogen Type III is more prone to generate gas.

The hydrocarbons generated at the source rock migrate to a permeable and porous rock which is referred to as reservoir rock having an impermeable cap which stops the hydrocarbon displacement. Most reservoir rocks are composed of sedimentary rocks as sandstone or limestones with the shales being a common reservoir seal. The water that was once filling the pores of a reservoir rocks is displaced by the migrating hydrocarbons and within the reservoir fluid stratification by gravitational effects may give rise to different reservoirs, with gas cap and water layers. Figure 5 brings a common reservoir and surface facility schema.



*Figure 5. Reservoir, production tubing and surface facilities in a crude oil production site. Two wells are represented one with mechanical pump recovery and the other producing by natural reservoir pressure reduction. X-tree, three phase separator and stocking units are also shown. (Photo taken at the stand of the China Petroleum Technology Development Corporation, CPTDC at Rio Oil and Gas 2014).*

A range of hydrocarbons deposits with different compositions and physical characteristics arise from the many processes of debris burial and subsequent transformation. Within such a spectrum, extremes can be characterized as coal, shale and bitumen, solid and semisolid hydrocarbon reserves, passing through liquid and gaseous hydrocarbons as petroleum and gas reservoirs. It is easy to get confused within the many terminologies utilized within the organic material production and processing chain. Speight<sup>8</sup>, separates organic materials in three main categories: Natural, Derived and Manufactured as it is shown in Table 1.

*Table 1. Division of organic material (adapted from Speight, 1982)*

<b>Natural Materials</b>	<b>Derived Materials</b>	<b>Manufactured Materials</b>
Natural gas	Saturates	Synthetic crude oil
Petroleum	Aromatics	Distillates
Heavy oil	Resins	Lubricating oils
Bitumen	Asphaltenes	Wax

Asphaltite	Carbenes	Residuum
Asphaltoid	Carboids	Asphalt
Ozocerite		Coke
Kerogen		Tar
Coal		Pitch

Kerogen, described earlier is the most abundant organic deposit. Among the natural materials the most important in the context of this thesis is petroleum.

Petroleum is a complex mixture of hydrocarbons and non-hydrocarbons in a solid, liquid or gaseous phase when in reservoir conditions, or mostly known as **live oil**. Once produced and depleted from its lighter fractions (<C7) petroleum is mostly referred as **dead oil**. Dead oil is a mixture of hundreds of thousands of molecules<sup>11</sup>. The great complexity of crude oil was well summarized by Boduszynsky<sup>12,13</sup> work which introduces the notion of crude oil being a continuum of molecules of varying molecular weight, aromaticity and heteroatom content. The discretization of each molecule present in crude oil is an extremely difficult. The pool of molecules present in crude oil is rather classically represented as fractions presenting common characteristics. One of the fractionation procedures separates crude oil in a basis of solubility and chromatography in four main fractions standing for the four first derived materials in Table 1: **saturates**, **aromatics**, **resins** and **asphaltenes**. Such a process is widely known as SARA fractionation and it is schematically shown in **Erreur ! Source du renvoi introuvable..**

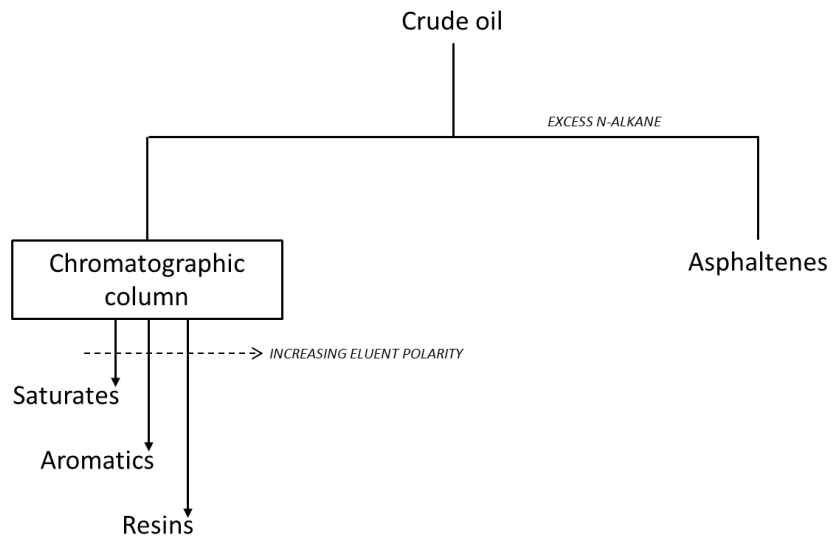


Figure 6. Crude oil SARA fractionation. Asphaltenes are precipitated from crude oils with excess *n*-alkane and separated from the maltenes by filtration. The maltenes are then percolated through a chromatographic column and the saturates, aromatics and resins are eluted with solvents of increasing polarity.

The asphaltene fraction is firstly separated from crude oil by excess of *n*-alkane. The crude oil depleted from asphaltenes normally referred to maltenes is further fractionated with the aid of chromatographic methods the other three fractions by are eluted with solvents of different polarities, yielding the resins, aromatics and saturates fractions.

### 1.1.1 The SARA fractions

The basic understanding of the main fractions presented in crude oil is a first step towards the comprehension of crude oil physical behavior and flow assurance problematics. A brief introduction to the four main fractions present in crude oil is completed. The emphasis is kept on the asphaltenes fraction.

#### 1.1.1.1 Saturates

Saturated hydrocarbons are constituted of normal or branched alkanes as well as cycloalkanes known as naphthenes. The paraffins are found within this fraction. Paraffin is one of the main subjects in petroleum production especially in offshore petroleum production where the very low temperatures on the seafloor causes them to crystallize and form deposits. Wax crystallization temperature is known as wax appearance temperature (WAT) or the cloud point of the crude oil<sup>14</sup>. Paraffins up to C<sub>80</sub> (MW= 1222 g/mol) were found in crude oil<sup>15</sup>. Wax is classically separated in macrocrystalline (<C<sub>40</sub>) and microcrystalline (>C<sub>40</sub>). Than et al.<sup>16</sup> points out for the low solubility of n-C<sub>50</sub> in pentane, indicating that is not surprising that such fraction would co-precipitate with asphaltenes. They observe >C<sub>40</sub> waxes tend to exist as fine solid suspended particles in the crude oil, prone to destabilization and deposition. The interaction of paraffin and asphaltenes is the subject of many studies<sup>16-22</sup>.

#### 1.1.1.2 Aromatics

The aromatics hydrocarbons containing one or more aromatic nuclei with the presence of naphthenes rings. In crude oils the percentage of aromatics and resins is a measure of the crude oil stability against asphaltenes destabilization by the colloidal index:

$$CII = \frac{\text{Saturates} + \text{Asphaltenes}}{\text{Resins} + \text{Aromatics}}$$

Higher indices indicating higher instability of the asphaltenes<sup>23,24</sup>.

#### 1.1.1.3 Resins

Resins and asphaltenes are closely related molecules with research indicating the possibility of the conversion of resins into asphaltenes by oxidation<sup>25</sup>. The major difference between both

classes of compounds present in crude oil is that resins are soluble in n-heptane and normally they do not have the tendency of self-association as it occurs within the asphaltene fraction. Resins were found to self-aggregate in high resinous crudes, increasing their viscosity<sup>26</sup>. Resins are insoluble in propane and its separation together with asphaltenes by liquid propane is known as deasphalting process within the context of crude oil refining. Resins encompasses a class of molecules with lower average molecular weights when comparing to asphaltenes but with significant overlap in molecular weight distribution with the asphaltene fraction. Resins are normally separated from the crude oil by the use of surface active materials, after the asphaltenes are precipitated by the use of alkanes. As their method of separation indicates they are constituted by surface active components, polar components, with acid and bases present in this fraction. To illustrate the problems that molecules pertaining to the resins can introduce in the crude oil production we may cite the tetrameric acids discovered in Norway. A family of molecules with 4 carboxylic functions were responsible for significant emulsion and sludge formations in separators<sup>27,28</sup>. Since Nellensteyn and Pfeiffer and Saal proposed the colloidal theory of asphaltenes in asphalt and bitumens, which was extended to crude oils, resins has been deemed to be the major stabilizing agents to the asphaltene particles in solution<sup>29</sup>. Early hypothesis on asphaltene colloidal stability in crude oils suggested that resins would be associated with asphaltenes and act as asphaltene stabilizers. Depletion of such a crude oil fraction would give rise to the collapse of crude oil dispersion within the major results: the asphaltene flocculation and depositions. Resins were fractionated in two main fractions R1 and R2. Fraction R1 was obtained from the precipitated asphaltenes by excess n-heptane, according to this study this precipitation yields a material which is composed of asphaltene-resin aggregates, thus, the R1

fraction is separated from the asphaltene-resin aggregates by Soxlet extraction. The R2 fraction is the resins which is not co-precipitated with asphaltenes and thus believed to play minor role in asphaltene stabilization. The R1 fraction was found to increase the asphaltene stability against precipitation as measured by high pressure near infra-red (NIR) measurements<sup>30</sup>. There is still no concrete conclusion regarding the real importance of resins on asphaltene stability in crude oils. Leon<sup>31</sup> proposes that resins form a layer on asphaltenes; penetrate in the asphaltene microstructure resulting in mixed asphaltene-resins particles. Mixed structures of asphaltenes and resins was also proposed by Koots and Speight<sup>32</sup>. Sedghi and Goual<sup>33</sup> pointed out by direct-current conductivity that resins would not act as asphaltenes stabilizers by a steric mechanisms but would rather increase asphaltene stability by the formation of mixed asphaltenes-resins aggregate as proposed by Rogel<sup>34</sup>. Hashmi and Firoozabadi<sup>35</sup> found a cooperative effect of resins and one asphaltene dispersant<sup>36</sup>.

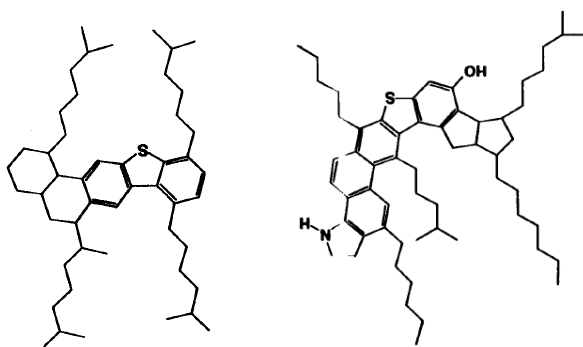


*Figure 7. Resin model molecules proposed by Murgich<sup>36</sup>. Reprinted with permission from Murgich, J.; Rodríguez, J. M.; Aray, Y. Molecular recognition and molecular mechanics of micelles of some models asphaltenes and resin. Energy & Fuels **1996**, 10 (7), 68–76. Copyright 1996 American Chemical Society.*

#### 1.1.1.4 Asphaltenes

Asphaltenes are the most polarizable group of molecules in crude oil. They are composed of fused aromatic molecules with different degrees of alkyl side chains and aliphatic rings. The asphaltenes carry the highest content in heteroatoms, mainly N, O, S, Fe and Ni. The asphaltene fraction will be discussed in more details in a later section.

### 1.2 Flow assurance issues

The use of hydrocarbon reserves remounts to 4000 BC in the Euphrates river where bitumen was used as a mortar to building stones as well as on pottering and boats<sup>8</sup>.

The exploration of liquid hydrocarbon reserves through drilling technique remounts to 347 AD in China. A well of 240 m deep drilled with bits attached to bamboos. The drilling technology much coming from the salt production process with the production of brine and natural gas.

The modern petroleum production era begins with the first commercial successful oil well in Titusville, Pennsylvania drilled by Edwin L. Drake, in 1859. Since then, with the advent of the internal combustion engines, the advancements in refining and petrochemistry crude oil has become a commodity and by far the dominant source of energy in the world.

From the reservoir to the refinery crude oils passes through a series of phases which are divided in three main sectors: *Upstream*, *Midstream* and *Downstream*. The Upstream sector encompasses the crude oil production from an *onshore* or *offshore* reservoirs. The midstream is the export of hydrocarbons by ships or pipelines to stocking centers or refineries. Downstream is mainly based on crude oil refining operations with the specification of marketable products as fuels or petrochemical feedstocks.

From the reservoir to the production facilities the produced fluids suffer from changes in pressure, temperature and composition and may yield different *flow assurance* problems. Flow assurance is the terminology utilized within petroleum production to refer to the collective of subjects related to the good maintenance of flowing capabilities. It encompasses the pore channels and thus the maintenance of a good reservoir permeability, the flowing of the produced fluids through the production tubing and pipelines to surface facilities and the proper export of crude oil to refining or stock centers. The first stage of produced fluid processing within the surface facilities are the separators. The purpose of the separators is to segregate the three produced phases, solid, liquid and gases and send them to purification before exporting or rejecting the fluids.

The major problems faced in crude oil or gas production are **emulsions, wax, hydrates, inorganic deposits (scale) and asphaltenes**<sup>37</sup>. Emulsion is one of the main flow assurance issue within crude oil production. Emulsions are formed by the vigorous agitation of two immiscible liquids creating dispersed droplets of one liquid, the dispersed phase, in the other liquid, the continuous phase. Emulsions are thermodynamically unstable with the gain in surface energy within the increase of interfaces of different interfacial tensions. Emulsion stability is accomplished by indigenous or foreign molecules having regions of affinity of each phase, the so called surfactants, which lowers the interfacial tension between the two phases yielding emulsion stabilization<sup>38</sup>. Emulsion stability can be also accomplished by fine solids which may have regions of differing wettability towards both liquids and may accommodate in the interface causing a steric stabilization of the emulsion. Asphaltenes and resins may adsorb on particle surfaces and be prone to stabilize emulsions<sup>39,40</sup>. A special case of emulsions stabilized by solids presenting well defined regions of

differing wettability towards the immiscible fluids is the case of Pickering emulsions<sup>41</sup>. The comprehension of emulsions and their mechanism of stabilization is of outmost importance from a flow assurance point of view: the presence of large interfacial area delimiting the oil phase and the water phase causes complex processes of mass transfer between the phases impacting produced water quality and ultimately ocean pollution. Within the interfaces, hydrolysable crude oil molecules as carboxylic acids causes huge deposit problems in separators when production water meets some conditions of pH and in the presence of calcium cations as it is the case of the calcium naphthenate formation<sup>27,28,42</sup>. Within the separators, emulsions are particularly troublesome with complex mechanisms of surfactant concentrations and the formation of very “difficult to break” emulsions in the water/crude oil interface, which are known as **rag layers**<sup>43</sup>. Emulsion destabilization can be reached by heating which have the effect of (i) increasing Brownian motion and the probability of droplets to coalesce and (ii) of changing the stability of surfactant molecules, especially non-ionic surfactants molecules at interfaces and promote emulsion destabilization. The formation of emulsions is sometimes desirable as a strategy of transporting heavy oils<sup>44</sup> or extracting trapped and normally immobile oils within the reservoir because of capillary effects.

High molecular weight linear or branched alkanes solidifies with the temperature decrease once the flowing system goes from the reservoir with high temperatures to the subsurface facilities. Such problems are particularly important in subsea production systems where the produced fluids are exposed to low temperatures within the bottom of the oceans of about 4 °C. The measures taken to avoid paraffin related problems can be separated in active and passive. Passive includes the insulation of flowlines and pipelines whereas active measures include the use of

paraffin cloud point depressants, mainly of surfactants, which may inhibit paraffin crystallization and growth and the maintenance of flowline temperatures by active heating.

As it is the case for emulsions, asphaltenes related problems occur almost in any phase of crude oil production process as well as they are detrimental in transport and refining phases of produced fluids<sup>38,45-49</sup>. Asphaltenes as the central subject of the present work are described to some extent of details in the next section. As it was already stated, asphaltenes resembles small units of kerogen, with fused aromatic moieties with alkyl side chains. Together with paraffins asphaltenes are the most insoluble or unstable material in crude oils, with their phase segregation or precipitation being triggered by changes in pressure, temperature and crude oil composition. In this regard, changes in crude oil solubility either by depressurization during crude oil production either by the effect of injected fluids within secondary and tertiary oil recovery techniques are prone to give rise to asphaltene problems. Among the *upstream* asphaltenes related issues one can enumerate: 1. precipitation within the bulk reservoir with subsequent pore blockage and decrease reservoir permeability<sup>50</sup>; 2. asphaltene precipitation and cake formation in near well bore region due to high pressure drops; 3. asphaltene precipitation within the production tubing and other tubulars which may be accompanied by its deposition; 4. asphaltene precipitation and deposition within pump propellers, valves and other fittings; 5. asphaltene precipitation by comingled flow from manifolds and 6. asphaltenes precipitation or accumulation in separators yielding sludge formation<sup>51</sup>. Asphaltenes play also a role on emulsions stabilization either by steric mechanisms, directly as in the form of precipitated or adsorbed particles or with acid molecules which are present also in the resins fractions and act as surfactants. Asphaltenes have been deemed to form Pickering emulsions as well as to adsorb in inorganic fines which are

further prone to migrate to interfaces and sterically stabilize emulsions<sup>41</sup>. When reservoir pressure is decreased the production is assured by secondary methods of recuperation which assists on increasing or maintaining reservoir pressure. Such techniques are mainly based on injection fluids into the reservoir, divided in miscible and immiscible flooding. Flooding techniques may disturb asphaltene stability and trigger asphaltene deposition<sup>52-54</sup>.

### 1.2.1 Asphaltenes

#### *1.2.1.1 The physical nature of asphaltenes*

The term asphaltene was coined by Jean Baptiste Boussingault, one of the first scientists to analyze the composition of bitumen, in 1837. Boussingault distilled bitumen at a temperature of 230 °C and obtained a liquid product which he named after petrolene given its similar nature to petroleum. With the aim of depleting the bitumen from its volatile compounds Boussingault submitted it to a thermal treatment of 250 °C until constant mass was achieved (45 to 50 hours in his experiments). He described the obtained fraction to be shining black presenting conchoidal fracture. He pointed out that this material is denser than water, have a soft point at 300 °C and that it decomposes before melting, naming them “asphaltene” as he found out great similarities between such material and asphalt. By oxidation reaction, he arrived to the molecular formula of asphaltenes as  $C_{40}H_{32}O_3$  or  $C_{80}H_{64}O_6$ . Moreover, he found out that the obtained material was insoluble in alcohol, but soluble in ether, vegetal oils and turpentine. According to Boussingault bitumens are formed by a mixture of petrolene and asphaltene, one having its great similarity to petroleum and the other to asphalt. The great differences in physical properties of bitumens is according to Boussingault due to the proportions of the two components forming the bitumen <sup>55</sup>.

The nature of asphaltenes in asphalts was analyzed by Nellensteyn in 1923 who introduces the concept of asphalts being a colloidal system of dispersed elemental carbon particles. The elemental carbon particles surrounded by adsorbed unsaturated hydrocarbons is called by Nellensteyn asphaltenes<sup>56</sup>. Pfeiffer and Saal<sup>57</sup> looking forward to understand bitumen rheology further developed the concept of Nellensteyn, proposing that asphaltic bitumen are composed of dispersion of asphaltene micelles in a pure viscous matrix called maltenes. The micelles being constituted of high molecular weight condensed aromatic hydrocarbons in its core and hydrocarbons having aromatic, naphthenic and aliphatic portions peptizing and stabilizing the cores. According to their publications no clear boundaries can be drawn between the central part of the micelle constituted mainly of asphaltenes and the continuous phase constituted mainly of maltenes, with a gradual transition essentially condensed aromatic molecules to the aliphatic molecules present. The non-Newtonian behavior of an asphaltic bitumen is explained by the degree of peptization of the asphaltenes as they schematically shown (Figure 8).

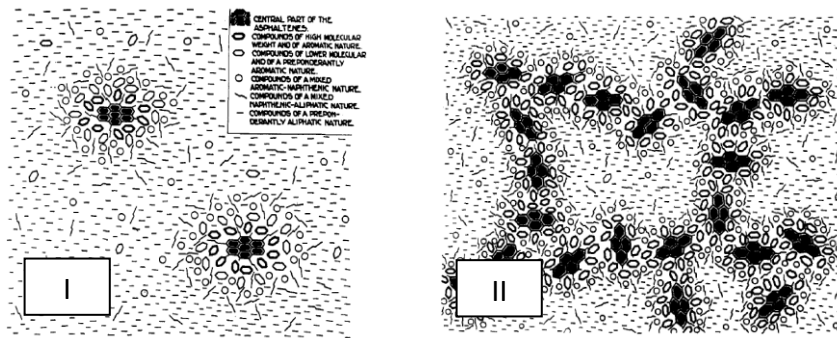


Figure 8. Schematics of micelles proposed by Pfeiffer and Saal<sup>57</sup> in 1939. (I) Fully peptized asphaltene cores and (II) micelles deficient in resins giving rise to a gel structure and non-Newtonian behavior. Reprinted with permission from Pfeiffer, J. P.; Saal, R. N. J. J. Asphaltic bitumen as Colloid System. Phys. Chem. 1940, 44 (2), 139–149. Copyright 1940 American Chemical Society.

The colloidal theory of the nature of asphaltenes in bitumen and asphalts introduces one school of thought on the mechanisms by which asphaltenes are stable. Nellensteyn in the conclusion of his doctoral thesis, writes “asphalt is elementary carbon, under the form of a colloidal suspension, that usually mainly consists out of hydrocarbons, and that is stabilized by substances, which can be strongly unsaturated hydrocarbons”. Nellensteyn<sup>58</sup> suggested that the asphaltenes are stabilized by layers of free radicals of low molecular weight while Pfeiffer and Saal<sup>57</sup> suggested that asphaltenes are stabilized by resins: “This part of hydrocarbons consists chiefly of hydrocarbons of an aromatic or of a combined aromatic-naphthenic-aliphatic nature and is by some authors referred to as resins”. At this point of the research presented here it is important to add that once the colloidal nature of asphaltenes was devised, researchers started to use the term micelles. Micelles and inverse micelles are however formed by different driving mechanism as it is pointed out by Friberg<sup>59</sup>. Although a misnomer, the term micelles was largely utilized within the asphaltene science and Critical Micellar Concentrations were probed by many experimental techniques<sup>60-63</sup>. Within the context of micellar hypothesis of the aggregation mechanisms of asphaltenes many researchers published on the values of Critical Micellar Concentration (CMC) for asphaltenes. When surfactant molecules form micelles in aqueous solutions they are unable to decrease interfacial tensions. Many researchers then measured the interfacial tension of water/oil interfaces with different concentrations of asphaltenes and indicated a value for the CMC, even though the apparent unconformity of using CMC for a system which does not support the terminology micelles. The macro structure of asphaltenes is needed to be addressed with new terminologies. In the first decade of our century some cornerstones were finally resolved: the molecular weight distribution of asphaltenes were set to be within the range of 500 to 1500 Da;

and their mechanisms of aggregation in toluene were solved as a stepwise aggregation mechanism involving different aggregation stages. A new terminology was then introduced referring to asphaltene state in toluene as **nanoaggregates**. According to this theory the nanoaggregates would form from balance between pi-pi interactions between aromatic nucleus and steric repulsion between peripheral alkane chains, or the counter balance between insolubilization process due to aromatic cores stacking and alkyl side chains increasing asphaltene solubility<sup>64</sup>. The term Critical Nanoaggregate Concentration was then coined to indicate the concentration of asphaltene at which nanoaggregates are formed<sup>65</sup>. The nanoaggregate configuration of asphaltene was however introduced much before by professor Teh Fu Yen and co-workers in 1961. By X-ray diffraction and based on a series of works indicating the presence of aromatic and alkyl moieties in the asphaltene, the high molecular weights which strongly depends on the measuring method thus indicating a “high degree of association” and a series of x-ray studies on asphaltene powders, they proposed an asphaltene model based on the stacking of aromatic moieties which they call asphaltene micelles, as shown in Figure 9<sup>66,67</sup>.

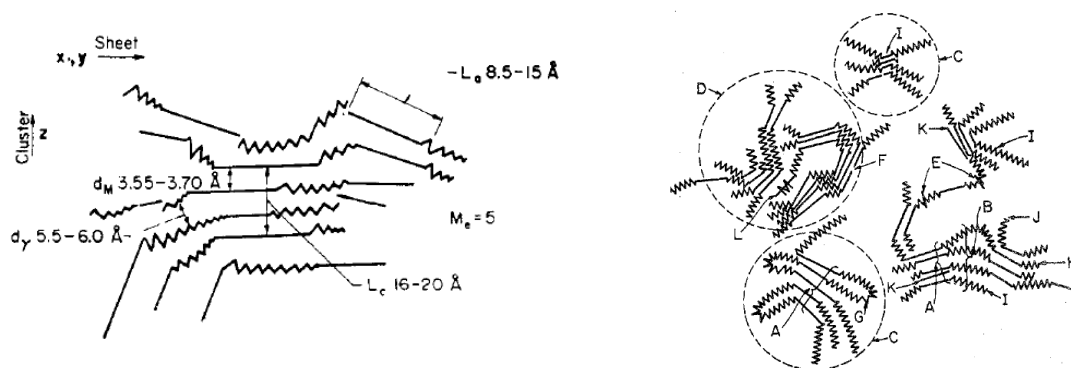


Figure 9. Proposed asphaltene aggregate structure by Teh Fu Yen and co workers<sup>66,67</sup>. Reprinted with permission from Yen, T. F.; Erdman, J. G.; Pollack, S. S. *Investigation of the Structure of Petroleum Asphaltenes by X-Ray Diffraction* Anal. Chem. **1961**, 33 (11), 1587–1594; and Dickie, J. P.; Yen, T. F. *Macrostructures of the asphaltic fractions by various instrumental methods*. Anal. Chem. **1967**, 39 (14), 1847–1852. Copyrights 1961 and 1967 American Chemical Society.

In 2009 Mullins<sup>68</sup> proposed a modification of the Yen model, which is now known as the Yen-Mullins model, introducing a range of hierarchical structures which are schematically shown in Figure 10.

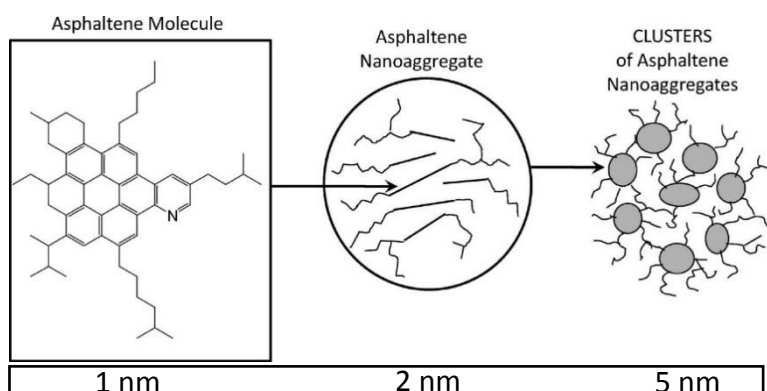
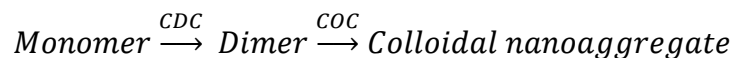


Figure 10. Asphaltene hierarchical structures proposed by Mullins<sup>68</sup>. Reprinted with permission from Mullins, O. C. *The modified Yen Model*. *Energy & Fuels* **2010**, 24 (4), 2179–2207. Copyright 2010 American Chemical Society.

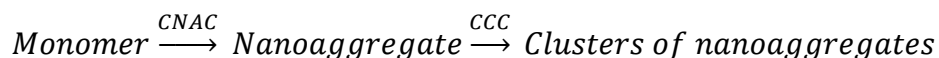
Within the proposed model the asphaltene aggregation state would depend on its concentration. In toluene, in concentrations smaller than 50 mg/L, asphaltenes would be mainly present in a molecular state. With increasing concentration, at about 50 to 150 mg/L asphaltenes would attain the critical nanoaggregate concentration with the molecules associating in nanoaggregates of about 3 nm. According Mullin’s theory the degree of association is dependent on the balance of pi-pi stacking interactions and steric hindrances imposed by the alkane lateral chains. At higher concentrations, the nanoaggregates would form clusters of nanoaggregates with sizes up to 300 nm<sup>68,69</sup>. Such information is in conflict with a Small Angle Neutron Scattering study<sup>70</sup> in which it is reported Radius of gyration for asphaltene particle sizes in the order of 5 nm in the concentration range of 2.5 to 85 g/L. Barré<sup>71</sup> studied the asphaltenes nanoaggregates in toluene correlating with

their properties in solution, at low and high concentrations. They showed that the asphaltene nanoaggregate radius of gyration ( $R_g$ ), Molecular weight ( $M_w$ ) and the second virial coefficient ( $A_2$ ) are interconnected through the fractal dimension ( $D_f$ ) of the aggregate. They summarize that the determined parameters are sufficient on describing many asphaltene solution properties as viscosity, adsorption, emulsion stability, among others. Eyssautier<sup>72</sup> used SANS and SAXS technique to study asphaltene nanoaggregates in toluene at concentrations of 5 g/L. They confirmed the asphaltene aggregate structure proposed by Yen and Mullins, with the asphaltene nanoaggregates characterized as a small cores surrounded by a shell of n-alkanes chains, yielding a disk like shape.

The proposition of the nanoaggregates as being the first aggregate state of asphaltenes was shown not account for what really occurs within asphaltene aggregation processes in toluene. Indeed, Evdokimov<sup>73-75</sup> found by refractive indexes experiments that asphaltenes associate at concentrations as small as 0.35 mg/L with a multitude of aggregation species appearing with increasing concentration. Contrary to the modified Yen model (Yen-Mullins model) they propose that asphaltenes in toluene aggregate to form dimers and oligomers before forming nanoaggregates. They schematically resume their early aggregation stages as follows, inserting terminologies as critical dimer concentration (CDC) as well as critical oligomers concentration (COC):



Contrary to what advocates Mullins<sup>68</sup>:



The formation of smaller aggregates than the nanoaggregates was also proposed by Acevedo<sup>76</sup> by thermos-optical studies on asphaltene solutions.

Critical nanoaggregate concentration was detected by ultrasound velocity measurements<sup>77</sup>, the authors wisely introduced the term Critical Nanoaggregation Region to characterize asphaltene concentrations propitious to form nanoaggregates. Moreover they discretize three phases of asphaltene aggregation with increasing asphaltene concentrations in toluene: “linear monomeric; non-linear critical nanoaggregation (CNR) and linear aggregated”.

The studies hitherto discussed were done with asphaltene in toluene, other studies point out to the presence of nanoaggregates in live crude oil by downhole fluid analysis<sup>78</sup> and centrifugation<sup>79</sup>.

An early (1957) study<sup>80</sup> of petroleum ultracentrifugation highlights that “there is a lack of unequivocal evidence on the presence of colloidal particles in petroleum despite extensive work involving osmosis, diffusion, optical properties, electrophoresis, ultrafiltration and other techniques” making reference to studies defending or criticizing the colloidal view of crude oils.

With the use of small angle scattering techniques (X-ray and neutron) the presence of asphaltene aggregates was greatly supported, but Sirota publishes in 2005 a critic to the common interpretation of such experimental evidences adding that the interpretation of the scattering were done taking into consideration the presence of colloidal particles. Sirota highlights that the scattering spectra of asphaltene in toluene can be interpreted as a solution near its phase separation, and that the asphaltene aggregation can be interpreted as a liquid-liquid phase transition within the asphaltene phase rich under its glass transition temperature thus having a solid aspect and buildup fractal aggregates<sup>81</sup>. Although the colloidal nature of asphaltene in crude oils is widely accepted solving many issues and opening up perspectives within phase

modeling, it is always valid to keep in mind the complexity of the system and the necessity to comprehend the real nature of asphaltene molecules and how do they act during crude oil production.

The modified Yen model takes into account that the pi-pi interaction between the aromatic cores of asphaltene molecules is the first driving force for their aggregation and that the aggregation proceeds until steric effects from the side alkane chains overcome such aggregating forces. Such a view of asphaltene aggregates is by one side oversimplified and has been pointed out by some authors to be of great interest to industrialists as it facilitates the appliance of asphaltene destabilization models. In fact, after the Yen model was introduced it was further refined to account for the presence of different types of molecules from the asphaltenes, resins or waxes and also metals to aggregation processes occurring in crude oil<sup>67,82</sup>. The refinement of such a theory may be summarized by the proposed supramolecular arrangement of the heaviest fractions of crude oil as it is proposed by Gray<sup>83</sup> and shown in Figure 11.

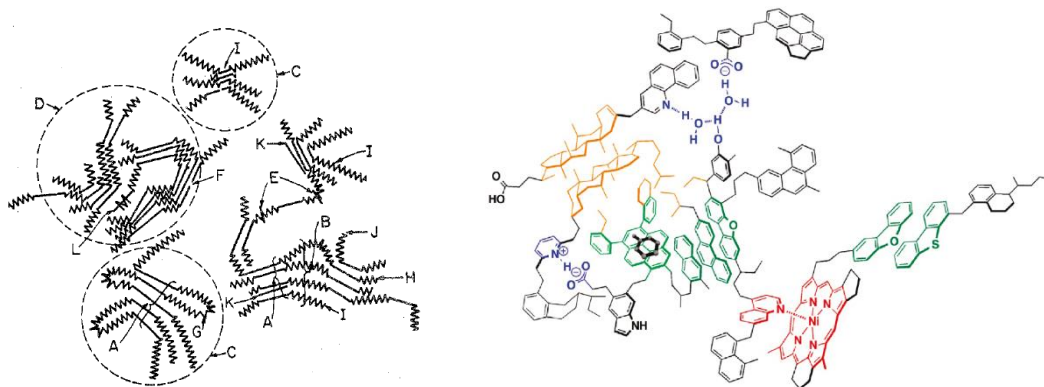


Figure 11. Supramolecular models for heavy organic fractions in crude oil. (A) Organization proposed by Dickie<sup>74</sup> in 1967 and (B) by Gray<sup>83</sup>, in 2011, defying the increasingly acceptance of asphaltene nanoaggregates as proposed by Mullins<sup>68</sup>. Reprinted with permission from Gray, M. R.; Tykwinski, R. R.; Stryker, J. M.; Tan, X. Supramolecular assembly model for aggregation of petroleum asphaltene. *Energy and Fuels* **2011**, 25 (7), 3125–3134; and Dickie, J. P.; Yen, T. F. Macrostructures of the asphaltic fractions by various instrumental methods. *Anal. Chem.* **1967**, 39 (14), 1847–1852. Copyrights 2011 and 1967 American Chemical Society.

Indeed the supramolecular theory of organization of heavy organics in crude oil is plausible and some studies advocate their effectiveness on explaining crude oil physical properties<sup>84</sup>.

A more conceptual model having in mind the compatibility of crude oils towards asphaltene destabilization was proposed by Wiehe<sup>11,85</sup> (Figure 12).

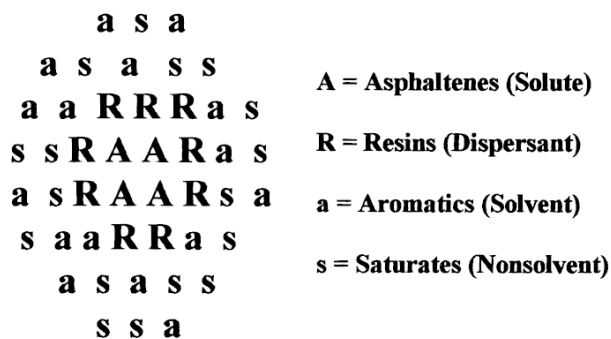


Figure 12. Physical model of petroleum according to Wiehe<sup>11,85</sup>. Reprinted with permission from Wiehe, I. A.; Kennedy, R. J. The Oil Compatibility Model and Crude Oil Incompatibility Energy and Fuels **2000**, 14 (1), 56–59. Copyright 2000 American Chemical Society.

The many different proposed aggregation states for asphaltenes have its basis on asphaltenes molecular interactions, which is summarized by Murgich<sup>86</sup> as being: Intermolecular charge transfer; Short-range exchange repulsion energy and weak inductive interaction; electrostatic (coulombic) interactions between molecular charges and Van der Waal interactions. Charge transfer mechanisms or acid-base interactions were reported to be able to reversibly solubilize asphaltenes from its aggregate state<sup>87</sup>. Unger<sup>88</sup> describes the resins and asphaltenes properties as a direct consequence of the presence of free radicals. The paramagnetic character of asphaltenes was also revealed by other study<sup>89</sup>. The presence of electrical charges<sup>90–92</sup>, the reversibility of zeta-potential within the asphaltene colloids as well as surface electrical charges reflected in sedimentation experiments are also highlighted as important interacting forces<sup>93</sup>.

Many experimental observations and theoretical calculations have unraveled the nature of asphaltenes in solvents or within its source hydrocarbons. Each study reveals one characteristics of the asphaltenes and is useful for drawing scientific lines out of the many speculations on their physical structures in solution. It is however important to keep in mind that asphaltenes have not a single or even a collection of molecules which can be discretized, and as such, may accommodate, some of the principles of the many scientific or speculation hypothesis that were to date published. For instance, it is known that a fraction of asphaltenes is not soluble in toluene and that a fractions is soluble in n-heptane at high pressure and high temperature conditions defying the most basic information on asphaltenes: its definition by solubility. The fact that some asphaltenes are not soluble in aromatic solvents was pointed out in the very beginning by high performance microscopy experiments where no asphaltenes particles were found within the crude oil but were discovered after the oil was treated with aromatic solvents<sup>94</sup>.

The overall structure of asphaltenes in solvents and in petroleum has not considerably changed since the studies developed by Pfeiffer and Saal<sup>95</sup>. The refining of the knowledge of asphaltenes physical-chemistry properties being one of the challenges for serving the industry with technological improvements on the way of dealing with asphaltenes problematics.

In the following sections an overview of the state of the art knowledge on the molecular structure of asphaltenes will be carried out, followed by an overview on the studies of asphaltene fractionation procedures.

#### *1.2.1.2 Asphaltene molecules*

Due to the cited tendency of asphaltenes to aggregate its molecular weight remained open to speculation for many decades. Early studies on asphaltenes molecular weight by vapor pressure

osmometry (VPO) and centrifugation indicated molecular weights ranging up to tens of thousands g/mol<sup>96,97</sup>. Steady State Fluorescence experiments showed that asphaltenes molecular weight range from 500 to 1500 g/mol with a mean value which is considered in most studies of 700 – 750 g/mol<sup>98</sup>.

Concerning the asphaltenes molecular structure since early publications it is agreed that they are constituted of aromatic and aliphatic moieties. The way such moieties are structured within the molecules thus surging two different school of thoughts, one proposing that the asphaltenes would present many aromatic nuclei linked by alkanes, the known archipelago model and the other proposing that asphaltenes are formed by a single fused aromatic core with side alkane chains, the continental (or island) model. The predominance continental or archipelago structures within the crude oil would greatly influence the aggregate structures of the asphaltenes: archipelago favoring macromolecular structures and the continental model mostly favoring the formation of asphaltenes aggregates as proposed by Yen and Mullins. Although many studies pointed out for the predominance of continental structures over archipelago ones, it now being elucidated that asphaltenes are composed of “abundant islands and archipelago structural motifs”<sup>99</sup>. Chacón-Patiño<sup>99</sup> states that “the asphaltene structure is a continuum of island and archipelago motifs” and that “the dominant structure (island or archipelago) depends upon the asphaltene sample”. The great emphasis on the past years on the predominance of continental structural motifs over archipelago is the shown to be probably another false paradigms on petroleum science leading to massive acceptance of some asphaltenes structures (nanoaggregates) over others (macromolecular structures).

The multitude of asphaltenes molecules was recently captured by Atomic Force Microscope experiments<sup>100</sup> (Figure 13).

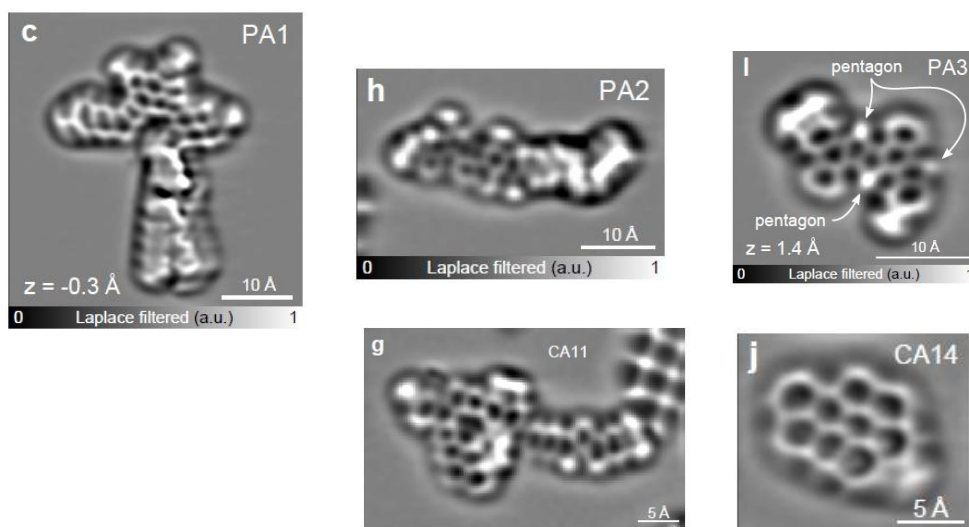


Figure 13. Atomic Force Microscopy images from petroleum (PA) and coal (CA) asphaltenes. Reprinted with permission from Schuler, B.; Meyer, G.; Peña, D.; Mullins, O. C.; Gross, L. J. Unraveling the molecular structure of asphaltenes by Atomic Force Microscopy. *Am. Chem. Soc.* **2015**, 137 (31), 9870–9876. Copyright 2000 American Chemical Society.

The AFM images point out for the predominance of continental structure of molecules over the archipelago ones, although pointing out for the presence of molecules with an archipelago wireframe where the aromatic nuclei are connected by a short aromatic chain (the study detected a single bond). The hypothesized molecules from coal and petroleum asphaltenes obtained by AFM are shown in Figure 14.

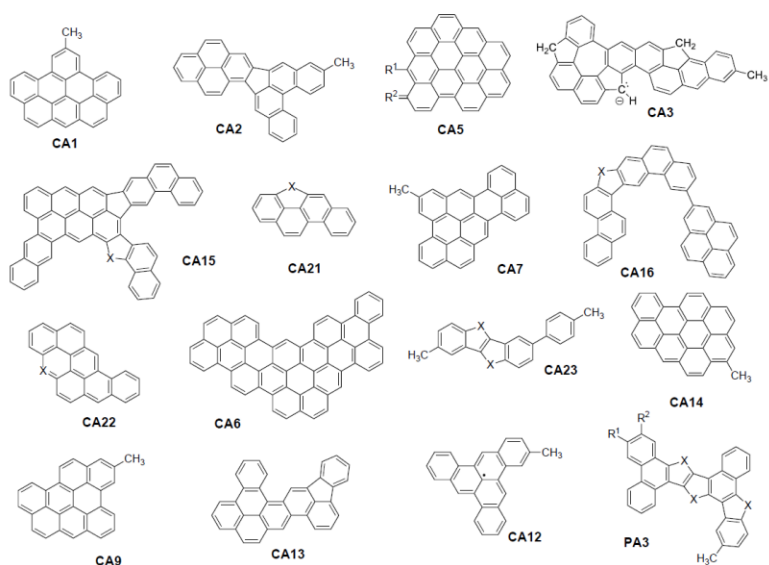


Figure 14. Coal and petroleum asphaltene molecules after Schuler<sup>100</sup>. Reprinted with permission from Schuler, B.; Meyer, G.; Peña, D.; Mullins, O. C.; Gross, L. J. Unraveling the molecular structure of asphaltenes by Atomic Force Microscopy. *Am. Chem. Soc.* **2015**, 137 (31), 9870–9876. Copyright 2015 American Chemical Society.

A second study<sup>101</sup> with asphaltenes coming from different sources further revealed the complexity of the asphaltene molecules (Figure 15). In Figure 15 there are represented molecules from crude oil (A1) and its formed asphaltene deposit (A2); from a heavy oil vacuum resid (B1) its hydroconverted product (B2); asphaltene from a steam cracked tar (C1) and bitumen asphaltenes (D1 and D2).

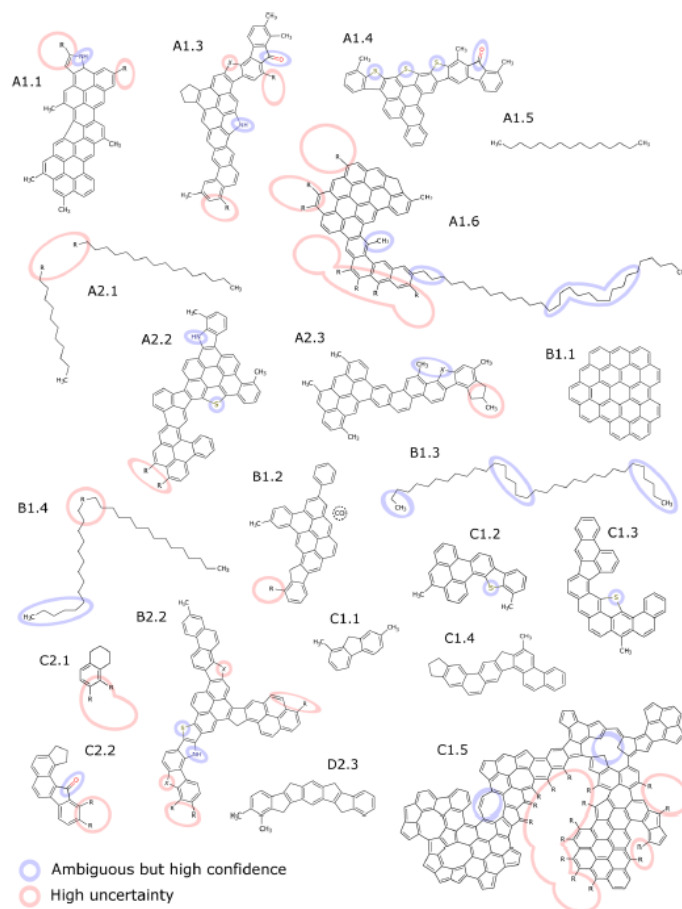


Figure 15. Asphaltene structures from different origins as hypothesized by Schuler<sup>101</sup>. Reprinted with permission from Schuler, B.; Meyer, G.; Peña, D.; Mullins, O. C.; Gross, L. J. Heavy oil based mixtures of different origins and treatments studied by Atomic Force Microscopy. *Am. Chem. Soc.* **2015**, 137 (31), 9870–9876. Copyright 2017 American Chemical Society.

The asphaltenes is known to carry the higher content in heteroatoms (N, O, S) and metals, mainly Nickel and Vanadium compared to the saturates, aromatics and resins. The solubility of asphaltenes in a diversity of solvents was reported elsewhere<sup>102</sup>.

Besides the molecular and aggregation behavior of asphaltenes in toluene, there has been reports on their complex behavior and phase changes with the appearance of different amorphous phases and liquid crystals<sup>103</sup>.

### 1.2.1.3 Asphaltene Fractions

The research on the average structure of asphaltenes in solvents or in crude oil as well as the discretization of the asphaltene molecules as it is shown in the last sections are one way of having information on the asphaltenes. A second way is to fractionate asphaltenes by solubility or surface activity to decrease polydispersity and capture the different problematic fractions within one given process on the hydrocarbon production chain. Kaminsky<sup>104</sup> fractionated asphaltenes with a premise that “different asphaltenes from around the world contain different amounts of specified fractions”. They fractionated asphaltenes by solubility in pentane-methylene chloride yielding four fractions which considerably differed in morphology and dissolution rates in toluene and dodecylbenzenesulfonic acid (DBSA)/heptane mixtures. The most polar fraction, precipitated with the 30:70 pentane to methylene chloride ratio presented the smallest rate of dissolution and a high content in metals which were deemed to be responsible to the high polarity of such a fraction.

Acevedo<sup>105</sup> fractionated asphaltenes by complexation with p-nitrophenol yielding two fractions, which he named after A1 and A2. Fraction A1 presenting a very low solubility in toluene, around 90 mg/L, being more aromatic, presenting less alkyl side groups, and higher concentration of metals<sup>106</sup>. Acevedo<sup>107</sup> points out that the fraction A2 is responsible for the stabilization of fraction A1 in toluene impeding its flocculation and complete phase separation.

The asphaltenes were fractionated using accelerated dissolution technique<sup>108,109</sup>, it was found basically two fractions which they called EDA and DDA standing for “easy to dissolve asphaltenes” and “difficult to dissolve asphaltenes”. The authors reported that “easy to dissolve asphaltenes”

play an important role in solubilizing and stabilizing the “difficult to dissolve asphaltenes”. Two main asphaltene fractions were also indicated by fluorescence spectroscopy technique.

### 1.2.2 Asphaltene destabilization

When dealing with the phenomenology of asphaltenes destabilization and deposition one realizes the great inhomogeneity of terminologies their meanings referring to the various stages of asphaltene colloidal destabilization or phase separation, to the point that some authors delineate their own meanings to the following terminologies: destabilization; flocculation; precipitation; deposition and adsorption. The great variety of terminologies used sometimes with contradictory meanings can be in part attributed to the contribution of researchers with different backgrounds perceiving each stage of the cited processes in a different manner but perhaps is mostly related to the uncertainties within the asphaltene supramolecular structure itself and the roles of the other petroleum constituents maintaining the delicate solution balance within the petroleum fluid.

### 1.2.3 Asphaltene adsorption

Adsorption processes are separated in two main categories according to the binding mechanisms: physisorption and chemisorption. Physisorption is the process of interaction of a molecule or particle to active sites in a solid through physical interactions which are mainly constituted of polar interactions. Chemisorption occurs when a solute give rise to a covalent chemical bonding with the solid substrate. Within the present work adsorption processes would mainly refer to physisorption processes as it is theorized to be the main interaction occurring between asphaltenes and solid surfaces. Asphaltene adsorption properties is widely reported in the literature with a good review by Adams<sup>110</sup>. Adams summarizes the sorbent active functional

groups as well the asphaltene functional groups (Figure 16). Langmuir and Freundlich types of adsorption isotherms were used to characterize asphaltene adsorption on a diversity of substrates.

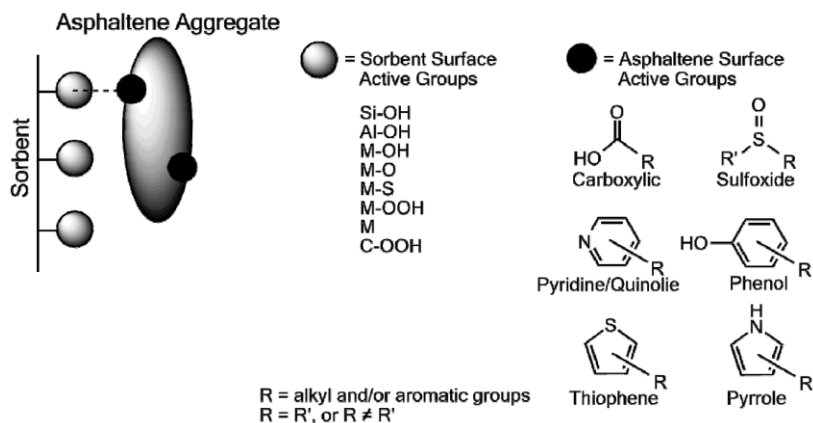


Figure 16. Sorbent active sites and asphaltene active groups involved in asphaltene adsorption processes. Reprinted with permission from Adams, J. J. Asphaltene adsorption, a literature review. *Energy & Fuels* **2014**, 28 (5), 2831–2856. Copyright 2014 American Chemical Society.

Asphaltene adsorption was also studied by quartz crystal resonator as it will be shown in details in a later section. Adams<sup>110</sup> emphasizes that the asphaltene masses obtained by quartz crystal resonators are systematically greater (2 – 9 mg/m<sup>2</sup>) than the ones obtained by adsorption measured by UV-Visible spectroscopy, which are in the 0.26 – 3.78 mg/m<sup>2</sup><sup>111,112</sup>.

#### 1.2.4 The onset of asphaltene destabilization and the asphaltene yield

The onset of asphaltene destabilization was recently shown to depend on the kinetics of asphaltene aggregation<sup>113</sup>. According to the study, asphaltene destabilization from crude oils had long been regarded as kinetically independent, contrary to what they showed that the asphaltene destabilization can take months or years depending on the nonsolvent concentration.

The same group has also showed that asphaltene deposition in capillary occurs considerably before the onset of asphaltene destabilization<sup>114</sup>.

The onset of asphaltene or heavy organics destabilization is known to vary with almost all experimental parameters. Thus, if the onset of asphaltene destabilization is being measured by titration the onset is known to be dependent on the titration rate and the temperature.

The onset of asphaltene flocculation varies with the utilized nonsolvent as shown in Figure 17<sup>115</sup>.

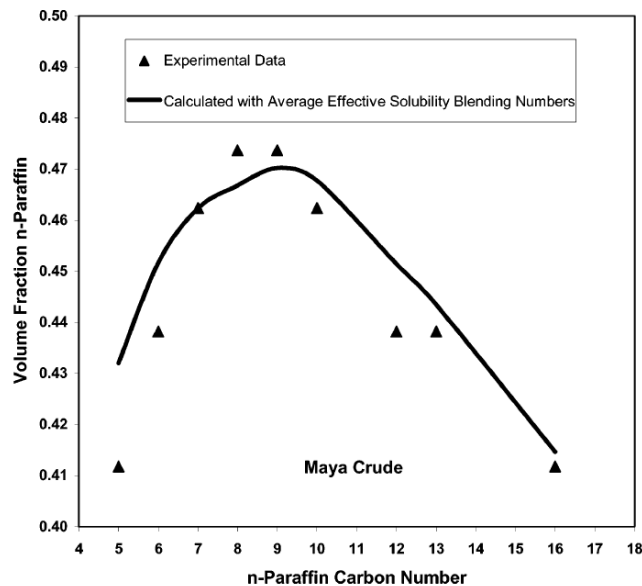


Figure 17. Onset of asphaltene flocculation variation according to the utilized nonsolvent. Reprinted with permission from Wiehe, I. A.; Yarranton, H. W.; Akbarzadeh, K.; Rahimi, P. M.; Teclemariam, A. The paradox of asphaltene precipitation with normal paraffins. *Energy & Fuels* **2005**, 19 (4), 1261–1267. Copyright 2005 American Chemical Society.

This paradox, as the solubility parameter of n-paraffins increases with their molecular weight is explained by Wiehe<sup>115</sup> as appearing due to the mixture of liquids of greatly different molecular sizes. Wiehe states that thermodynamic models based on the solubility parameter are able to predict such a maximum.

The amount of precipitated asphaltenes increases with decreasing n-alkane molecular weight as shown in Figure 18<sup>102</sup>. This increase is in part due to the overlap of the precipitated material with the material known to form the resin fraction.

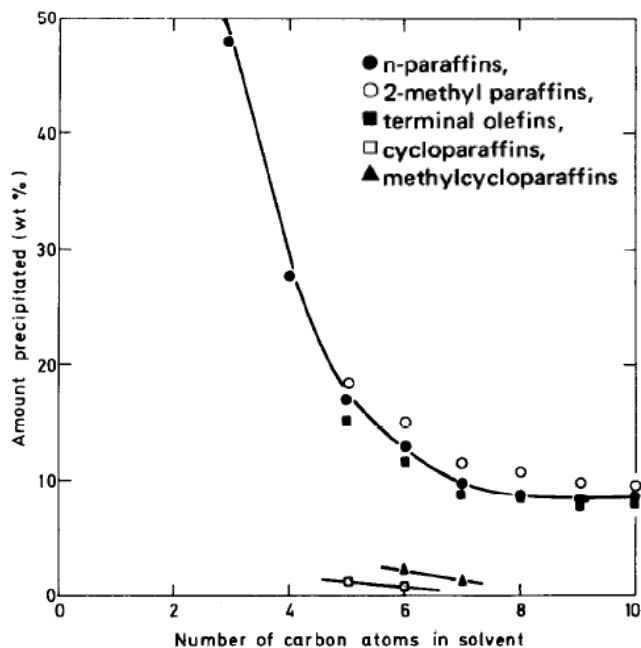


Figure 18. Amount of precipitated asphaltenes as a function of paraffin hydrocarbon. Reprinted with permission from Mitchell, D. L.; Speight, J. G. The solubility of asphaltenes in hydrocarbon solvents. Fuel **1973**, 52 (2), 149–152. Copyright 1973 Elsevier.

The asphaltene solubility in crude oil and model systems has been largely studied by using solubility parameters as a part of a regular solution approach.

$$\delta = \left( \Delta H^v - \frac{RT}{V} \right)^{1/2} \dots\dots\dots(1)$$

The yield in asphaltenes varies with the quantity of utilized solvent with a plateau at more than 30 times the volume of nonsolvent to the crude oil volume<sup>8</sup>. A reduction on asphaltene yield, at higher volumes of precipitant was also reported as it was shown by Sieben<sup>116</sup>.

The aggregation kinetics of destabilized asphaltenes were early studied by Anisimov<sup>117</sup> and Yudin<sup>62</sup> who found that the kinetics and stability of asphaltenes aggregates are rather affected by the nature of the solvent. Yudin<sup>62</sup> studied asphaltenes solution in toluene and found asphaltene aggregation limited by diffusion at initial stages of aggregation with subsequent reaction limited aggregation taking place. They observed that at asphaltenes concentrations smaller than the so known “critical micellar concentration” only diffusion limited aggregation would take place.

### 1.2.5 Methods of detection of asphaltene destabilization

Onset of asphaltene destabilization is routinely detected by near-infrared spectroscopy<sup>118,119</sup> and optical microscopy<sup>120–122</sup> but many other methods are available<sup>123–125</sup>. Surface plasmon resonance (SPR) seems especially promising to study the kinetics<sup>113</sup> of this process because of its independence on asphaltene particle sizes<sup>126</sup>. The ability to detect the least soluble asphaltenes<sup>127</sup> and obtain accurate onsets of asphaltene destabilization<sup>128</sup> directly impacts models on asphaltene destabilization and deposition<sup>129–131</sup>. Figure 19 displays an example of a classical experimental schema for measuring asphaltene destabilization onset at high pressure.

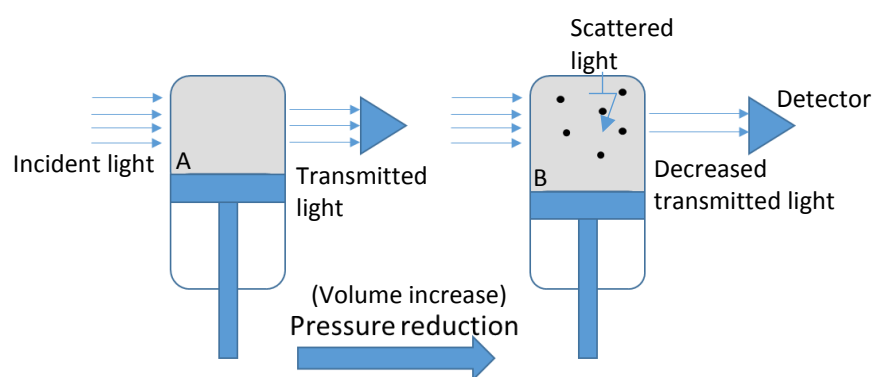


Figure 19. Classical experimental assembly for detecting asphaltene destabilization at high pressure conditions. (A) System with stable asphaltenes and (B) system with destabilized asphaltenes presenting a reduction in the light transmission due to light scattering caused by the presence of particles.

### 1.2.6 Methods of studying asphaltene deposition

Asphaltenes deposition from crude oils is usually evaluated by capillary tube experiments<sup>132,114</sup>, flow loops<sup>133</sup> and core flooding tests<sup>134</sup>. Other methods encompassing the buildup of an Taylor-Couette devices<sup>135,136</sup> and of packed columns<sup>137</sup> have also been proposed. Several fundamental questions regarding this deposition need to be addressed: possible existence of a critical particle size<sup>137,138</sup>, impact of the aggregation kinetics<sup>139</sup>, roles of shear rates and pressure gradients<sup>138</sup>. Eskin<sup>136,140,141</sup> found that asphaltenes aggregates greater than 100 nm would not deposit, and they estimated the size of the deposited particles around several nanometers. Figure 20 brings a classical experimental schema when assessing asphaltene deposition.

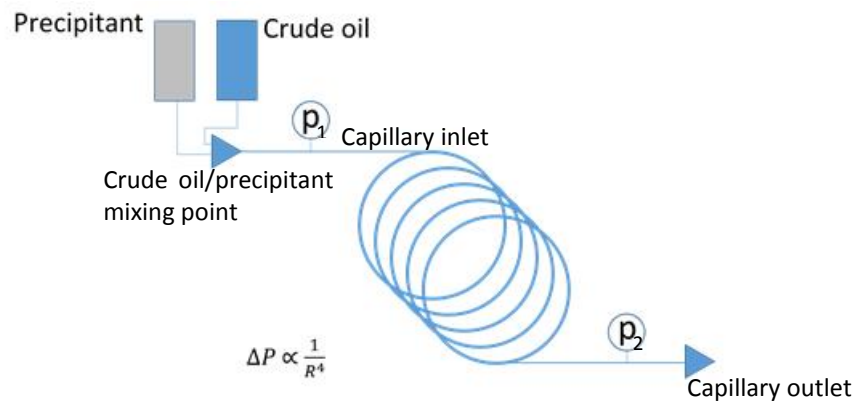


Figure 20. Classical experimental assembly for detecting asphaltene deposition. Crude oil and an asphaltene precipitant are mixed prior to be flown through a capillary tube. The capillary inlet and outlet pressure ( $P_1$  and  $P_2$ ) are constantly measured. Asphaltene deposition is estimated by calculating the decrease of the capillary radius, with the Hagen-Poiseuille law, taken into account the pressure drop  $(P_2 - P_1)$ <sup>132</sup>.

Each of the employed techniques are also sensitive to one scale on deposit formation. If taken that asphaltenes are present in crude oil from angstroms to hundreds of nanometers and when destabilized give rise to deposits which are mainly constituted of tens of micrometers, one can

trace the asphaltene deposition scale in order to address correctly each experimental work. In Figure 21 we propose such a division.

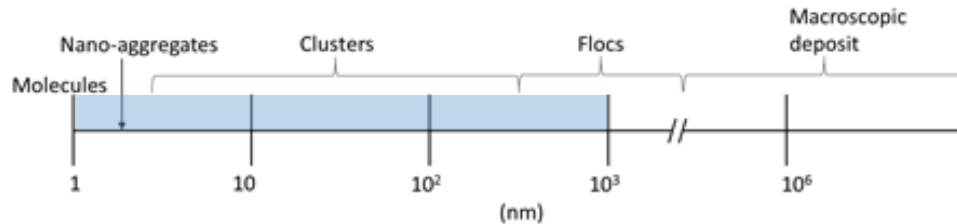


Figure 21. Size scale on asphaltene particles inducing deposition.

The evaluation of asphaltenes and other crude oil components deposition processes by quartz crystal resonator is done within the size scale of molecules, nanoaggregates, clusters and particles with a couple of micrometers, i. e., small floccs, as it is shown by the shaded zone in Figure 21.

### 1.3 Phase separations and organic deposits

The research on crude oils may have become too Cartesian with processes of fractionation and molecular identification. In the case of some organic deposits the fractionation and ultimate identification of problematic molecules succeeded as it is the case for the tetrameric acid family<sup>27</sup>. For the case of asphaltenes, resins and high molecular weight paraffins the fractionation and ultimate molecular and organic functions identification may not be the best strategy for the comprehension of destabilization and deposition because of the intricate interaction of such fractions. A first step in comprehending the great complexity of organic deposits is to study their composition and classification.

Mousavi-Dehghani<sup>123</sup> demonstrate the possible existence of seven different phase transitions related to heavy organic compounds. Apart from the phase transitions related to the paraffin fraction, cloud-point (WAT) and pour-point, they hypothesize that asphaltene and resins may give rise to 5 distinct phase separations, which they refer to **asphaltene precipitation onset (APO)**; **asphaltene + resin flocculation onset (ARFO)**; **asphaltene + resin deposition onset (ARDO)**; **asphaltene micellization onset (AMO)** and **asphaltene coacervation onset (ACO)**.

### 1.3.1 Interpretations of the process of asphaltene destabilization and deposition

The process of asphaltene destabilization, floc formation and deposition is generally not well understood. The asphaltene aggregation has been interpreted in terms of fractal aggregation theory which explains many of the experimental observations. The asphaltene aggregation process is described to present characteristics or being limited by diffusion and limited by reaction, with some studies pointing out that such constraints are mostly related to the asphaltene concentration in solution and the solvent solubility towards asphaltenes. Diffusion and reaction limited aggregation are based on the how the deposition mass is varying with time. Diffusion limited aggregation being proportional to the square root of time and reaction limited processes obeying to other relations.

In the conceptual point of view some studies proposed mechanisms and different phases to explain the processes occurring once asphaltenes are destabilized until they attain macroscopic dimensions and precipitate.

Vargas<sup>142</sup> proposed a model (Figure 22) based on scanning electron microscopy (SEM) in which dissolved asphaltene nanoaggregates when destabilized give rise to **primary particles** with diameter in the order of 300 – 500 nm. Primary particles aggregate in **micro-aggregates** with sizes

greater than 1  $\mu\text{m}$ . Such processes are deemed to be reversible. The aging of the micro-aggregates according to Vargas et al. is prone to give rise to a solid-like phase which if thermally treated (120  $^{\circ}\text{C}$ ) do not dissolve in contact with crude oil.

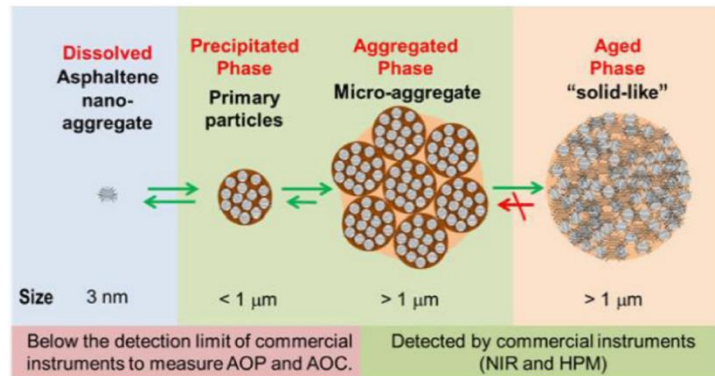


Figure 22. Occurring processes once asphaltenes are destabilized according to Vargas<sup>142</sup>.

Tanaka<sup>143</sup> by X-ray diffraction (XRD), SAXS and SANS experimental evidences proposes a aggregation mechanisms with the nanoaggregates or as it is named by them "**core aggregates**" as the basic units which are capable of yielding two higher aggregates stages: a **medium aggregate** which is the product of the interaction of the core aggregates and the media (maltenes, oils or solvents); **fractal aggregates**, including diffusion or reaction limited aggregates, where the aggregation process is largely independent on the surrounding media. Typical sizes for medium aggregates are 5 to 50 nm and for fractal aggregates the hypothesized sizes are greater than 100 nm.

Theophylaktos<sup>144</sup> studied the aggregated structure of flocculated asphaltenes by small angle X-ray scattering. They concluded that with the addition of n-heptane there is a compaction of the internal structure of the aggregates from scales ranging from 2.5 nm to 1  $\mu\text{m}$ .

# Chapter 2

## 2. Quartz crystal resonator and flow assurance

### 2.1 Introduction to the QCR technique

Quartz crystal displays delocalization of electrical charges when a force is applied to its structure. Such phenomenon was discovered by the brothers Curie at the end of the 19<sup>th</sup> century<sup>145,146</sup> and was named *piezoelectricity* which means literally electricity from pressure. The inverse-piezoelectric effect consists of the deformation of a piezoelectric material when a voltage is applied to it. If an alternating voltage is applied to the piezoelectric material it can be put to resonate when the natural resonance frequency of the body is reached. This principle was used for the first time by Nicholson in 1918 with the creation of the first patent on piezoelectric oscillators. At first the oscillators were utilized in time and frequency control as well as electromechanical transducers. Nowadays, piezoelectric resonators, mainly quartz crystal resonators (QCR), have been largely employed for sensing and micro-weighting purposes.

QCR are constituted by a properly cut quartz crystal sandwiched between electrodes which excite the quartz crystal to vibration and ultimately resonance. Different cuts quartz crystals present different resonance changes within temperature variations. Figure 23 shows the crystallographic cut of an AT-cut quartz crystal as well as its temperature variation. The AT-cut quartz crystal is normally used as they present less temperature variations around 25 °C.

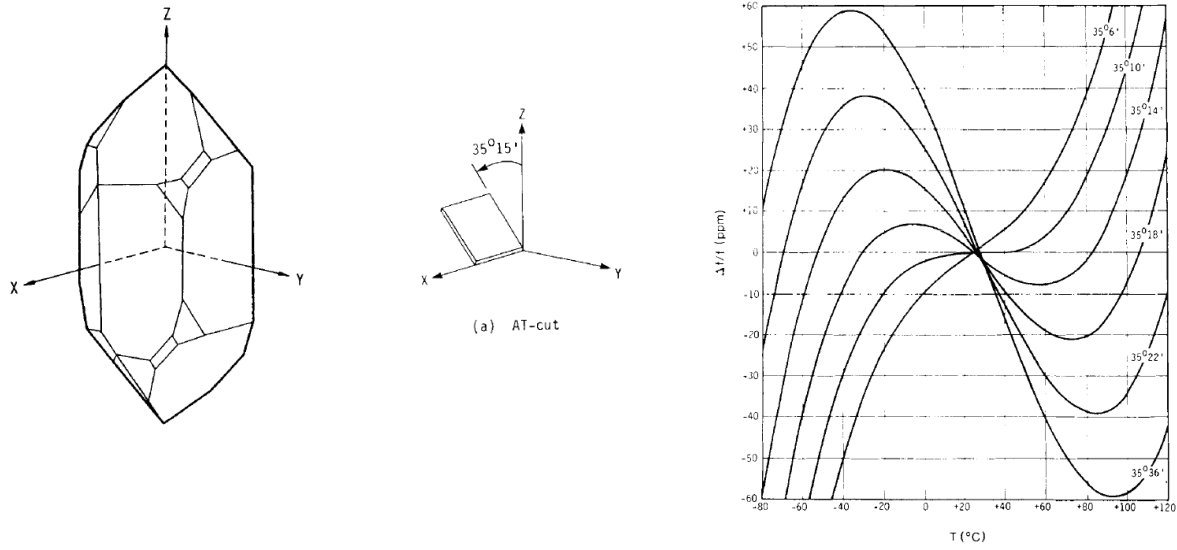


Figure 23. AT-cut quartz crystal and the temperature sensitivity of different quartz crystals cuts.

Quartz crystal resonators present low energy dissipation. This characteristic is well represented by the quality factor, which is the ratio of the stored energy to the dissipated energy in each oscillation cycle (Equation 2).

$$Q = \frac{2\pi E_{\text{stored}}}{E_{\text{dissipated}}} \dots \dots \dots (2)$$

Dissipated energy is normally quantified by the use of the inverse of the quality factor, assigned as the dissipation factor ( $D$ ), or by the use of bandwidth ( $I$ ) when impedance analysis is applied to collect quartz crystal resonance parameters. Such quantities are related according to Equation 3.

$$D = Q^{-1} = \frac{2\Gamma}{F_n} \dots \dots \dots (3)$$

Where,  $F_n$  is the quartz crystal resonance frequency with the subscript  $n$  standing for harmonic number.

Sauerbrey<sup>147</sup> ; Nomura<sup>148,149</sup>; Bruckenstein<sup>150</sup>; Kanazawa<sup>151</sup> and Muramatsu<sup>152</sup> established the theoretical and experimental basis for the use of quartz crystal resonators as micro-weighting or sensing applications in gaseous or liquid environments.

In 1959 Sauerbrey<sup>147</sup> utilized an AT-cut quartz crystals to determine resonance frequency changes due to an added overlayer on the quartz surface. As the masses measured were in the scale of 10<sup>-6</sup> g, Sauerbrey coined the terminology quartz crystal microbalance (QCM). Sauerbrey showed that the thickness increase of a laterally homogeneous and thin over layer on a quartz surface induces a change in the quartz resonance frequency according to Equation 4.

$$\frac{\Delta F}{F_0} = -\frac{\Delta h}{h} = -\frac{\Delta m_q}{\rho_q A h} = -\frac{\Delta m}{\rho_q A h} \dots \dots \dots (4)$$

Where  $F_0$  is the natural or fundamental resonance frequency of the quartz crystal,  $h$  stands for quartz crystal thickness,  $\rho_q$  stands for quartz density and  $A$  for quartz crystal active surface area ( $\approx$  electrode area). Equation 3 is known as Sauerbrey equation and although it is rigorously valid for over layers with the same quartz crystal acoustic impedance and with infinitesimal mass it was already shown that the equation returns good results on loads representing 10 to 15% of the quartz crystal mass<sup>153,154</sup>. The natural resonance frequency of a quartz crystal is related to its thickness according to Equation 5.

$$F_0 = \frac{v}{2h} \dots \dots \dots (5)$$

Where,  $v = \sqrt{\mu_q / \rho_q}$  is the velocity of the transversal shear wave within the bulk quartz crystal and  $\mu_q$  the quartz crystal shear modulus. Equation 4 and 5 can be combined to yield an equation

relating changes masses directly to the sensed changes in quartz crystal resonance frequency (Equation 6).

$$\Delta m = -\frac{A\sqrt{\mu_q\rho_q}}{2F_0^2}\Delta F \dots\dots\dots(6)$$

The use of quartz crystal under liquid environment was firstly thought to be not feasible due to large viscous damping that the liquid imposes to the quartz vibration. This thought was broken when Nomura<sup>148,149</sup> and following works by Bruckenstein<sup>150</sup>, Kanazawa<sup>151</sup> and Muramatsu<sup>152</sup> during the 1980s established experimental and theoretical basis for their use in liquids. Johannsmann<sup>155</sup> emphasizes that the basis of the use of piezoelectric resonators under liquid environment were, however, established much before in the 1930s by the work developed by Mason and McSkimin and collected within the book written in 1948 by Mason<sup>156</sup>.

The immersion of the quartz crystals in liquids were found to yield a change in resonance frequency proportional to the square root of the product density and viscosity of the liquid media (Equation 7).

$$\Delta F = -\frac{F_0^{3/2}}{\sqrt{\pi}\sqrt{\mu_q\rho_q}}\sqrt{\rho_l\eta_l} \dots\dots\dots(7)$$

Where  $\rho_l$  and  $\eta_l$  stands for liquid density and viscosity. The immersion of the quartz crystal resonator in liquids yields a viscous damping which is also directly proportional to the density and viscosity product of the liquid media (Equation 8).

$$\Delta \Gamma = \frac{F_0^{3/2}}{\sqrt{\pi}\sqrt{\mu_q\rho_q}}\sqrt{\rho_l\eta_l} \dots\dots\dots(8)$$

In the case other harmonics are utilized, the changes in frequency and dissipation, for the cases shown in Equations 5 to7, can be expressed as shown in Equations 9, 10 and 11.

$$\Delta F_n = -\frac{2F_0^2}{nA\sqrt{\mu_q\rho_q}}\Delta m \dots\dots\dots(9)$$

$$\Delta F_n = -\frac{f_0^{3/2}}{\sqrt{\pi}\sqrt{\mu_q\rho_q}}\sqrt{\rho_l\eta_l}\frac{1}{\sqrt{n}} \dots\dots\dots(10)$$

$$\Delta\Gamma = \frac{f_0^{3/2}}{\sqrt{\pi}\sqrt{\mu_q\rho_q}}\sqrt{\rho_l\eta_l}\frac{1}{\sqrt{n}} \dots\dots\dots(11)$$

Quartz crystal resonance is fully defined by a change in resonance frequency ( $\Delta F_L$ ) and dissipation ( $\Delta\Gamma_L$ ) due to loads on the quartz surface. The two information can be conveniently gathered as a complex change in resonance frequency. Changes in complex frequency shift due to loads on the quartz surface can be determined by evaluating the acoustic load impedance on the surface (Equation 12). The small load approach applies when the ratio in resonance frequency change imputed by the load in relation to the resonance frequency of the unloaded quartz is smaller than 0.02<sup>154</sup>.

$$\Delta\tilde{F} = \Delta F + i\Delta\Gamma = \frac{2F_0i}{\pi}\frac{\tilde{Z}_L}{Z_q} \dots\dots\dots(12)$$

Where  $\Delta\tilde{F}_L$  is the complex shift in resonant frequency composed of real part ( $\Delta F$ ) and imaginary part ( $\Delta\Gamma$ ) accounting for dissipative effects.  $F_0$  stands for fundamental resonant frequency of the quartz;  $Z_q$  stands for quartz acoustic impedance ( $\sqrt{\mu_q\rho_q}$ ) and  $\tilde{Z}_L$  stands for acoustic load

impedance on the quartz surfaces. The complex acoustic load impedance is calculated by the ratio of the tangential stress to tangential velocity for a propagating plane wave on the quartz surface (Equation 13)<sup>155</sup>.

$$\tilde{Z}_L = \frac{\hat{\sigma}_S}{\hat{v}_S} \dots \dots \dots (13)$$

Quartz crystal resonance frequency and bandwidth data can be obtained by three techniques: 1. oscillator circuit; 2. Ring-down method and 3. Impedance analysis. Oscillator circuits are normally adapted to the measure one overtone, with the resonance frequency obtained by the aid of a frequency counter. Bandwidths, and thus, energy dissipation, are not easily withdrawn from the circuit amplifier. Oscillators also have values of oscillation frequency ( $F_{osc}$ ) differing from the acoustic resonance frequency ( $F_n$ ) from the quartz crystal. Such differences are not constant with different loads which poses complications on the correct quartz acoustic resonance frequency determination. Ring-down method, which is utilized within the most commercially available quartz crystal resonator equipment, is based on the excitation of the quartz by radio-frequency pulse (RF pulse). The pulses are shut off and the decay of the induced electrical current is recorded over time. Quartz resonance frequency and energy dissipation ( $D$ ) are then withdrawn from the current *versus* time profile. Complex resonant frequencies can be directly obtained with the aid of a network analyzer<sup>157,158</sup> with the determination of the quartz crystal electrical admittance ( $\tilde{Y}_{el}$ ). The network analyzer excites the quartz at different alternating voltage frequencies and records the quartz electrical admittance or equivalently electrical impedance ( $\tilde{Z}_{el} = 1/\tilde{Y}_{el}$ )<sup>155</sup>.

$$\tilde{Y}_{el} = G_{el} + iB_{el} \dots \dots \dots (14)$$

The conductance ( $G_{el}$ ) and susceptance ( $B_{el}$ ) spectra of admittance ( $\tilde{Y}_{el}$ ) are used to determine quartz resonance frequencies ( $F_n$ ) and bandwidths ( $\Gamma_n$ ). Resonance frequency is obtained at maximum conductance and bandwidth is obtained from the half-width at half-height of the conductance spectra (Figure 24).

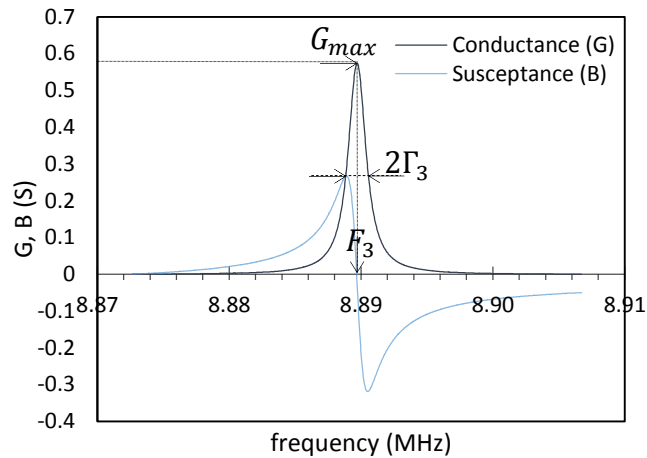


Figure 24. Admittance analysis of a 3 MHz quartz crystal resonating at its 3<sup>rd</sup> overtone ( $n=3$ ). The real (Conductance-G) and imaginary parts (Susceptance-B) of admittance is shown. At quartz resonance conductance is at its maxima and susceptance is zero.  $2\Gamma_n$  is obtained directly from the frequency window between maximum and minimum susceptance. These points are equivalent to the half width at half band of the conductance spectra.

### 2.1.1 Effect of roughness

Besides the changes in frequency and dissipation due to smooth and elastic added overlayer, as well as due to pure Newtonian liquid, deposited material roughness also give rise to complex frequency changes. Heterogeneities can be separated in vertical roughness ( $h_r$ ) and a lateral roughness ( $l_r$ ). The changes frequency and dissipation induced by deposited material roughness can be determined by Equations 15 and 16.

$$\frac{\Delta F}{F_0} \approx \frac{-1}{\pi Z_q} \sqrt{\frac{\rho_l \omega \eta_l}{2}} \left( 1 + 3\sqrt{\pi} \frac{h_r^2}{l_r \delta} - 2 \frac{h_r^2}{\delta^2} \right) \dots \dots \dots (15)$$

$$\frac{\Delta \Gamma}{F_0} = \frac{1}{\pi Z_q} \sqrt{\frac{\rho_l \omega \eta_l}{2}} \left( 1 + 2 \frac{h_r^2}{\delta^2} \right) \dots \dots \dots (16)$$

Where  $\delta$  stands for shear wave penetration depth or decay length. In Newtonian liquids the decay length is obtained by Equation 17.

$$\delta_n = \left( \frac{\eta_l}{\pi n F_0 \rho_l} \right)^{1/2} \dots \dots \dots (17)$$

The calculation of decay length for other cases, as in the case of the presence of an elastic or viscoelastic deposit is shown by Hilmman<sup>159</sup>.

### 2.1.2 Effect of pressure and pressurized liquid

The effect of pressure on the quartz crystal frequency change was first studied by Stockbridge<sup>160</sup> and Susse<sup>161</sup> they found a linear change in resonance frequency with pressure (Equation 18).

$$\Delta F_p = F_0 \alpha \Delta P \dots \dots \dots (18)$$

More recently Cassiède<sup>158,162-164</sup> and Daridon<sup>165</sup> developed a model for probing viscosity of liquids at high pressure using a quartz completely submerged in the fluid. Such model is brought in Equations 19 and 20.

$$\Delta F_{P,l} = \left[ -n(2C_m(\alpha_\infty - \kappa_v + \kappa_h)\rho_l h_{interface}) - \sqrt{n} \frac{C_m}{\sqrt{\pi F_0}} \left( \frac{\alpha_\infty}{2} - \kappa_v + \kappa_h \right) \sqrt{\rho_l \eta_l} \right] P \dots \dots \dots (19)$$

$$\Delta\Gamma_{P,l} = \left[ \sqrt{n} \frac{C_m}{\sqrt{\pi F_0}} \left( \frac{\alpha_\infty}{2} - \kappa_v + \kappa_h \right) \times \sqrt{\rho_f \eta_f} (1 + R_{interface}) \right] P \dots\dots\dots(20)$$

Where  $\alpha_\infty$ ,  $\kappa_v$  and  $\kappa_h$  stands for temperature variation coefficient, quartz crystal volumetric and linear compressibility.

## 2.2 Quartz crystal applied to crude oil research

Quartz crystal technique has been used since 2002 to study crude oil systems. Among the most usual research topics are asphaltene and resins adsorption. Crude oil asphaltenes destabilization onset, crude oil bubble point and wax appearance temperature were also investigated by quartz crystal resonator technique. In the following passage, the studies are briefly summarized.

Quartz crystal resonator technique applied to crude oil research is rather recent being the first publication on asphaltenes and resins adsorption and deposition on hydrophilic surfaces by Ekholm<sup>166</sup>. Ekholm prepared solutions of asphaltenes, resins and crude oil in toluene, heptane and mixtures (50:50) of them. The concentrations varied from 0.025 to 5 g/L. The solutions were injected into a flow cell where a quartz crystal of natural resonance frequency of 5 MHz was exposed to the solutions. The frequency and dissipation were recorded to the 3<sup>rd</sup> harmonic. They found that resins in heptane formed an elastic layer on the electrodes surfaces. When solutions of resins in heptane-toluene mixtures are utilized it is observed that the adsorbed amount of resins decreases with increasing toluene mass fraction. The asphaltene solutions were observed to give rise to adsorbed/deposited elastic layers at lower concentrations in toluene and viscoelastic layers at higher concentrations and reach no plateau as observed by resins. Ekholm indicates that resins were not capable of desorbing pre-adsorbed asphaltenes nor adsorb on asphaltenes. The adsorption of diluted crude oil gave rise to a more dissipative layer when

compared to the mixtures of resins and asphaltenes heptane-toluene solutions. When washed with toluene, they found that the amount of irreversible adsorbed material was smaller than the case when extracted resin-asphaltene solutions were utilized. They conclude that such differences would come from the effect of the other crude oil components like waxes and paraffin.

Xie<sup>167</sup> utilized extracted asphaltene solutions (10 – 200 ppm) in heptane-toluene and pentane-toluene mixtures to access asphaltene deposition regime (diffusion or reaction limited) and asphaltene depositing particle sizes and diffusion coefficients. They found no plateau for the asphaltene adsorbed mass. Asphaltene particles sizes were estimated to range from 30 to 120 nm with their diffusion coefficients ranging from  $3 \cdot 10^{-11}$  to  $1 \cdot 10^{-11}$  m<sup>2</sup>/s. The asphaltene adsorption was found to be diffusion limited. Xie also points out that although the asphaltene adsorption by itself may cause little problem in production, it could be of significant importance in facilitating asphaltene deposition.

Goual<sup>168</sup> evaluated diluted bitumen in heptane-toluene solution adsorption at the oil/water interface by using a quartz crystal coated with silica gel. Two main adsorption regimes were found, a non-steady regime at low bitumen concentrations and a steady state regime at high bitumen concentrations. In light of such regimes Goual explains emulsion stability as a function of the asphaltene/resins ratio.

Hannisdal<sup>39</sup> performed a multi-harmonic analysis to study the adsorption of asphaltenes, resins and mixtures of them on silica surfaces and their correlation to asphaltene coated particle stabilized emulsions. He utilized asphaltene concentrations of approximately 8 g/L and found that asphaltene irreversibly adsorbed on silica with the adsorbed mass estimated as 5.6 mg/m<sup>2</sup>.

Hannisdal points out that the adsorbed mass is greater than the adsorption of non-associating polymers which are in the range of 1-3 mg/m<sup>2</sup>. Asphaltene and resins mixtures in toluene were observed to yield similar adsorption as in the case of asphaltene solutions. Adsorption of resins solution in toluene (~8g/L) was observed to be minor and reversible when rinsed with toluene. Dudasova<sup>112</sup> analyzed the adsorption of asphaltenes in quartz crystals coated with silica, titanium, alumina and FeO<sub>x</sub>. The solutions were prepared in toluene and heptane-toluene in concentrations varying from 0.01 to 1 g/L. It was found little influence of the surface material on the amount of deposited asphaltenes (1.5 – 9.8 mg/m<sup>2</sup>), being adsorption mostly related to the quality of the solvent and not to the surface wettability.

Rudrake<sup>169</sup> utilized the QCM and X-ray photoelectron spectroscopy (XPS) to investigate asphaltene adsorption on metal surfaces. Solutions of extracted asphaltenes re-dissolved in toluene in concentrations ranging from 0.05 to 1.5 g/L were utilized. The adsorbed layer estimated by XPS were found to be in the range of 5 to 8 nm with QCM values calculated to be around 8.3 nm for all the probed concentrations.

Abudu<sup>170</sup> studied the adsorption of diluted crude oils by a multi-harmonic analysis reaching qualitative (softness and aging) and quantitative (deposit thicknesses) information on the adsorbed asphaltene layer. Abudu used good and bad asphaltene solvents on the crude oil dilution. Asphaltene concentration varied from 0.5 to 30 wt %. When crude oil was diluted with toluene, film thicknesses were found to be around 3 nm, with higher thicknesses being obtained once crude oils were diluted with asphaltene nonsolvent.

Farooq<sup>171</sup> accessed asphaltene desorption by saline aqueous solutions using QCM. Asphaltene desorption was found to be minor with low saline aqueous solution with desorption occurring mostly in highly concentrated electrolyte solutions (3.5 wt%).

Zahabi<sup>172</sup> studied the asphaltene adsorption in gold, hydrophilic and hydrophobic silica. They evaluated the asphaltene adsorption after the asphaltene onset of destabilization was achieved finding a strong increase deposition. For asphaltene solutions in toluene they estimated asphaltenes particle sizes from 18 to 472 nm from the QCM data. Particle sizes obtained from NMR and microscopy were not in accordance with QCM results making them to point out for the possible non reliability of particle sizes calculated from QCM experiments. Deposit porosity was evaluated at 0.85 - 0.9 with open aggregates or polymer brush structures. The studies calculating diffusion coefficients with the quartz crystal resonator take into account the analysis of the first rates. Flowing a asphaltene solution on the quartz crystal resonator, the rates of change in surface concentration are related to the bulk concentration, the particles diffusion coefficient and are inversely proportional to the square root of time, as shown in Equation 21.

$$\frac{d(\Gamma_{surface})}{dt} = C \left( \frac{D_f}{\pi t} \right)^{\frac{1}{2}} \dots\dots\dots(21)$$

Such studies are normally done with keeping a bulk constant asphaltene concentration with a direct integration of equation (21) as shown in equation (22)

$$\Delta\Gamma_{surface} = \frac{CD_f^{1/2}}{\pi^{1/2}} \sqrt{\Delta t} \dots\dots\dots(22)$$

Using the quartz crystal resonator with the application of the Sauerbrey approach most of the studies utilized the calculated deposited mass and the experimental run time to determine the slope on Equation 22, thus obtaining diffusion coefficients. The majority of the studies goes further on to determine the sizes of the adsorbing particles by employing the Stokes-Einstein equation.

$$D_f = \frac{k_B T}{3\pi\eta_l d_p} \dots\dots\dots(23)$$

Where  $k_B$  is Boltzmann's constant,  $T$  is absolute system temperature,  $\eta_l$  is liquid viscosity and  $d_p$  stands for particle's diameter. Such approach on determining asphaltene particles diffusion coefficients and consequently particles diameter although frequently applied in the context of quartz crystal is criticized in other studies.

Tavakkoli<sup>173,174</sup> utilized extracted asphaltenes and diluted crude oils in heptane-toluene solutions to model asphaltenes deposition under flow conditions, accessing depositing asphaltenes particle sizes. Kiasari<sup>175</sup> utilized a 10 MHz quartz crystal resonator to model asphaltenes deposition on stainless steel. Subramanian<sup>176</sup> utilized the quartz crystal resonator to evaluate the adsorption of different asphaltene fractions on gold surfaces. Tapio<sup>177</sup> studied the desorption of adsorbed asphaltenes by various solvents with quartz crystal resonator.

Daridon<sup>178</sup> probed asphaltene flocculation from diluted crude oils and live oils by quartz crystal resonator. By analyzing frequency and dissipation data it was concluded that onset of asphaltene precipitation was accused by both parameters. The onset of asphaltene destabilization found by the quartz crystal resonator coincided with the ASCI rating<sup>179</sup> for determining the onset of asphaltenes destabilization. Cardoso<sup>180</sup> and Daridon<sup>7</sup> measured the asphaltene phase envelope

with a quartz crystal resonator immersed in a pressurized cell. Daridon<sup>181</sup> and Orlandi<sup>182</sup> measured live oil bubble point utilizing quartz crystal resonator totally immersed in crude oil. Pauly<sup>183</sup> and Cassiède<sup>184</sup> detected wax crystallization by quartz crystal resonator in model systems.

Recently Joonaki<sup>185</sup> published a very good study on the assessment of inhibitors influence on the onset of asphaltene destabilization, which he calls asphaltene appearance point (AAP), by UV-Vis-NIR spectrophotometry and quartz crystal totally immersed in crude oil at high pressure high temperature. Joonaki<sup>185</sup> claims that the use of the quartz crystal resonator makes it possible not only the evaluation of the eventual delaying on the asphaltene destabilization onset pressure but also the evaluation of rates of asphaltene deposition. Although this is possible, the report does not bring information on quartz crystal energy dissipation, which may lead to wrong conclusions. When evaluating rates of deposition as well as deposit structuring (one of the objectives of the present work) a thorough analysis of resonance frequency and energy dissipation over many overtones of resonance is better suited.

#### 2.2.1 Observations concerning the researched systems and experimental schematics

The above findings were mainly accomplished either with solutions of extracted crude oil components (asphaltenes and resins) in organic solvents at low concentrations, or in diluted crude oils. These extractions or dilutions are not innocuous since they may induce changes in the physical state of the asphaltenes and in their interaction with the remaining crude oil components<sup>186–190</sup> posing challenges in mechanisms comprehension.

The majority of the studies were performed with the aid of a flow cell (Figure 25-A) being a part of an open circuit where the solution with the analyte is injected.

Less common is the use of closed or semi-opened systems with the quartz totally immersed in the analyte solution (Figure 25-B). Given the great complexity in crude oil molecules, their surface activity and their aggregate state, both systems may provide very different data mainly related to mass balances and to the complexity crude oil adsorption and deposition processes. Such complexity was well described by Tóth<sup>134</sup> who found consecutive and competitive processes during asphaltenes deposition.

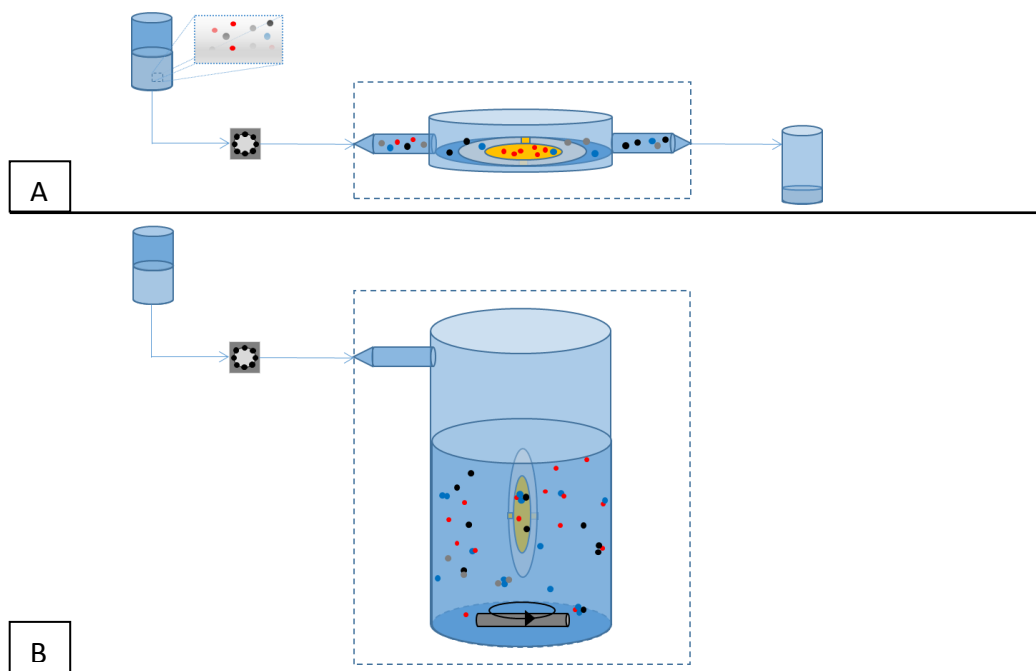


Figure 25. Two different experimental schematics when using quartz crystals to research on crude oil adsorption/deposition processes. (A) Mostly used experimental assembly. A stable or unstable solution of extracted asphaltenes or diluted crude oil is injected into a flow cell in fairly low flow rates ( $\mu\text{L}/\text{min}$ ). Normally one quartz side is exposed to the analyte. (B) Experimental assembly utilized in the present work. The quartz is totally immersed in crude oil, diluted crude oils, or solutions of extracted asphaltenes in toluene. The asphaltenes are destabilized in situ by the injection of *n* asphaltene nonsolvent. An asphaltene good solvent may also be used to study changes in crude oil viscosity due to dilution.

2.3 New approach on the utilization of QCM to access heavy organics destabilization and deposition from crude oils (live or dead)

The present thesis was envisaged in an attempt to apply the quartz crystal resonator technique totally immersed in crude oil (Figure 25-B) to detect asphaltene destabilization onset and to interpret asphaltene deposition processes.

Asphaltene destabilization and deposition is triggered by two methods: change in crude oil composition by smooth and continuous n-heptane and by doing step solubility changes. Such a processes were chosen to mimic asphaltenes destabilization undergoing under production conditions: gradual solubility changes related to depressurization processes during flow through pipelines or in the reservoir and step solubility changes undergone under fluid mixture processes, for example, in manifolds.

The ability of quartz crystals to access bulk (flocculation) and interfacial (adsorption/deposition) phenomena, by recording complex changes in resonance frequency, is used to follow up asphaltenes destabilization and deposition.

The possible occurring process during asphaltenes destabilization and deposition are not trivial. Two extrema of deposit configuration, when asphaltenes are destabilized, are schematically shown in Figure 26.

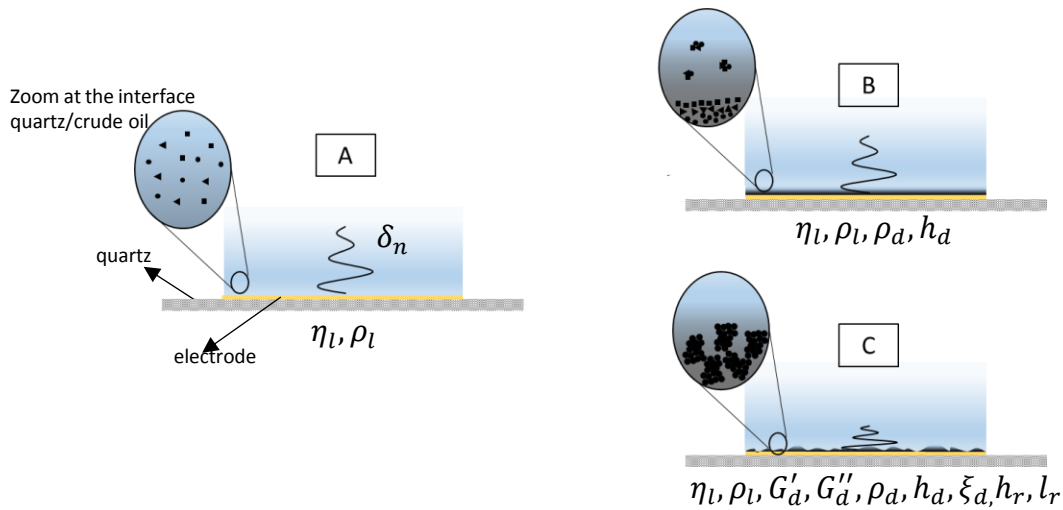


Figure 26. Schematics from the possible yielding asphaltene deposits on the gold electrodes. One electrode is shown for clarity. (A) One side of the quartz exposed to a crude oil with stable asphaltenes. (B) and (C) one side of the quartz crystal exposed to crude oil with destabilized asphaltenes forming a smooth and elastic deposit as exposed in (B) or a rough and viscoelastic deposit as shown in (C).

Figure 26-A exhibits a non-scaled schematic of the quartz immersed in crude oil or crude oil/n-heptane mixtures under the onset of asphaltene destabilization. The inset of Figure 26-A pictures the presence of dispersed or solubilized asphaltenes, different geometric forms stand for different asphaltene solubility fractions<sup>104,105,116</sup>. The main load on the quartz surface comes from liquid (crude oil + n-heptane mixture) density and viscosity. Other loads are needed to be accounted for when the onset of asphaltene destabilization is attained. Notably, the formation of a deposit on the electrode surfaces. Figure 26-B and C shows two deposit configuration extrema. The system in which quartz crystal is subjected to an elastic deposit and Newtonian viscous loads is represented in Figure 26-B. The energy dissipation in such a system comes ideally from Newtonian liquid load. Such a configuration is completely characterized by solving liquid density and viscosity and deposit density and thickness ( $\eta_l, \rho_l, \rho_d, h_d$ ) from the impedance

analysis. On the other extremum (Figure 26-C) a laterally heterogeneous, viscoelastic, porous and rough asphaltenic deposit is formed. In such a case the numbers of parameters influencing the complex resonant frequency shifts greatly increases, with the addition of complex shear modulus ( $\tilde{G}_d = G'_d + G''_d$ ), deposit permeability, or its characteristic length  $\xi_d$ , as well as lateral and vertical deposit inhomogeneity<sup>191-194</sup>. The system can rapidly become very complicated. Within intermediate deposit structures, i. e., laterally homogeneous and viscous deposits with low porosity and roughness ( $\xi_d, h_r, l_r, \ll \delta_n$ ), the application of a viscoelastic model is well defined<sup>195</sup>. In the case in which deposit is rigid but porous or laterally inhomogeneous, complex resonant frequencies are dependent on discontinuity sizes compared to the shear wave penetration depth and a number of studies were done to quantify such a deposits<sup>192-194,196-199</sup>.

When analyzing asphaltene destabilization and deposition the interpretation of frequency and bandwidth data in colloidal systems undergoing aggregation and deposition is important. Adsorption of colloidal particles onto the quartz surface can yield inertial or elastic loads depending on the contact stiffness between the particle and the quartz<sup>200,201</sup>. Inertial load reaches negative frequency shifts while elastic loads give rise to parallel resonating systems which can result in positive frequency shifts. The dissipation of adsorbed nanospheres (10 nm) was studied by Johannsmann<sup>202</sup>. He highlights that the dissipation was more related to the geometry of the particles attachment to the surface rather than to the internal properties of the particles. Experimentally and with the aid of finite element method calculations (FEM) they pointed out that a maximum in dissipation appears when hard spheres are deposited on the quartz surface. Such maximum was related to the quartz surface coverage. With the increase in surface coverage particles movement are inhibited causing a decrease in energy dissipation. The effect of lateral

heterogeneity of adsorbing colloidal particles was reported by Johannsmann<sup>203</sup>, he stated that for low coverage (below 50%) the particle layer exhibited Sauerbrey like behavior (inertial and elastic load). The deposition of micrometer sized particles was studied by Peschel<sup>204</sup>. Peschel observed positive frequency shifts interpreted as the influence of the particles resonance to the resonance of the quartz crystal. Porous deposits can yield high energy dissipation. For a porous deposited layer the energy dissipation will mostly depend upon the size of the pores compared to the shear wave penetration depth. If the pore is smaller than the penetration depth liquid is immobile and will mostly contribute for the frequency shifts through as a mass load, known as the missing mass effect. For bigger pores there is a significant dissipation and consequent damping of the quartz crystal resonance<sup>6</sup>. Another way of analyzing deposition of discrete particles is with the ratio of changes in dissipation and resonance frequency, the known DF plot<sup>2</sup>.

Reviakine<sup>205</sup> provides a useful table on various methodologies of analysis of resonance frequency and energy dissipation when the quartz is used to study different deposits in a liquid environment.

The possible deposit configurations are summarized in Figure 27. Deposits in Figure 27 are shown in only one side of the quartz for clarity.

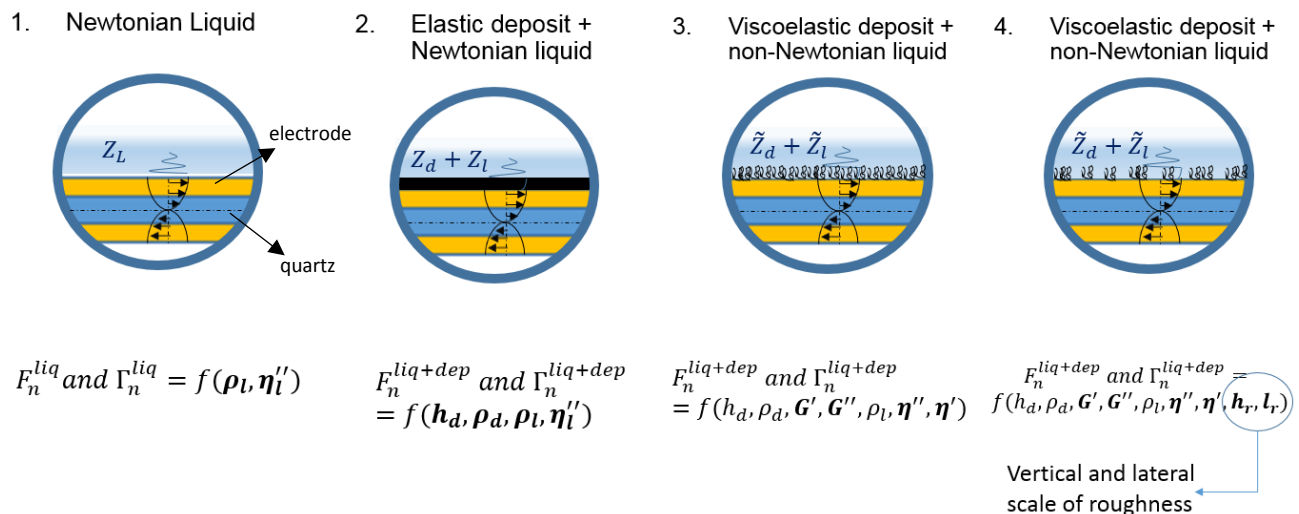


Figure 27. Various deposit and liquid loads on the quartz crystal surface. Only one quartz side is shown for simplicity. The parameters influencing frequency and bandwidth data is shown in each case.

## 2.4 Modeling

The modeling of the  $\Delta\tilde{F}_L$  data for the asphaltene precipitation and deposition from crude oils was performed taking into account the case of an elastic deposit and Newtonian fluid loads. The precipitation and deposition from extracted asphaltenes in toluene solutions were qualitatively evaluated since they yielded high energy dissipation.

The acoustic load impedance ( $Z_L$ ) for the case of an elastic deposit in a Newtonian liquid (Figure 26-B or Figure 27-2) is shown in Equation 24<sup>206</sup>:

$$Z_L = Z_d \frac{Z_l + Z_d \tanh(\gamma_d h_d)}{Z_l + Z_d \tanh(\gamma_d h_d)} \dots \dots \dots (24)$$

With  $Z_l$  the liquid acoustic impedance;  $Z_d$  standing for acoustic impedance of the asphaltene deposit;  $\gamma_d$ , the wave propagation constant and  $h_d$  the thickness of the deposit. The complex resonance frequency change was shown to be related to the ratio of impedances of the quartz load and the quartz (Equation 25)

$$\Delta\tilde{F}_L = \Delta F_L + i\Delta\Gamma_L = \frac{2F_0 i Z_L}{\pi Z_q} \dots \dots \dots (25)$$

Substituting Equation (24) in Equation (25) the real and imaginary parts of the complex resonant frequency are shown in Equations 26 and 27<sup>158,162,165</sup>.

$$\Delta F_L = -n2C_m \rho_d h_d - \sqrt{n} \frac{C_m}{\sqrt{\pi F_0}} \sqrt{\rho_l \eta_l} \dots \dots \dots (26)$$

$$\Delta\Gamma_L = \sqrt{n} \frac{C_m}{\sqrt{\pi F_0}} \sqrt{\rho_l \eta_l} \dots \dots \dots (27)$$

Where  $n$  stands for harmonic number (1, 3, 5 or 7) and  $F_0$  for ratio of resonance frequency to overtone order at high harmonics of resonance (7<sup>th</sup> overtone in this work) under vacuum

conditions;  $C_m$  stands for Sauerbrey coefficient ( $C_m = 2 F_0^2 / \sqrt{\rho_q \mu_q}$ ). Equations 26 and 27 are the direct application of the method developed elsewhere<sup>158,162,165</sup> to determine viscosity of liquids. The approach however is different, since the interfacial layer ( $h_d$ ) is not virtual as modeled by the former works and is rather taken as the buildup of an asphaltenic deposit. Equation 4 was simplified by the exclusion of the parameter  $R_{interface}$ <sup>162</sup> as it is no aim of the present work to accurately determine viscosity of the crude oil and its mixtures with n-heptane although some experimental values on viscosity are added.

The change in resonance frequency (Equation 26) can be summarized by a mass and viscous loads as it is shown in Equation 28.

$$\Delta F_n = n\Delta F_m + \sqrt{n}\Delta F_\eta \dots \dots \dots (28)$$

When Equation 28 is divided by  $n$  a linear relation between  $\Delta F_n/n$  and  $1/\sqrt{n}$  arises, being deposit thickness determined by its intercept and liquid density-viscosity product by its slope.

From Equation 27 it is directly deduced that  $\Delta \Gamma_n/\sqrt{n}$  yields a constant value which is used to determine the density-viscosity product from the liquid media.

$$\frac{\Delta \Gamma_n}{\sqrt{n}} = \Delta \Gamma_\eta \dots \dots \dots (29)$$

The viscous effect ( $\Delta \Gamma_\eta$ ) is calculated as the average of the  $\Delta \Gamma_n/\sqrt{n}$  over the recorded harmonics but the fundamental, i. e., the 3<sup>rd</sup>, 5<sup>th</sup> and 7<sup>th</sup> overtones of resonance.

According to the model presented in Equation 28 and 29, the change in resonance frequency normalized by the harmonic number should be a linear function of the inverse of the square root of the harmonic number and the bandwidth normalized by the square root of the harmonic

number should be constant, as the model does not account for dissipative effects. Thus such data was plotted from the raw data of the experiment of one crude oil with collection from the 3<sup>rd</sup> to 15<sup>th</sup> harmonics and are exposed on Figure 28.

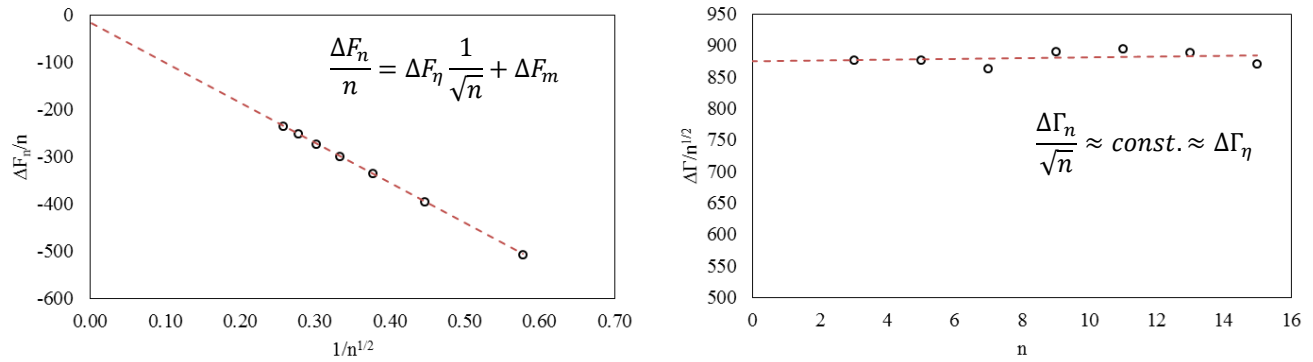


Figure 28. Schematics on the model application and definition of  $\Delta F_m$ ,  $\Delta F_\eta$  and  $\Delta \Gamma_\eta$ .

# Chapter 3

## 3. Materials and Methods

### 3.1 Dead crude oils

Five crude oils with different asphaltenes concentrations were utilized. Table 2 shows their density, viscosity, and the results of their SARA analysis in saturates, aromatics, resins and asphaltenes. Heptane and toluene densities and viscosities at 25 °C is also shown in Table 2.

*Table 2. Physical properties and SARA analysis of the utilized fluids. Viscosities and densities were evaluated at 25 °C and atmospheric pressure. The colloidal index of each oil is also added (see page 11 for details).*

Fluid	Density kg/m <sup>3</sup>	Viscosity 10 <sup>-3</sup> Pa.s	Saturates	Aromatics	Resins	n-C <sub>7</sub>	Colloidal instability index (CII)
						Asphaltenes	
(wt %)							
A	975	89.6	15.6	18.3	53.0	11.9	0.4
B	895	34.4	32	51.6	16.4	6.5	0.6
C	898	37.8	52.8	31.8	11.3	3.4	1.3
D	977	207.0	37.4	44.1	16.1	2.2	0.7
E	889	139.5	62.8	18.3	16.5	2.5	1.9
Heptane	679	0.388					
Toluene	862	0.551					

The crude oils were used as received from the industry. Toluene and n-heptane were purchased from Sigma Aldrich with purity of 99.9 wt % and used with no further purification. N-pentane was also utilized as a precipitant in order to compare resins effect on deposit buildup.

According to the colloidal instability indexes (CII) crude oil E is the most stable towards asphaltenes precipitation followed by crude oils C, D, B and A in this order.

### 3.2 Live crude oils

Two live oils were utilized on the measurement of asphaltene stability towards nitrogen injection.

Their compositions are shown in Table 3.

*Table 3. Live crude oils composition.*

Component	Live Oil 1		Live Oil 2	
	mol %	Mw	mol %	Mw
N <sub>2</sub>	0.6	28.0	1.0	28.0
CO <sub>2</sub>	0.1	44.0	0.1	44.0
C <sub>1</sub>	19.7	16.0	19.6	16.0
C <sub>2</sub>	5.1	30.1	5.6	30.1
C <sub>3</sub>	6.2	44.1	8.5	44.1
i – C <sub>4</sub>	1.4	58.1	1.4	58.1
n – C <sub>4</sub>	3.3	58.1	5.6	58.1
i – C <sub>5</sub>	1.4	72.2	2.1	72.2
n – C <sub>5</sub>	1.9	72.2	2.9	72.2
Fraction +C <sub>6</sub>	2.6	84.9	3.8	84.2

Fraction C <sub>7+</sub>	57.7	268.3	49.4	224.0
--------------------------	------	-------	------	-------

---

### 3.3 Asphaltenes extraction

The asphaltenes were extracted from dead oils by following a modified IP-143 procedure which consists of precipitating asphaltenes from the crude oil with 40 volumes of n-heptane per gram of crude oil. The crude oil is pre-heated to 60 °C for at least one hour until the asphaltene precipitation was done. After adding n-heptane, the system was left agitating during 24 hours and then was filtered with a 0.2 µm PTFE filter. The filter cake was washed with warm n-heptane until a colorless effluent was achieved. The asphaltenes were dried under nitrogen atmosphere.

### 3.4 Quartz crystal

It consists of a highly polished AT-cut beveled quartz disk purchased from International Crystal Manufacturing Co. (Oklahoma City, Oklahoma, USA). It has a fundamental frequency of 3 MHz and a blank diameter of 13.6 mm (Figure 32). Two electrodes were deposited on its faces on the central plano-plano portion by vacuum evaporation of an adhesive layer of titanium of 10 nm thickness followed by a 100 nm thick layer of gold. The gold electrodes have the same diameter of 6.7 mm.

### 3.5 Atmospheric pressure experimental apparatus

The schematics of atmospheric experimental assembly is shown in Figure 29. It consists of a glass mixing vessel on top of a magnetic stirrer and kept at constant temperature ( $\pm 0.05^\circ\text{C}$ ), in an oven during the entire experiment (The circulation and injection system is composed of a reservoir of

precipitant put on a scale ( $\pm 0.001$  g), Viton<sup>®</sup> tubes ( $D_i = 0.8$  mm), glass flow cell with optical path of  $400 \mu\text{m}$  and two peristaltic pumps.

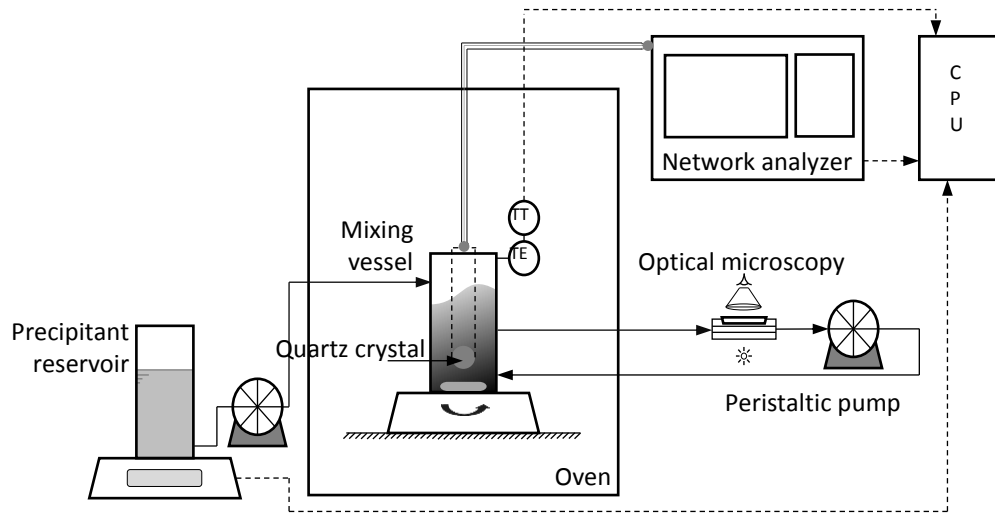


Figure 29. Schematics of the experimental assembly for experiments at atmospheric pressure.

### 3.6 Asphaltene destabilization procedures

The asphaltene destabilization was triggered by two methods: a continuous injection of nonsolvent and a step injection of nonsolvent above and under the estimated onset of asphaltene destabilization.

The continuous nonsolvent injection was done by injection rates varying from 3 to 9 mg/s in a system with initial mass of 20 g of crude oil. The titration procedure was idealized in order to approximate to a virtual infinitesimal change in crude oil–n-heptane solubility change in an attempt to detect the role of different asphaltene fractions during deposition, i. e., to approach phase separation equilibrium. Figure 30 brings a typical curve on the n-heptane mass fraction as a function of experimental run time for the highest mass flow rate ( $\sim 9$  mg/s). Numbers 1 and 2 indicates the baseline collection and the decreased mass flow rate in the beginning of the titration

to assure good mixing of the system avoiding localized asphaltene precipitation. Titration was proceeded to n-heptane mass fractions from 0.8 to 0.9.

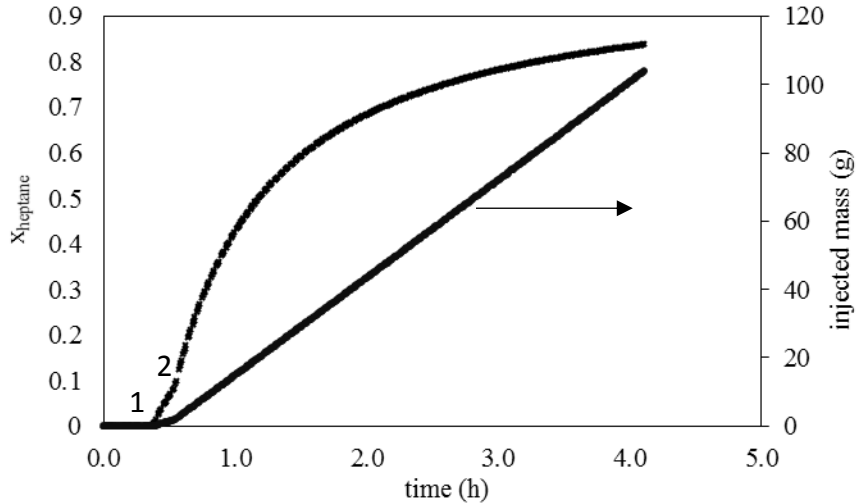


Figure 30. Experimental run time and achieved n-heptane mass fractions during continuous crude oil titration. N-heptane was injected at a constant mass flow rate as is shown by the second y-axis. A baseline collection of frequency and bandwidth is done with the n-heptane injection starting at (1). The n-heptane injection from (1) to (2) is performed at lower mass flow rate to assure good mixing from the viscous crude oil with n-heptane. At (2) the n-heptane mass flow rate is adjusted to the desired experimental flow rate ( $\sim 9$  mg/s).

### 3.7 Acquisition Method

Before each experiment the quartz is cleaned by rinsing with toluene and gently dried by air blown. Then it is introduced in the empty mixing vessel inside the oven and allowed to temperature equilibrate. The resonance of the quartz in air is recorded first. Next, the quartz is taken out and  $20 \pm 0.050$  g of crude oil are added to the mixing vessel. The quartz is then immersed in the crude oil and acquisition of frequency and bandwidth is started. The n-heptane titration is performed by using a peristaltic pump with a constant mass flow rate of  $8 \pm 0.5$  mg/s and the crude oil/precipitant mixture is kept well mixed by the magnetic stirrer during the entire

experiment (Figure 29). The crude oil titration with asphaltene good solvents was also performed, toluene and cyclohexane were utilized. Frequency and bandwidth data from the dilution experiments were compared with the signals obtained with the experiments using asphaltene nonsolvents to obtain onsets of asphaltene destabilization.

Conductance and susceptance spectra were obtained from the circuit scattering parameters (Equation 30), furnished by the vector network analyzer (Agilent E5071C with 3 MHz – 500 MHz frequency range) with the aid of an in-house developed program on LabVIEW®. 1601 points are recorded around resonance with a -5 dBm output level, a 300 Hz IF bandwidth and a smoothing aperture of 1.5% to reduce random noise effect on measurements. The maximum conductance, corresponding to the resonance frequencies are obtained by interpolation of 5 points around the maximum.

$$G + iB = \frac{1}{Z_0} \frac{1 - S_{11}}{1 + S_{11}} \dots\dots\dots(30)$$

Where  $Z_0$  stands for network characteristic impedance. The fundamental, 3<sup>rd</sup>, 5<sup>th</sup> and 7<sup>th</sup> ( $n = 1, 3, 5$  and  $7$ ) harmonics of resonance are recorded during the experiments but only 3<sup>rd</sup>, 5<sup>th</sup> and 7<sup>th</sup> harmonics were used for the analysis. The fundamental resonance mode suffers from effects related to the finite quartz and electrode sizes<sup>207</sup>. Harmonics with orders higher than 7 suffer from effects of spurious resonating modes<sup>195</sup> arising from the high viscous loads at low crude oil dilution.

The frequency and bandwidth of the quartz in air ( $F_n^{air}$  and  $\Gamma_n^{air}$ ) are recorded as the reference state to later calculations of changes induced by loads on the electrode surfaces ( $\Delta F_n^L = F_n^{load} - F_n^{air}$  and  $\Delta \Gamma_n^L = \Gamma_n^{load} - \Gamma_n^{air}$ ). Once  $F_n^{air}$  and  $\Gamma_n^{air}$  are acquired, the quartz is taken out from the

glass mixing vessel and  $20 \pm 0.050$  g of crude oil are added. The quartz is then totally immersed in the crude oil and the acquisition of frequency and bandwidth is started.

The frequency and bandwidths analysis were performed as a function of solvent or anti-solvent mass fraction and also as a function of experimental run time. Both analysis are important to comprehend mechanisms as it was observed that some processes were mainly independent on bulk solubility and thus independent on nonsolvent content.

### 3.8 High pressure experimental apparatus

The main part of the experimental setup consists of a variable volume cell closed at one end by a high pressure plug screwed to the cell (Figure 31). Electrical connections are inserted hermetically through the cap connecting the quartz crystal resonator to the Network analyzer by SMA connectors and coaxial cables to shield radio frequency and other electromagnetic disturbances. The cell has a maximum volume of  $50 \text{ cm}^3$  and is fitted with two valves, one near to the end plug serving as inlet valve, and the other in the middle of the cylinder serves as discharging valve. The volume is controlled by a step motor which can be operated to work at isobaric conditions (variable volume) or constant rates of depressurization or pressurization. The cell is placed horizontally as well as the quartz sensor so as it probes only the liquid phase whatever the existence or nonexistence of a gas cap. The cell is equipped with a pressure transducer which is placed in direct contact with the probed solution in order to avoid dead volumes. A pressure calibration with temperature is performed with the aid of a calibrating pressure gauge directly connected to the cell. Temperature is adjusted with the aid of a thermostatic bath with heating fluid circulation in the interior of the cell wall. The cell is equipped with an accurate position sensor that allows recording piston position changes and therefore volume variations with a

relative uncertainty of 0.05%. The working range of the cell is from vacuum to 100 MPa and from 273.15 to 423.15 K. The standard error in pressure measurement is less than 0.06 MPa in the full experimental pressure range (0.01-100 MPa). The temperature control has a stability of 0.1 K. Homogenization inside the cell is provided by means of magnetic stirring. The magnetic bars are prevented from touching the quartz crystal by a perforated plate.

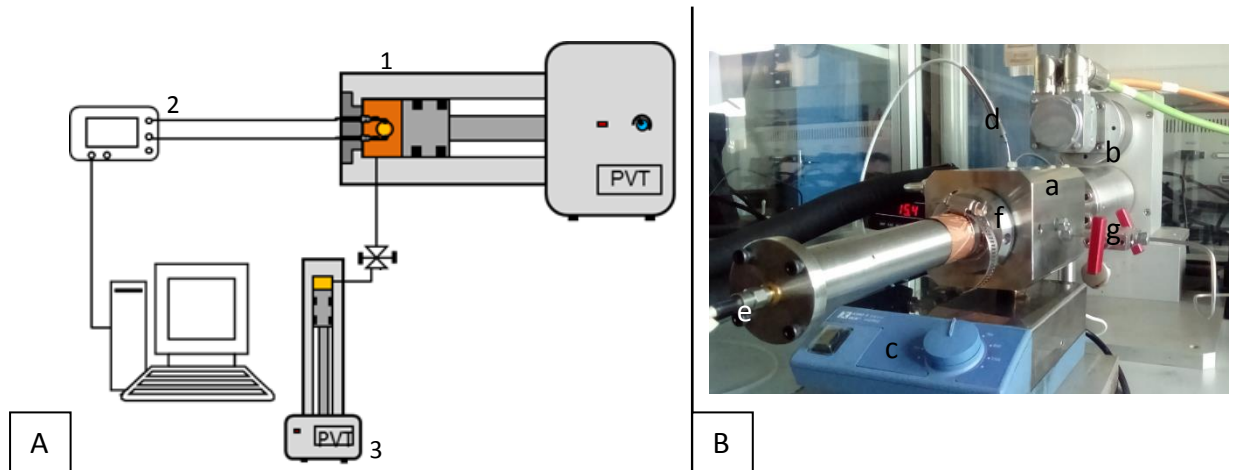


Figure 31. (A) High pressure experimental apparatus. (1) High pressure PVT cell with the quartz crystal resonator. (2) Network analyzer and (3) high pressure syringe pump. (B) An image of the high pressure equipment (a); step motor (b); magnetic stirrer (c); temperature probe (d); coaxial cable and connector (e); high pressure cap (f) and connected needle valves for injecting asphaltene destabilizers or cleaning procedures (g).

### 3.8.1 Constant mass expansion test

Bubble point and asphaltene destabilization measurements were evaluated by performing constant mass expansion tests. After the frequency and bandwidth for the quartz crystal under vacuum conditions the fluid is loaded in the pre evacuated cell. The live oils are homogenized in a parallel system in which it is left under the reservoir temperature for at least 24 hours. The live oil transfer to the high pressure cell is done with the aid of an insulated stainless steel tube fitted with a valve. The transfer is done stepwise by opening and closing the valve until the pressure at

the cell reaches the same pressure of the live oil bottle. The pressure of the live oil reservoir is kept constant by a hydraulic system. After the PVT cell is partially filled with the live crude oil the system is kept during several hours at a pressure much greater than its saturation pressure to equilibrate. Then, an isothermal depressurization is performed with a constant recording of pressure-volume data in order to detect bubble point. In order to keep the fluid in thermodynamic equilibrium during its expansion, it is permanently agitated and the speed in expanding the cell is limited so as to not exceed a decrease in pressure of 0.3 MPa per minute. During decompression, the resonant frequency  $F_n$  and dissipation  $\Gamma_n$  of the quartz crystal sensor are recorded and plotted as a function of time or pressure. From these measurements, shift in resonant frequency  $\Delta F_n$ , and dissipation  $\Delta \Gamma_n$ , due to liquid contact are calculated. As long as pressure remains above bubble conditions, both density and viscosity of the under saturated fluid decrease as pressure drops. Consequently,  $\Delta \Gamma_n$  decreases as pressure falls. After the appearance of the second phase, further decompression yields two opposite effects. The former is related to the release of light components in the gas phase as pressure decreases. It makes liquid more dense and viscous and therefore leads to an increase of  $\Delta \Gamma_n$ . The latter is directly associated to pressure effect on liquid properties. It leads to a reduction of the density viscosity product. That results in a decrease of  $\Delta \Gamma_n$ . Usually, release of light components dominates and  $\Delta \Gamma_n$  increases as pressure fall below the bubble point pressure. In this case, dissipation measurements carried out across the phase boundary present a minimum which can be used to estimate the bubble point pressure of the investigated system. If direct pressure effect is more significant than composition change below saturation pressure, the dissipation of the quartz resonator decreases along both single and bi-phase region as pressure drops but presents a break in slope when phase boundary is crossed.

In an opposite way  $\Delta F_n$  versus pressure exhibits a maximum at the saturation point during flash expansion. When the system is above the bubble point pressure, density and viscosity are reduced by decompression. This effect leads to an increase of the resonance frequency of the sensor. Once below the saturation pressure, release of light component effect dominates and the change in resonance frequency largely increases. Mass deposition also impacts the resonance frequency and may interfere with viscous effects if adsorption ( $h_{interface}$ ) changes when crossing the liquid-vapor phase boundary.

### 3.9 The asphaltene onset of asphaltene destabilization determination

Asphaltene onset of destabilization was determined by two methods. A Grunberg-Nissan type mixing rule, as it was applied in a previous work<sup>178</sup>, and the derivative of frequency and bandwidth data as a function of n-heptane mass fraction as it was suggested. The Grunberg-Nissan type mixing rule was employed as shown in Equations 31 and 32.

$$\Delta\Gamma = e^{x_{C7} \ln \Delta\Gamma_{C7} + (1-x_{C7}) \ln \Delta\Gamma_{oil} + x_{C7}(1-x_{C7})G} \dots\dots\dots(31)$$

$$\Delta F = \Delta F_{oil} + \frac{\Delta\Gamma_{oil}}{1+R} + x_{C7}L - e^{x \ln \frac{\Delta\Gamma_{C7}}{1+R_{interface}} + (1-x_{C7}) \ln \frac{\Delta\Gamma_{oil}}{1+R_{interface}} + x_{C7}(1-x_{C7})G} \dots\dots\dots(32)$$

Where,  $G$  and  $L$  are fitting parameters;  $x_{C7}$  stands for n-heptane mass fraction injected in the crude oil,  $\Delta F_{oil}$  and  $\Delta\Gamma_{oil}$  stands for resonance frequency and bandwidth for the pure crude oil;  $\Delta\Gamma_{C7}$  for bandwidth obtained with pure heptane and  $R_{interface}$  is one parameter to correct for roughness of the gold electrode on the evaluation of the viscosity of the solution. The influence of  $R_{interface}$  parameter in the equation to onset point determination is minimal<sup>158</sup> when considering other uncertainties. In the present work the parameter  $R_{interface}$  was not

evaluated and set equal to zero. Thus the theoretical change in frequency with n-heptane addition was evaluated by the simplified Equation 32, as shown in Equation 33.

$$\Delta F = \Delta F_{oil} + \Delta \Gamma_{oil} + x_{C7}L - e^{x_{C7} \ln \Delta \Gamma_{C7} + (1-x_{C7}) \ln \Delta \Gamma_{oil} + x_{C7}(1-x_{C7})G} \dots\dots\dots(33)$$

# Chapter 4

## 4. Results

### 4.1 Crude oil titration with an asphaltene solvent

#### 4.1.1 $\Delta f_n$ and $\Delta \Gamma_n$ as a function of toluene or cyclohexane mass fraction

In order to verify the validity of the proposed model the titration of crude oil with an asphaltene good solvent was done. Figure 32 and 33 present the change in resonance frequency and bandwidth as a function of toluene and cyclohexane mass fraction for crude oil C. The fundamental, third, fifth and seventh overtones of resonance are shown. The data are plotted as a function of the square root of the overtone number. The experiments were performed at atmospheric pressure and 25 °C.

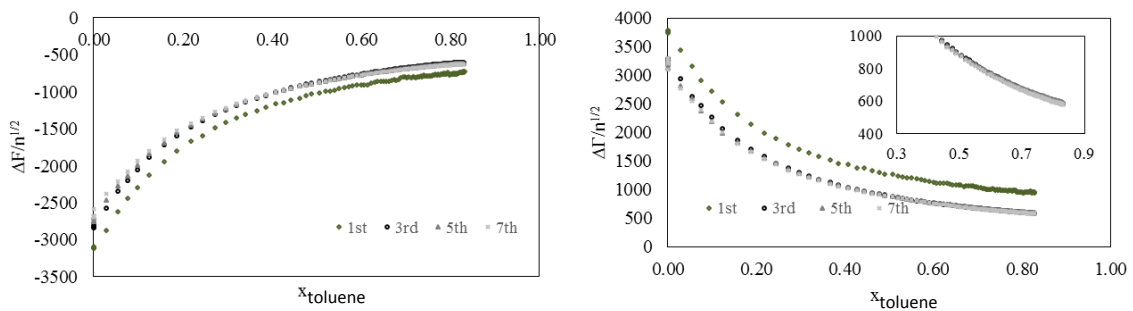


Figure 32. Crude oil C diluted with toluene, response in resonance frequency and bandwidth as a function of toluene mass fraction ( $x_{\text{toluene}}$ ).

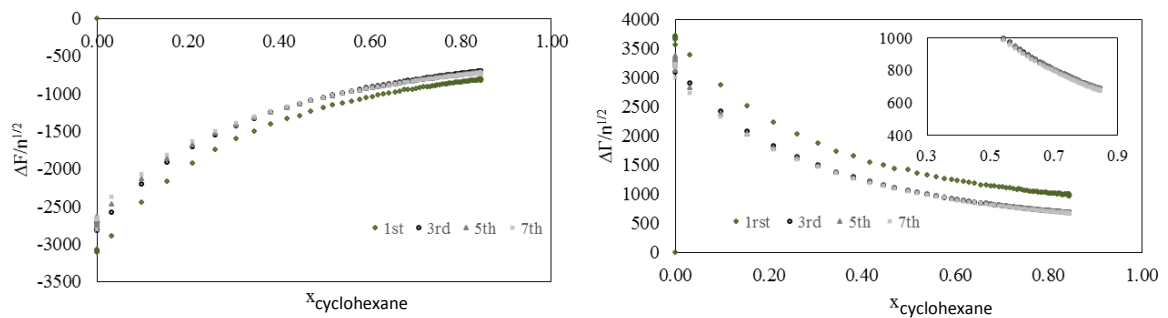


Figure 33. Change in resonance frequency and bandwidth due to cyclohexane continuous injection into crude oil C.  $x_{\text{cyclohexane}}$ = cyclohexane mass fraction.

The crude oil dilution with toluene or cyclohexane induces a decrease in the viscosity of the mixture within the whole titration region. Such viscosity decrease is reflected by an increase in the quartz crystal resonance frequency and a bandwidth decrease proportionally to the media square root of the density-viscosity product (Equation 7 and 8).

The fundamental frequency is shown to display a large difference in relation to the 3<sup>rd</sup>, 5<sup>th</sup> and 7<sup>th</sup> harmonics. This different behavior for the fundamental harmonic is explained by its greater sensitivity to the quartz dimensions. The inter-harmonic spreading is observed to come to a minimum with a change in the relative magnitudes. This is exemplified on Figure 34 for the resonance frequency change. The inter-harmonic minima obtained within the crude oil dilution procedure may arise from the viscosity changes and how each resonance frequency responds to it. At high viscosity, the quartz crystal poor coupling with the bulk crude oil, induces the quartz slipping effect. At high dilution, lower overtones are observed to give the highest resonance frequency changes. Part of such differences is also related to the measuring technique which sweeps the overtones of resonance at different system compositions due to the continuous n-heptane injection as illustrated in Figure 35. However, such frequency dependence on harmonic numbers is observed before the toluene injection procedure starts as it is highlighted by the analysis of the frequency and bandwidth changes as a function of experimental run time (Figure 36).

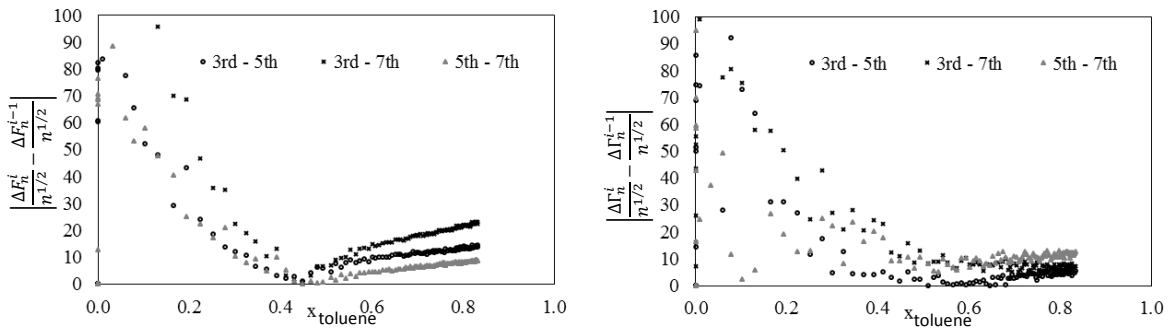


Figure 34. Inter-harmonic spreading from the normalized frequency and bandwidths as a function of toluene mass fraction (Crude oil C)

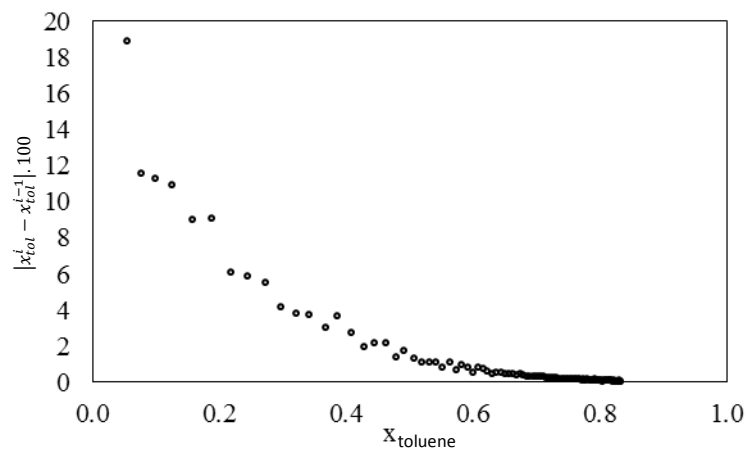


Figure 35. Variations in system composition with toluene injection for each cycle of measurement of complex resonance frequency data by the network analyzer (from the 3<sup>rd</sup> to 7<sup>th</sup> overtone).

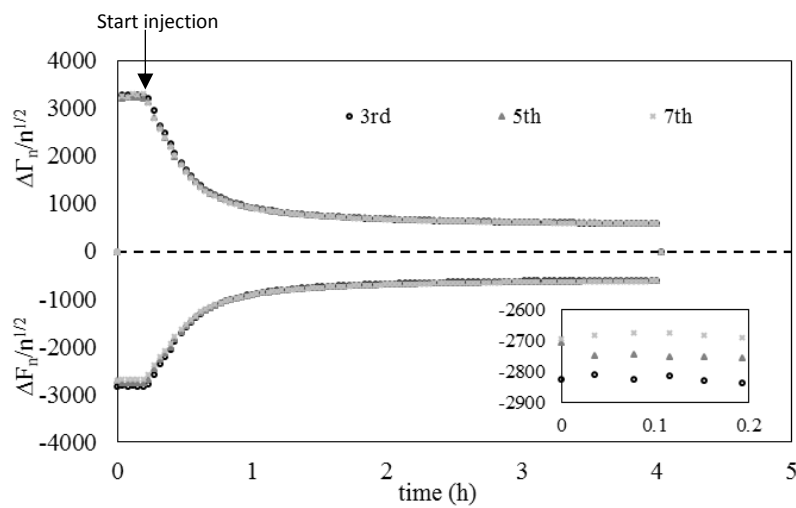


Figure 36. Resonance frequency and bandwidth changes for toluene injection into crude oil C as a function of time.

#### 4.1.2 Model application: density-viscosity and $h_{interface}$ determination

The model presented by Equations 21 and 22 was applied the collected changes in frequency and bandwidth in the crude oil dilution experiment. The model splits the resonance frequency as being a result of two contributions: elastic and smooth deposit mass ( $\Delta F_m$ ) and Newtonian liquid ( $\Delta F_\eta$ ) loads. Bandwidth is assumed to arise only from Newtonian liquid load ( $\Delta \Gamma_\eta$ ). Figure 37 brings the model calculated profiles of  $\Delta F_m$ ,  $\Delta F_\eta$  and  $\Delta \Gamma_\eta$ .

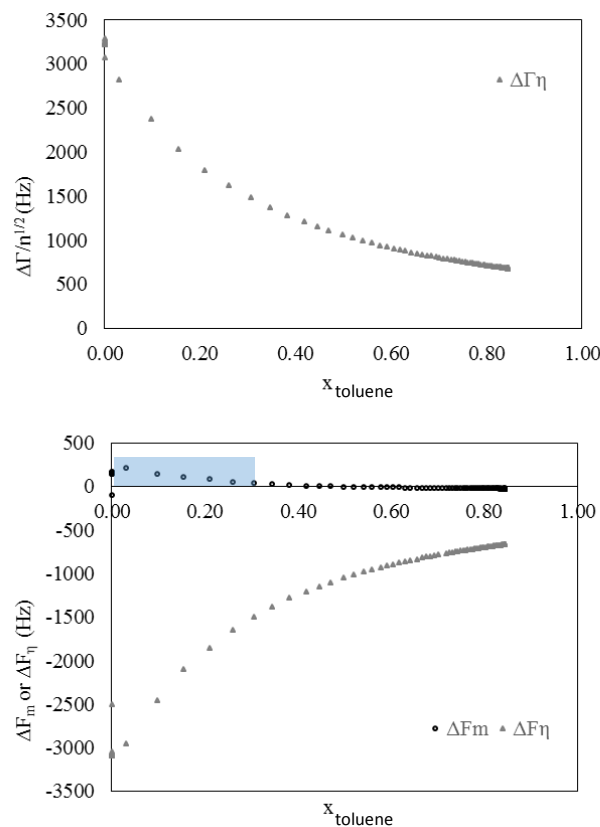


Figure 37.  $\Delta F_m$ ,  $\Delta F_\eta$  and  $\Delta \Gamma_\eta$  determination for the continuous dilution of crude oil C with toluene at 25 °C and atmospheric pressure.

The high inter-harmonic spreading at higher system viscosities (low toluene content) is solved by the model as a positive resonance frequency due to mass effects (shaded area in Figure 37). Such positive frequency change leads to the calculation of a negative deposit thicknesses, which is

unrealistic. Thus, at high crude oil viscosities the thicknesses must be taken as a virtual parameter which takes into account interfacial effects, in particular slipping at the interface quartz fluid, which disturbs the correct viscosity measurement. From  $\Delta F_m$ ,  $\Delta F_\eta$  and  $\Delta \Gamma_\eta$ , the density-viscosity product and the  $h_{interface}$  are obtained (Figure 38).

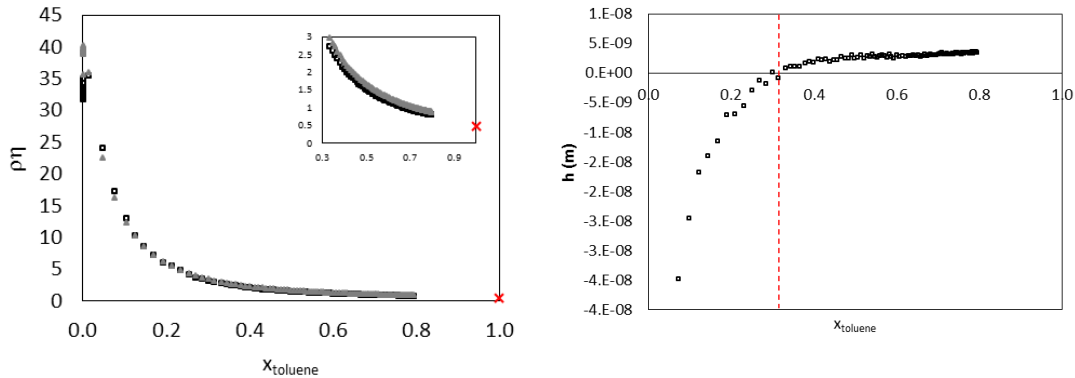


Figure 38. Density-viscosity product and thickness of the interfacial layer as determined from the viscous and mass contributions to change in resonance frequency and bandwidth. Crude oil C continuously injected with toluene at 25

The density-viscosity products calculated from the changes in bandwidth are slightly greater than the ones obtained by the change in frequency data. This may be explained by not taking into account interfacial effects as quartz roughness and other interfacial factors which were grouped under a  $R_{interface}$  in other studies on determining with precision the viscosity of liquids under high pressure<sup>165</sup>. The  $h_{interface}$  is observed to assume negative values at low dilution and values not exceeding 10 – 15 nm within the studies crude oils at higher dilutions. The negative values of  $h_{interface}$  may be explained in terms of quartz crystal slipping at high viscosities, i. e., bad coupling of the shear wave within the surrounding liquid. At greater dilution  $h_{interface}$  becomes positive mainly accounting for liquid trapping.

With the most viscous utilized crude oil, crude oil D ( $\eta_D = 207 \text{ mPa}\cdot\text{s}$ ), the  $h_{interface}$  was strongly negative at low dilution as it is shown in Figure 39.

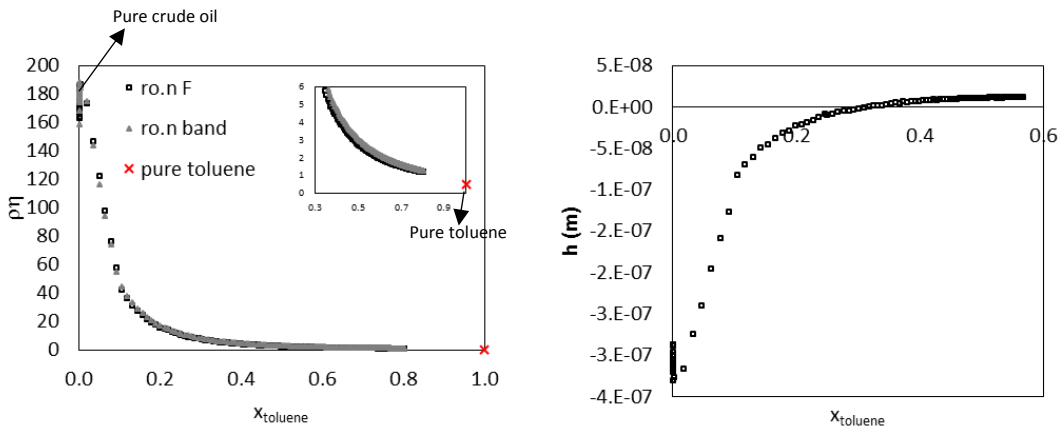


Figure 39. Density-viscosity product and  $h_{interface}$  for the dilution of crude oil D with toluene at 25 °C and atmospheric pressure.

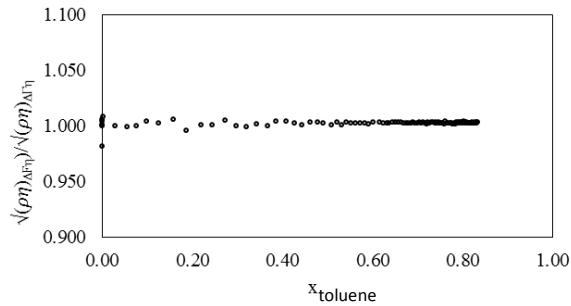


Figure 40. Ratio between the model calculated density-viscosity products from change in resonance frequency and bandwidth data for the dilution of crude oil D with toluene.

At low dilutions the high crude oil viscosity is interpreted as negative interfacial thickness higher than 300 nm due to quartz crystal slipping. Besides the high discrepancy on the calculated  $h_{interface}$ , the density viscosity data obtained at  $x_{tol} = 0$  with the quartz crystal resonator is within only 10% error when compared to the experimental data obtained with a viscometer and a densimeter. The understanding of the phenomena affecting  $h_{interface}$  estimation at high and low viscosities is important. The  $h_{interface}$  within the experiments of asphaltene destabilization

and deposition by nonsolvent injection is interpreted as a deposit thickness ( $h_{deposit}$ ), with the correct interpretation of deposition depending on such sides effects being interpreted as negative deposit thicknesses. Such phenomenology may be an impediment on properly interpreting data when analyzing high viscous systems. However, with the systems studied within the present Thesis, the negative character of the  $h_{deposit}$  was not observed to be relevant since at the onset conditions the system was already diluted and with  $h_{interface}$  not exceeding 30 nm thick. Figure 41 brings the case for the obtained  $h_{deposit}$  for the crude oil A, which presented the lowest n-heptane mass fraction resulting in asphaltene destabilization, thus, destabilization occurring with low system dilution and high viscosity.

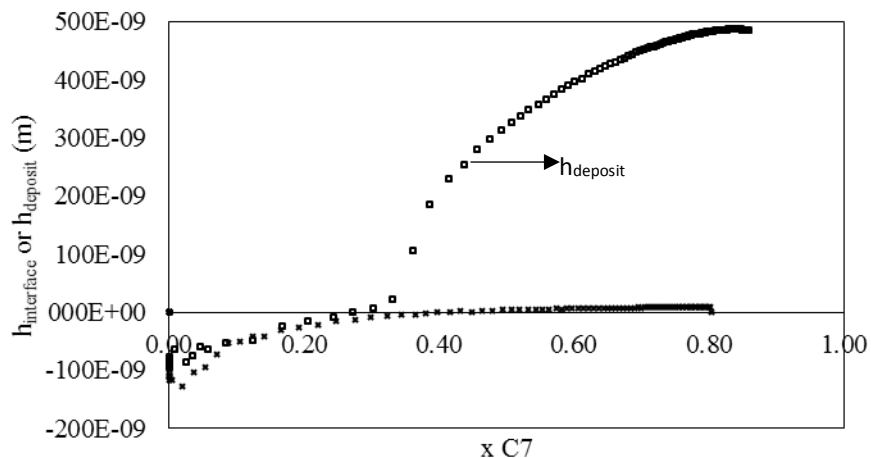


Figure 41. Comparison between model calculated thicknesses for the interfacial layer in the case of the continuous injection of toluene and n-heptane in crude oil A.  $h_{interface}$  becomes  $h_{deposit}$  for the case of crude oil titration with an asphaltene nonsolvent. 25 °C and atmospheric pressure.

The estimated onset of asphaltene destabilization from crude oil A was at a n-heptane mass fraction between 0.24 and 0.27, where the calculated  $h_{interface}$  is in the range of -19 to -15 nm, 5% of the total obtained asphaltene deposit thickness at the end of the n-heptane injection procedure. Although the negative magnitudes of  $h_{interface}$  before the onset of asphaltene

destabilization were observed to be negligible when studying the asphaltene deposit thicknesses, the use of viscous systems added considerably uncertainties on the process of asphaltene onset of destabilization determination as it is discussed later on the thesis. A summary of the  $h_{interface}$  obtained for some of the crude oils is shown in Figure 42.

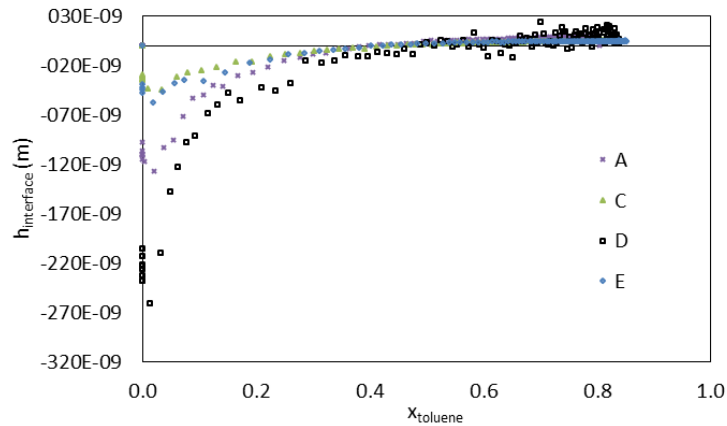


Figure 42.  $h_{interface}$  for the dilution of crude oils A, C, D and E with toluene at 25 °C and atmospheric pressure.

## 4.2 Crude oil Titration with an asphaltene nonsolvent

### 4.2.1 $\Delta f_n$ and $\Delta \Gamma_n$ as a function of $n$ -heptane mass fraction ( $x_{C7}$ )

The change in resonance frequency and bandwidth for the continuous  $n$ -heptane injection into crude oil C is shown in Figure 43. The 3<sup>rd</sup>, 5<sup>th</sup> and 7<sup>th</sup> overtones of resonance are shown. The response in  $\Delta F$  and  $\Delta \Gamma$  (3<sup>rd</sup> harmonic only) for the crude oil dilution with toluene is also shown for comparison. The data are plotted as a function of  $n$ -heptane mass fraction ( $x_{C7}$ ).

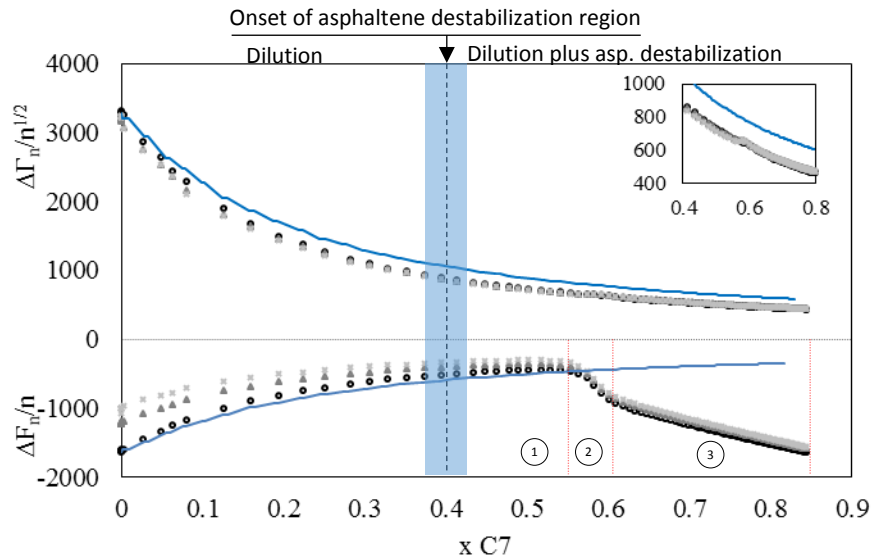


Figure 43. Change in resonance frequency and bandwidth for the continuous *n*-heptane injection in crude oil C at 25 °C. Circles, squares and crosses standing for 3<sup>rd</sup>, 5<sup>th</sup> and 7<sup>th</sup> overtones of resonance. Full blue lines obtained from the crude oil dilution with toluene. Number 1, 2 and 3 indicates the different regimes occurring within the change in resonance frequency above asphaltene onset of destabilization.

The continuous toluene injection into crude oil, depicted in Figure 43 as the full blue lines, causes a decrease of the system density and viscosity which yields increasing  $\Delta F$  and decreasing  $\Delta \Gamma$  values throughout the entire titration region. The crude oil titration with an asphaltene precipitant does not yield the same responses in  $\Delta F$  and  $\Delta \Gamma$  and two main regions are clearly distinguished during the titration. From  $x_{C7} = 0$  to  $x_{C7} = 0.4$  the *n*-heptane injection decreases the density and the viscosity of the system and the resonating parameters absolutely decrease similar to what occurs in the case of toluene injection. This region in which the quartz load impedance is dominated by density and viscosity is referred to as **dilution region** throughout this work and is delimited by the vertical dashed line in Figure 43. The dashed line indicates the onset of asphaltene destabilization with its determination discussed in a later section. With the

asphaltenes destabilization a new region within the experiment appears, the **dilution plus destabilization**, in which additional loads on the quartz crystal arrive. Such loads, mainly assigned to the buildup of an asphaltenic deposit ( $h_d$ ) on the electrode surfaces, cause a decrease in the shift in resonance frequency with different regimes of  $\Delta F_n$  as a function of  $x_{C7}$ . From the onset at  $x_{C7} = 0.4$  to  $x_{C7} = 0.56$  (number 1 in Figure 43) only a small decrease in resonance frequency with n-heptane mass fraction is observed. No change in bandwidth is detected. From  $x_{C7} = 0.56$  to  $x_{C7} = 0.60$  (number 2 in Figure 43) it can be observed a steep drop in resonance frequency data from the deposition profile. A slightly increase or jump in bandwidth can be observed (inset of Figure 43). Finally, from  $x_{C7} = 0.60$  to the end of the n-heptane injection ( $x_{C7} = \sim 0.85$ ) a third constant rate of resonance frequency decrease with n-heptane mass fraction is observed. The deposition profile  $\Delta F_n/n$  versus  $x_{C7}$  was observed to be independent on the agitation and shearing conditions achieved in the glass mixing cell.

Two hypothesis are proposed to explain such changes. The first is related to the quantity of the deposited material and the second is related to deposit morphology. The mass of precipitated asphaltenes is known to be higher close to the onset and decrease with increasing n-heptane addition as it is shown by the asphaltene yield curve<sup>116</sup>. The morphology asphaltenes deposits was reported to vary within the asphaltene precipitation and were divided in micro-asperites and macro-asperities according to Amin<sup>208</sup>.

Although the high polydispersity of particle sizes due to aggregation and flocculation processes once asphaltenes are destabilized, with sizes going from the nanometer to thousands of microns, bandwidth shifts within the dilution plus destabilization region stays low and almost imperceptible during the asphaltene deposition. The low bandwidth shifts induced by the

asphaltenic deposit is highlighted in the inset of Figure 44 where the bandwidth in the dilution plus destabilization region for the n-heptane and toluene titration is magnified.

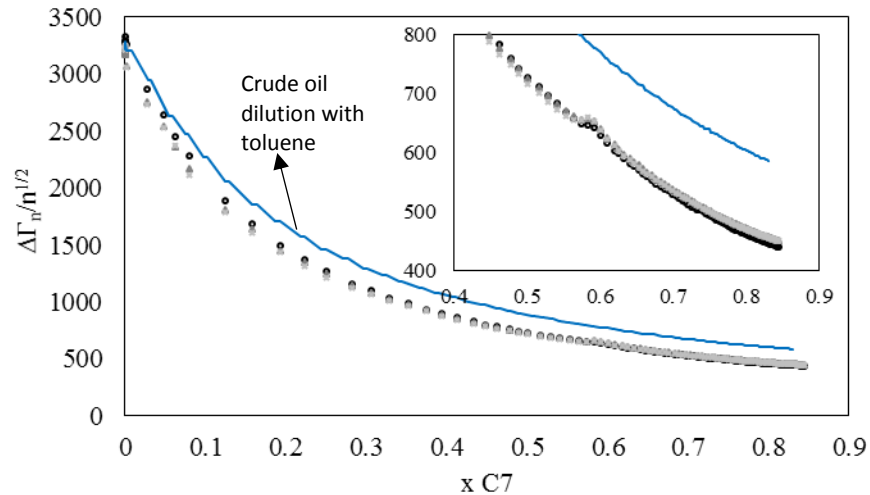


Figure 44. Bandwidth change profile for the n-heptane injection into crude oil C at 25 °C and atmospheric pressure. Circles, squares and crosses standing for 3<sup>rd</sup>, 5<sup>th</sup> and 7<sup>th</sup> overtones of resonance. Full blue lines obtained from the crude oil dilution with toluene.

Although this low bandwidth was found to occur for crude oils C, D and E (Figures 44, 47 and 48), this was not the case for crude oil B with 6.8 wt% of n-heptane asphaltenes (Figure 45).

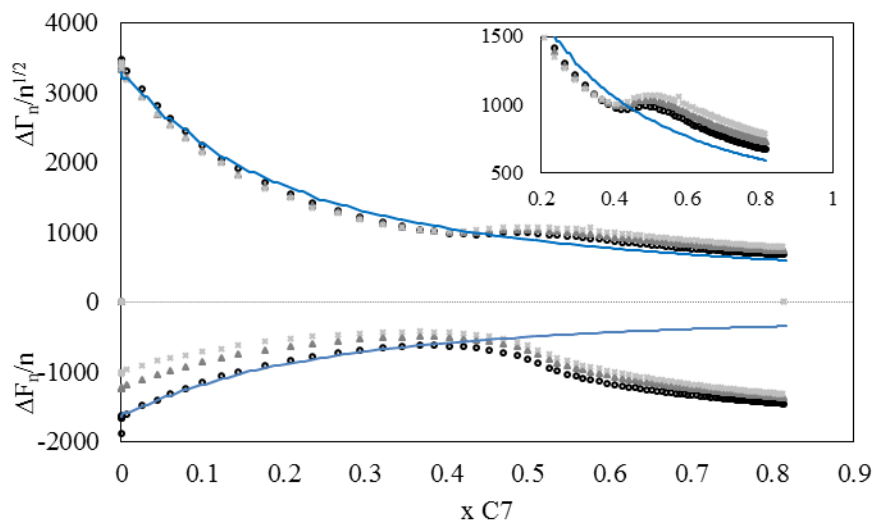


Figure 45. N-heptane or toluene injection into crude oil B at 25 °C and atmospheric pressure. Circles, squares and crosses standing for 3<sup>rd</sup>, 5<sup>th</sup> and 7<sup>th</sup> overtones of resonance. Full blue lines are obtained from the crude oil dilution with toluene.

Interestingly, the most asphaltenic crude oil utilized in the present study, crude oil A, with 11.9 wt% n-heptane asphaltenes also displayed a low bandwidth profile with the asphaltene destabilization (Figure 46).

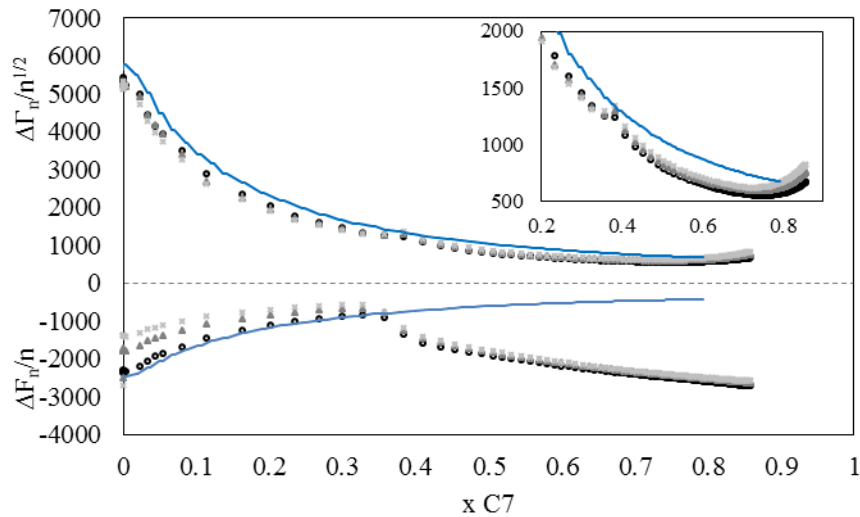


Figure 46. N-heptane injection into crude oil A at 25 °C and atmospheric pressure. Circles, squares and crosses standing for 3<sup>rd</sup>, 5<sup>th</sup> and 7<sup>th</sup> overtones of resonance. Full blue lines are obtained from the crude oil dilution with toluene.

The deposit from crude oil B is more dissipative and has greater bandwidth inter-harmonic spreading ( $\Delta\Gamma_n/n^{1/2}$  in inset of Figure 45) than deposits from crude oil C although the high similarity on density and viscosity of both oils. The higher energy dissipation from deposits obtained from crude oil B can be due to the deposit viscoelasticity or deposit physical structure. The apparent constant bandwidth inter-harmonic spreading over the dilution plus destabilization region is an indication that the energy dissipation is mostly coming from the formation of a viscoelastic deposit. This deposit is considered to as being weakly dissipative when comparing with other studies<sup>3,209,210</sup> on deposition of colloidal particles and is considered as an elastic

deposit. The same pattern on resonance frequency and bandwidth profiles were obtained for all the probed oils. Figures 47 and 48 bring the profiles for crude oils D and E.

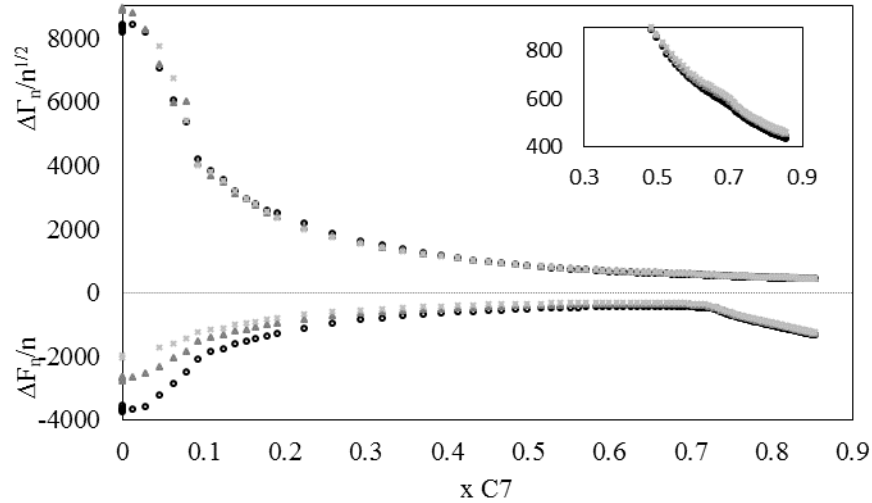


Figure 47. Change in Frequency and bandwidth for the continuous n-C7 injection in crude oil D at 25 °C and atmospheric pressure. Circles, squares and crosses standing for 3<sup>rd</sup>, 5<sup>th</sup> and 7<sup>th</sup> overtones of resonance.

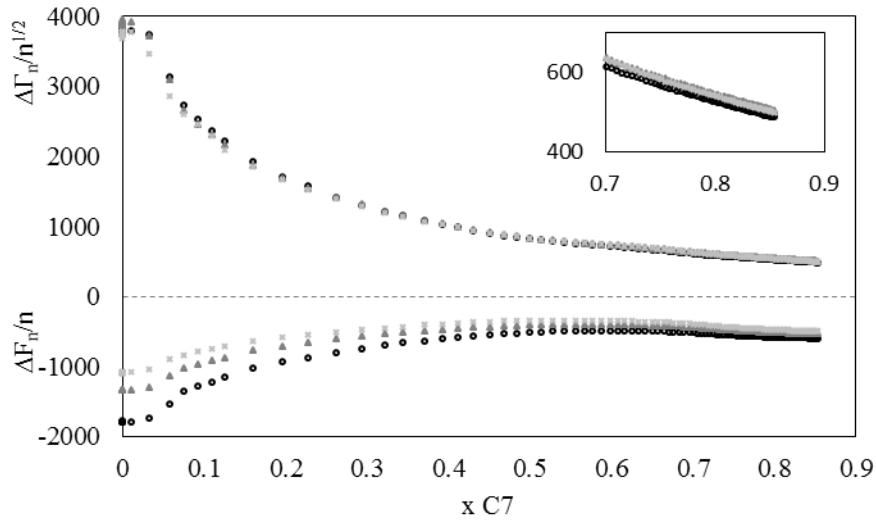


Figure 48. Change in Frequency and bandwidth for the continuous n-C7 injection in crude oil E at 25 °C and atmospheric pressure. Circles, squares and crosses standing for 3<sup>rd</sup>, 5<sup>th</sup> and 7<sup>th</sup> overtones of resonance respectively.

The asphaltene destabilization by continuous n-heptane injection was also probed on other crude oils which were not characterized by SARA analysis or physical parameters. The profiles of resonance frequency and bandwidths for such oils are shown in Figures 49 to 51.

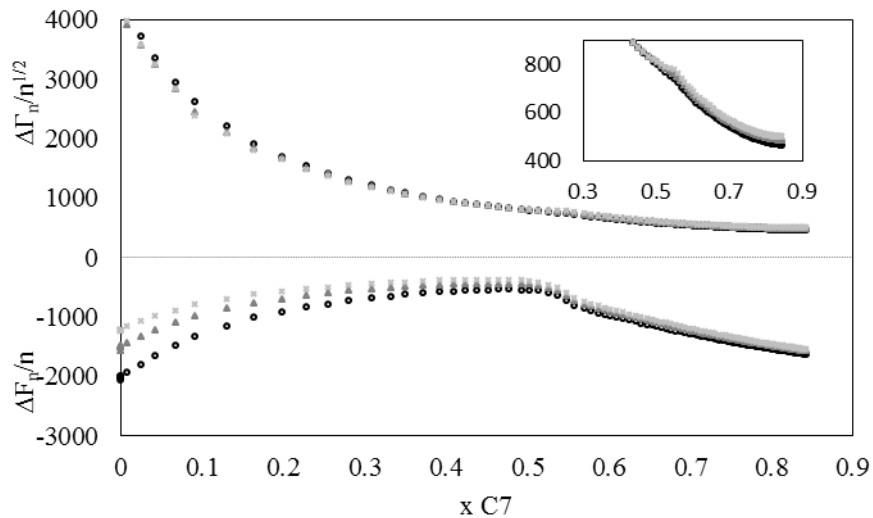


Figure 49. Change in Frequency and bandwidth for the continuous n-C7 injection in crude oil F at 25 °C and atmospheric pressure. Circles, squares and crosses standing for 3<sup>rd</sup>, 5<sup>th</sup> and 7<sup>th</sup> overtones of resonance respectively.

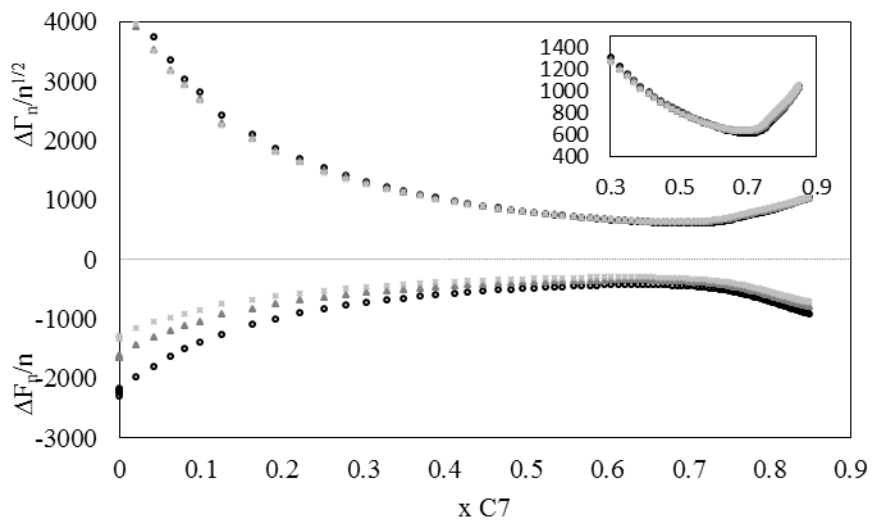


Figure 50. Change in Frequency and bandwidth for the continuous n-C7 injection in crude oil G at 25 °C and atmospheric pressure. Circles, squares and crosses standing for 3<sup>rd</sup>, 5<sup>th</sup> and 7<sup>th</sup> overtones of resonance respectively.

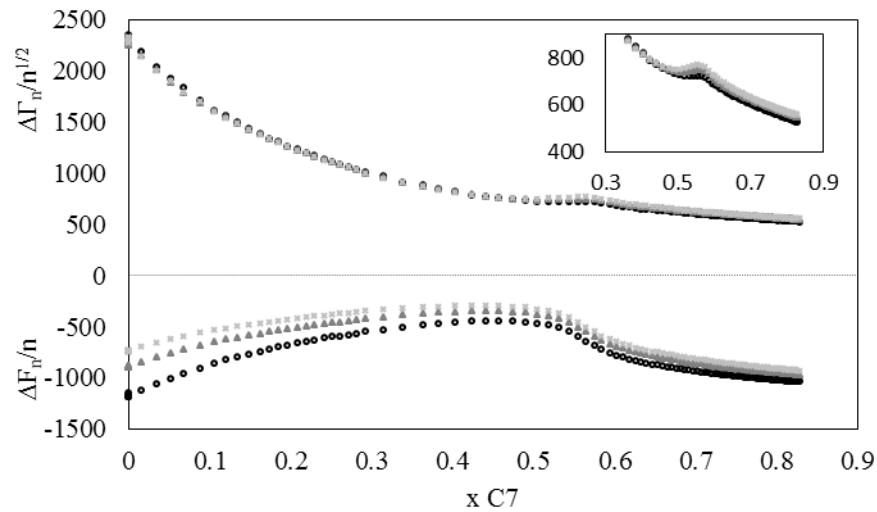


Figure 51. Change in Frequency and bandwidth for the continuous n-C7 injection in crude oil H at 25 °C and atmospheric pressure. Circles, squares and crosses standing for 3<sup>rd</sup>, 5<sup>th</sup> and 7<sup>th</sup> overtones of resonance respectively.

#### 4.2.2 $\Delta F_n$ and $\Delta \Gamma_n$ as a function of experimental run time

Changes in frequency and bandwidth as a function of experimental run time are presented in Figure 52 for the continuous n-heptane and toluene injection into crude oil C. The stop in the n-heptane injection is marked by a diamond. The bandwidth profile ( $\Delta \Gamma_n/n^{1/2}$ ) reveals a minimum which appears slightly before the end of the n-heptane injection. After the minimum the bandwidth linearly increases with time reaching no stabilization even after 10 hours. In this period of time the analysis of  $\Delta F_n/n$  versus experimental run time reveals a linearly decreasing signal.

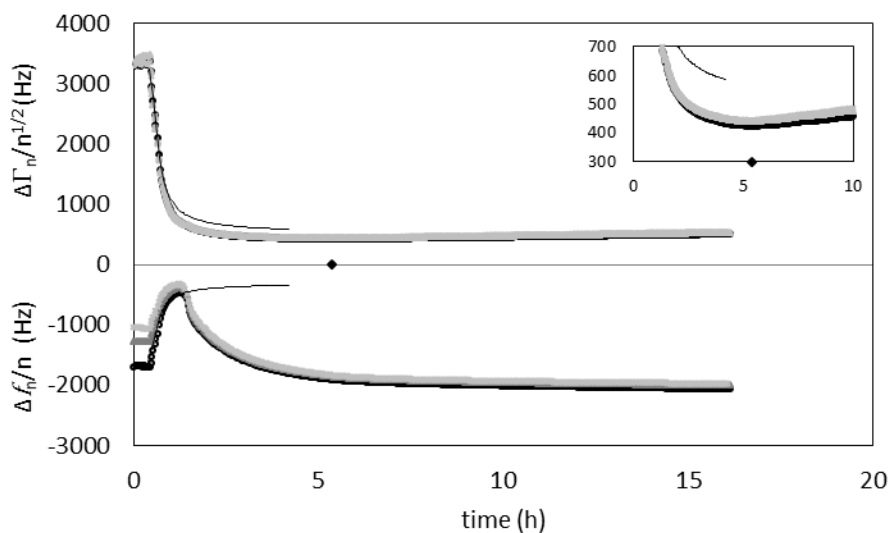


Figure 52. Quartz impedance analysis as a function of time for the continuous injection of n-heptane into crude oil B. Dilution with toluene is also added for comparison as depicted by the full line. The diamond indicates the end of the n-heptane injection. The inset enlarges the bandwidth profile as a function of time for the region in which bandwidth starts to increase. Circles, squares and crosses standing for 3<sup>rd</sup>, 5<sup>th</sup> and 7<sup>th</sup> overtones of resonance respectively.—3<sup>rd</sup> harmonic for toluene injection.

For crude oil A at the same experimental conditions the minimum in bandwidth arrived much before the conclusion of the n-heptane titration as it is highlighted by the inset on Figure 46. The bandwidth minima for the n-heptane titration of crude oil A appears at  $x_{C7} = 0.78$  before the end of the n-heptane titration at  $x_{C7} = 0.85$ . Beyond the minima, the bandwidth apparently exponentially increases with n-heptane mass fraction. However, the analysis of  $\Delta\Gamma_n/n^{1/2}$  as a function of experimental run time reveals the same linear increase of bandwidth with time (Figure 53).

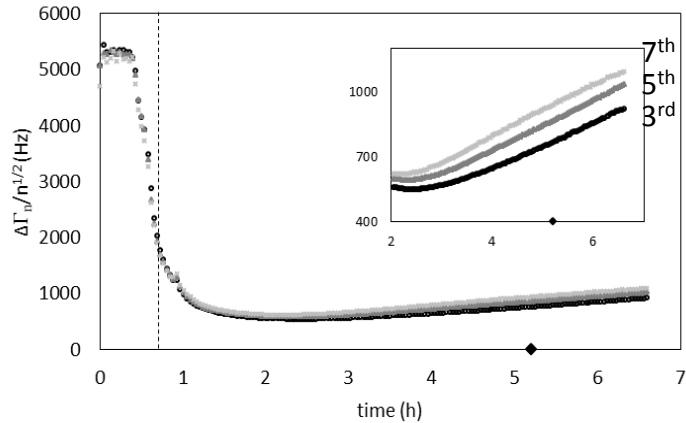


Figure 53. Bandwidth profile ( $\Delta\Gamma_n/n^{1/2}$ ) as a function of time for the *n*-heptane continuous injection into crude oil A. The vertical dashed line indicates the onset of asphaltene destabilization and the diamond (◆) the end of the *n*-heptane injection. The bandwidth minima is shown to appear much before the end of the *n*-heptane injection. The spreading between harmonics augments after the bandwidth minima. The augmentation of the bandwidth appears to be independent on the *n*-heptane injection as no discontinuities or curve inflections are observed at the end of the injection (see inset).

The increase appears to be independent on *n*-heptane mass fraction, since no break in  $\Delta\Gamma_n/n^{1/2}$  versus time is observed when titration is stopped (diamond in Figure 53). The apparent non-dependence of the increase in bandwidth with *n*-heptane mass fractions higher than 0.78 suggests that deposition processes occurring beyond the bandwidth minimum are weakly or not related with media solubility changes. The increase of the spreading of  $\Delta\Gamma_n/n^{1/2}$  data after the bandwidth minima can be interpreted in terms of deposit lateral heterogeneity<sup>210</sup>. The increase in bandwidth after the minima was observed to be dependent on the system agitation and the temperature. Such phenomena will be further discussed when the temperature effect on change in frequency and bandwidths profiles are analyzed.

#### 4.2.3 The analysis of the deposit energy dissipation

Information on deposit energy dissipation is crucial for interpreting deposit and bulk physical properties. A smooth elastic deposit and perfectly coupled to the electrodes do not dissipate energy. Dissipative effects arise from deposit viscoelasticity, deposit physical structure mainly roughness and porosity inducing hydrodynamic energy losses or a poor coupling between the deposit and the resonator surfaces.

The decoupling of deposit energy dissipation from the energy dissipation arising from bulk viscosity is firstly done by considering the energy dissipation of the deposit at the last experimental point ( $x_{C7} \approx 0.85$ ) and subtract it from the energy dissipation of the bare quartz crystal (without asphaltenic deposit) in pure heptane. This is conservative as the bulk viscosity at  $x_{C7} \approx 0.85$  is not the viscosity of pure heptane. The energy dissipation calculated by the last points reveals deposit normalized bandwidths per  $n$  ( $(\Delta\Gamma_n^{dep.}/2n)$ ) varying from 10 to 80 Hz with the corresponding dissipation factors ( $\Delta D^{dep.}/2$ ) varying from  $9.4 \times 10^{-6}$  to  $58.2 \times 10^{-6}$ . The presented values are divided by 2 in order to represent one electrode loaded for comparison with the almost totality of reported studies which utilizes one side of the electrode exposed to the liquid media. Table 4 shows the energy dissipation of crude oil C, which yielded very small energy dissipation considering the deposit load mass load ( $\Delta F_n/n$ ) and for crude oil B which gave rise to the most dissipative asphaltenic deposit. The estimation of the mass load and deposit thickness in each electrode considering the elastic approach are also shown in Table 4.

Table 4. Normalized frequency and dissipation factor for due to asphaltenic deposit load at  $x_{C7}=0.85$ . Changes in resonance frequency within one electrode and penetration depth estimations from the predictions of density and viscosity (see section V, sub-section 3) are shown. The shear wave penetration depths ( $\delta_n$ ) estimations for each harmonic are: 3<sup>rd</sup>= 145 nm; 5<sup>th</sup>= 110 nm and 7<sup>th</sup> = 90 nm. The dissipation factor for the bare quartz in pure heptane for the three harmonics are as follows: 3<sup>rd</sup> =  $1.5 \times 10^{-6}$ ; 5<sup>th</sup>=  $1.1 \times 10^{-6}$  and 7<sup>th</sup>=  $0.9 \times 10^{-6}$ .

Overtone of resonance	$\frac{\Delta F_n}{n} \Big _{oil+hep.}^{x=0.85} - \frac{\Delta F_n}{n} \Big _{oil+tol.}^{x=0.85}$ (Hz)	Deposit thickness (nm)	$\Delta D_{dep.} = (\Delta D_{oil+hep.} - \Delta D_{hep.}) \times 10^{-6}$ (dimensionless)
<b>Crude oil C</b>			
3 <sup>rd</sup>	840	350	18.1
5 <sup>th</sup>	837	349	16.4
7 <sup>th</sup>	787	329	16.3
<b>Model</b>	787	330	-
<b>Crude oil B</b>			
3 <sup>rd</sup>	603	251	58.2
5 <sup>th</sup>	586	244	51.2
7 <sup>th</sup>	578	241	50.8
<b>Model</b>	521	217	-

The magnitudes on energy dissipation can be considered low when analyzing other studies on deposition of monodisperse or weakly polydispersed colloidal particles<sup>3,203,209,210</sup> in which shifts in frequency due to deposition were smaller than 300 Hz and dissipation factors stayed in the order of  $10^{-5}$ . The small energy dissipation obtained for the asphaltenic deposits, besides the high deposit loads, is a first indication of its physical nature and configuration: low dissipation is mostly obtained by laterally homogeneous and elastic deposits or weakly viscous deposits. Laterally homogeneous and elastic materials also give rise to superposition of  $\Delta \Gamma_n/n^{1/2}$  over the entire titration region and superposition of  $\Delta F_n/n$  once deposit is formed<sup>205</sup>.

In order to access how deposit dissipation evolves during the asphaltenic deposit buildup a Grunberg-Nissan type mixing rule<sup>178</sup> was applied to the dilution region and then extrapolated to the dilution plus deposition region to have theoretical energy dissipation values associated only to bulk viscosity. The experimental points were then subtracted from the fitted extrapolated points and deposit dissipation profile was obtained. The Grunberg-Nissan type equation was utilized as it was applied elsewhere<sup>178</sup> to model quartz response due to simple dilution. A maxima in energy dissipation within the beginning of the deposit formation is observed to occur in all probed oils, with one example shown for crude oil C in Figure 54 for the 7<sup>th</sup> overtone of resonance.

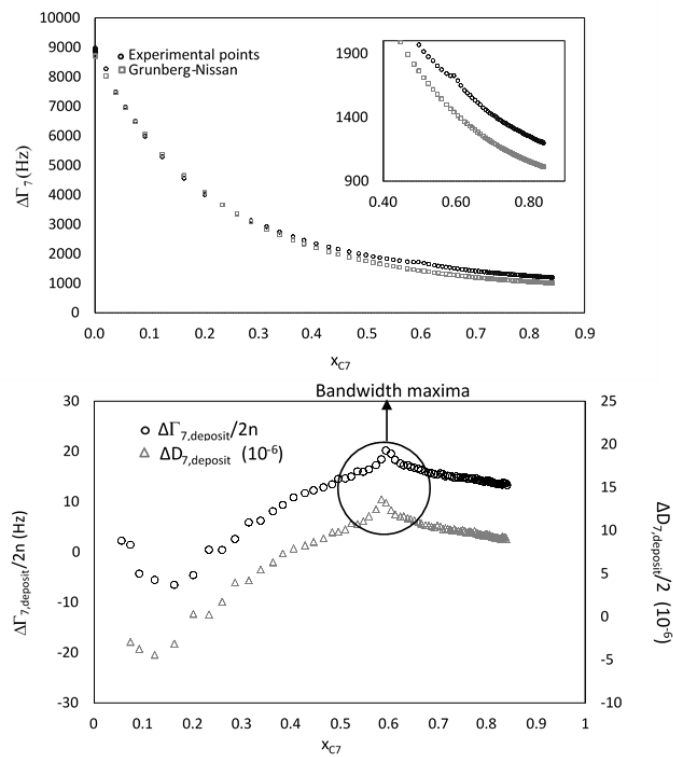


Figure 54. Change bandwidth and dissipation factor due to deposition on one electrode surface for the seventh harmonic obtained by applying a Grunberg—Nissan-type mixing rule with one adjustable parameter to the crude oil/n-heptane mixture<sup>178</sup>. The values are for one electrode side.

The low values on deposit dissipation, despite high deposit loads observed within the frequency shifts and the uncertainty in relation to the deposit structure prompted us to model the occurring processes by taking into account elastic deposit and Newtonian liquid loads as described by Equations 21 and 22. Before applying the cited model to the change in resonance frequency and bandwidth data, a discussion is performed on how the asphaltene onset of destabilization was obtained.

#### *4.2.4 The onset of asphaltene destabilization*

The onset of asphaltene destabilization by continuous asphaltene nonsolvent titration is known to depend on many variables<sup>211</sup>. Besides the many variables which demands a carefully experimental specification when onsets are envisaged to be determined, the experimental limitations on the asphaltene destabilization detection is another complicating factor. The asphaltene destabilization is normally a continuous function dependent on the precipitant mass fraction. This adds further difficulties on precisely defining onset points. In some experimental techniques, as NIR spectroscopy it is a common practice to fit a curve on the region before the onset of asphaltene destabilization and characterize the onset by its deviation from such a curve. In the context of the utilization of quartz crystal technique, Daridon<sup>178</sup> utilized a Grunberg–Nissan type mixing rule to model the viscosity before the onset of asphaltene destabilization when accessing onset of asphaltene destabilization from diluted crude oils. They reported the coherence of their onset values to the ones obtained by microscopy after 24 hours, the ASIST test. The fact that the work was done with diluted crude oil resulted in fairly smooth curves in the region characterized in the present work as **dilution region**, the experimental points obtained before the asphaltene onset of destabilization. Besides that, the dilution of the crude oil in

toluene confers a Newtonian character to the system which may be not the case at low dilutions when using the whole crude oil. The titration of crude oil with nonsolvent adds some complications for the determination of the asphaltene destabilization point. Such complications arising mainly due to the huge viscosity variations within the crude oil titration which may influence the clear detection of onset points by the bandwidth change and to the highly elastic characteristics of the firsts deposited asphaltenes together with their probable small amount in the crude oil, which does not induce appreciable changes in resonance frequency and bandwidth compared to the changes occurring with the continuous viscosity reduction. Furthermore, when using the whole crude oil, asphaltene adsorption effects before the onset of asphaltene destabilization may contribute to a frequency decrease due to the electrode crude oil interface which may induce different frequency changes at different system viscosities. Finally, when a mixing rule is applied, there is an incertitude in relation to the last point, which is still considered to be a stable region for asphaltenes, for the fitting optimization process. When using the quartz crystal to probe asphaltene destabilization from diluted oils or whole crude oils at higher temperatures some of the issues related to the viscosity is radically decreased and the onset can be more easily determined<sup>7</sup>. Despite all the incertitude, some methods on estimating the onset of asphaltene destabilization from the quartz impedance analysis data are presented, such methods may be used together to determine the onset of asphaltene destabilization.

#### 4.2.4.1 Asphaltene onset of destabilization by an analysis of rate of resonance frequency change

By taking advantage of the high sensitivity of the quartz on system viscosity changes and deposited masses, the derivative of change in frequency versus n-heptane mass fraction can be analyzed and compared with the rates obtained within the dilution procedure. Such method of

analyzing rates of resonance frequency changes is not subjected to the uncertainty that may appear when utilizing an equation to model the dilution region. Figure 55 presents the derivative analysis.

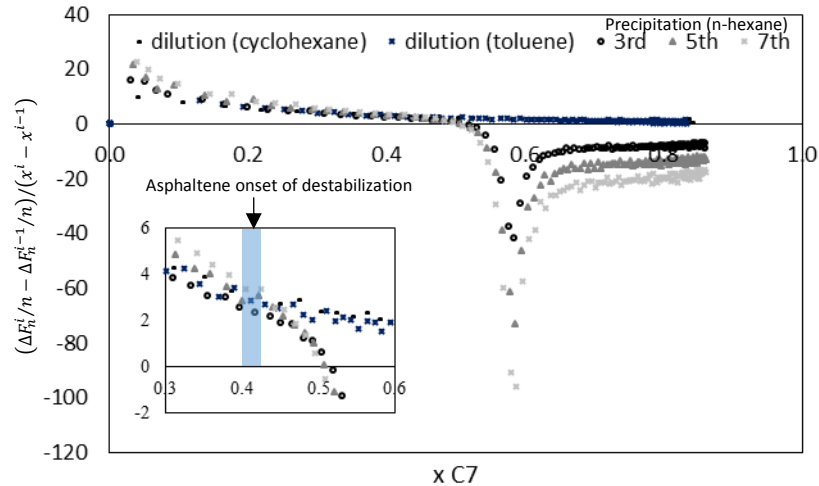


Figure 55. Asphaltene onset of destabilization by analysis of derivatives of changes in resonance frequency relative to the asphaltene solvent or nonsolvent mass fraction. Two asphaltene solvents were used: toluene and cyclohexane. Asphaltene precipitation performed by n-hexane. The inset shows the n-heptane mass fraction points in which the derivative of the asphaltene destabilization experiment diverges from the pure dilution. The 3<sup>rd</sup>, 5<sup>th</sup> and 7<sup>th</sup> harmonics of resonance are shown for the n-heptane titration. Only the third harmonic is shown for the dilution experiments (cyclohexane and toluene). Crude oil C, all the experiments were performed at 25 °C and atmospheric pressure.

#### 4.2.4.2 Asphaltene onset of destabilization by the application of a mixing rule for viscosity

A modified Grunberg-Nissan type equation, as reported elsewhere<sup>178</sup>, was utilized to fit the dilution region in Figure 56. Due to the fact that the harmonics sweep are done within different n-heptane mass fractions (Figure 35), it was preferred to use the fitting procedure using only one overtone of resonance, the 3<sup>rd</sup> overtone. It was also preferred to use the non-normalized overtone of resonance value.

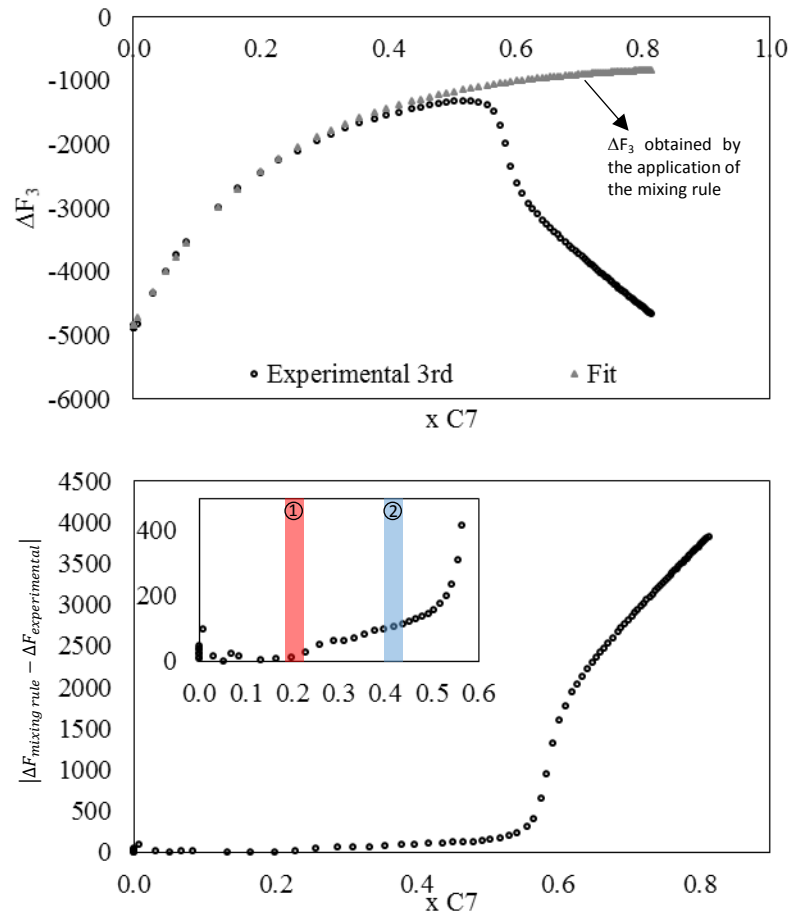


Figure 56. Onset of asphaltene destabilization determination by the fitting of a mixing rule to the dilution region and extrapolating to the case of  $x_{C7}=1$ . (1) Onset of asphaltene destabilization obtained by the deviation from the experimental points to the mixing rule and (2) onset of asphaltene destabilization obtained by the derivative method. Crude oil C at 25 °C and atmospheric pressure.

Such method when applied at high viscous systems suffers from some difficulties mostly related to choosing of the points considered to be stable towards asphaltenes destabilization in order to optimize the fitting procedure. This method is considered conservative by the author and may yield highly under estimated onsets of asphaltene destabilization. This fact can be observed in the inset of Figure 56 where the onset obtained by the deviation from the mixing rule (1) is accused to appear much earlier than the onset evaluated by the derivative method (2).

When analyzing the method to experiments at higher temperatures to diminish viscosity effects, the same problem is encountered. The fit of the experiment of destabilization of asphaltenes from crude oil C at 45 °C is shown in Figure 57. Despite the fact that the onset of destabilization is observed to be in between  $x_{C7} = 0.40$  and  $x_{C7} = 0.50$ , the analysis of the mixing rule fit may induce the estimation of consistently lower onsets of asphaltene destabilization (inset on Figure 62).

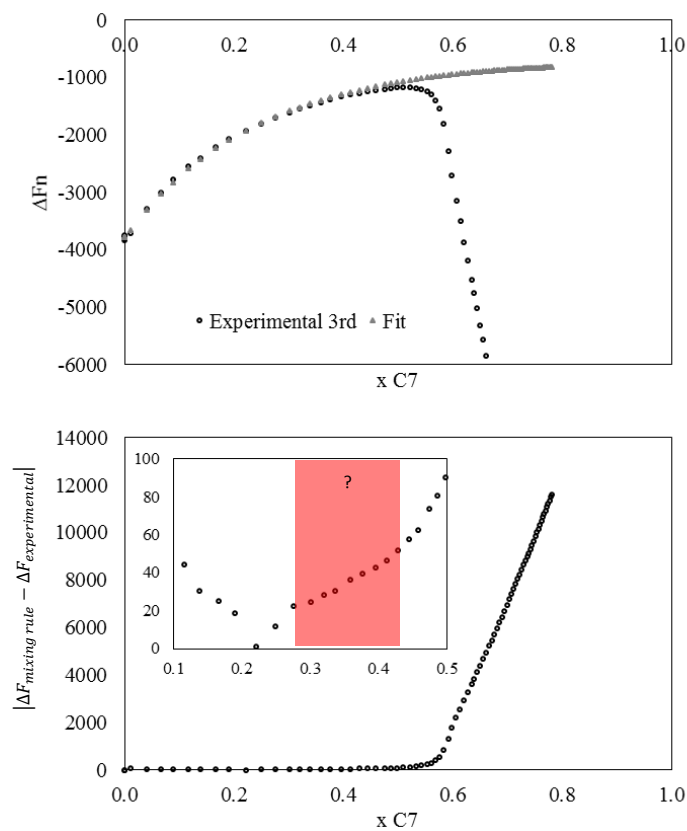


Figure 57. Asphaltene onset of destabilization by fitting a mixing rule to the third overtone of resonance for the continuous asphaltene destabilization from crude oil C at 45 °C and atmospheric pressure.

In summary, due to the magnitudes of the data, the fitting of a mixing rule is not enough for clearly defining the onset point of asphaltene destabilization from crude oils.

#### 4.2.4.3 Asphaltene onset of destabilization by the inter-harmonic spreading

When pure viscous effect is the only load on the quartz crystal resonator the frequency change is proportional to  $\sqrt{\eta}$ . Thus, the analysis of the inter-harmonic spreading when normalized by  $\sqrt{\eta}$  indicates possible effects arising from other loads rather than viscous load. In Figure 58, the frequency change profile normalized by  $\sqrt{\eta}$  and the inter-harmonic spreading for such system are shown. The inter-harmonic spreading is observed to be high at lower crude oil dilutions, gradually decrease with decreasing viscosity, arrive to zero, and then increases. The inter-harmonic spreading for the crude oil C diluted with toluene is shown to present the same tendency (Figure 39) and thus this method although very simple may not provide accurate onsets of asphaltene destabilization. The determined onset of asphaltenes destabilization are, however, in the same range as the ones obtained by the derivative method (between  $x_{c7} = 0.4$  and  $x_{c7} = 0.5$ )

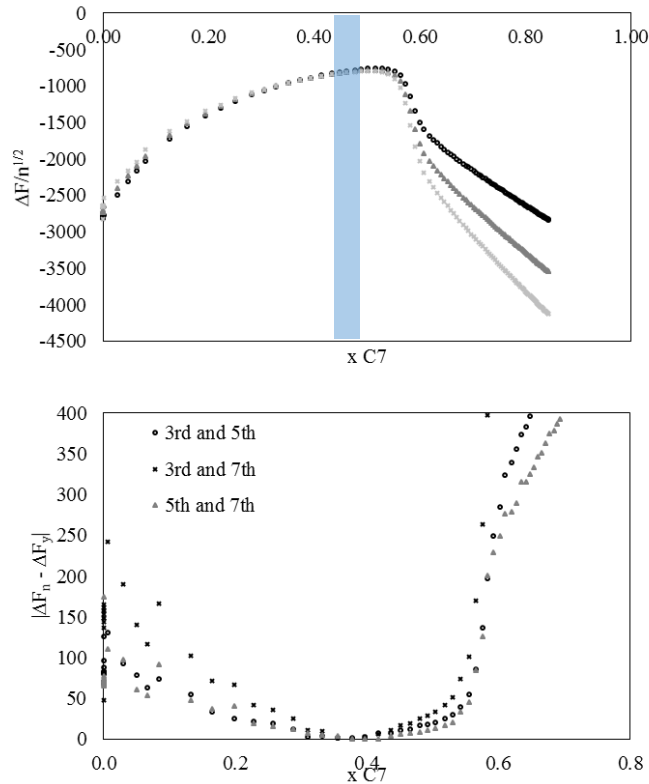


Figure 58. Inter-harmonic spreading analysis for detecting onset of asphaltene destabilization. Blue stripe represents onset conditions.

#### 4.2.4.4 Asphaltene onset of destabilization by the first inflexion point on $h_{interface}$

This method may be a powerful manner of determining the asphaltene onset of destabilization since it takes into account many occurring interfacial phenomena, gathering them in the model calculated  $h_{interface}$  or  $h_{deposit}$ . As it was reported in the crude oil dilution with asphaltene solvent section, the  $h_{interface}$  within the titration procedure is negative at high viscosities and becomes positive at high dilutions and thus, low viscosities, however, the  $h_{interface}$  presents no inflexion point when an asphaltene solvent is utilized. This is not the case when the crude oil is titrated with an asphaltene non solvent, with the  $h_{interface}$ , in this case  $h_{deposit}$ , presenting a first inflexion point as it is shown in Figure 59. The analysis of both curves suggests that the asphaltene onset of precipitation within the crude oil C is occurring before  $x_{C7} = 0.4$ , contrary to

what was obtained with the derivative and inter-harmonic spreading methods. It is important to note that as this parameter is taking into account many interfacial effects it may also be sensible to pre-adsorbed asphaltenes within the titration procedure.

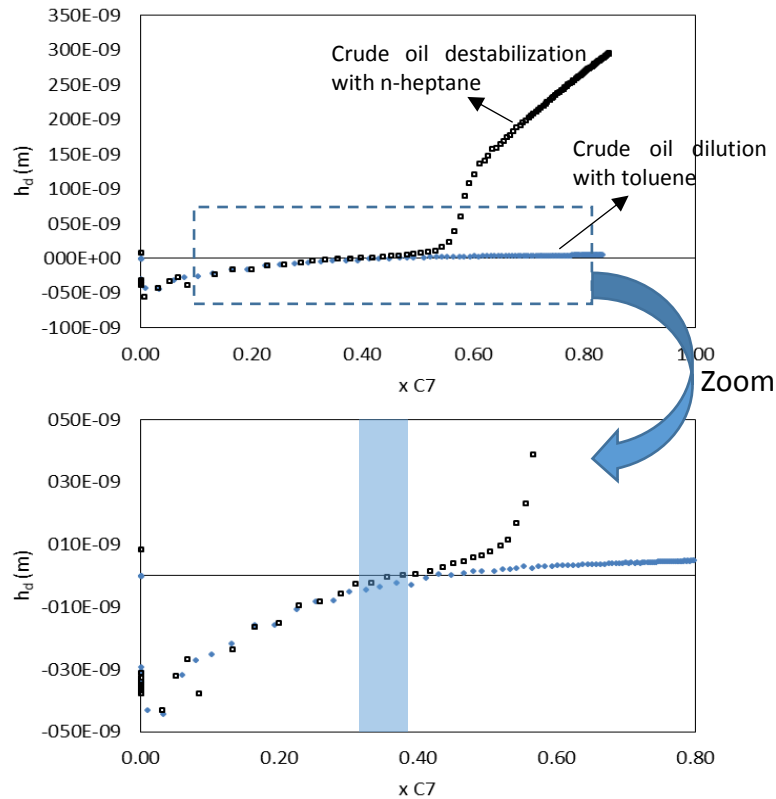


Figure 59. Asphaltene onset of destabilization determined by the analysis of  $h_{interface}$  and  $h_{deposit}$ . Crude oil C at 25 °C and atmospheric pressure.

#### 4.2.5 Observation concerning the onset of asphaltene destabilization by quartz crystal resonator

The methods for determining onsets of asphaltene destabilization, from  $\Delta F$  data, were developed having in mind that the quartz crystal high sensitivity to interfacial phenomena would present would yield highly accurate onset of asphaltenes destabilization by detecting the destabilization of the least soluble asphaltenes. Such asphaltenes, present in less amounts in the crude oil, give rise to a slower aggregation kinetics and thus a late detection by methodologies which are based

on destabilized asphaltene particles sizes detection. However, the high quartz crystal resonator sensitivity to the bulk and interfacial phenomena, allied to the high viscosities encountered in some systems and to the elastic nature of the first deposits, increase uncertainties when trying to assign the asphaltene destabilization onset point. Such characteristics of the quartz crystal resonator is for no means prohibitive to its further application within the asphaltene destabilization onset detection of the most problematic systems. The increase laboratory experience and the application of other techniques to characterize the electrode surface during the asphaltene nonsolvent injection in the crude oil, may lead to a high decrease in the uncertainties within the onset point determination. Within the context of the present work, the considered onset of asphaltene destabilization will be taken as the deviation derivative of frequency in relation to the n-heptane mass fraction deviation in relation to the dilution case with toluene.

#### 4.2.6 Model application

##### 4.2.6.1 $\Delta F_m$ , $\Delta F_\eta$ and $\Delta \Gamma_\eta$ profiles

The application of the model (Equation 20 and 21 and Figure 28) to the impedance analysis performed during the n-heptane injection in the five crude oils exposed in Table 2 is shown from the most to the less asphaltenic on Figures 60 to 64. Each Figure brings the bandwidth profile ( $\Delta \Gamma_n$  versus  $x_{C7}$ ), which is assumed by the model of coming only from bulk viscosity ( $\Delta \Gamma_\eta$ ), and the frequency profile ( $\Delta F_n$  versus  $x_{C7}$ ) which is assumed to arise from two contributions: bulk viscous load ( $\Delta F_\eta$ ) and deposited mass load ( $\Delta F_m$ ). Such information is presented on the left side of each figure. On the right side an amplification of dilution plus destabilization region is exposed with smoothed model calculated curves. The derivative of  $\Delta F_n$  versus  $x_{C7}$  or  $C7H8$  is used to



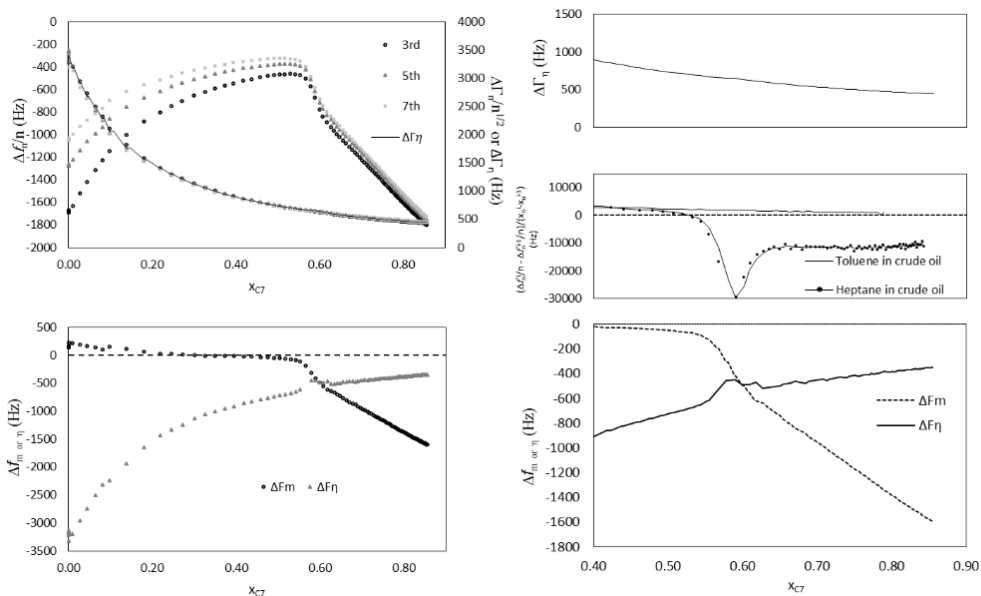


Figure 62. Impedance analysis and model application for the *n*-heptane continuous injection into crude oil C.

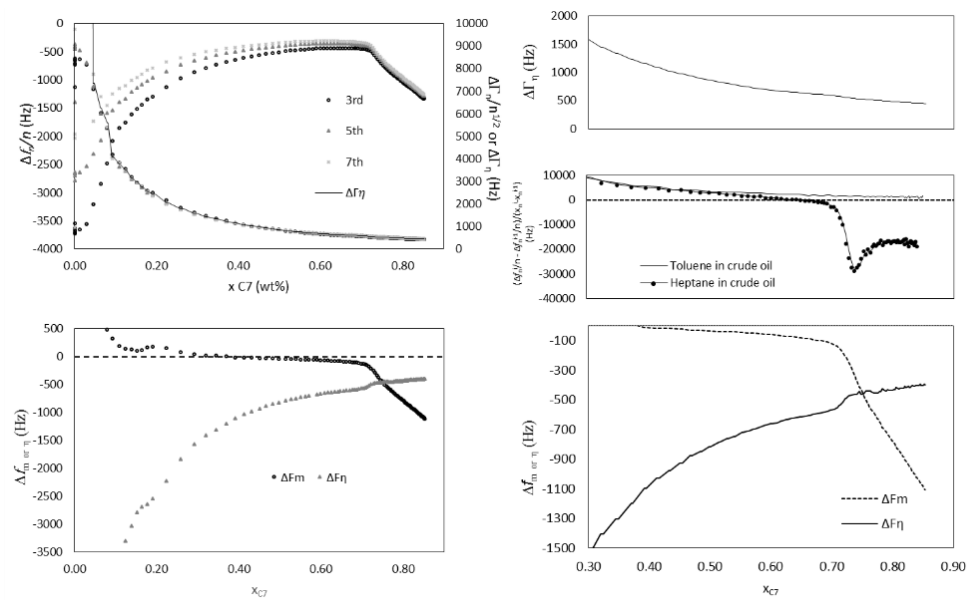


Figure 63. Impedance analysis and model application for the *n*-heptane continuous injection into crude oil D.

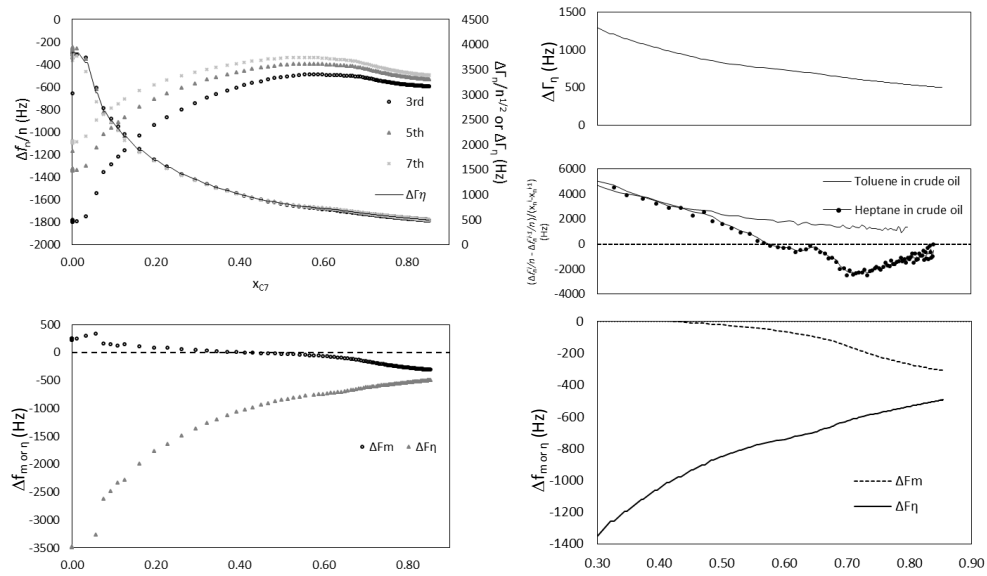


Figure 64. Impedance analysis and model application for the n-heptane continuous injection into crude oil E.

#### 4.2.6.2 Density-viscosity and $h_{deposit}$ determination

The density-viscosity product ( $\rho\eta$ ) obtained from the changes in frequency and bandwidth due to bulk viscosity ( $\Delta F_{\eta}$  and  $\Delta\Gamma_{\eta}$ ) present the same profiles for all the studied crude oils. The  $\rho\eta$  profile obtained from  $\Delta\Gamma_{\eta}$  assume values slightly greater than the obtained from  $\Delta F_{\eta}$  on the destabilization plus deposition region, as it is shown in Figure 65.

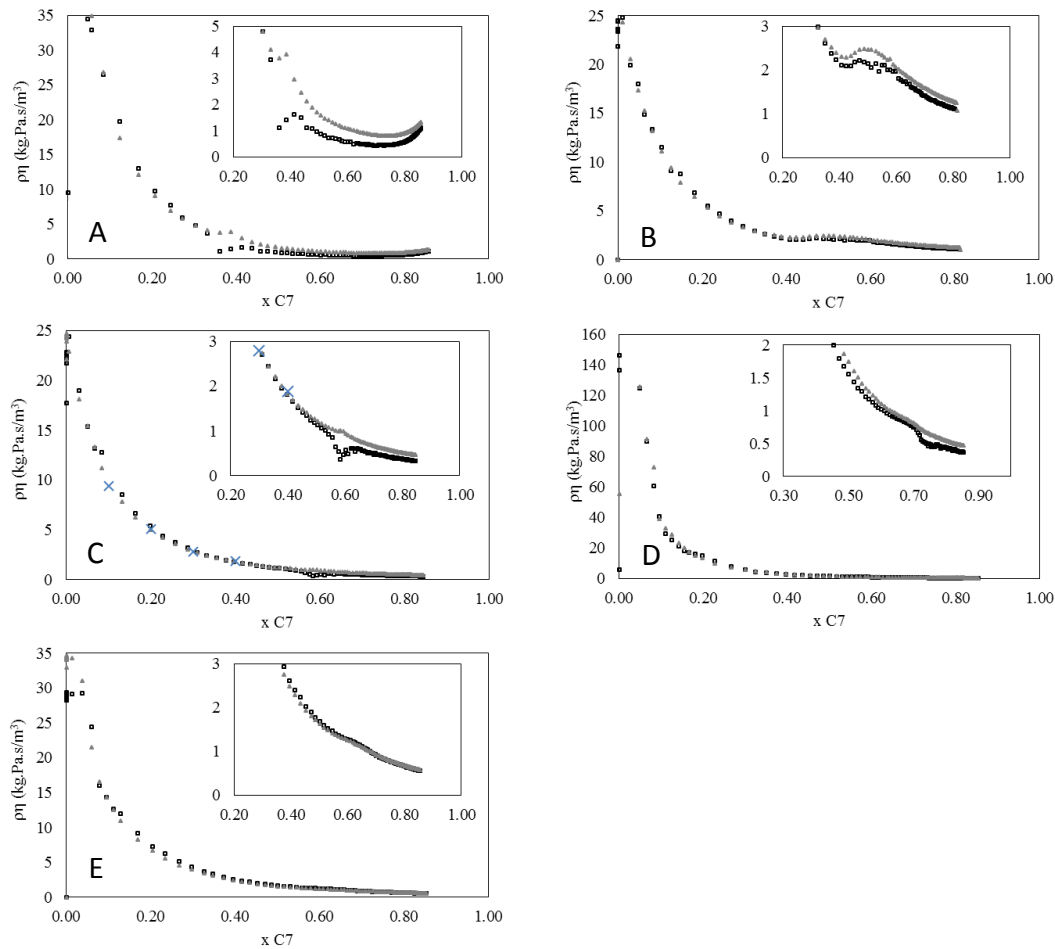


Figure 65. Density-viscosity ( $\rho\eta$ ) product from the resonance frequency and bandwidth changes due to viscous effects ( $\Delta\Gamma_\eta$  and  $\Delta F_\eta$ ) obtained by the model application (Equations 21 and 22). Experimental  $\rho\eta$  values are added for crude oil C. Triangles:  $\rho\eta_{\Delta\Gamma_\eta}$ , squares:  $\rho\eta_{\Delta F_\eta}$  and crosses:  $\rho\eta_{exp}$ .)

Besides the small deviations from the predicted density-viscosity profile from frequency and bandwidth on the dilution plus destabilization region, the applied model describes well the  $\rho\eta$  profile from the bulk media, as it is highlighted by the collected experimental points within crude oil C (Figure 65-C). The bandwidth minimum and its further increase during the n-heptane titration is present only in the case of crude oil A. Such and increase is not due to bulk viscosity but is rather an apparent interfacial viscosity. At the asphaltene destabilization the density-

viscosity profile predicted from bandwidth changes present a maxima and the density-viscosity profile predicted from changes in resonance frequency changes present a minimum for all the oils except for oils B and E. These apparent contradictory responses to a viscosity increase due to asphaltene destabilization and the formation of asphaltene deposit on the gold surfaces should be related to an interfacial phenomena occurring within the asphaltene destabilization, as a gel formation, or deposit structuring.

The fact that density-viscosity product determined by resonance frequency and bandwidths are coherent is an evidence of the possible good agreement from the model determined deposit thicknesses ( $h_d$ ) with real values. The good agreement of the determined deposit thicknesses with real values was already proposed when the bandwidth profile was observed to be small compared to the thickness of the deposit itself (magnitudes of  $\Delta F$  in relation to the magnitudes of  $\Delta \Gamma$ ). However due to the weak dissipative nature of the deposits the thicknesses are overestimated. The calculated thicknesses from  $\Delta F_m$  profile shown in Figures 65 – 69, and referred to one electrode only were estimated considering deposit density<sup>212</sup> of  $1200 \text{ kg/m}^3$ .

The data are shown in Figure 66.

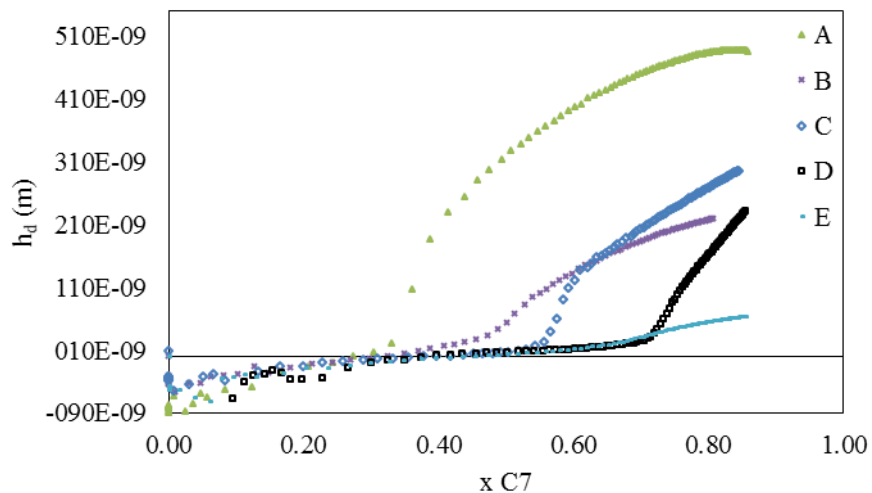


Figure 66. Deposit thicknesses obtained during the *n*-heptane continuous injection into the five studied crude oils.

The  $h_d$  calculated by the model is influenced by other effects as surface rugosity, viscoelasticity and interfacial coupling between the liquid and the gold electrode, thus their direct comparison are not straight forward. Other experimental techniques are needed in order to confirm thicknesses values obtained by the quartz crystal resonator and to compare deposits between oils which allowing the assessment of the deposition propensity of asphaltenes.

#### *4.2.7 Discretization of regions within the titration*

The n-heptane injection into the five studied crude oils give rise to similar patterns of  $\Delta\Gamma_\eta$ ,  $\Delta F_\eta$  and  $\Delta F_m$ . Four different regimes were identified within the dilution plus destabilization region which are all present in the case of crude oil A and are schematically shown in Figure 67 which brings the  $\Delta\Gamma_\eta$  profile (upper panel), the numerical derivative of  $\Delta F_3$  versus  $x_{C7}$  (intermediate panel) and toluene, and in the lower panel,  $\Delta F_m$  and  $\Delta F_\eta$  profiles as a function of n-heptane mass fraction.

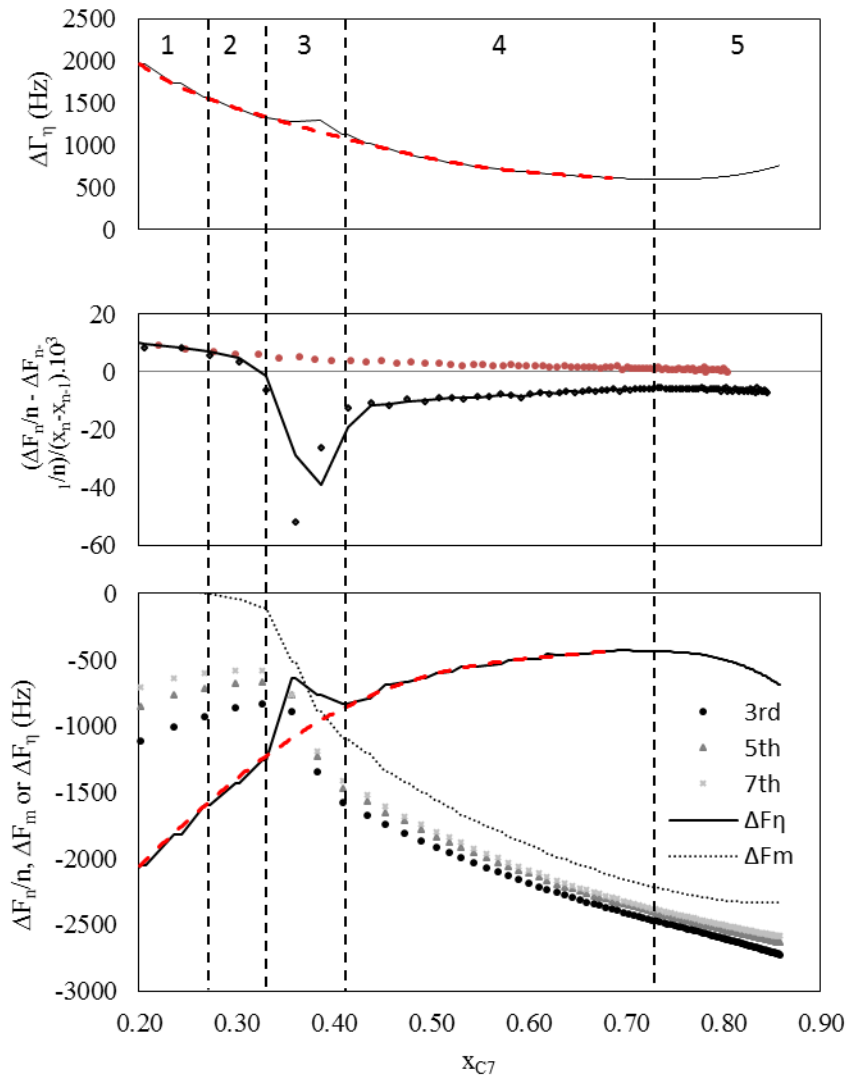


Figure 67. Discretized regions during asphaltene destabilization and deposition by *n*-heptane into crude oil A. Upper panel:  $\Delta\Gamma_\eta$ ; middle panel: derivatives of frequency change in relation to *n*-heptane mass fractions (black) and toluene mass fractions (red); Lower panel: Normalized frequency changes ( $\Delta F_n/n$ ) and model calculated  $\Delta F_m$  and  $\Delta F_\eta$ . Numbers 1 to 5 indicates different regions appearing titration of the studied crude oils with *n*-heptane.

The discretization of regions and sub-regions are done with the aid of the intermediate panel with the exception of the beginning of the fifth sub-region which is taken from the minimum from the bandwidth profile. An analysis of the regions and sub-regions is discussed as following. From the beginning of the *n*-heptane titration to  $x_{C7} = 0.26$  the main phenomena is the crude oil dilution, thus characterizing the dilution region. At  $x_{C7} = 0.26$  asphaltene destabilization occurs giving

rise to a new region denominated dilution plus destabilization in the present work. Such a region is divided into 4 sub-regions which are present, to a greater or lesser extent, in all analyzed crude oils. The sub-regions are manifestations of physical processes occurring in the bulk and on the quartz electrode/liquid interface. Their discretization is of great importance for unraveling the mechanism of asphaltene deposit buildup. Sub-region 2 occurs from  $x_{C7} = 0.26$  to  $x_{C7} = 0.31$ . Within this sub-region it is hypothesized that the least soluble/stable asphaltenes destabilize and are sensed by the quartz:  $\Delta F_m$  linearly decreases with the n-heptane addition,  $\Delta F_\eta$  and  $\Delta\Gamma_\eta$  are rather insensitive for the destabilization of such asphaltenes. From  $x_{C7} = 0.31$  to  $x_{C7} = 0.41$  (sub-region 3) there is a maxima in  $\Delta\Gamma_\eta$  and  $\Delta F_\eta$  (except for crude oil B). This effect as sensed by the quartz crystal within the  $\Delta\Gamma_\eta$  and  $\Delta F_\eta$  is an indication that the main occurring phenomena in the third sub-region is not only the bulk viscosity increase as a result of asphaltene precipitation. A bulk viscosity increase would reflect maximum in  $\Delta\Gamma_\eta$  and a minimum in  $\Delta F_\eta$ . Thus, in this third region other phenomena are disturbing the measures of frequency and bandwidth due to bulk viscosity and it could be the structuration of a first layer of deposit or a change in electrode/liquid interface coupling. In the third region  $\Delta F_m$  is observed to linearly decrease in a faster rate with n-heptane titration in comparison with the second region which supports the hypothesis that in this region  $\Delta\Gamma_\eta$  and  $\Delta F_\eta$  are disturbed by the formation of a first asphaltenic deposit layer. Sub-region 4 starts at  $x_{C7} = 0.41$  and finishes at  $x_{C7} = 0.73$ .  $\Delta F_m$  linearly decreases with n-heptane mass fraction (in a different rate as it was observed for sub-regions 2 and 3) and  $\Delta\Gamma_\eta$  and  $\Delta F_\eta$  decrease following the same pattern as before the onset of asphaltene destabilization as it is highlighted by the red dashed line in the upper and lower panels. Region 5 starts at the minimum in  $\Delta\Gamma_\eta$ , ( $x_{C7} = 0.73$ ). The interpretation of the fifth sub-region is better accomplished by considering its

evolution with time as such a region is mostly independent on n-heptane injection, and thus solubility conditions.  $\Delta\Gamma_\eta$ ,  $\Delta F_\eta$  and  $\Delta F_m$  obtained by the model application as a function of time for the fifth sub-region is shown in Figure 68.

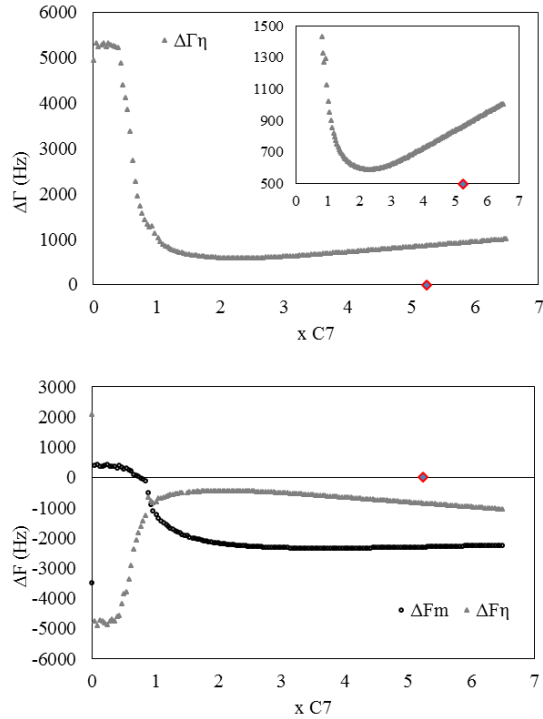


Figure 68. Model calculated change in frequency and bandwidth as a function of time for the continuous injection of n-heptane into crude oil A.

On the fifth sub-region the change in bandwidth increases linearly with time as well as the absolute value of the shift in resonance frequency due to viscous effects ( $\Delta F_\eta$ ). With longer times they tend to stabilize with small drifts (on the order of milihertz/hour). Contrary to what occurs within the change in resonant frequency and bandwidth due to viscous effects, the frequency shift due to deposit buildup ( $\Delta F_m$ ) stabilizes and in this case even present a small decrease. This is consistent with some studies where the leveling of the resonance frequency due to deposition is characteristic of a high particle surface coverage<sup>203</sup>. The fifth sub region may appear in the experiments at 25 °C when the bandwidth decrease due to n-heptane injection (viscosity

decrease) is surpassed by the bandwidths shifts arising from dissipative effects due to asphaltene deposition. During experiments at higher temperatures this region appeared at lower n-heptane mass fractions and was dependent on n-heptane injection. The experiments at higher temperatures are presented later on this manuscript.

#### *4.2.8 Recording of more overtones of resonance*

The analysis of more overtones of resonance besides the 3<sup>rd</sup>, 5<sup>th</sup> and 7<sup>th</sup> where performed. Such analysis is important when the application of other models is envisaged, for instance, the application of a viscoelastic models. The experiment was conducted with an initial crude oil mass of 40 g for crude oil C in contrast to the other experiments so far presented. The reason for the utilization of double of the initial crude oil mass is that the experimental procedure was conceived to furnish deposit samples in coupons to be analyzed by Atomic Force Microscopy. This section then brings an analysis of the profile of resonance frequency and energy dissipation (bandwidth) for all the overtones of resonance, but also an analysis of the possible role of the initial asphaltene mass in the system. As it is a closed system, the asphaltene mass is duplicated within the experiment at 40 g/L. The n-heptane injection rate was kept constant at 8 mg/s.

The resonance frequency change normalized by  $n$  and  $n^{1/2}$  are shown in Figure 69.

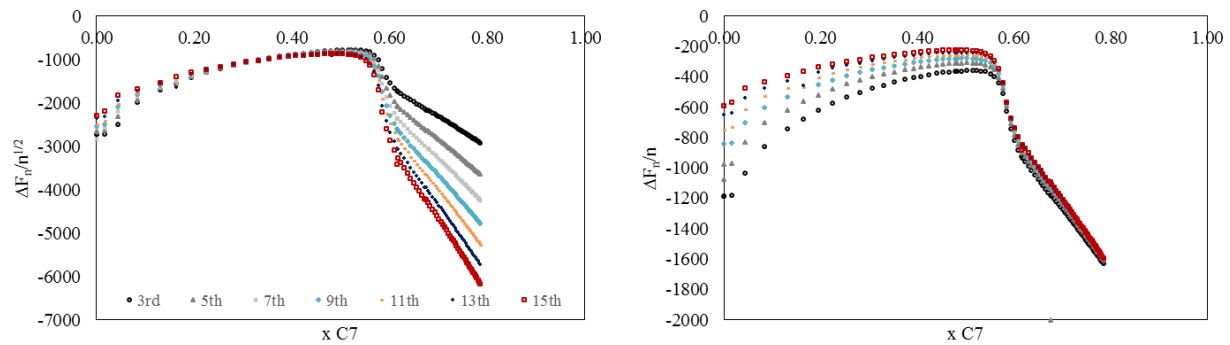


Figure 69. Change in resonance frequency and bandwidth up to the 15<sup>th</sup> overtone of resonance. Crude oil C at 25 °C and atmospheric pressure.

It can be observed that at low dilution there is a significant scattering of the signals normalized by  $n^{1/2}$ . Such effect is probably due to the poor coupling of the quartz crystal with the fluid due to the high system viscosity. When the deposit is formed, it is however observed that all the overtones of resonance converge indicating that even the highest overtone of resonance with a penetration depth of 70 nm indicates a homogeneous deposit.

The deposit bandwidth profile is shown in Figure 70. It can be observed that for higher harmonics the bandwidth minimum arises within decreased n-heptane mass fraction, as it is highlighted in the inset of Figure 70 by the dashed line. It can be also observed that for overtones greater than 7 the bandwidth profiles are higher and increase with the overtone. All signals however display the same pattern.

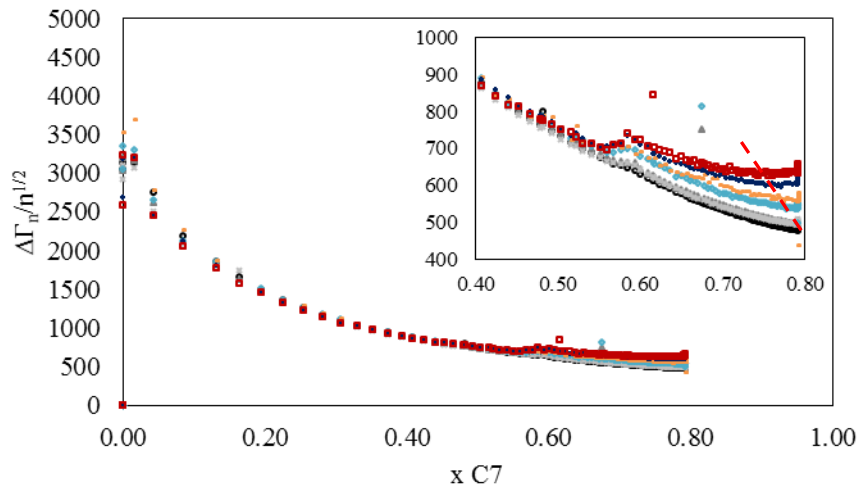


Figure 70. Bandwidth profile for the n-heptane injection into crude oil C at 25 °C, recording of seven overtones of resonance. The red dashed line indicates the earlier appearance of the bandwidth minima with higher overtones of resonance.

Figure 71 brings a comparative of the calculated density-viscosity profiles for the model application within the first three harmonics and for all the harmonics. It can be observed that the model calculated density-viscosity profile at the dilution region is the same when using the three

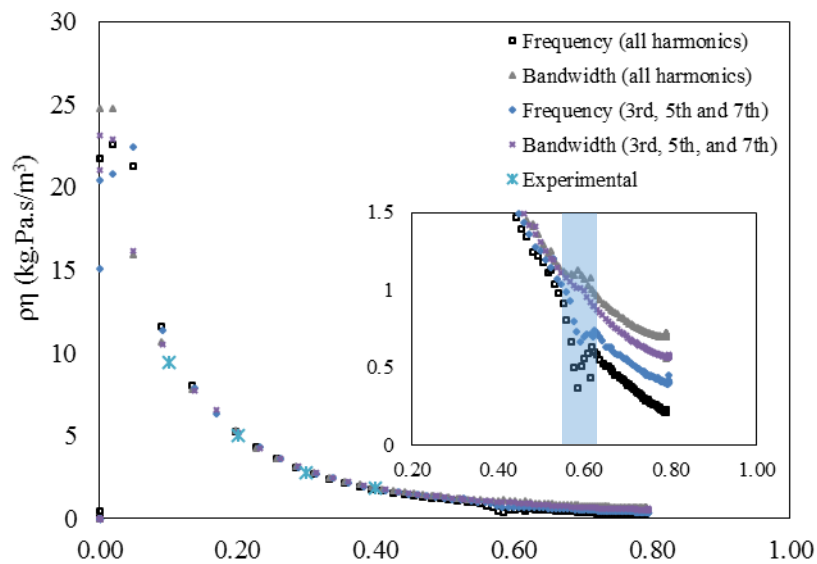


Figure 71. Comparison between the model calculated density-viscosity product using the three and seven overtones of resonance. Crude oil C at 25 °C and atmospheric pressure.

first overtones and all the range. However, the predicted density-viscosity profiles after the onset of asphaltene destabilization is shown to differ considerably when the higher overtones are utilized, possibly because of the higher inhomogeneity present at smaller size scales which are sensed with higher overtone orders.

Figure 72 brings a comparative of de the deposit thickness for the case when the initial crude oil mass titrated with 20 and 40 g and also a comparative of the system change in composition as a function of time for both experiments.

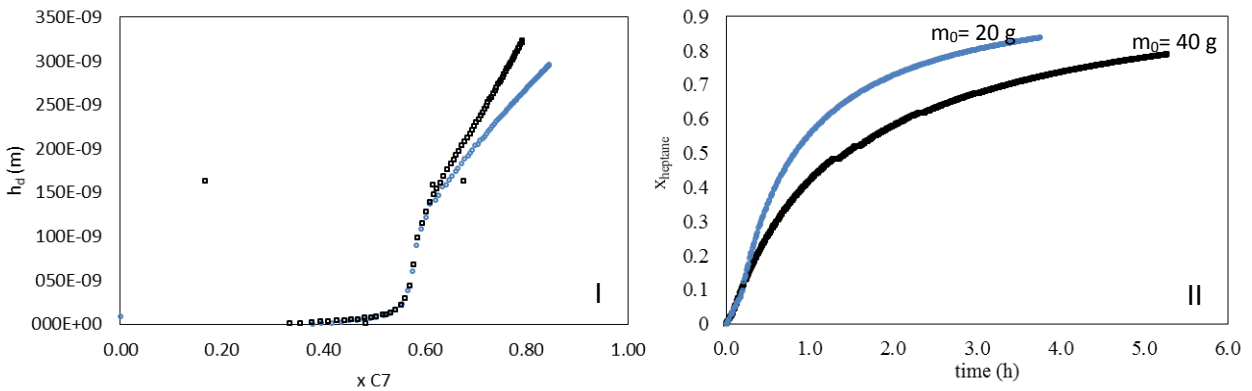


Figure 72. Comparative of deposit thicknesses obtained with the continuous n-heptane injection in 20 g of crude oil (blue) and in 40 g (black squares). Crude oil C at 25 °C and atmospheric pressure.

It is observed that the system with the double amount of asphaltenes give rise to an only slightly thicker asphaltene deposit. It could be argued that such difference is coming from the utilization of all harmonics. Thus the 3<sup>rd</sup>, 5<sup>th</sup>, and 7<sup>th</sup> harmonics were utilized to calculate  $h_{deposit}$  in the same experiment with the initial crude oil mass of 40 g and the data was compared to the  $h_{deposit}$  from the case of initial crude oil mass equal to 20 g. The comparative is shown in Figure 73, where it can be observed that a difference is arising from the use of more harmonics but this is not the only factor affecting the signal. Besides the increase in asphaltene mass and the effect of other overtones, the slowest rate of n-heptane composition change (Figure 72, II) may play a role in

deposit buildup. This may be clarified in a further experimental procedure where the n-heptane titration was stopped at many different n-heptane concentrations (next section).

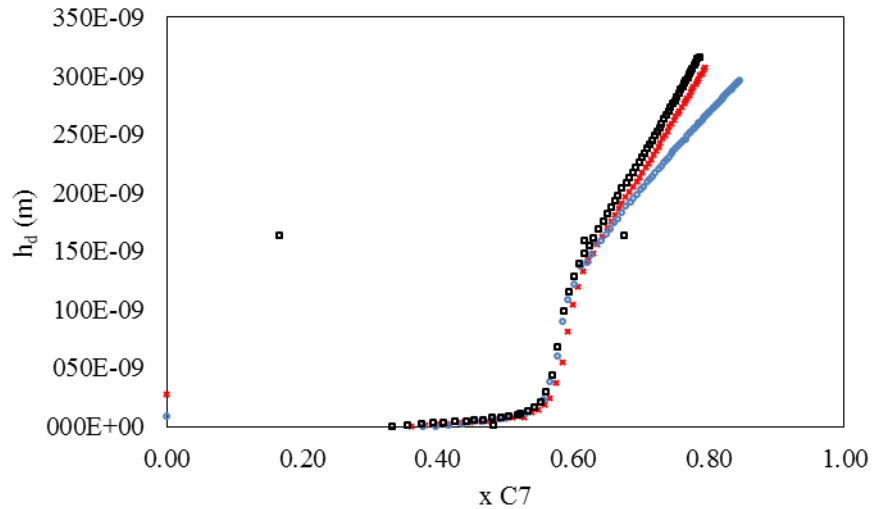


Figure 73. Comparative of  $h_{deposit}$  obtained from the experiment with initial mass of 20 g (3<sup>rd</sup>, 5<sup>th</sup> and 7<sup>th</sup> utilized overtones – blue), and 40 g (3<sup>rd</sup>, 5<sup>th</sup>, and 7<sup>th</sup> overtones – red; and all the overtones – black squares). Crude oil C at 25 °C and atmospheric pressure.

Having all the overtones of resonance it is convenient to plot the basis of the applied model for some compositions of n-heptane along with the experiment. Such procedure permits an evaluation of the coherence of the applied model in critical points as at  $x_{heptane} = 0.58$  as shown in Figure 71 (shaded area) where the change in resonance frequency displays an anomalous behavior with a net positive change, translated as a sudden decrease in bulk viscosity. The model was applied to different n-heptane mass fractions as it is shown from Figure 74 to 86.

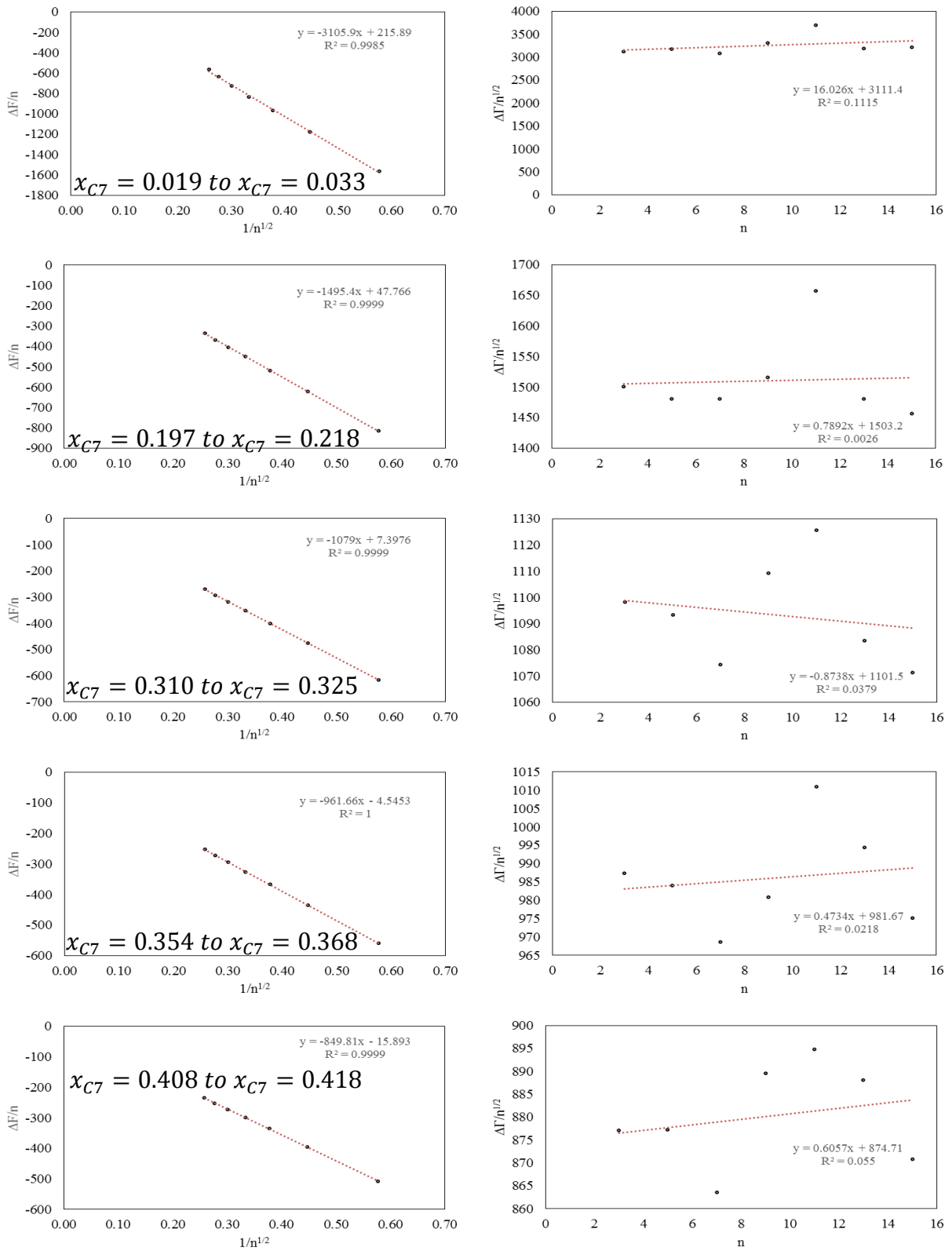


Figure 74. Model application for different  $n$ -heptane mass fractions. Continuous  $n$ -heptane injection into crude oil C.

(1)

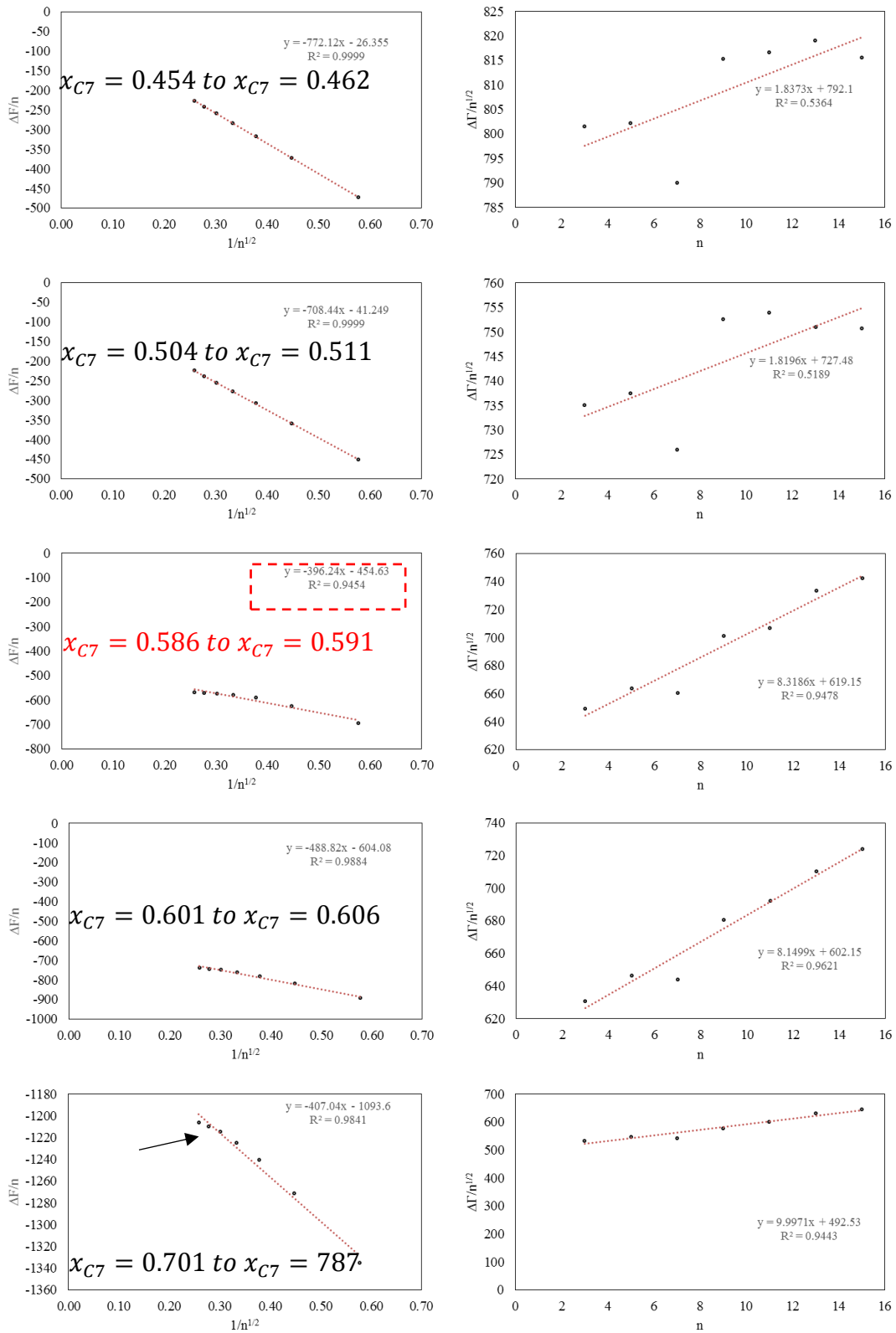


Figure 75. Model application for different n-heptane mass fractions. Continuous n-heptane injection into crude oil C. (2)

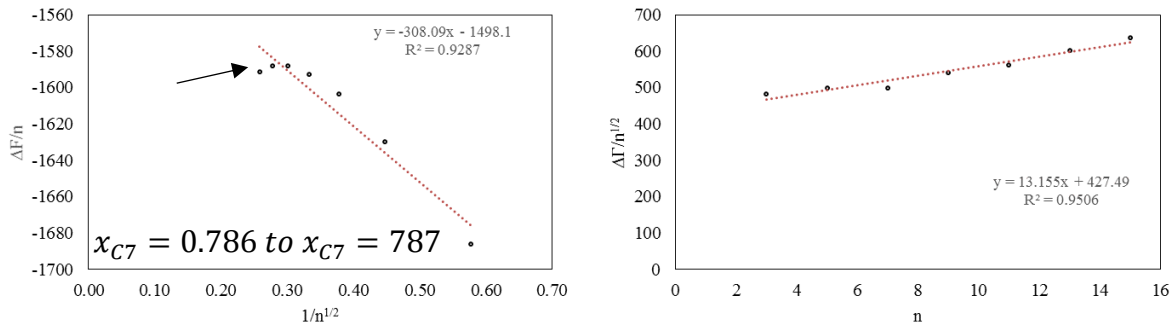


Figure 76. Model application for different *n*-heptane mass fractions. Continuous *n*-heptane injection into crude oil C. (3)

It can be observed that the model displays a good fitting in the dilution region. At  $x_{C7} = 0.57$ , at the point with the anomalous behavior observed within the change in frequency and bandwidth due to the bulk viscosity, the fit presents a correlation of  $r = 0.94$  and the normalized bandwidth presents a bigger spreading from the expected constant value. At higher *n*-heptane mass fractions, the higher overtones are not anymore in line with the smaller overtones (indicated by arrows in Figures 75 and 76) and a significant spreading in bandwidth is observed. Such behavior on frequency and bandwidth may highlight the viscoelasticity of the asphaltenic deposit. A viscoelastic model was applied to the points with a *n*-heptane mass fraction higher than  $x_{C7} = 0.45$ , the results in estimated deposit thickness and bulk density-viscosity product were observed not to vary significantly from the applied elastic model.

#### 4.2.9 Other experiments probing various asphaltene deposition aspects

After the basic understanding on the frequency and bandwidths profiles for the continuous *n*-heptane injection to the whole crude oil at 25 °C, other experiments were performed in order to probe the aspects influencing the asphaltene destabilization and, thus, the way the quartz crystal resonator measures it by the changes in the complex resonance frequency. Such experiments include the analysis of the complex resonance frequency profile when *n*-heptane injection is

stopped before and after the onset of asphaltene destabilization; the evaluation of the possible influence of the quartz crystal electrical behavior on deposition of asphaltenes once they are destabilized; the effect of the possible first asphaltene deposited layer as it is observed by the strong decrease in  $\Delta F_m$  in Figure 43. After struggling with experimental reproducibility issues, the effect of thermal treatment before the experiments, was observed to play a role on the bandwidth profile and for the last topic the asphaltenic deposit at the end of the destabilization was rinsed with n-heptane and its resonance profile probed in pure n-heptane and air as well when dissolving it with the continuous toluene injection is exposed.

#### 4.2.9.1 Intermittent n-heptane injection

In order to evaluate how the system evolves when the n-heptane injection is stopped and a constant composition on asphaltene precipitant is maintained, the n-heptane injection into crude oil C was stopped at various n-heptane mass fractions, either above or under onset conditions. The titration was proceeded at 3 mg/s. Figure 77 brings the profile of n-heptane mass fraction variation with time for the experiment.

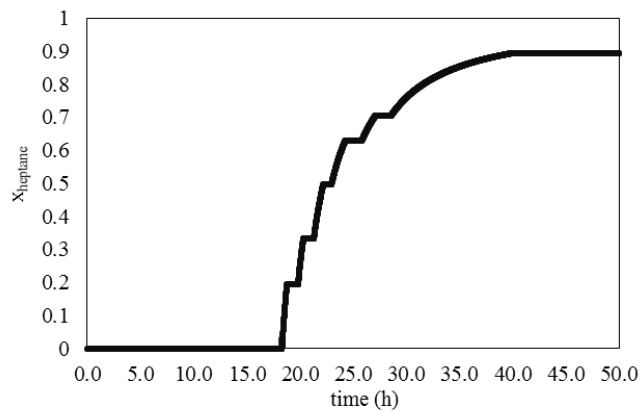


Figure 77. N-heptane mass fraction as a function of experimental run time for an intermittent n-heptane injection into crude oil C at 25 °C and atmospheric pressure.

The changes in resonance frequency and bandwidth as a function of time are shown in Figure 78. A baseline was collected for 20 hours in which it was observed a rate on changes in resonance frequency of -4 Hz/h and in bandwidth of 44 Hz/h. Such unstable baseline is an indicative that asphaltene adsorption may be occurring. Drifts in resonance frequency associated to the quartz crystal are normally less than 1 Hz/h which arrives mainly from quartz crystal piezoelectric stiffening<sup>155</sup>. The high increase in bandwidth may be also caused by a restructuration of the crude oil colloidal structure within the interface electrode/oil. The baseline was neglected in the other experiments as they were started within some minutes after the quartz is dipped in the crude oil.

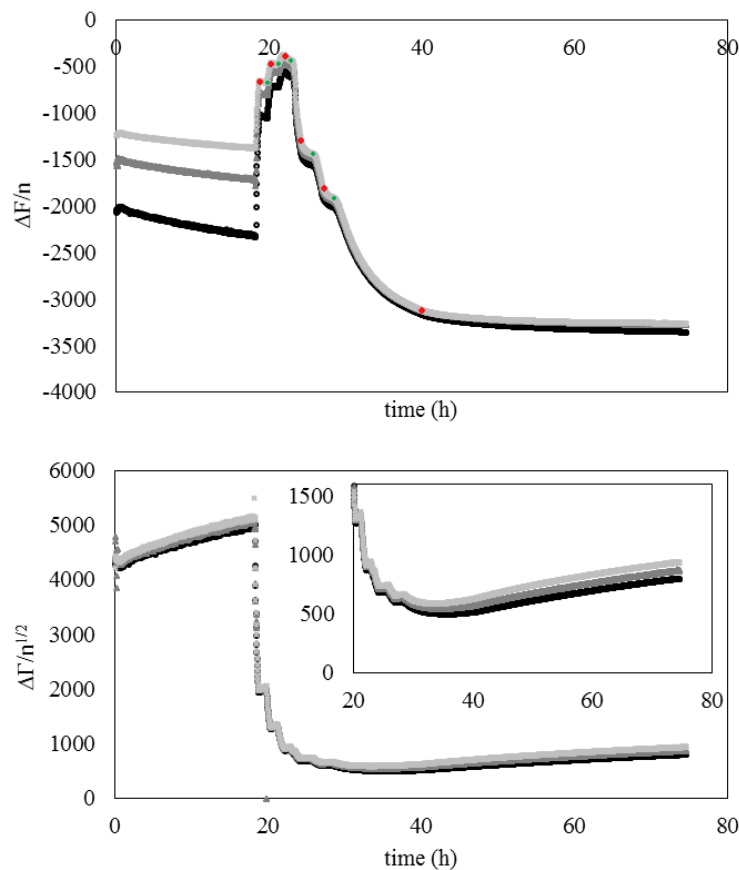


Figure 78. Intermittent *n*-heptane injection into crude oil C at 25 °C and atmospheric pressure. Circles, squares and crosses standing for 3<sup>rd</sup>, 5<sup>th</sup> and 7<sup>th</sup> overtones of resonance.

After the baseline collection the n-heptane injection is started. Figure 78 brings indicated as red diamonds when the n-heptane injection is stopped and green crosses when it is restarted.

The interruption in n-heptane injection above the onset of asphaltene destabilization displayed a resonance frequency stabilization over 2 hours (Figure 79). The bandwidths profiles were shown to respond more rapidly with stop in the titration indicating the predominance of the viscosity influence on the bandwidth profile. In the first n-heptane stop titration period after the onset of destabilization, the bandwidth profile displayed an increase of 10 Hz while the frequency profile accused a decrease of 100 Hz. The decay on change in frequency data versus experimental time at one fixed n-heptane mass fraction is an indication of the decay on the presence of destabilized particles prone to deposit. The decay on change in frequency data with experimental run time above the onset of asphaltene destabilization for the continuous titration was observed to be much longer than the experimental procedure in which asphaltenes are destabilized by a sudden n-heptane addition at mass fractions above the onset of asphaltene destabilization. This phenomenon was interpreted in terms of the competitive aggregation/deposition effects. Within the context of the study of asphaltene deposition by quartz crystal resonator totally immersed in crude oil, one of the conclusions is that the primary particles forming the asphaltene deposit are the particles naturally present in the crude oil, either in nanoaggregates or in a molecular state. The experimental evidences, highlighted by the small bandwidths profiles, suggest a smooth deposit, with roughness not much greater than the shear wave penetration depth in n-heptane ( $\approx 100 \text{ nm}$ ), thus the deposit should be build up from particles much smaller than 100 nm.

The experiment with intermittent n-heptane injection was shown to display a higher inter-harmonic spreading at the end of the n-heptane injection when compared to the experiment without n-heptane stopping (Figure 80).

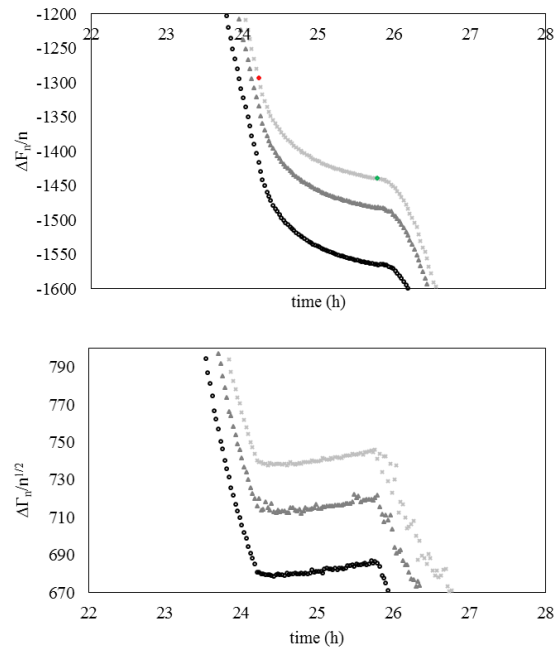


Figure 79. Frequency and bandwidth profiles when the n-heptane injection is stopped at the dilution plus destabilization region. Circles, squares and crosses standing for 3<sup>rd</sup>, 5<sup>th</sup> and 7<sup>th</sup> overtones of resonance.

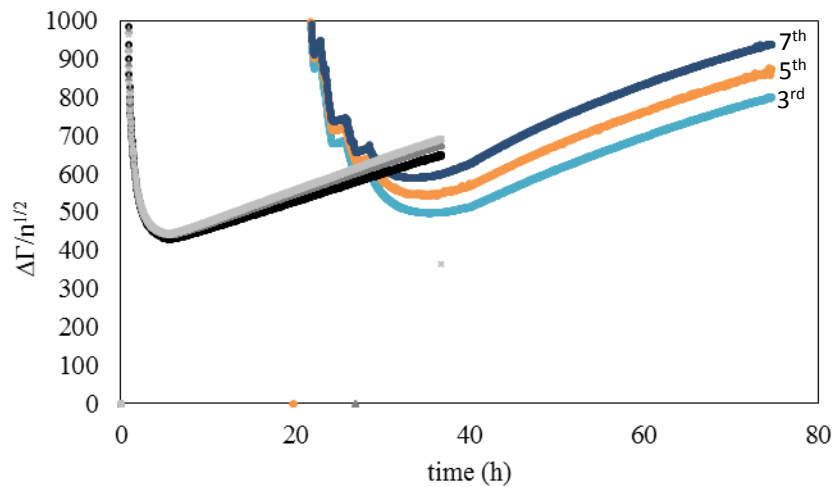


Figure 80. Comparison between bandwidth profiles from the continuous n-heptane injection into crude oil with continuous and intermittent n-heptane injection.

Figure 81 brings the change in frequency and bandwidth profiles as a function of n-heptane mass fraction for the intermittent experiment and continuous n-heptane injection. The decrease in resonance frequency assigned to the asphaltene deposition was significantly higher for the experiment with an intermittent n-heptane injection, which is translated by an increase in the model calculated deposit thickness (Figure 82).

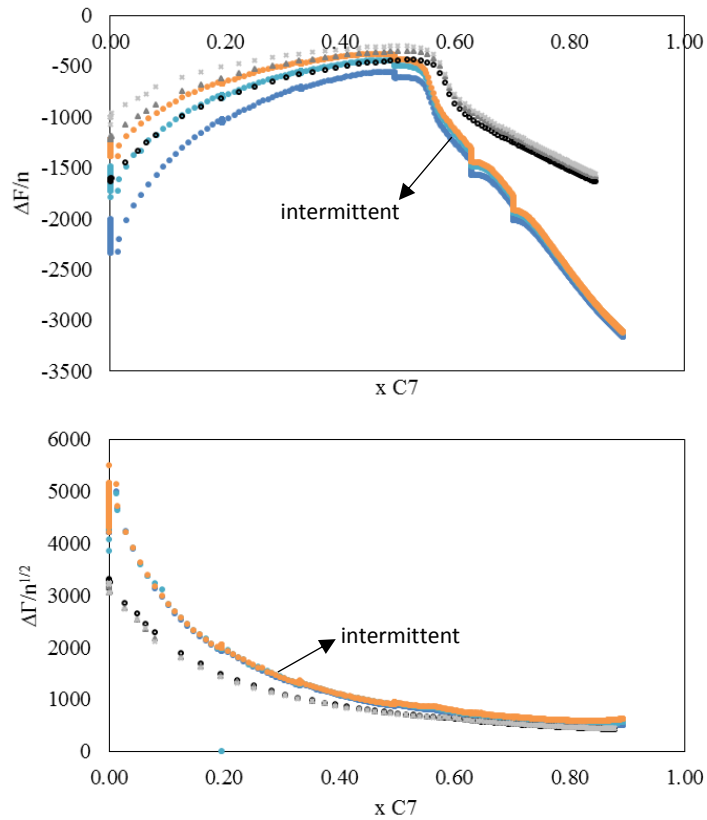


Figure 81. Frequency and bandwidth profiles for the continuous and intermittent (i) n-heptane injection into crude oil C as a function of n-heptane mass fraction.

In Figure 82 it can be observed that the thinnest deposit is obtained at the highest n-heptane injection rate without stopping and the thickest deposit is obtained at the lowest injection rate and with an intermittent injection. Figure 82 also summarizes a tendency of an increase of deposit growth with experimental runtime. This data should be looked carefully as the dissipation data between experiments are not equivalent (Figure 80) and may be the source of the observed rate of increase of the asphaltenic deposit.

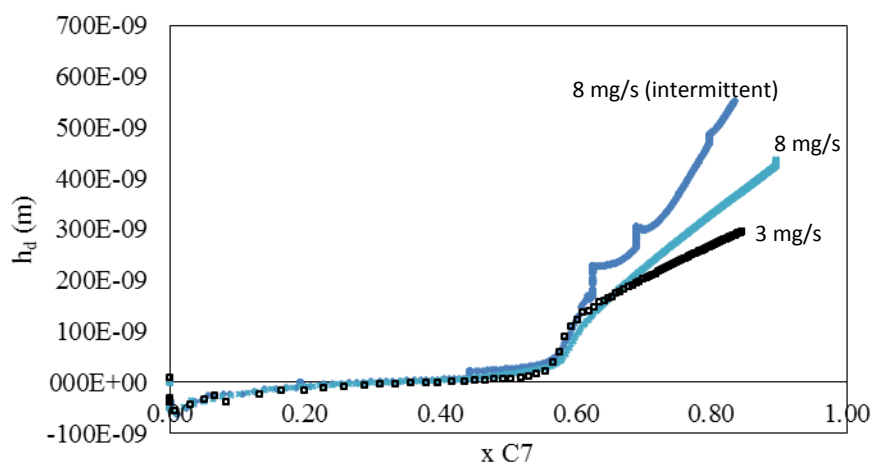


Figure 82. Comparative of deposit profiles obtained from the *n*-heptane injection into crude oil C at 3 mg/s; 8 mg/s and 8 mg/s with intermittent *n*-heptane injection.

One piece of experimental evidence which points out for the minor role of the bandwidth spreading or increase within the rate of deposition is shown in Figure 83 and consists of the frequency and bandwidth profiles for the destabilization of asphaltenes from crude oil C doped with dodecanoic acid. It was observed that the use of such organic acid induces the formation of a very dissipative deposit, which in turns give rise to a model calculated thickness roughly doubled from the ones obtained when the crude oil is used without the organic acid. In Figure 88-I it can be observed that the huge bandwidth obtained when the oil is doped with dodecanoic acid gives the same deposit thicknesses as the one obtained without such chemical, and with much smaller bandwidth profile (Figure 83-II). One aspect which is also important is the apparent dependency on the time in which it was maintained at *n*-heptane mass fractions before the onset of destabilization is reached. This can be interpreted as a colloidal reorganization or even nano/micrometric phase separation which is more uniform at higher experimental runtime. The information is pertinent and important for a risk assessment where the crude oil is submitted to high residence times in a near or close to near onset of asphaltene destabilization. The hypothesis should be checked with the aid of other techniques of analysis.

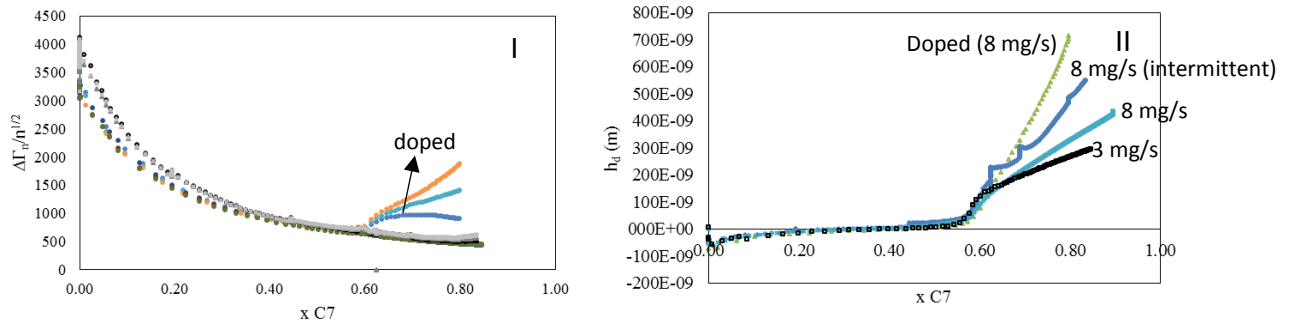


Figure 83. (I) Bandwidth profiles for the continuous n-heptane injection into crude oil at 3 mg/s; 8 mg/s; 8 mg/s (intermittent injection) and at 8 mg/s with dodecanoic acid at 2 wt%. (II) Model calculated deposit thickness for the exposed experiments.

#### 4.2.9.2 Quartz activity evaluation

There were some questions on the possible influence of the quartz alternating electrical field and thus electrode electrical charges inducing the continuous deposition of asphaltene particles when they are destabilized. Thus, crude oil C was continuously titrated with n-heptane and the quartz crystal was shut off in the dilution plus destabilization region for 2 hours and then it was restarted. The rate of frequency decrease yielded by the continuous asphaltene deposition was observed not to change in the period when the quartz crystal resonator was shut off as it is shown on Figure 84. Thus, there is no influence of the quartz crystal electrical field in the asphaltene deposition above the onset of destabilization.

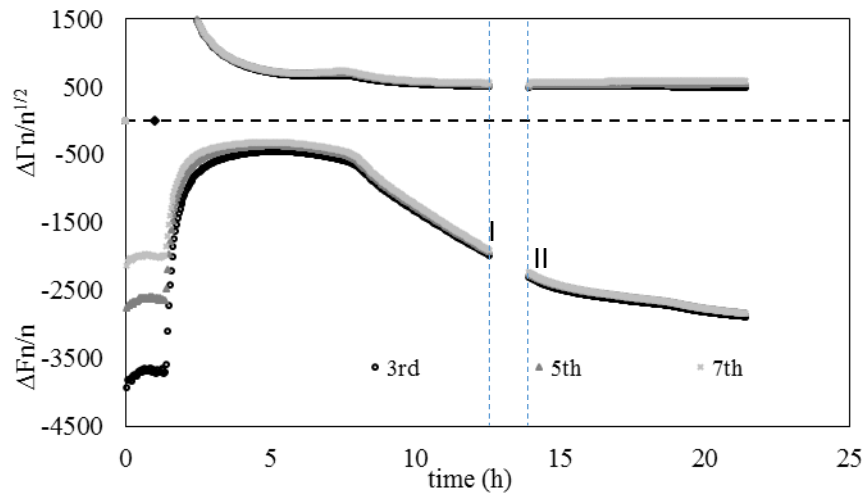


Figure 84. Quartz activity evaluation on the frequency and bandwidth changes. (I) The quartz crystal was shut off and turned on after 2 hours (II). The n-heptane mass flow rate was kept constant during the entire experiment.

#### 4.2.9.3 The influence of the first layer

It was also questioned if the first step decrease in resonance frequency observed in almost all the experiments with the whole crude oils were coming from the deposition of a first asphaltenic deposit layer which could have an influence on the deposition of subsequent layers. In order to shed some light to the question an experiment was done in which, after the formation of the first layer, the quartz crystal was cleaned with n-toluene and re-submerged in the crude oil/n-heptane mixture. The n-heptane titration was stopped during the cleaning procedure and was re-started right after the immersion of the quartz crystal, with the parallel re-collection of resonance frequency and bandwidth data. The result in change in resonance frequency as a function of time and n-heptane mass fraction ( $x_{C7}$ ) is shown in Figure 85.

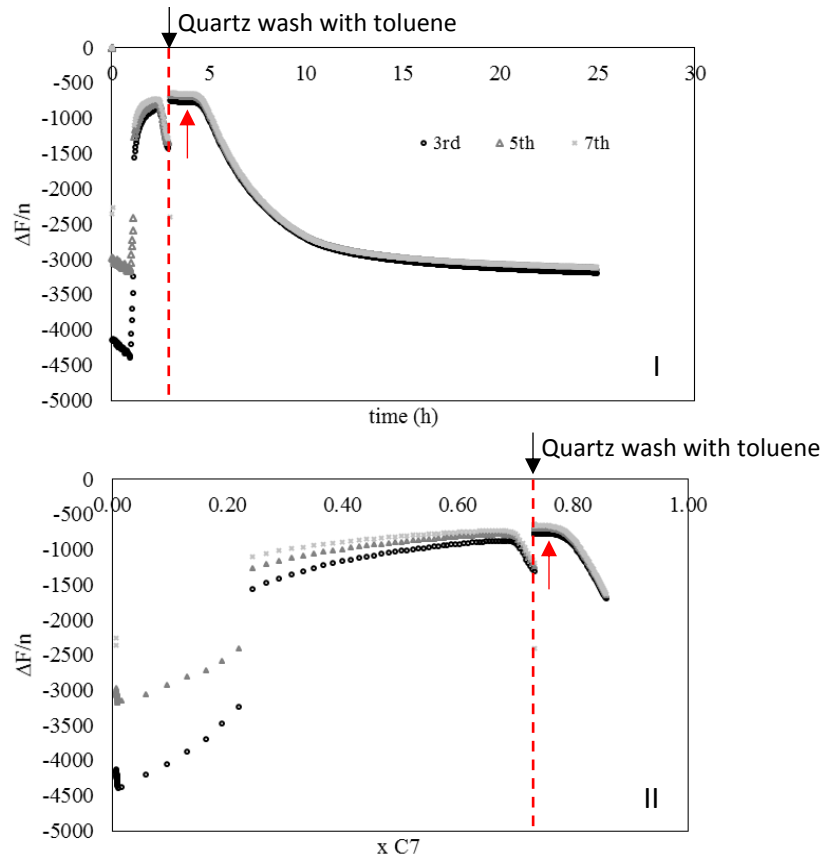


Figure 85. Evaluation of the influence of the first deposited asphaltene layer on deposit build up. (I) Changes in resonance frequency as a function of time. The time of the cleaning procedure is not shown. (II) Changes in resonance frequency as a function of n-heptane mass fraction ( $x_{C7}$ ). During the cleaning the n-heptane injection was stopped. Red arrows indicate the lag on the detection of deposition after the quartz was cleaned. Circles, squares and crosses standing for 3<sup>rd</sup>, 5<sup>th</sup> and 7<sup>th</sup> overtones of resonance respectively.

The cleaning of the quartz crystal with toluene removes the asphaltenic deposit making the frequency change return to its value before the onset of asphaltene destabilization. Although the n-heptane injection is started right after the quartz is re-inserted in the system, it can be observed that there is a lag between the beginning of the injection and the decrease of the resonance frequency (red arrows in Figure 85). Such lag is magnified in Figure 86 for the change in resonance

frequency as a function of n-heptane mass fraction ( $x_{C7}$ ). The lag was significantly greater than the ones occurring with the restart of the n-heptane injection in the case of the intermittent n-heptane injection (Figure 79).

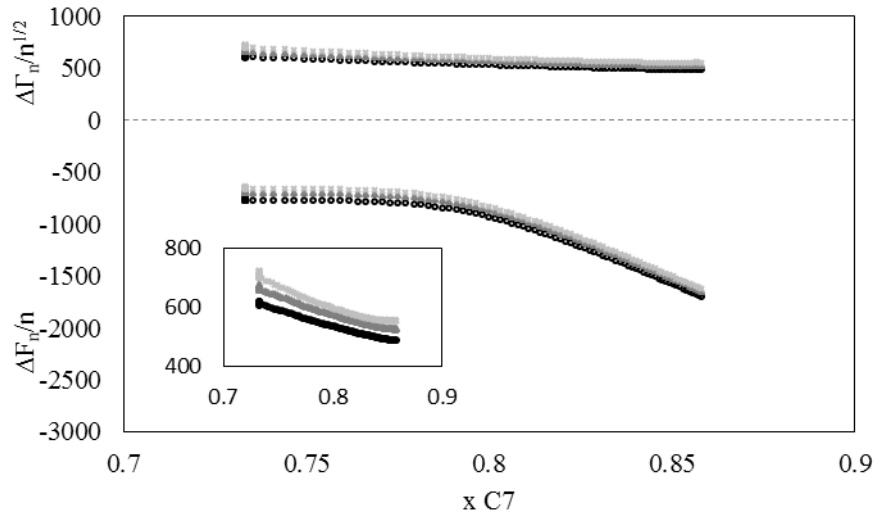


Figure 86. Deposition profile after the quartz crystal was cleaned with toluene and re-submerged in the crude oil/n-heptane solution. The inset magnifies the changes in bandwidth highlighting its imperceptible variation despite the fact that a deposit yielding 1000 Hz in frequency change is created on the gold electrodes. Circles, squares and crosses standing for 3<sup>rd</sup>, 5<sup>th</sup> and 7<sup>th</sup> overtones of resonance respectively.

The inset of Figure 86 highlights the rather imperceptible bandwidth changes even if a deposit yielding a resonance frequency change of 1000 Hz is created. Thus highlighting the very elastic nature of such deposit. The optical microscopy images of the formed asphaltenic deposit after the cleaning procedure and subsequent deposition is shown in Figure 133-VI.

#### 4.2.9.4 The temperature memory

The first experiments in the context of the present work were done by firstly pre-heating the crude oil at 60 °C at least for one hour to melt paraffin and homogenize the oils. After heated, the crude oil was sampled in the mixing vessel and let stabilize at 25 °C until the experiment was started. The temperature equilibration process took from 20 to 30 minutes and the temperature

was checked with a thermocouple directly inserted in the crude oil. Other experiments were done without heat treatment before sampling the oil from the storage vial. Both experiments displayed different profiles of resonance frequency change and more importantly bandwidth changes. The comprehension of this phenomena is crucial to obtain reproducible experiments and can also reveal some differences in the asphaltenes physical state in the bulk of the crude oil.

Experiments were done in order to research the temperature treatment effect on the asphaltenes deposition profile as detected by changes in resonance frequency and bandwidth. From the crude oil storage vial two samples were taken. One of the samples was heat treated before the n-heptane continuous injection. The heat treatment consisted in keeping the sample at 60 °C for two hours. After the two hours the sample was cooled down to 25 °C and the n-heptane injection started. The experiment on the other sample was performed without heat treatment. Both experiments were performed at 25 °C. The results showed a systematic change in the deposition profile between the experiments. Notably, the crude oil submitted to heat treatment yielded deposit bandwidth profile with a clear maxima and higher inter-harmonic spreading (Figure 87).

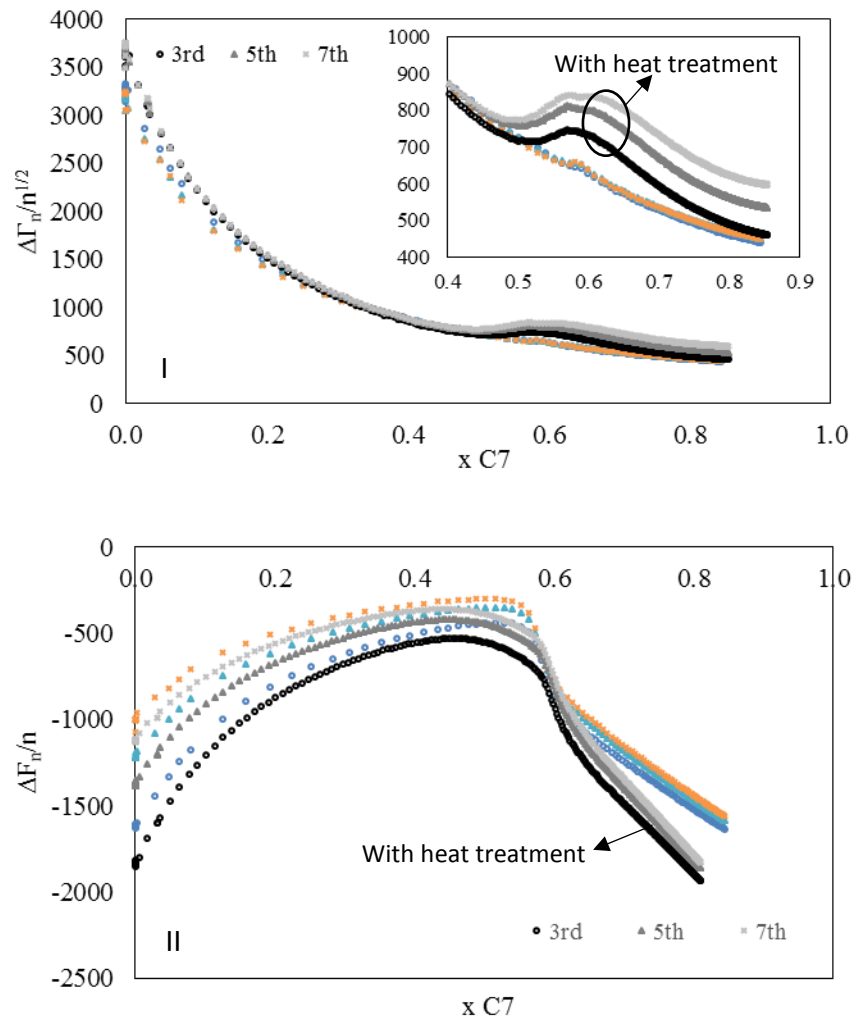


Figure 87. Bandwidth (I) and resonance frequency (II) profiles for the continuous n-heptane injection into crude oil which was or not submitted to heat treatment at 60 °C. The experiment with the heat treated crude oil is indicated by the arrows. Crude oil C at 25 °C and atmospheric pressure.

As it is observed, the deposition process when the crude oil was exposed to mild heat treatment give rise to a more dissipative asphaltene deposit layer. The high bandwidth, i. e., deposit energy dissipation is either coming from the formation of a viscoelastic layer or from the formation of a laterally heterogeneous layer, and further characterization is needed in order to draw conclusions. However, as the inter-harmonic spreading is kept constant in the deposition region

it is possible that the greater dissipation is coming from deposit viscoelasticity. The change in resonance frequency is shown to be more negative in the case where the oil was exposed to the heat treatment, in accordance with the higher dissipation. Another experiment was performed in order to further probe this memory effect of the petroleum structure with temperature and its influence on deposit build up. The crude oil was heated for 2 hours at 60 °C and then it was kept at 25 °C for 2 hours. The bandwidth from the three experimental cases is shown in Figure 88. The bandwidth change, i. e., the deposit configuration or its physical characteristics is dependent on the time after the heat treatment was performed. This indicates that the phenomenon occurring on the petroleum structure upon heat treatment presents a relaxation over time. Considering that the increase in bandwidth due to temperature treatment comes from an increase in deposit viscoelasticity rather than from inhomogeneity, the higher bandwidth may appear due to a different physical configuration in the molecular, aggregate or macromolecular structure of asphaltenes in the bulk of the crude oil. Many studies which emphasize the change in physical properties of asphaltenes within a mild range of temperature point out for the asphaltenes physical behavior changes in such temperature ranges. A recent study<sup>213</sup> reported on zeta potential of asphaltene solutions at 20 and 60 °C, with a correlation with yielded particle sizes upon asphaltenes destabilization. They reached the conclusion that at higher temperatures the asphaltenes present higher stability through higher steric hindrances due to their alkyl corona. At lower temperatures they found that van der Waals attraction more significant facilitating aggregation. They report that the equality on collision efficiency in relation to temperature is non-real, with a lowering in the collision efficiency, reaching aggregation, with the increase in temperature. In this context, the author proposes that the quartz crystal resonator is probably

probing the buildup of a more viscous layer coming from the different asphaltene or nanoaggregate alkyl chain corona and further their intermolecular or inter-particle interaction.

One may also argue about the role of paraffin in the deposit build up and the rise in bandwidth. If paraffin are indeed responsible for the observed phenomena, then it is concluded that paraffin plays a key role in asphaltene deposition. It may be argued that the role of paraffin is crucial since crude oil C has 58.8 wt % of saturated hydrocarbons. However, the same changes in bandwidth profiles for crude oil A, which has only 15.6 wt % in saturated hydrocarbons, were observed (Figure 91). The phenomenon is complex and should be further analyzed with the aid of other characterization techniques. Its importance is clear since the quartz crystal is presenting an averaged phenomenon clearly indicating the role of the crude oil structure and its influence on deposit build up.

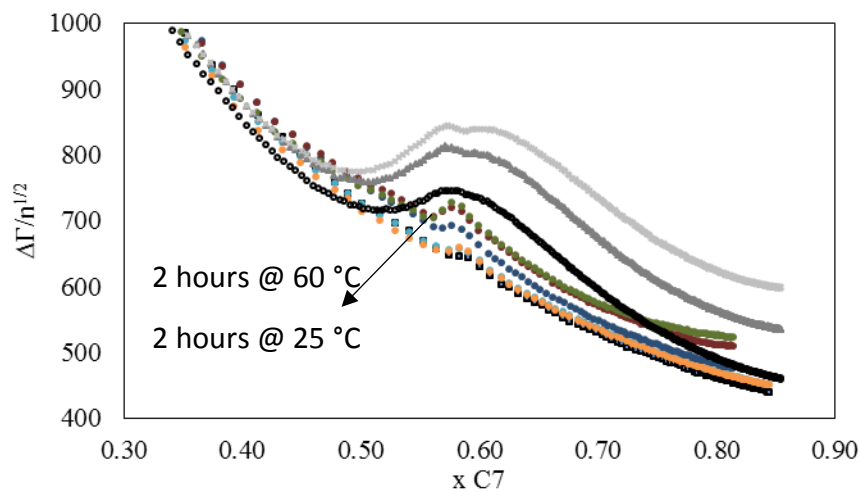


Figure 88. Effect of temperature treatment on bandwidth changes induced by asphaltene deposition.  $x_{C7}$  stands for *n*-heptane mass fraction

The density-viscosity product obtained by the model application in the case of the crude oil with heat treatment (Figure 87) is shown in Figure 89. It is interesting that the calculated density-viscosity obtained by the  $\Delta F\eta$  and  $\Delta\Gamma\eta$  have the same profiles with an apparent increase in bulk viscosity once the asphaltene are destabilized. Despite the fact that the density-viscosity product predicted by the change in resonance frequency had a small valley (arrow on the inset of Figure 89), it displayed a very different profile from the experiments with no heat treatment or with heat treatment. The experiment with heat treatment and 2 hours at 25 °C showed the same profile as the one with no heat treatment as it is shown in Figure 90, I and II respectively.

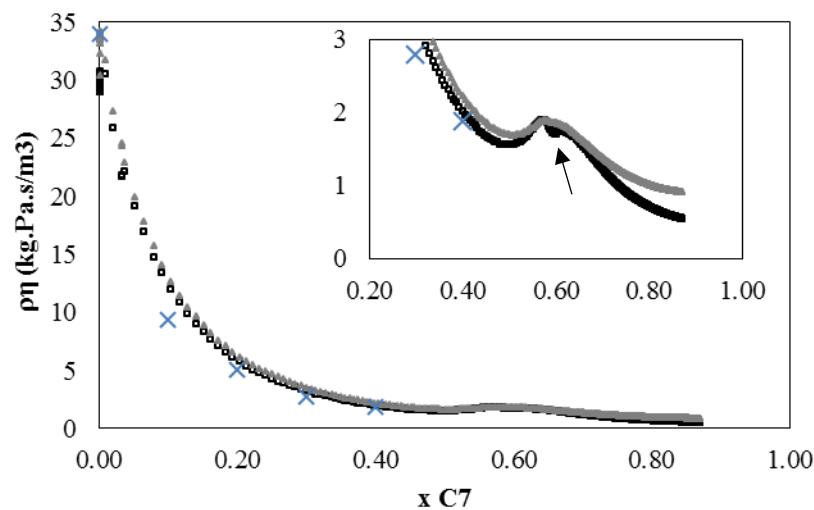


Figure 89. Density-viscosity products as obtained from the change in frequency and bandwidth data for crude oil C with heat treatment before experiment. Circles, squares and crosses standing for 3<sup>rd</sup>, 5<sup>th</sup> and 7<sup>th</sup> overtones of resonance. Big blue crosses are experimental density-viscosity values.

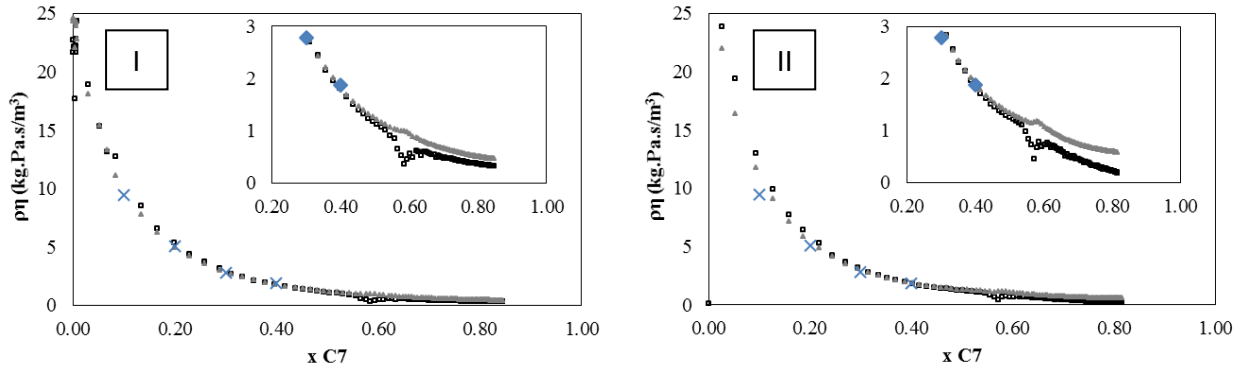


Figure 90. Density-viscosity profile for crude oil C with no heat treatment (I) and with 2 hours heat treatment and 2 hours at 25 °C (II).  $x_{C7}$  stands for *n*-heptane mass fraction.

The fact that the applied model does not account for dissipative effects does not invalidate the physical observations and how the model interprets the changes in the complex resonance frequency. With the application of further techniques to evaluate the system laterally homogeneity a viscoelastic model should be applied and further interpretation on the occurring processes may be withdrawn. Indeed, it should also be difficult to decouple the many occurring processes and perhaps the application of a model with more fitting variables may greatly bypass the real processes in complex shear modulus and complex viscosity determinations.

Two concurrent effects may be occurring to explain what is observed in Figure 89: 1. The buildup of a dissipative deposit for the reasons exposed before (change in the physical state of the heavy fractions of crude oil), giving rise to the interpretation of an overall increase in apparent interfacial viscosity from bandwidth and frequency data; 2. The former observed decrease in the apparent interfacial viscosity, which was observed to be not normal, and possibly assigned to an interfacial phenomenon. This case may be a case in which the deposit acoustics may constructively interfere with the quartz resonance frequency. Such acoustic interference can happen at deposit thickness

close to the shear wave penetration depth length or with other deposit structures which may resonate constructively with the quartz crystal resonance.

The effect of the crude oil heat treatment before the experiments was also evaluated by probing the asphaltene destabilization from the most asphaltenic, and least paraffinic, crude oil (crude oil A, with 11.9 wt % n-C7 asphaltenes). Figure 91 brings the bandwidth profile from the case where the crude oil was let at 60 °C (I) for two hours, then brought to 25 °C for the n-heptane injection and impedance analysis to start, and for the case in which no heat treatment was performed (II).

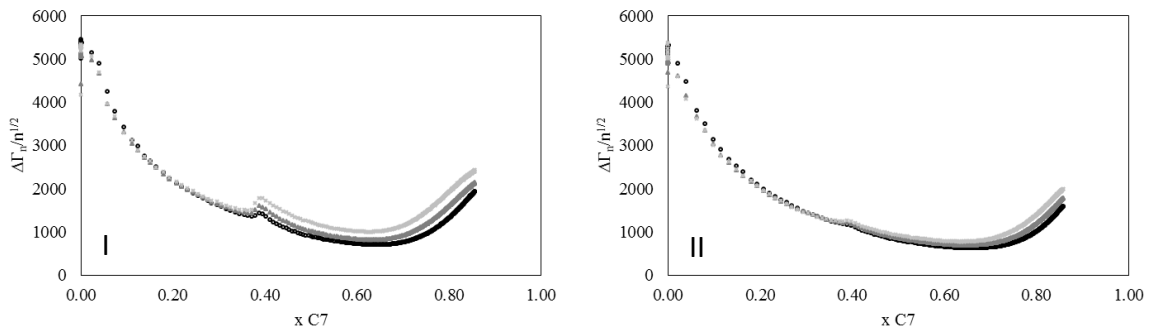


Figure 91. Bandwidth profile for crude oil A with heat treatment (I) and without heat treatment (II).  $x_{C7}$  stands for n-heptane mass fraction.

The superposition of both experiments within the dilution plus deposition region is shown in Figure 92.

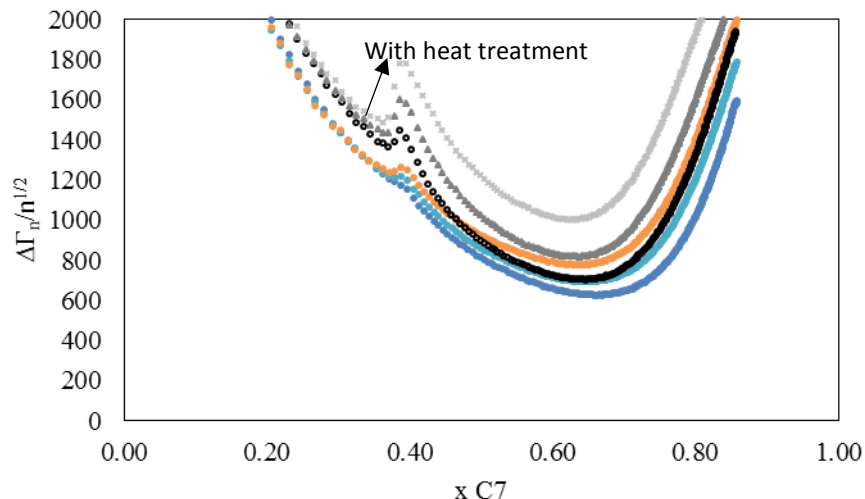


Figure 92. Differences in bandwidth profile when the crude oil is submitted to heat treatment before the n-heptane injection to crude oil A. Both experiments were done at 25 °C.  $x_{C7}$  stands for n-heptane mass fraction.

#### 4.2.9.5 Deposit in heptane, air and dissolution with toluene

In order to probe various deposit aspects three experimental procedures were done at the end of the continuous n-heptane injection into crude oil C.

1. After the n-heptane injection the quartz crystal was taken out of the mixing vessel, abundantly rinsed with n-heptane and submerged in pure n-heptane. The frequency and bandwidth data of the quartz crystal with the asphaltenic deposit in pure heptane was recorded for more than 20 hours. The model calculated thicknesses obtained from the deposit in pure heptane were compared to the deposit thickness obtained at the end of the n-heptane titration procedure into crude oil C.
2. The deposit was then taken out from the pure n-heptane solution, dried by air blown and the impedance analysis of the quartz crystal with the dried asphaltenic deposit under atmospheric conditions was performed. The obtained deposit thickness was compared with the calculated deposit thickness of the deposit in pure n-heptane or at the end of the n-heptane injection into crude oil C.
3. A third experimental procedure consisted in re-immersing the quartz with deposit in pure n-heptane ( $m_{\text{hep}} \approx 20 \text{ g}$ ), and injecting toluene at a rate of 3 mg/s. This procedure was done in order to probe the asphaltenic deposit dissolution.

The same deposit was used in order to perform the three described experimental procedures. The deposit was created by the continuous n-heptane injection into crude oil C, to which heat treatment was applied. The frequency and bandwidth profiles for such experiment is shown in Figure 93, as a function of n-heptane mass fraction and in Figure 94 as a function of time.

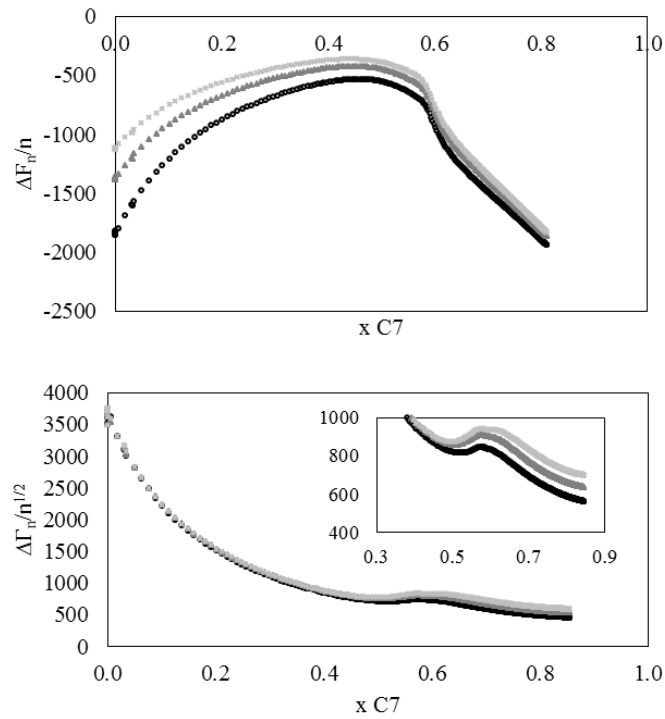


Figure 93.  $\Delta F$  and  $\Delta \Gamma$  as a function of *n*-heptane mass fraction ( $x_{C7}$ ) for the continuous *n*-heptane injection into crude oil C at 25 °C and atmospheric pressure.

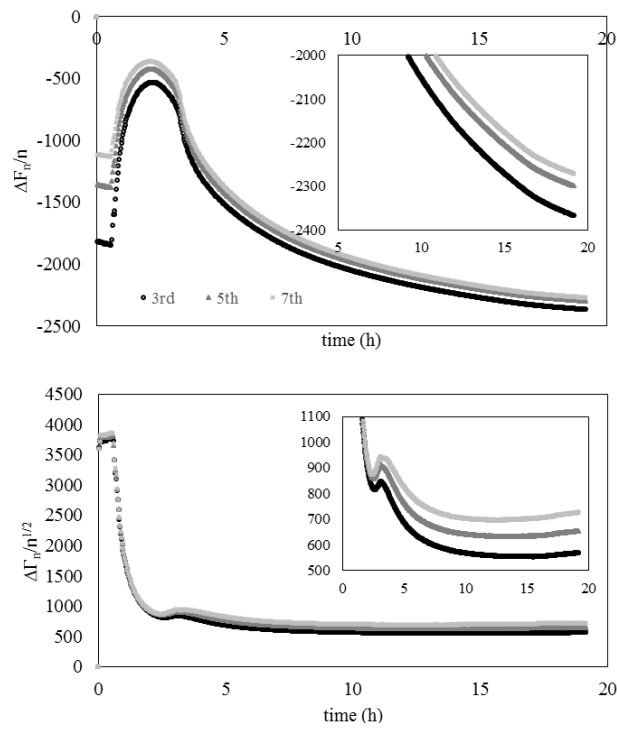


Figure 94.  $\Delta F$  and  $\Delta \Gamma$  as a function of time for the continuous *n*-heptane injection into crude oil C at 25 °C and atmospheric pressure.

The frequency and bandwidth profiles for the quartz crystal rinsed with n-heptane and immersed in pure heptane is shown in Figure 95.

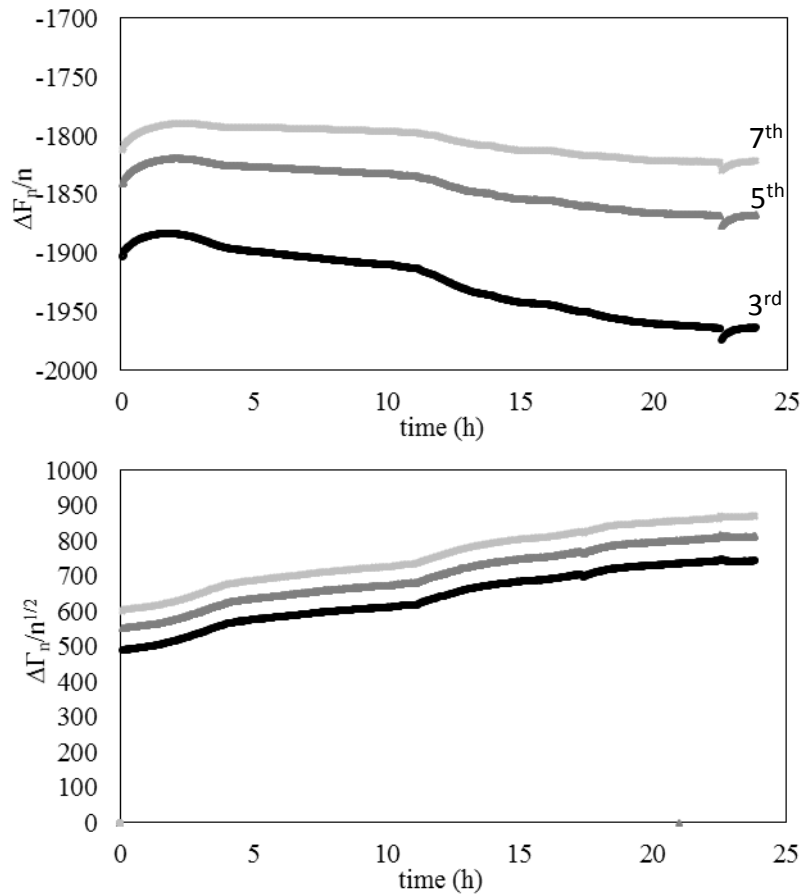


Figure 95.  $\Delta F$  and  $\Delta \Gamma$  as a function of time for the quartz crystal with asphaltenic deposit obtained at the end of the experiments exposed in Figures 93 and 94. The system was kept at 25 °C during the entire experiment.

The resonance frequency changes displayed a decrease in relation to their values at the end of the n-heptane injection as it shown in Figure 100. The bandwidth profile however decreased of about 50 Hz but does not have a significant variation within the inter-harmonic spreading. The data indicates that the washing with pure n-heptane may have striped out the perhaps not tightly bound deposited layer. The frequency and bandwidth changes for the deposit in pure n-heptane also display an overall drift of -3 Hz/h and 11 Hz/h respectively, indicating possible aging issues

within the deposit. However the observed drift in frequency and dissipation are not translated by appreciable change in deposit thickness as it is observed on Figure 96. The deposit build up profile obtained the destabilization of crude oil C with n-heptane (Figures 93 and 94) is also shown in Figure 96. It can be observed that a thickness of 100 nm may have been removed by the washing process with n-heptane or that surface inhomogeneity is decreased, decreasing the missing mass effect.

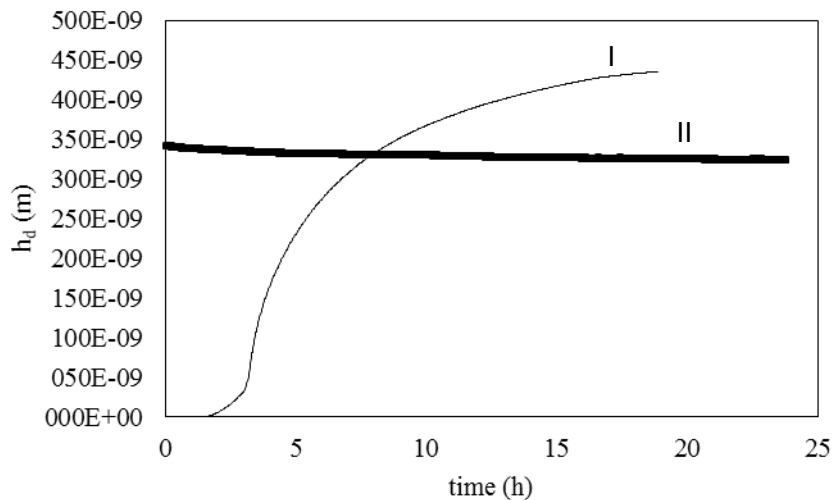


Figure 96. Comparison of the model calculated deposit thicknesses for the crude oil C titrated with n-heptane (I) and the thickness obtained when washing the deposit and immersing it in pure n-heptane (II). The experiments were done at 25 °C and atmospheric pressure.

In fact, it can be observed a negative drift in the calculated thickness when the asphaltenic deposit is in pure n-heptane, indicating that part of the asphaltenes may be re-dissolving and increasing the surface roughness which is reflected as an apparent increase on viscosity. Figure 97 brings the density-viscosity product obtained from changes in frequency and bandwidth for the experiment exposed in Figure 95. The dashed red line indicates the product density-viscosity for the pure n-heptane.

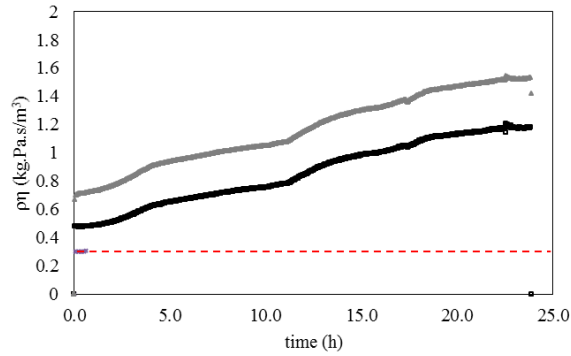


Figure 97. Model calculated density-viscosity profile from changes in frequency and bandwidth as a function of time for the asphaltenic deposit in pure n-heptane. The red line is the density-viscosity product obtained when the clean quartz crystal (with no asphaltenic deposit) is immersed in pure n-heptane.

After the experiment with the pure heptane the quartz was dried and the resonance parameters collected at atmospheric conditions. Figure 98 brings the results on resonance frequency data and estimated deposit thickness. It can be observed that in air the deposit thickness is observed to be more than 100 nm thinner than when it was in n-heptane. Thus putting in evidence the inhomogeneity of the deposit contributing for an apparent deposit thickness. Deposit thicknesses were studied by Atomic Force Microscopy and the results are shown in a later section.

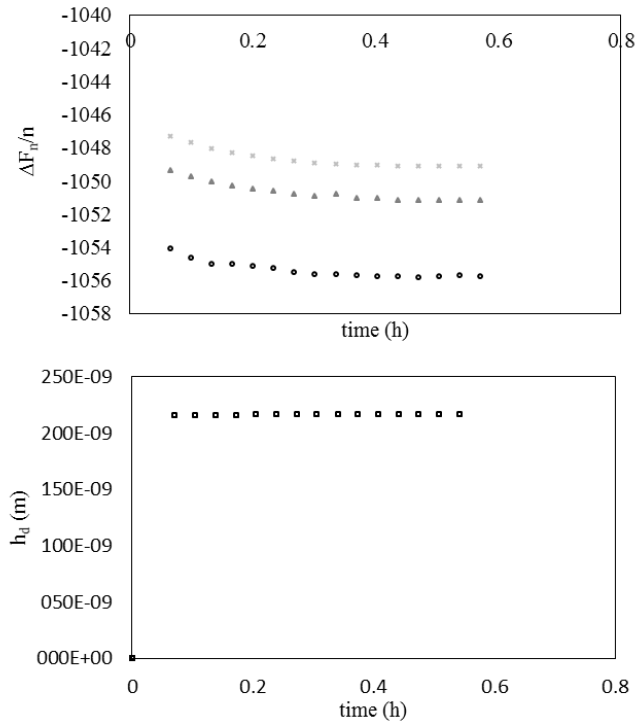


Figure 98. Quartz crystal resonance frequency change and estimated deposit thickness for the asphaltenic deposit in air at 25 °C.

The last experimental procedure to study the deposit was to submit it to dissolution by submerging it in n-heptane and continuously injecting toluene. This experimental procedure can be of interest to study deposit dissolution onset with or without chemicals in order to envisage treatment strategies. Figure 99 brings the frequency and bandwidth profile, as a function of toluene mass fraction, for such experiment.

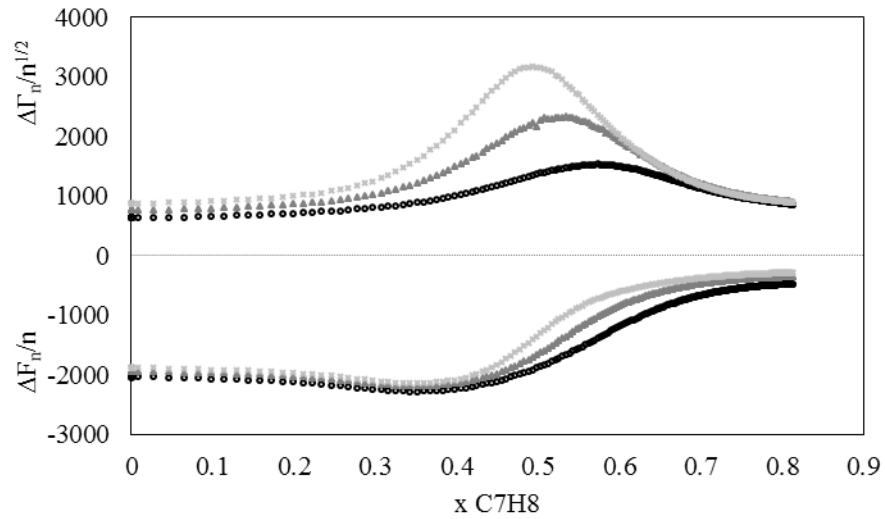


Figure 99. Changes in frequency and bandwidth, as a function of toluene mass fraction, for the asphaltenic deposit dissolution by continuous toluene injection into pure *n*-heptane. Circles, squares and crosses standing for 3<sup>rd</sup>, 5<sup>th</sup> and 7<sup>th</sup> overtones of resonance.  $x_{C7H8}$  stands for toluene mass fraction.

It can be observed that the detection of the onset of deposit dissolution definition may be not an easy task. From  $x_{C7H8} = 0$  to  $x_{C7H8} \approx 0.20$  it can be observed a linear decrease in resonance frequency, which may be assigned for the toluene density and viscosity. However, from  $x_{C7H8} \approx 0.20$  to  $x_{C7H8} \approx 0.35$  the decrease in resonance frequency is intensified before it begins to increase due to the asphaltenic deposit dissolution. Bandwidth profiles are observed to display maxima values which coincides with the inflexion points from the resonance frequency profiles. The seventh harmonic presents the bandwidth maximum in smallest toluene mass fraction and the third in the highest. This is expected since the inhomogeneity appearing from the deposit dissolution would increase in size as the deposit is dissolved. The higher decrease in resonance frequency from  $x_{C7H8} \approx 0.20$  to  $x_{C7H8} \approx 0.35$  could be interpreted as a deposit swelling before detaching from the surface or by an increase in the roughness which give rise to a negative resonance frequency change surpassing the positive frequency change which would be yielded

by the loss of deposited mass. Figure 100 brings the resonance parameters as a function of experimental run time.

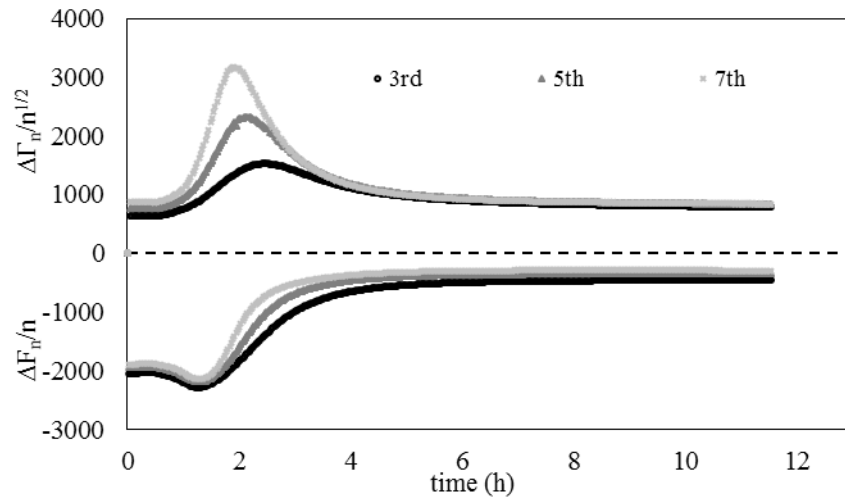


Figure 100. Changes in frequency and bandwidth, as a function experimental run time, for the asphaltenic deposit dissolution by continuous toluene injection into pure *n*-heptane. Circles (black), squares and crosses (light gray) standing for 3<sup>rd</sup>, 5<sup>th</sup> and 7<sup>th</sup> overtones of resonance.

#### 4.2.10 Crude oil titration with an asphaltene non solvent at higher temperatures: $\Delta\Gamma$ interpretation

The evaluation of the temperature on asphaltene destabilization and more importantly the deposition phenomena at atmospheric pressure is perhaps a suitable starting point in order to begin to interpret experiments with recombined and live oils which are normally at higher temperatures. The ultimate goal is to interpret processes occurring at high pressure (Figure 1). However, the available high pressure techniques to evaluate deposition, and give support to the interpretations made with the use of quartz crystal resonators, are far less abundant than the characterizing techniques at atmospheric pressure. The other difference within the asphaltene destabilization at high pressure and the experiments at atmospheric pressure is that the asphaltene destabilization at high pressure (recombined and live oils) are induced by lighter *n*-

alkanes (<C7). For instance, the injection of n-pentane gave rise to significant deposit energy dissipation which is perhaps a result of the deposit being enriched in resins, which are softer than asphaltenes, and thus, more viscoelastic. The role of gaseous or supercritical asphaltene precipitants on heavy organic material deposition from the crude oil may also be a challenge on the correct interpretation of changes in frequency and dissipation data when the crude oil is destabilized. Some spectroscopy and optical techniques, as Surface Plasmon Resonance and Infra-red Microscopy may be applied successfully in order to arrive to a correct interpretation of the deposition profile as it appears from the perspective of the frequency and bandwidth changes. As many of the techniques to analyze high pressure deposition *in situ* are still in development, the adopted strategy was to analyze first the temperature effect.

Crude oil C and D were titrated with n-heptane at different temperatures (25, 35, 45 and 55 °C) and the quartz crystal resonance frequency and bandwidth changes were recorded. At higher temperatures, bandwidth changes were considerably higher than the ones obtained within experiments at atmospheric pressure. This fact prohibits to some extent the interpretation of frequency data, without having more information on deposit configuration. Thus, in the following analysis only changes in bandwidth were qualitatively described.

As the experiments at higher pressure gave rise to a significant energy dissipation, the change in frequency was used only to evaluate the onset of asphaltene destabilization. The change in bandwidth profile for the crude oil C titration with n-heptane at 25, 35, 45 and 55 °C is shown in Figure 101.

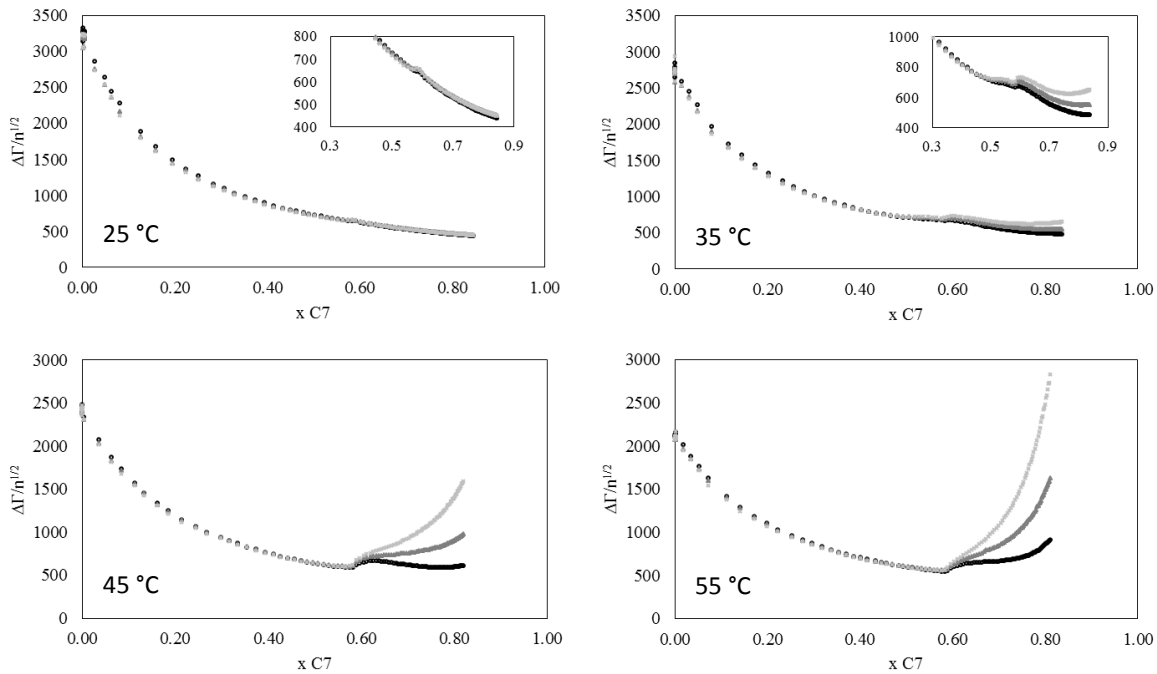


Figure 101. Bandwidth changes for the crude oil C titration with n-heptane at different temperatures. Circles (black), squares and crosses (light gray) standing for 3<sup>rd</sup>, 5<sup>th</sup> and 7<sup>th</sup> overtones of resonance respectively.

At higher temperatures the asphaltene deposition give rise to systematically higher energy dissipation and inter-harmonic spreading with increasing n-heptane content, with no plateau achieved before the end of the titration at  $x_{C7} \approx 0.8$ . In fact, what can be observed is that the fore mentioned minimum in bandwidth and its further increase which was pointed out to be independent on n-heptane content is approaching the first maximum in bandwidth with a fusion of both effects. The bandwidth increase is more pronounced for the 7<sup>th</sup> harmonic with the smallest shear wave penetration depth.

At 25 °C, for the majority of the studied crude oils, the increase of the bandwidth at higher n-heptane content observed to be linearly dependent on time and was mainly assigned to the deposition of particles in the micrometer range giving rise to significant interface roughness, thus yielding increasing bandwidth and bandwidths spreading. The concomitant deposition of particles

in the nanometer range and in the micrometer range are inducing different bandwidths profiles and the effect of both may be decoupled to some extent. In order to further evaluate the temperature influence on asphaltene deposit buildup the bandwidths changes are shown as a function of experimental runtime in Figure 102.

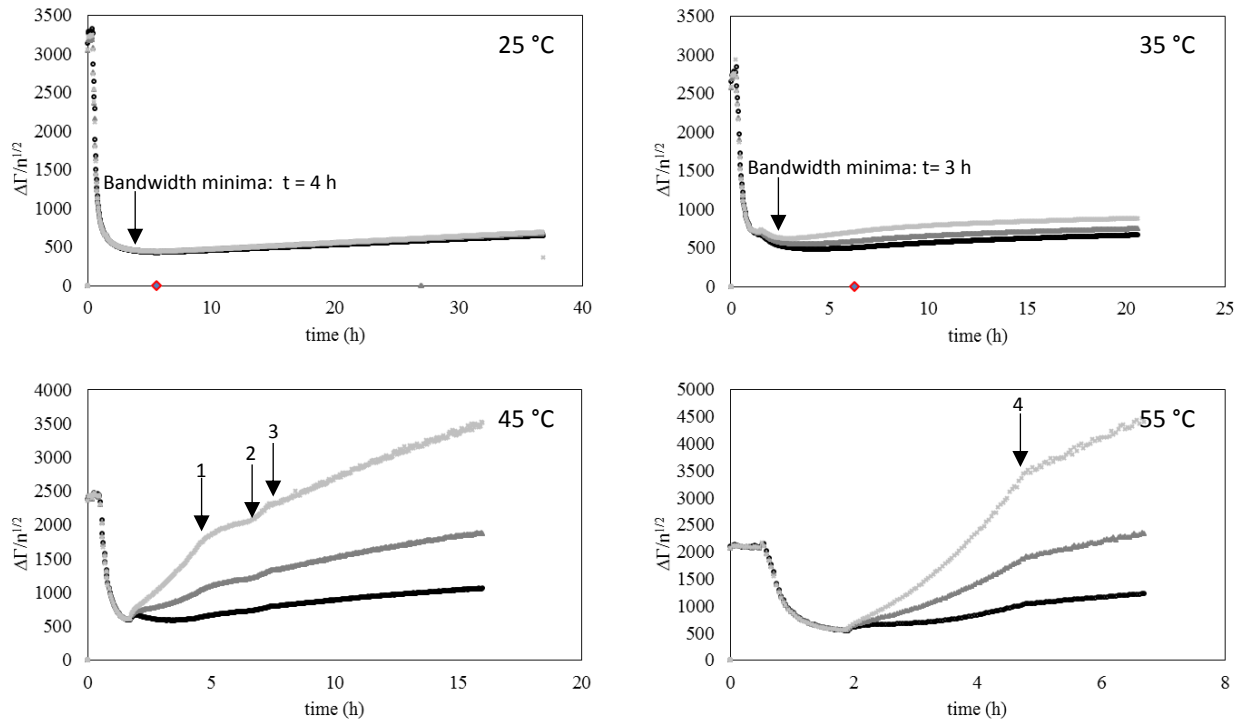


Figure 102. Bandwidths profiles as a function of experimental run time for the titration of crude oil C with heptane at different temperatures. Arrows: (1) n-heptane stop injection; (2) n-heptane injection re-start; (3) and (4) n-heptane injection and system agitation are stopped. Circles (black), squares and crosses (light gray) standing for 3<sup>rd</sup>, 5<sup>th</sup> and 7<sup>th</sup> overtones of resonance respectively.

With increasing temperature, the rate of increase from the bandwidths at longer times, after the onset has been reached, also accelerates. Also the inter-harmonic spreading is significantly higher the higher the temperature indicating a possible heterogeneous deposit. At 25 °C it was mentioned that the bandwidth attains a minimum before starting rising linearly with time. Such rise was observed to be related to the system agitation and thus probably to the deposition of

micrometer sized asphaltene flocs. In addition, at 25 °C the following rise in bandwidth was observed not to be dependent on system composition in n-heptane, as no break in the bandwidths profile is observed when titration stops (red diamonds in Figure 102 – 25 and 35 °C). The titration at 35 °C accuses a bandwidth minimum appearing much before in the titration. At 45 °C and 55 °C, no bandwidth minimum is observed and the steep rise in bandwidth is now observed to be dependent on system composition, or solubility towards asphaltenes and agitation. This is schematically shown in the case of the titration at 45 °C: at the point 1 injection was stopped and the bandwidth profile is observed to increase in a smaller rate; at point 2 the n-heptane injection is re-started and the bandwidth is found to regain its rate of increase and at point 3 the injection and the agitation is stopped and a rate of increase in bandwidth is diminished but maintains constant until the end of the experiment. At 55 °C, point 4 indicates when the system agitation and also the n-heptane injection is stopped, with a clear dependence of the deposition profile in this region within system agitation. At 55 °C, the increase in bandwidth before the end of the n-heptane injection do not present a constant rate increase with time, assuming higher values at higher n-heptane concentrations.

The effects observed with the temperature increase are then hypothesized of arising from two concurrent effects: i. the asphaltene destabilization at the nanometer level contributing to the formation of a smooth deposit which may present higher viscoelasticity; ii. The deposition of flocs at comparable or greater sizes than the shear wave penetration depth giving rise to a porous and rough deposit and thus yielding dissipative effects. Considering such an approach to the system interpretation the remarkable occurring phenomena within such experiment is the apparent

higher deposition propensity of the particles greater than the shear wave penetration depth at higher temperatures.

The analysis of the temperature influence on asphaltenes deposition as perceived by bandwidth data for crude oil D is shown in Figure 103. Four different temperatures were evaluated, 25, 35, 45 and 55 °C, the results in bandwidths are shown as a function of experimental run time.

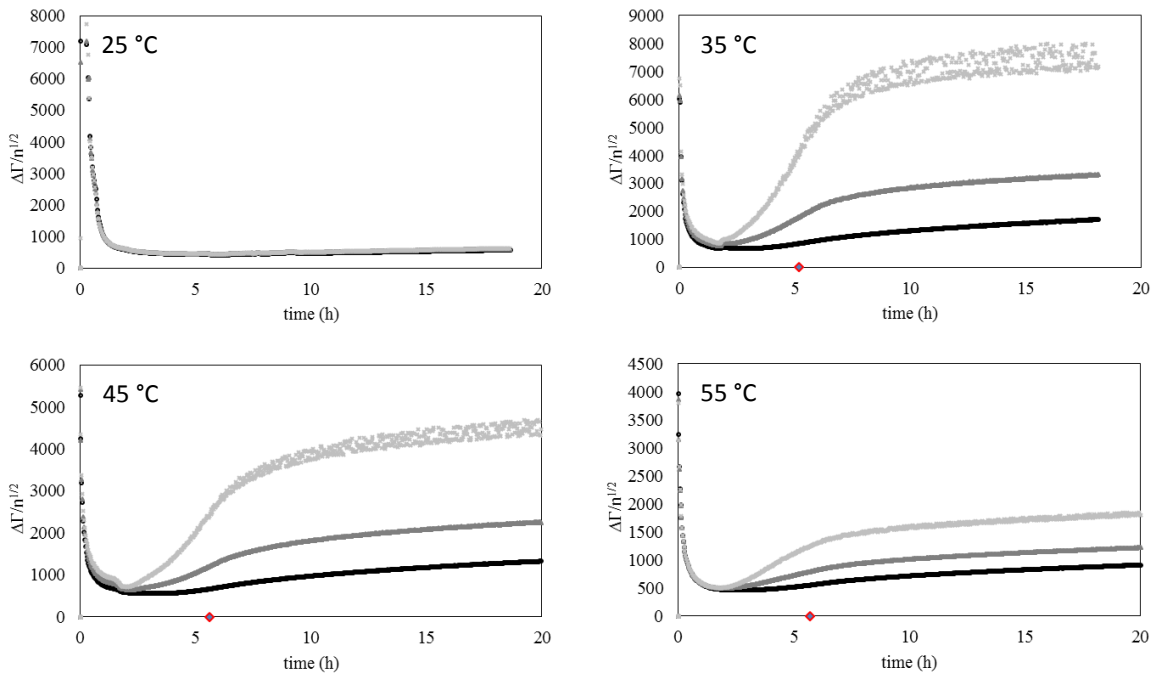


Figure 103. Change in bandwidth as a function of experimental run time for crude oil D titrated with n-heptane at various temperatures. Circles (black), squares and crosses (light gray) standing for 3<sup>rd</sup>, 5<sup>th</sup> and 7<sup>th</sup> overtones of resonance. Red diamonds: n-heptane injection stop.

The increase in bandwidth profile at longer times is shown to pass through maximum around 35 °C, decreasing with increasing temperature. The bandwidth profile is also observed to be dependent on system composition in n-heptane as it is observed that at the end of the n-heptane injection there is a change in the bandwidth profile with time. The system was agitated until the

end of the experiment, thus the agitation influence on the constant rise in the bandwidth profile with time after the end of the n-heptane injection was not evaluated.

Crude oil C and D display clearly different bandwidths profiles changes as a function of experimental temperature. Many interpretations may be posed, as still the knowledge of such systems is in its infancy. The hypothesis that upon temperature increase bigger flocs are somehow more prone to deposit is one of the interpretation which requires further investigation. Another interpretation may be based on the possible deposit physical change with consolidation and micro fracturing due to the known brittleness of the asphaltic material (Figure 133-VII). However, the cited microscopy, presented on Figure 133-VII, was performed after cleaning the deposit with n-heptane and the observed cracks are mostly coming from the drying effects once the n-heptane is evaporated. The resolubilization of materials composing the deposit at higher n-heptane content and higher temperatures could also play a role. The simply increase in the quantity of destabilized asphaltene could be another explanation, although some studies points out for the decrease in asphaltene yield at higher temperatures and not the contrary<sup>214</sup>.

At the end of the experiment with crude oil D at 45 °C (Figure 103) the quartz was taken out of the mixing vessel, cleaned and re-submerged in the precipitated asphaltene solution for 4 hours to check how the bandwidth would evolve with the possible deposition of micrometer sized particles. The normalized bandwidths as well as the normalized frequencies are shown in Figure 104. It is observed that besides deposition is occurring, as shown by  $\Delta F_n$  data, bandwidth data present only a minor increase, with a parallel increase in inter-harmonic spreading. Such fact could be an indication that the high bandwidth profiles, at higher temperatures, are actually arising from deposit restructuration of disintegration (appearance of fractures).

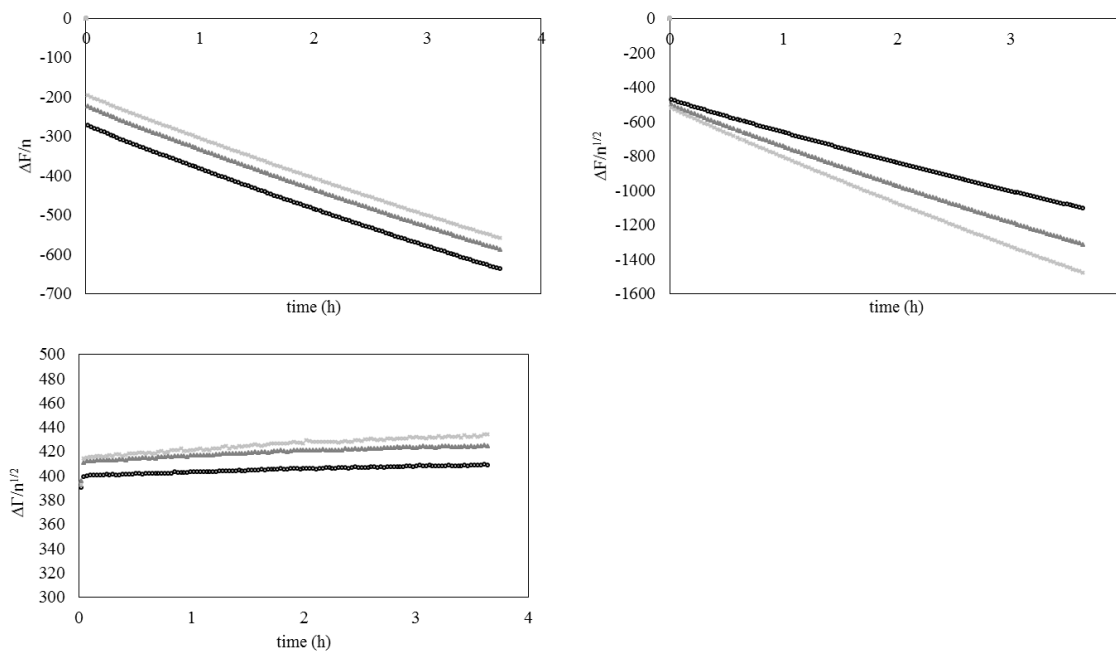


Figure 104.  $\Delta F$  and  $\Delta\Gamma$  for a clean quartz crystal immersed in precipitated asphaltenes at 45 °C. Circles (black), squares and crosses (light gray) standing for 3<sup>rd</sup>, 5<sup>th</sup> and 7<sup>th</sup> overtones of resonance.

The significantly different bandwidths profiles for the asphaltenes deposition at higher temperatures is an indication of how asphaltene deposition may be crude oil specific. This in no means an impediment for the quartz crystal resonator to be applied in order to interpret such systems. In fact, what is focused in this thesis is the possible interpretations of many occurring processes as an intent of classifying and categorizing the many possible cases. With the increase in our expertise, a pool of knowledge may be build where specific asphaltenes more prone or less prone to deposition under various circumstances can be detected by the quartz crystal resonator.

#### 4.2.11 Diluted crude oil and extracted asphaltenes destabilization and deposition

To gain greater insight on asphaltene deposition processes we probed two other systems: crude oil diluted with toluene and solutions of extracted asphaltenes in toluene. Crude oil dilution for probing asphaltene destabilization onset is already used in some techniques. With the quartz, besides the onset conditions, the interpretation of deposition phenomenon was researched. As

the great majority of the studies related to asphaltenes, especially particle sizes determinations, was done with solutions of extracted asphaltenes in toluene it was also of our interest to research on such a systems and compare with what is occurring when using the whole crude oil.

In order to probe the effect of crude oil dilution and the use of extracted asphaltenes in toluene two solutions were prepared: 1. Crude oil C was diluted with toluene until a concentration on asphaltenes reached 10 g/L and 2. An n-heptane extracted asphaltene solution from crude oil C was prepared at the same asphaltene concentration of 10 g/L. Figure 105 brings the frequency and bandwidth profile when such systems were destabilized at 25 °C by a continuous n-heptane injection. The change in resonance frequency is shown as a function of the square root of harmonic number for the detection of onset conditions by the inter-harmonic spread increase.

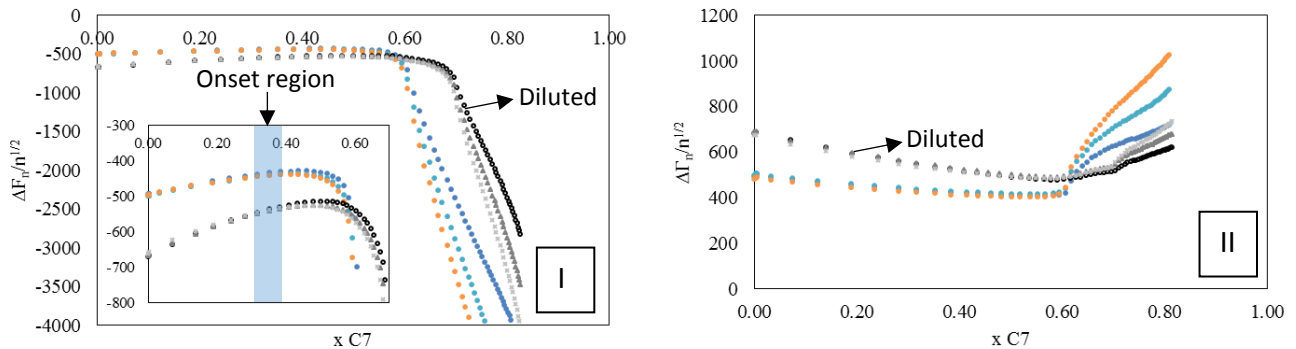


Figure 105. Comparison between changes in resonance frequency (I) and bandwidth (II) for the asphaltene precipitation from a diluted crude oil C and a solution of extracted asphaltenes (from crude oil C) in toluene. The asphaltene concentration in both experiments was 10 g/L.

The analysis of the frequency profile shows an onset of asphaltene destabilization, detected here as an spreading of the inter-harmonics, around  $x_{C7} = 0.4$  for both cases, extracted asphaltenes and diluted crude oil (inset on Figure 110-I). The onset obtained when fitting the mixing rule is shown in Figure 111.

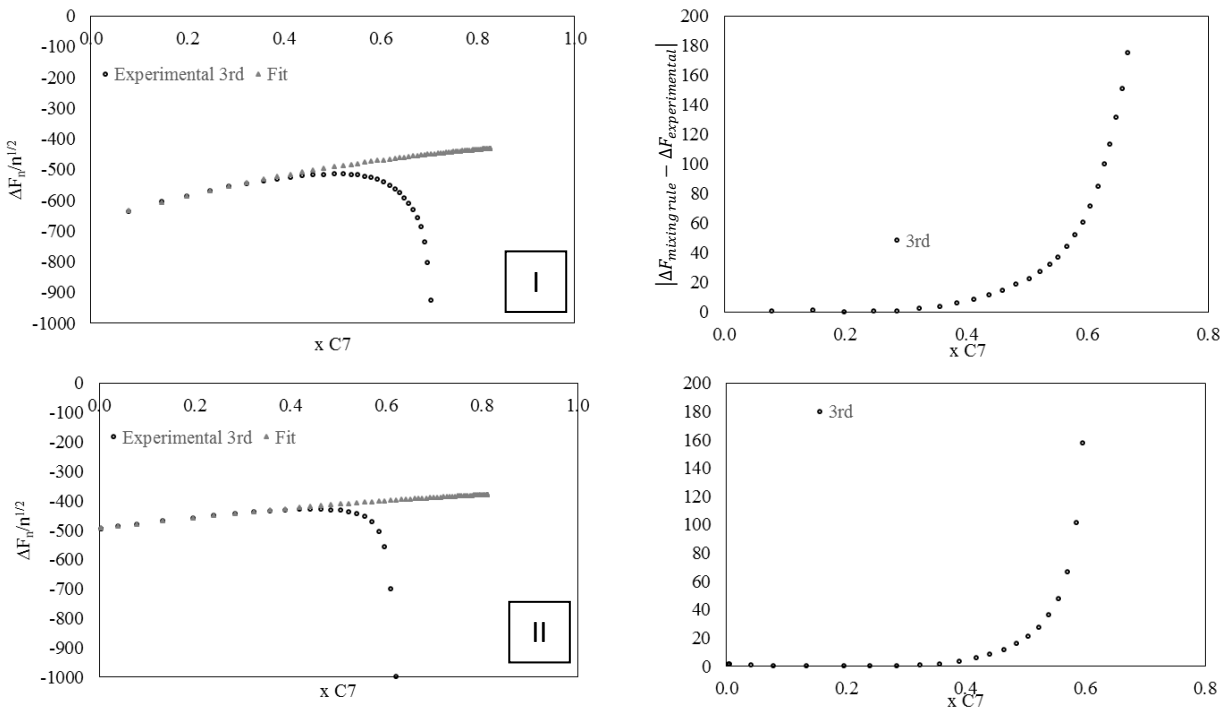


Figure 106. Onset determination for the case of diluted crude oil (I) and extracted asphaltenes (II) by the fitting and optimizing a dilution mixing rule to the same *n*-heptane mass fraction range (from  $x_{hep}=0.02$  to  $x_{hep} = 0.28$ ).

It can be observed that with the use of such a method, the onset in the case of a solution of extracted asphaltenes appears before when compared to the diluted crude oil. The derivative analysis is shown in Figure 107.

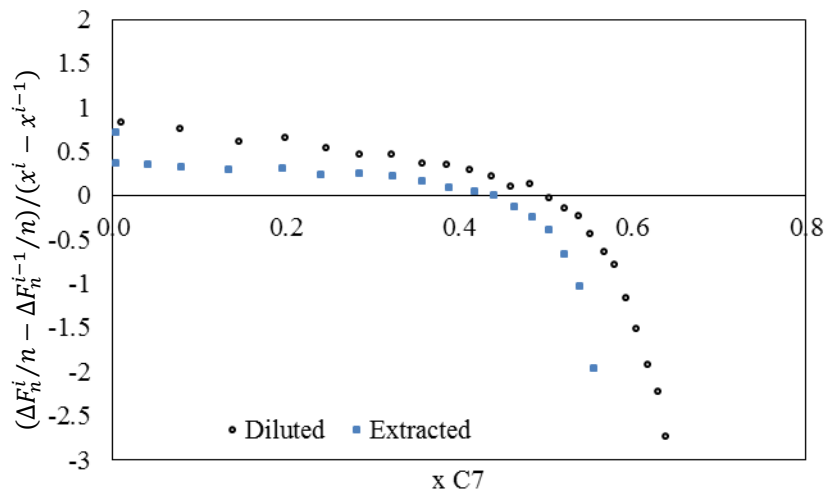


Figure 107. Derivative of frequency as a function of *n*-heptane mass fraction for the continuous destabilization of asphaltenes from diluted crude oil (oil C) and from a solution of extracted asphaltenes in toluene. Initial asphaltene concentrations: 10 g/L. Experiments performed at 25 °C.

When analyzing the derivative the onset of extracted asphaltene destabilization seems to be occurring within smaller n-heptane mass fractions than the one obtained with the use of the whole crude oil. Although some divergences are observed between the onset determination methods, the onset is observed to be occurring from  $x_{C7} = 0.3$  to  $x_{C7} = 0.4$ . The rather low bandwidth variation within such n-heptane mass fractions (Figure 105) points out for the very elastic nature of this first deposit layer as well as for the unreliable character of the use of the bandwidth profile to detect onset conditions. The destabilization of dilute crude oil presented a bandwidth increase smaller than the observed for extracted asphaltenes. The bandwidth profile for both experiments are observed to differ considerably within n-heptane mass fractions greater than  $x_{C7} = 0.6$ . From  $x_{C7} = 0.3$  to  $x_{C7} = 0.4$  the onset of asphaltene destabilization is hardly accused (Figure 108).

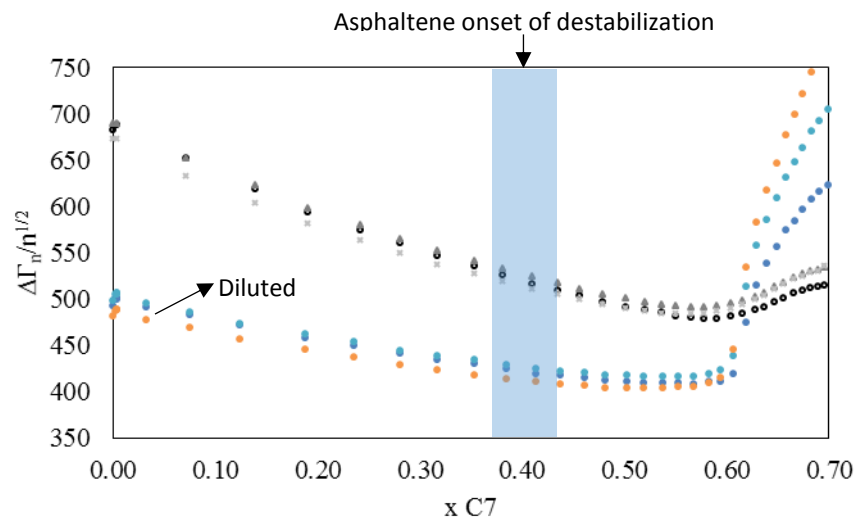


Figure 108. Bandwidths profiles for the asphaltene destabilization from diluted and extracted asphaltenes, both solutions were utilized with 10 g/L of asphaltenes. The onset of destabilization is observed to be occurring from  $x_{C7} = 0.3$  to  $x_{C7} = 0.4$  (from  $\Delta F$  data) and is hardly accused by the bandwidth profile, despite the low system viscosities.

At  $x_{C7} = 0.6$  the bandwidth profile for extracted asphaltenes strongly increases, until the end of the n-heptane injection. The bandwidth profile for the case of extracted asphaltenes present two regions after  $x_{C7} = 0.6$ . From  $x_{C7} = 0.6$  to  $x_{C7} = 0.7$  the bandwidth rises without presenting considerable inter-harmonic spreading and from  $x_{C7} = 0.7$  to the end of the n-heptane injection presents a higher rate of increase and the harmonics start to diverge (Figure 105-II).

An asphaltene solution of 10 g/L in toluene was prepared from the asphaltenes extracted from crude oil A. The resonance frequency and bandwidth profiles for the continuous n-heptane injection into such a solution are shown in Figure 109 and 110.

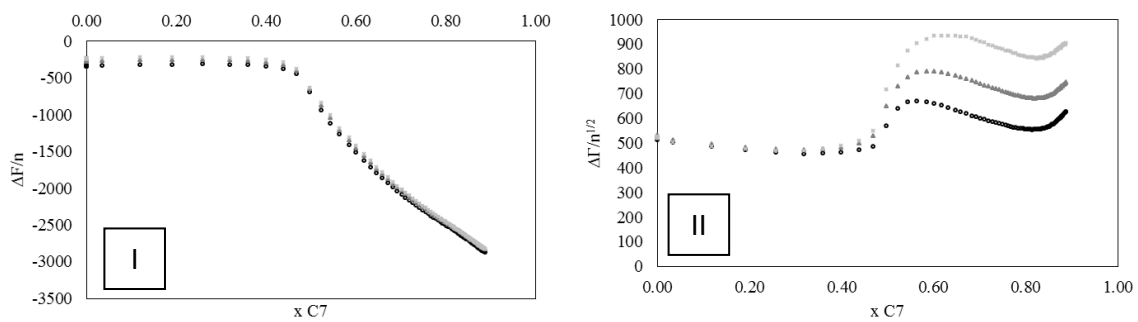


Figure 109. Response in the change in resonance frequency (I) and bandwidth (II) as a function of n-heptane mass fraction for the destabilization of extracted asphaltenes (crude oil A) in toluene (asphaltene concentration: 10 g/L). Circles (black), squares and crosses (light gray) standing for 3<sup>rd</sup>, 5<sup>th</sup> and 7<sup>th</sup> overtones of resonance respectively.

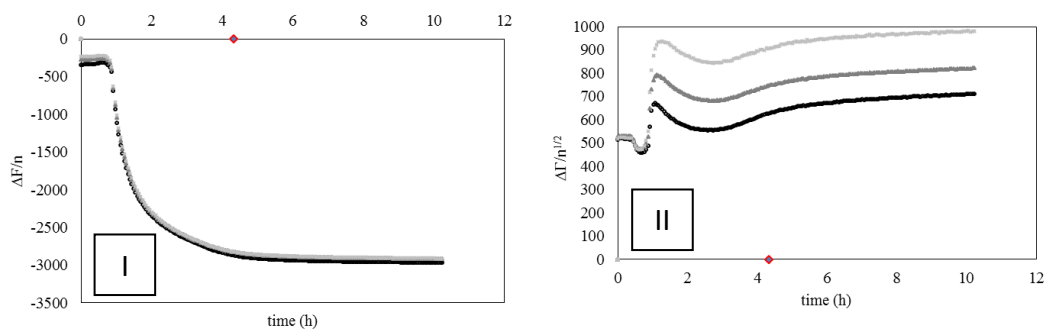


Figure 110. Response in the change in resonance frequency (I) and bandwidth (II) as a function of experimental run time for the destabilization of extracted asphaltenes (crude oil A) in toluene (asphaltene concentration: 10 g/L). Circles (black), squares and crosses (light gray) standing for 3<sup>rd</sup>, 5<sup>th</sup> and 7<sup>th</sup> overtones of resonance respectively. Red diamond: n-heptane injection stop.

The asphaltene destabilization from a solution of extracted asphaltenes from crude oil A give rise to a maximum in bandwidth data and a constant inter-harmonic spreading until the end of the experiment (Figure 109-II and Figure 110-II).

For checking the reproducibility of the experiments the same sample was probed after two days from the solution preparation. The results are shown in Figure 111. The aged asphaltene solution gave dissipation values slightly smaller than the freshly prepared solution. This indicates a possible role from asphaltenes particle sizes and asphaltenes resolubilization to the bandwidth profile. The onset of asphaltenes destabilization was observed to be invariable within the aging period. The onset of extracted asphaltenes from crude oil A is observed to occur at the same mass fractions as within the experiment with the whole crude oil (Figure 112).

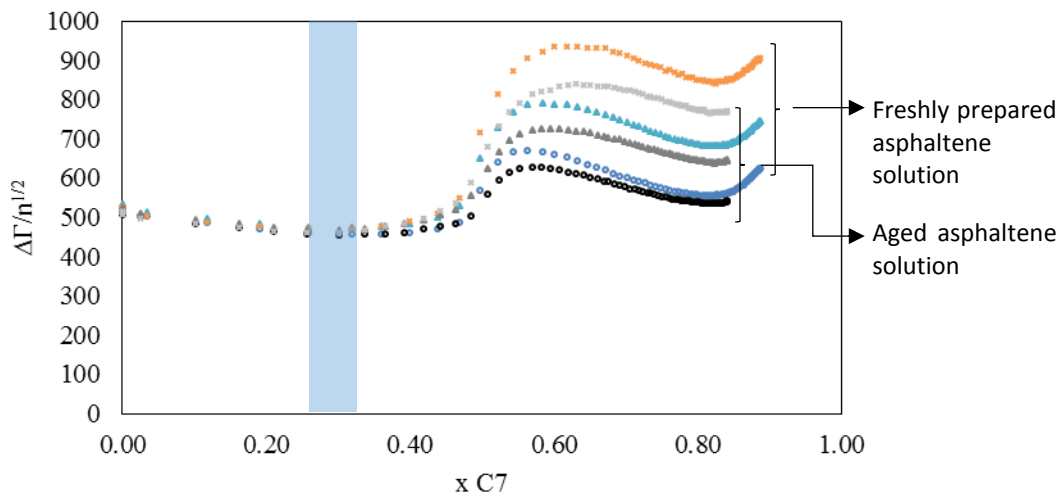


Figure 111. Freshly prepared and aged asphaltene solution effect on bandwidth profile. Circles, squares and crosses standing for 3<sup>rd</sup>, 5<sup>th</sup> and 7<sup>th</sup> overtones of resonance respectively. Blue rectangle: asphaltene onset of destabilization region.

#### 4.2.12 Bandwidth profiles obtained from crude oils and extracted asphaltenes

Figure 112 presents a comparison between the bandwidth data obtained by a continuous n-heptane titration of crude oil A, which has an asphaltene concentration of 116 g/L, and the n-heptane continuous injection into a solution of extracted asphaltenes (from crude oil A) with an asphaltene concentration of 10 g/L. The bandwidth profile from the asphaltene destabilization and deposition from the crude oil is observed to be rather low taken that its asphaltene concentration is more than ten times greater than the asphaltene solutions. The inter-harmonic spreading, indicating possible inhomogeneity is also much smaller for the destabilization of asphaltenes directly from crude oils.

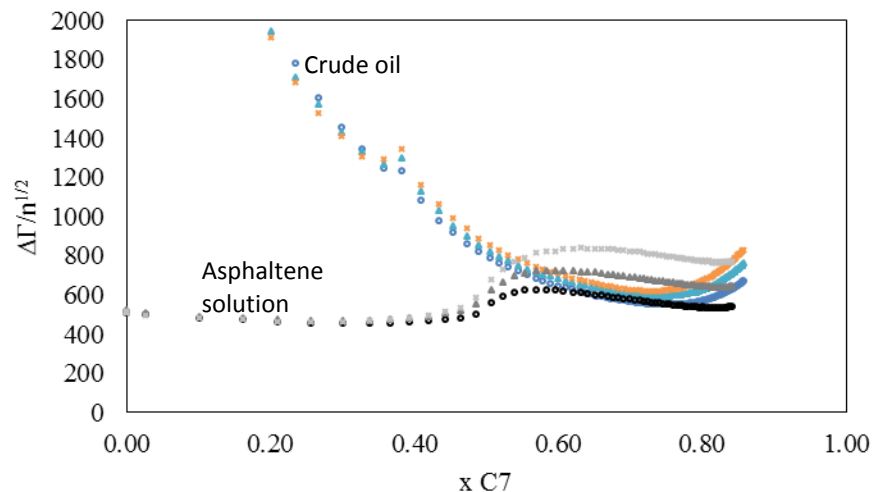


Figure 112. Comparison between bandwidth profiles for the asphaltene destabilization from crude oil A ( $C_{asp} = 116$  g/L) and from extracted asphaltenes (crude oil A) in toluene ( $C_{asp} = 10$  g/L). Circles, squares and crosses standing for 3<sup>rd</sup>, 5<sup>th</sup> and 7<sup>th</sup> overtones of resonance respectively. Initial masses of crude oil and asphaltene solution: 20 g.

In order to compare experiments with the same initial asphaltene concentration, an extracted asphaltene (from crude oil C) solution was prepared at  $C_{asp}^C = 31 \text{ g/L}$ , the same asphaltene concentration presented in the crude oil. The bandwidth profile from the destabilization of the asphaltene solution and the crude oil C by a continuous n-heptane injection is shown in Figure 113.

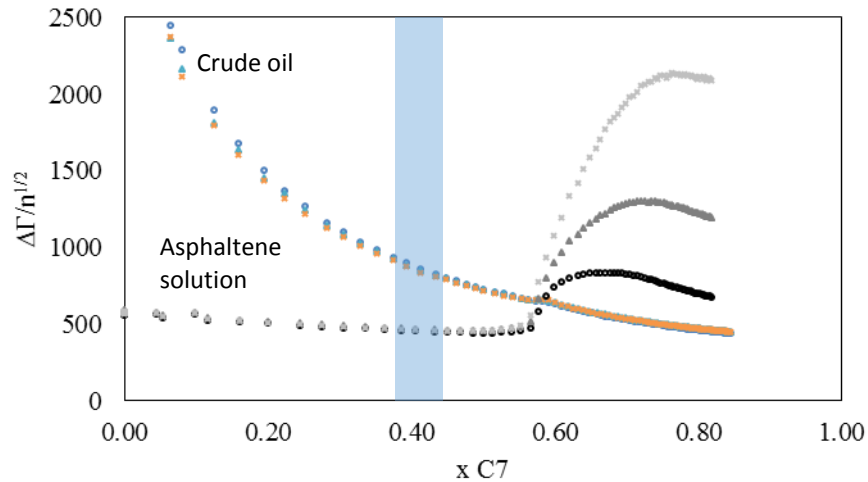


Figure 113. Comparison between bandwidth profiles from de continuous destabilization of crude oil and extracted asphaltenes with n-heptane injection. Blue rectangle: asphaltene destabilization region. Crude oil C and asphaltenes from crude oil C. 25 °C and atmospheric pressure.

As it is observed, the onset of asphaltenes destabilization as it was determined by changes in resonance frequency data to be around  $x_{C7}=0.45$  (blue rectangle in Figure 113) is hardly accused in both experiments, with the crude oil and with the concentrated asphaltene solution. The great difference between both experiments is the big bandwidth increase and its maxima appearing with the destabilization of extracted asphaltenes in toluene. As it was observed for the case of extracted asphaltenes of crude oil A at  $C_{asp}^A = 10 \text{ g/L}$  (Figure 111), the bandwidth profile attains a maximum value which is harmonic dependent. The maxima with the harmonic number is an indication that the maximum may be related to the lateral inhomogeneity and to the particles

attachment and movement on the electrode surface. As it was reviewed in section 2.4 of the present work, the deposition of colloidal particles give rise to a bandwidth maximum which is related to the surface coverage, particle geometry and movement. The difference in bandwidth profiles can be mostly related to the colloidal state of asphaltenes in each media and how deposition is proceeding in each case. At high concentrations in toluene, asphaltenes are known to be prone to form bigger aggregates would could deposit similarly to already mentioned reports on proteins and viruses, with colloidal sizes up to 120 nm. In the crude oil, even at high concentration asphaltenes may be present being a part of smaller aggregates, but also, the molecularly solubilized asphaltenes could play an important role on deposit formation in the case of the whole crude oil. The observed differences between both experiments have the potential of providing further understanding on asphaltene deposit formation in both media and link the experimental work done using model oils to the occurring phenomena in the crude oil.

In order to evaluate asphaltene concentration effects on bandwidth data a solution of extracted asphaltenes in toluene was prepared at 10 g/L and the continuous n-heptane injection was performed. Figure 114 brings the bandwidth profiles obtained when using asphaltene solution concentrations of 10 and 31 g/L.

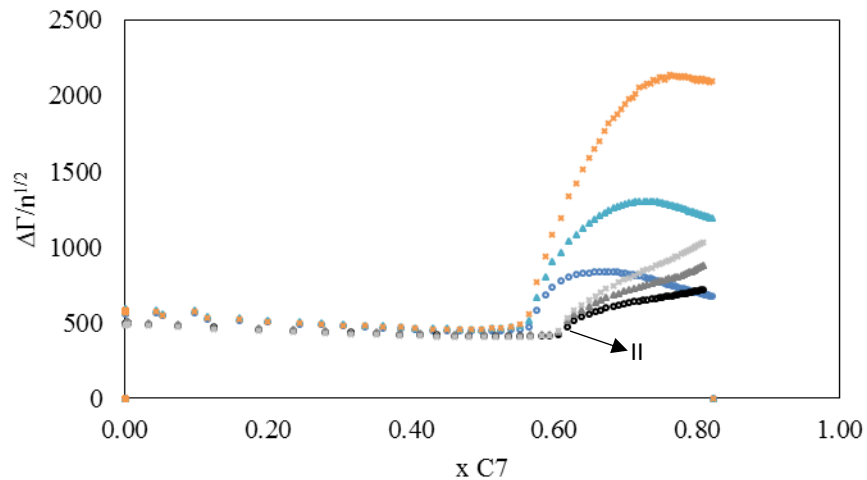


Figure 114. Extracted asphaltenes in toluene destabilization by continuous *n*-heptane injection at 25 °C. I.  $C_{asp}=31$  g/L and II.  $C_{asp}=10$  g/L. Crude oil C.

The decrease in asphaltene concentration induces a decrease in bandwidth profile as well as a delay on asphaltene onset of destabilization. No bandwidth maximum is observed at smaller concentration for the case of extracted asphaltenes of crude oil C at 10 g/L, contrary to what was observed in the case of extracted asphaltenes from crude oil A at the same concentrations in toluene (Figure 111).

#### 4.3 The use of production chemicals: onset and deposition assessment.

The use of asphaltene inhibitors and dispersants was done directly in the crude oil and the asphaltene destabilization was proceeded with the continuous *n*-heptane injection. A proprietary chemical asphaltene inhibitor, dodecylbenzenesulfonic acid and dodecanoic acid were tested. The concentrations ranged from 0.5 to 2 wt %. The chemicals were mixed with crude oil C at 60 °C. They were let under agitation at 60 °C for at least one hour. The samples were kept for at least 24 hours at ambient temperature before the experiments were done. All the experiments were performed at 25 °C and atmospheric pressure.

#### *4.3.1 Crude oil plus proprietary chemical*

Proprietary inhibitor was added to crude oil C until the desired inhibitor mass fractions of 0.5; 1 and 2 wt % were attained. The crude oils treated with the proprietary inhibitor were then submitted to a continuous n-heptane injection at 25 °C and atmospheric conditions. Figure 115 brings the change in resonance frequency normalized by harmonic number and the bandwidths normalized by the square root of the harmonic number for the titrations. The frequency and bandwidth profiles for n-heptane injection into crude oil without inhibitor is shown in Figure 115 as the blank experiment.

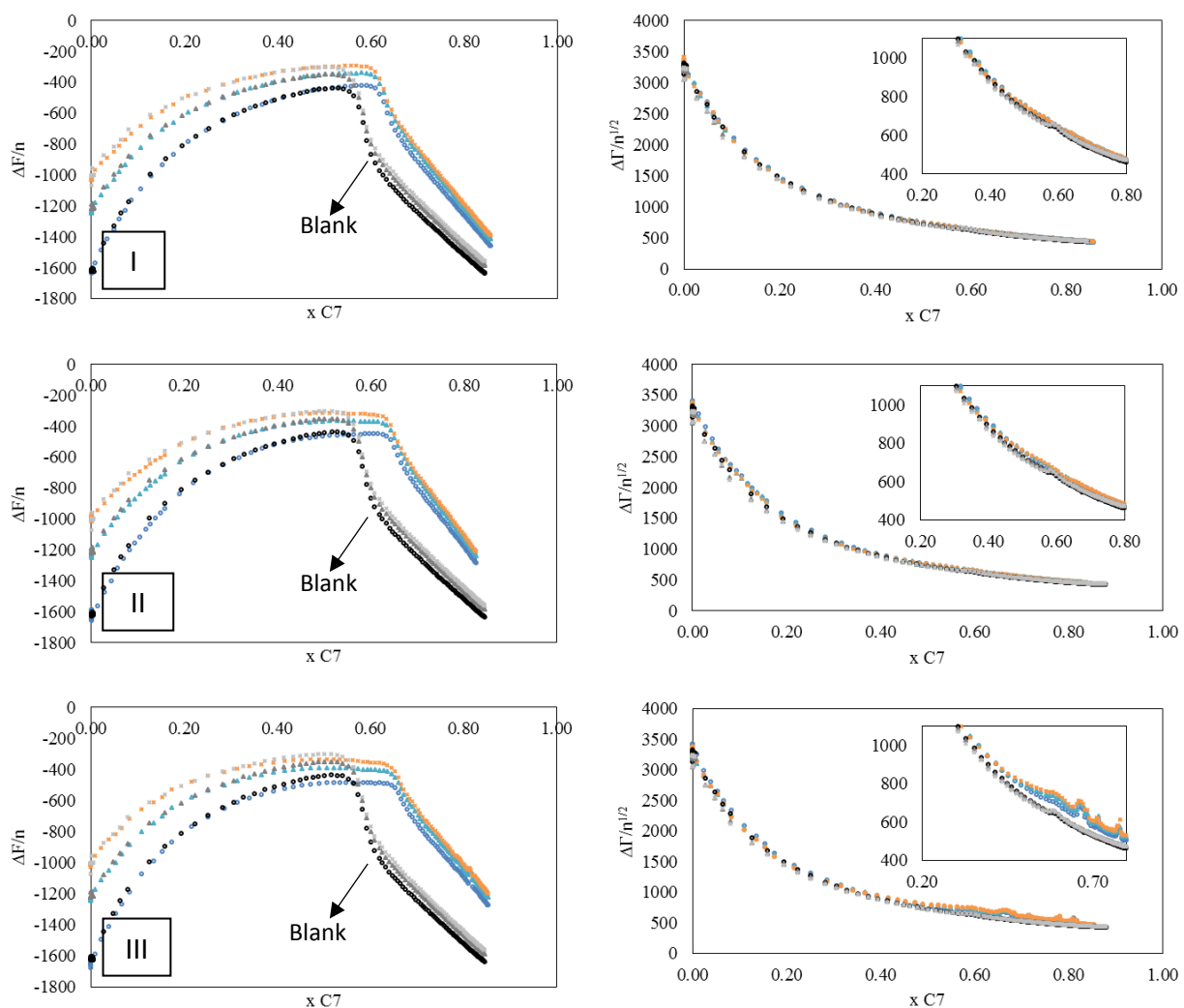


Figure 115.  $\Delta F/n$  and  $\Delta \Gamma/n^{1/2}$  profiles for the continuous titration of crude oil C with different concentration of commercial inhibitor. I (I) 0.5 wt %; (II) 1 wt % and (III) 2 wt % (colored point). The crude oil without inhibitor is shown as the blank experiment. Experiments performed at 25 °C and atmospheric conditions.

The bandwidth profiles (right column on Figure 115) are observed not to considerably change when using the proprietary inhibitor in comparison with the blank experiment. The same does not occur with the resonance frequency profile which is observed to vary when the inhibitor is used. With increasing inhibitor concentrations it is observed an increase in the n-heptane mass fraction needed to induce the first step change in resonance frequency change. This can be

clearly observed by the horizontal arrow in Figure 116 which brings the derivatives of the frequency changes relative to the n-heptane mass fraction for such experiments. Then dilution of crude oil C with toluene and cyclohexane are also added in Figure 116.

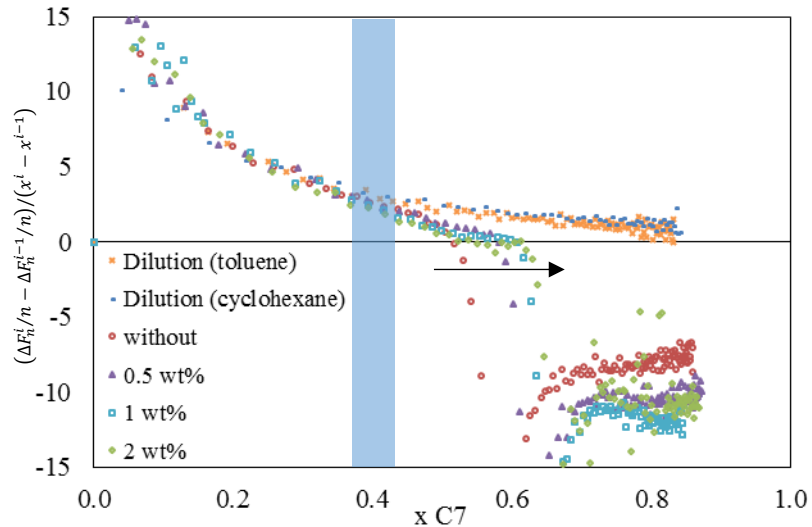


Figure 116. Derivative of frequency versus n-heptane mass fraction for the continuous n-heptane injection into crude oil C treated or not with proprietary inhibitor. The derivatives from the dilution experiments (with cyclohexane and toluene) are also added. The horizontal arrow indicates the increase in the delay of the first steep decrease in resonance frequency change which is higher the higher the inhibitor concentration. Blue rectangle: onset of asphaltene destabilization region.

The blue rectangle in Figure 116 highlights that the onset of asphaltene destabilization may be not delayed by the use of this inhibitor. What is observed is a delay in the appearance of the first steep resonance frequency change, i. e., the sub region 3 as classified before (see. Figure 67). The delay being higher the higher the inhibitor concentration (horizontal arrow in Figure 116). The chemical may be acting inhibiting the massive asphaltene destabilization but it is observed to be somewhat ineffective towards the stabilization of the most unstable asphaltenes. Figure 117 brings the calculated deposit thickness for the experiments shown in Figure 115.

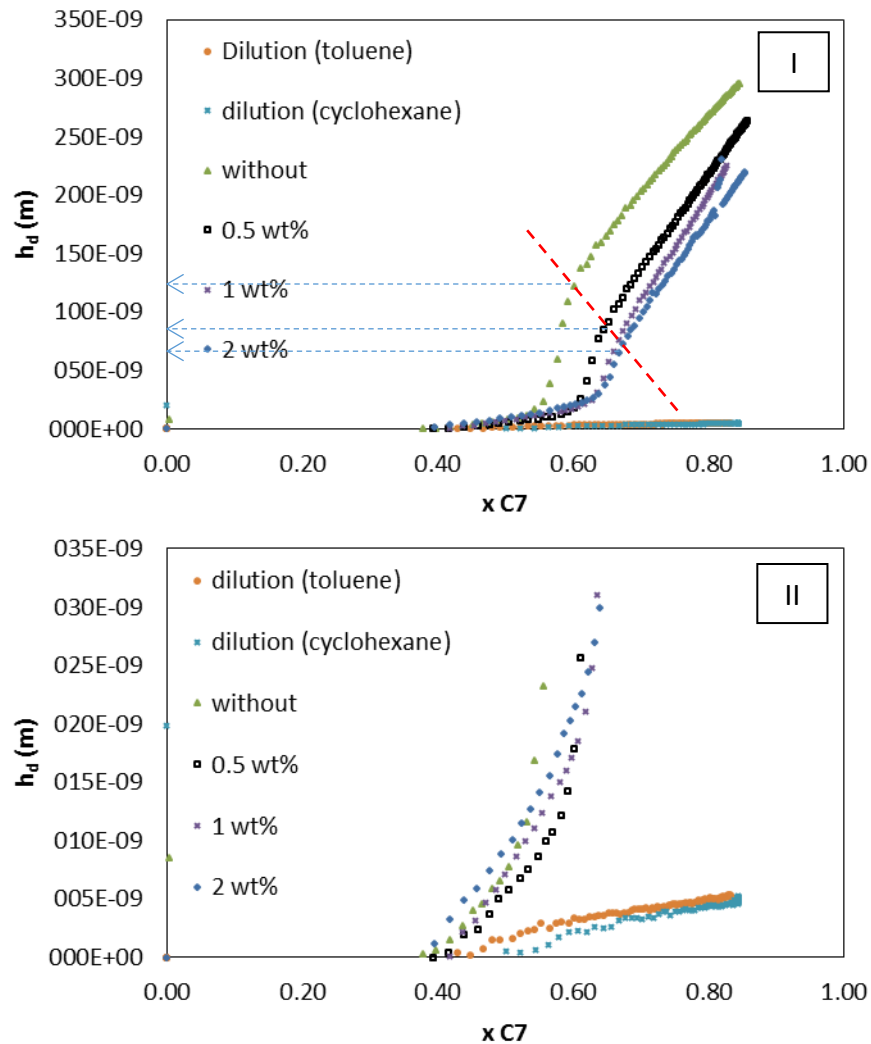


Figure 117. Deposit thicknesses obtained by the continuous *n*-heptane injection into crude oil C, with or without proprietary chemical inhibitor. The thicknesses obtained with the dilution (toluene and cyclohexane) experiments are also added. Horizontal arrows in (I) indicates the decrease in the thickness of the deposited layer. (II) Magnification of the region where the precipitation experiments diverges from the dilution experiments.

It can be observed that the use of such inhibitor may decrease the obtained deposit thicknesses. Moreover, the thickness of the asphaltenic deposit at the sub region 3 is also significantly reduced as it is shown by the horizontal arrows in Figure 117-I. Figure 117-II enlarges the region in which the precipitation experiment diverges from the pure crude oil dilution.

### 4.3.2 Crude oil plus Dodecylbenzenesulfonic acid (DBSA)

Crude oil C was mixed with DBSA at 0.5; 1 and 2.5 wt % and submitted to a continuous n-heptane injection. The change in frequency and bandwidth profiles for the three DBSA concentrations in crude oil C as well as for the case of the crude oil without DBSA is shown on Figure 118.

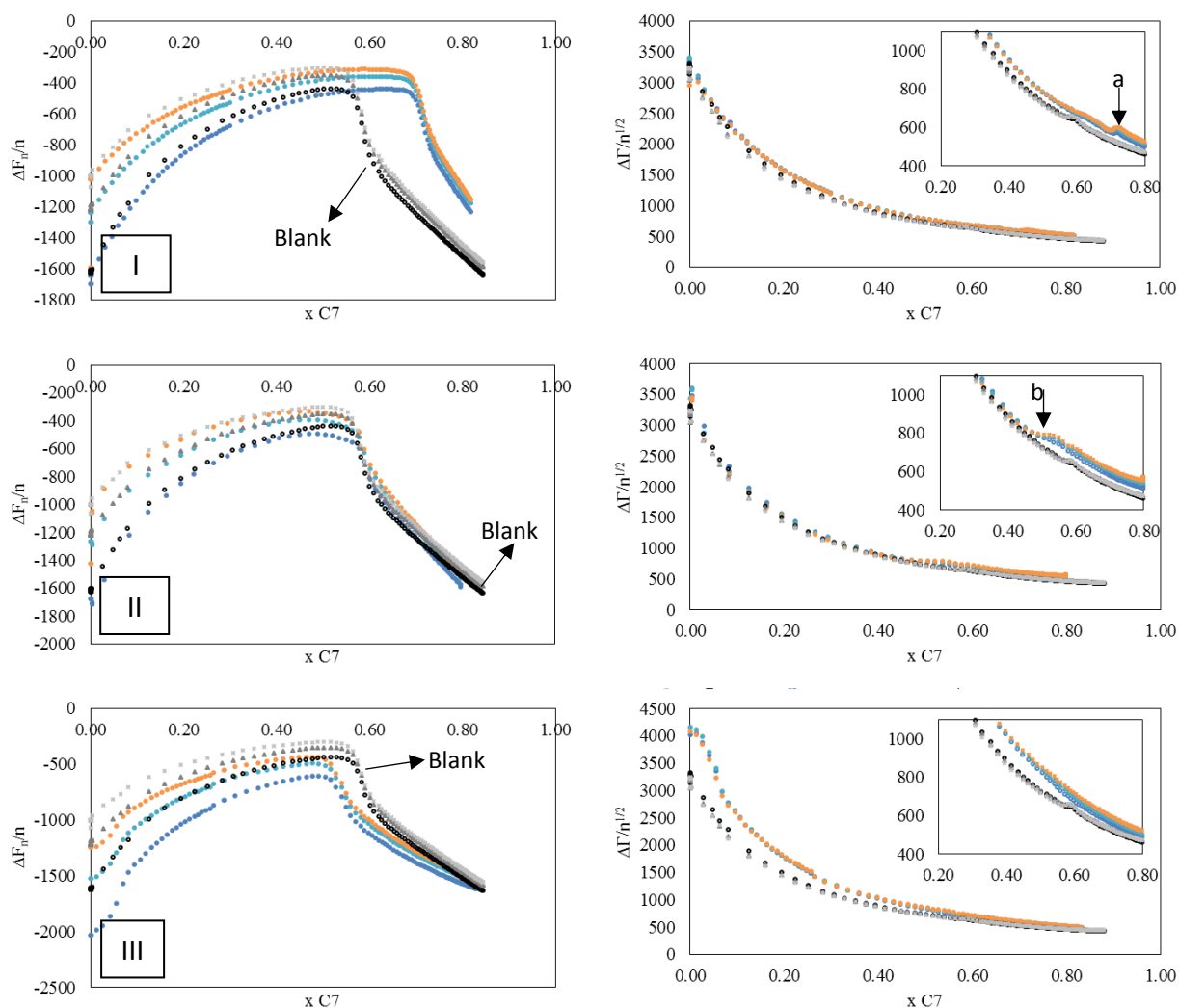


Figure 118.  $\Delta F/n$  and  $\Delta \Gamma/n^{1/2}$  profiles for the continuous titration of crude oil C with different concentration of DBSA (colored points). I. 0.5 wt %; II. 1 wt % and III. 2.5 wt %. The crude oil without DBSA is indicated as the blank experiment.

Figure 118 and the derivative analysis on Figure 119 show an apparent worsening on the onset of asphaltene destabilization for the crude oil doped with 2.5 wt % of DBSA (“1” in Figure 119). For the case of the utilization of DBSA at 1 wt % the onset seems to be invariable (“2” in Figure 119). For crude oil with 0.5 wt % DBSA the derivative shows that for the case of the first steep decrease in resonance frequency is significantly delayed to  $x_{C7} = 0.67$  against the  $x_{C7} = 0.50$  for the case of no use of DBSA (“3” in Figure 119). However the onset is observed to be at the same mass fractions was the one obtained without DBSA (“4” in Figure 119). Bandwidths profiles presented some differences for the cases when DBSA was utilized, such differences are shown in the insets of Figure 123. It can be observed that the first notable disturbance on the bandwidth profile arrived first, compared to the blank, when 1 wt % DBSA was used (“a” in Figure 118). When the crude oil was doped DBSA at 0.5 wt % such disturbance appeared before (“b” in Figure 118).

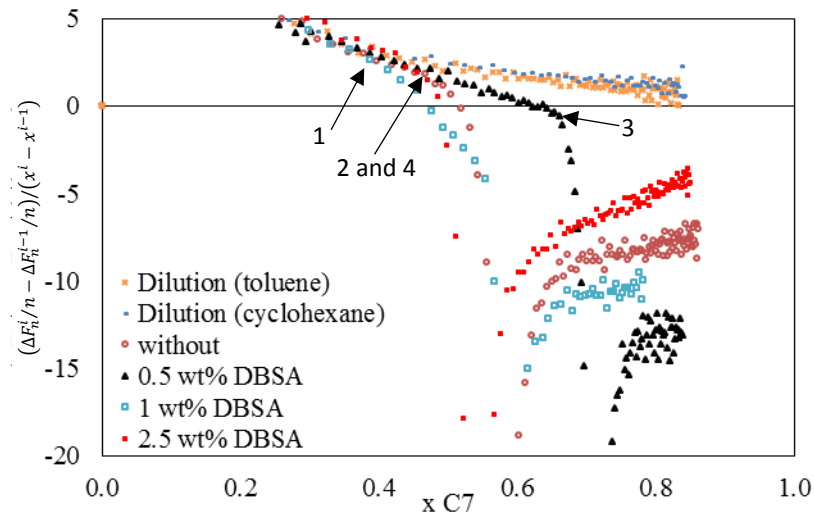


Figure 119. Derivative of frequency versus *n*-heptane mass fraction for the cases of crude oil C dilution and precipitation with the addition of DBSA at different concentrations.

Calculated deposit thicknesses are shown in Figure 120. The use of 2.5 wt % of DBSA yielded the thickest deposit with a reduction on deposit thickness when using crude oil with 0.5 wt % DBSA.

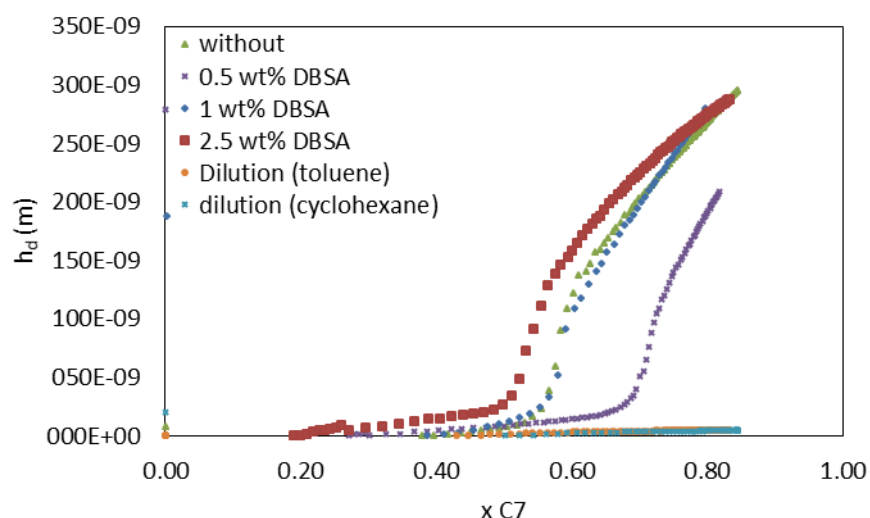


Figure 120. Deposit thicknesses obtained when crude oil C doped with different concentrations of DBSA is continuously titrated with *n*-heptane at 25 °C. Blank experiment is indicated as without in the legend on the graph.

The observed occurring effect of worsening on the asphaltene destabilization point and deposition was already reported in the literature. Goual<sup>215</sup> found a gradual increase in asphaltene precipitation amount when using 0.3, 0.5 and 1 wt % DBSA. Contrary to what we observe, Goual reports that the onset of asphaltene destabilization was shown to slightly increase in such a range. At higher DBSA concentrations (5 wt %) they observed a reduction in precipitated asphaltene amount with a significant increase in onset on asphaltene onset of destabilization. They pointed out for the possible role of non-negligible electrostatic interactions in relation to dispersion forces. Goual<sup>215</sup> also cites studies reporting positive<sup>216</sup> and negative<sup>217</sup> effects due to the use of DBSA towards asphaltenes destabilization and deposition. Wang<sup>218</sup> showed that DBSA has different stabilizing effects within asphaltenes coming from different oils. Wang found that the asphaltenes which were more stabilized by DBSA presented more acidic functions, and the asphaltenes which were indifferent to the treatment with DBSA were enriched in basic sites.

#### 4.3.3 Crude oil plus dodecanoic acid

Dodecanoic acid was utilized to evaluate the role of carboxylic functions on the asphaltene precipitation and deposition. Crude oil C was doped with dodecanoic acid at 2 wt %. The destabilization was done by continuously injecting n-heptane at 8 mg/s and 25 °C. The changes in resonance frequency and bandwidth for the experiment are shown in Figure 126. The experiment of the crude oil destabilization without inhibitor is also added in figure 121.

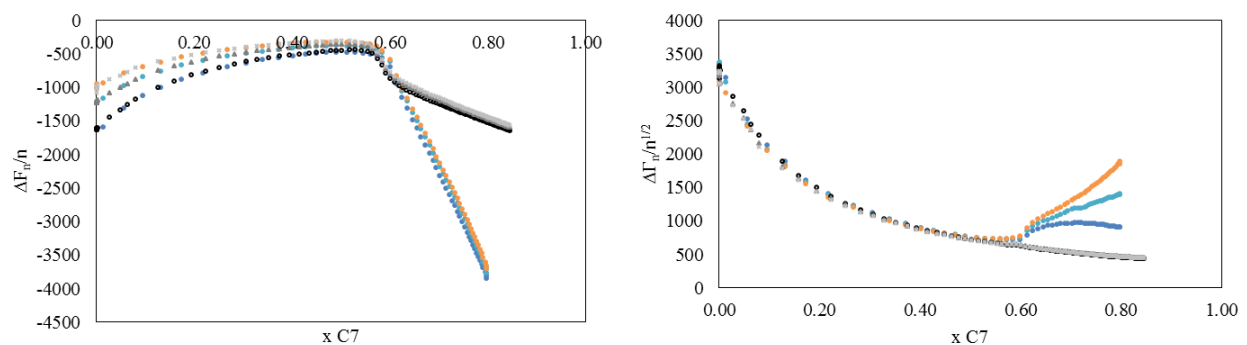


Figure 121. Change in resonance frequency and dissipation profile for the destabilization of asphaltenes from crude oil C doped with dodecanoic acid (2 wt %) (colored symbols) and the blank experiment.

It can be observed that the titration of crude oil C doped with dodecanoic give rise to a highly dissipative deposit mostly resembling the obtained cases with extracted asphaltenes (Figure 105). Figure 122 brings the derivative analysis for the change in frequency in relation to the n-heptane mass fraction.

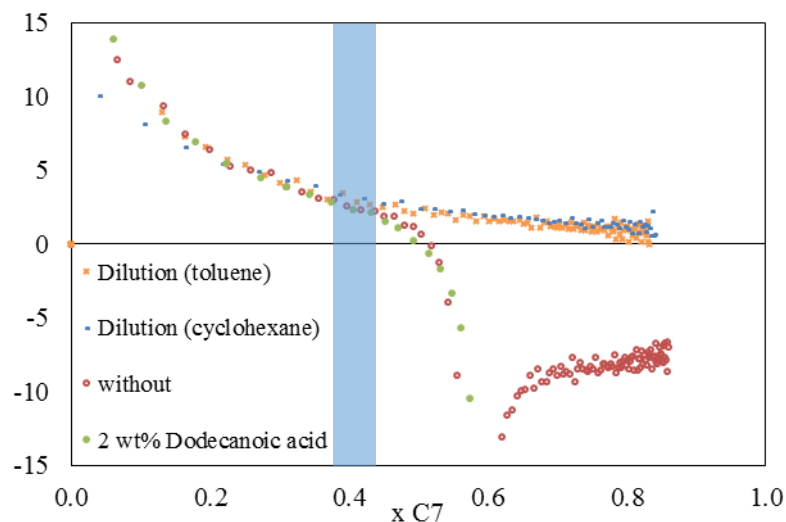


Figure 122. Derivative of frequency versus *n*-heptane mass fraction for the continuous injection of *n*-heptane into crude oil C doped with dodecanoic acid (2 wt %).

The onset of asphaltene destabilization is not shown to significantly change with the use of an organic carboxylic acid (blue rectangle in Figure 122). Because of the high bandwidth, the model calculated thickness is more than doubled (Figure 123). Naturally, under such high conditions of energy dissipation, and high inter-harmonic spreading, the model is far to be valid. Earlier in this work it was highlighted that the *n*-heptane stop injection and the slower rate of *n*-heptane injection would induce thicker deposits to be seen by the model, but the bandwidths observed at such cases were much weaker than ones obtained with dodecanoic acid. This was interpreted that the slowest asphaltene destabilization induces thicker deposits to be formed putting in evidence competitive aggregation and deposition processes.

It can be hypothesized that the use of dodecanoic acid induces great differences in the asphaltene deposit structure which can be intrinsically related to the interactions occurring between acid groups and the asphaltenes in the bulk yielding different structures which would display different deposition processes.

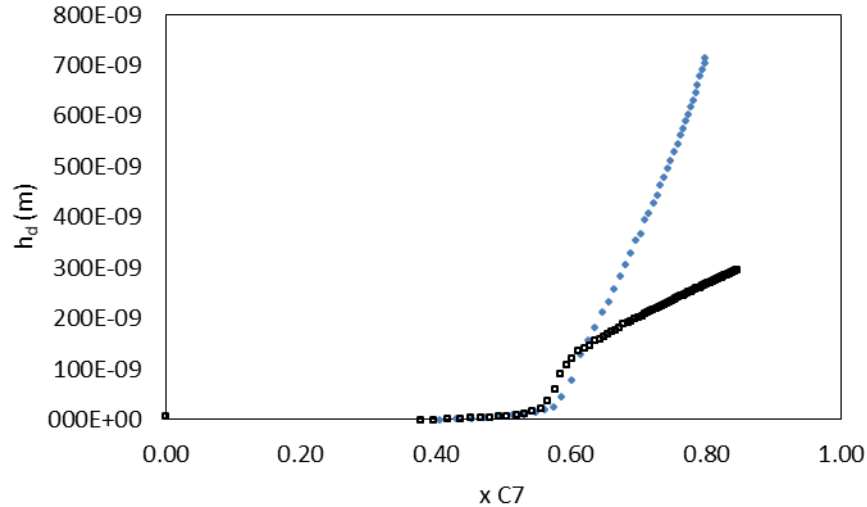


Figure 123. Model calculated deposit thickness for the destabilization of crude oil doped with dodecanoic acid (full diamonds) and for the crude oil C with no chemical (squares). The high bandwidth yielded by the crude oil destabilization in the presence of dodecanoic acid yield an estimated deposit thickness much greater than the ones obtained with the crude oil without the chemical.

#### 4.4 The step asphaltene destabilization

In crude oil production asphaltenes are destabilized under different processes. In the case of crude oil depressurization during production the gradual crude oil solubility change towards asphaltenes, at least before bubble point conditions, was simulated with a continuous n-heptane injection. The evaluation of asphaltenes deposition when a sudden solubility change is applied to crude oil may be the other situation where asphaltenes may pose significant challenges. Such conditions are encountered in manifolds, and other mixing fluid operations where solubility changes are rapidly imposed. Experiments were performed to prove the asphaltene destabilization from crude oils when a sudden, or step, n-heptane addition is done.

A step n-heptane injection to crude oil C was done bringing the mixture to the n-heptane mass fraction of  $x_{C7} = 0.86$ , thus above the onset of asphaltene destabilization. The frequency and bandwidth changes as a function of experimental runtime is shown in Figure 124.

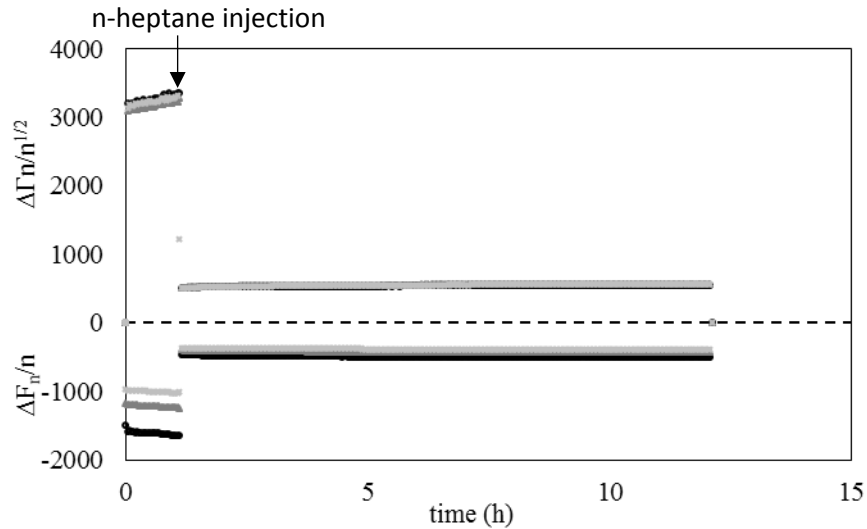


Figure 124. Step n-heptane injection into crude oil C to an n-heptane mass fraction of 0.86. Circles (black), squares and crosses (light gray) standing for 3<sup>rd</sup>, 5<sup>th</sup> and 7<sup>th</sup> overtones of resonance.

After a baseline collection, the n-heptane was injected at once in the mixing vessel (arrow in Figure 124), this caused a sudden decrease in the bandwidth profile and a sudden increase in the resonance frequency profile mainly due to the system viscosity decrease. After the n-heptane injection the resonance frequency and bandwidth profiles are present only small drifts which lasted until the end of the experiment, after 10 hours (Figure 125).

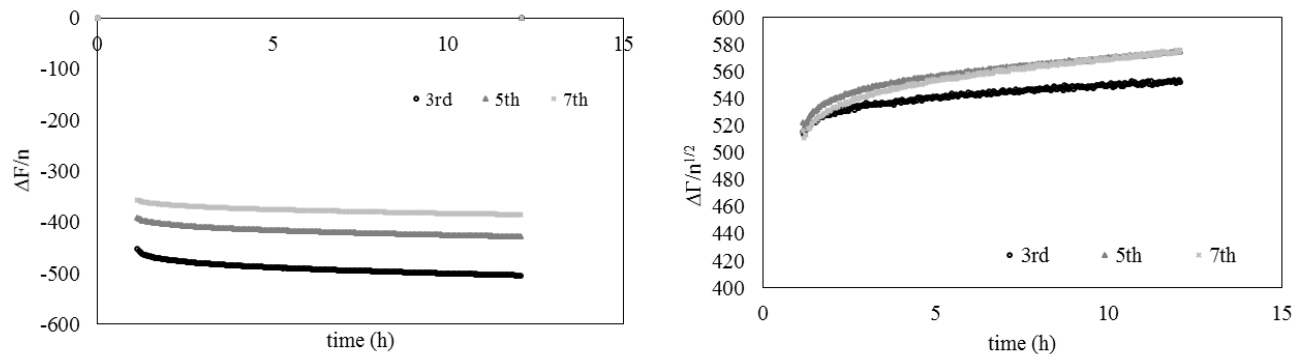


Figure 125. Zoom in the change in frequency and bandwidth data after the step *n*-heptane addition. Circles (black), squares and crosses (light gray) standing for 3<sup>rd</sup>, 5<sup>th</sup> and 7<sup>th</sup> overtones of resonance respectively.

The drifts were observed to be smaller than the ones obtained at the end of the continuous *n*-heptane injection experiments. Moreover, the frequency and bandwidths obtained after the step *n*-heptane addition approaches the signals obtained when a clean quartz crystal is immersed in heptane. The evidences suggest that there is a negligible asphaltene deposition at the nanometer size scale occurring in the step experiment. The asphaltene deposition could be occurring mostly by the deposition of flocs greater than 1  $\mu\text{m}$  which are not sensed by the quartz.

The model calculated bulk density-viscosity as well as the deposit thickness for the step *n*-heptane injection is shown in Figure 126.

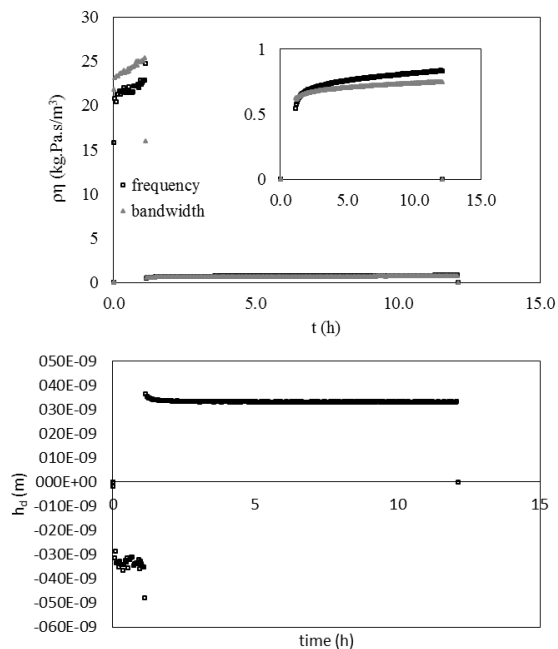


Figure 126. Model calculated density-viscosity and deposit thickness profile for the step n-heptane injection into crude oil C above onset of asphaltene destabilization conditions.

The deposit is shown to maintain the same thickness of around 35 nm from the crude oil destabilization up to 15 hours of experimental run time. The density-viscosity profile is observed to be higher than the values obtained with a clean quartz immersed in heptane, but a good agreement between the values obtained from frequency and dissipation data is obtained.

The analysis of the step n-heptane injection experiments are even more complicated than the analysis of the continuous n-heptane injection since at once many aggregate sizes with different asphaltene solubility classes would appear. Besides such complexity, it is still worth to check the profiles in order to try to understand the different phenomena. One interesting feature within the step experiments is the rapid depletion on nano sized particles capable of depositing, and forming a film which could be sensed by the quartz as an increase of deposit thickness over time.

The same experimental procedure was done with the crude oil presenting the highest concentration on asphaltenes, crude oil A (11.9 wt % n-C7 asphaltenes). The resonance frequency and bandwidth profiles are shown in Figure 127 and the density-viscosity profiles as well as the calculated deposit thickness are shown in Figure 128.

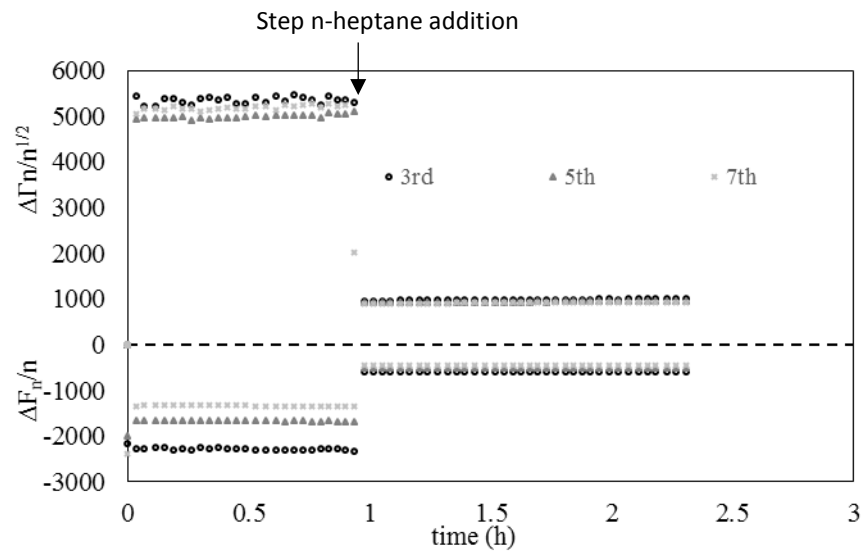


Figure 127. Step n-heptane injection into crude oil A to an n-heptane mass fraction of 0.87. Circles (black), squares and crosses (light gray) standing for 3<sup>rd</sup>, 5<sup>th</sup> and 7<sup>th</sup> overtones of resonance.

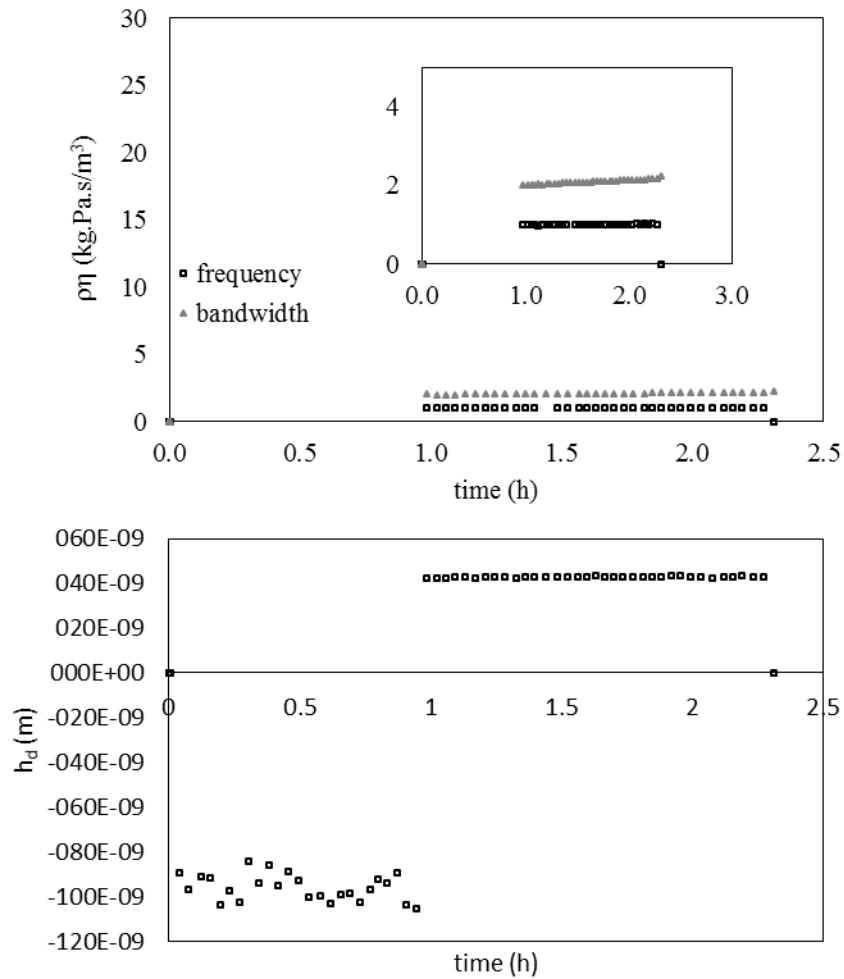


Figure 128. Model calculated density-viscosity and deposit thickness profile for the step n-heptane injection into crude oil A above onset of asphaltene destabilization conditions ( $x_{hep}=0.87$  wt %).

As it was observed for the step n-heptane injection into crude oil C, the deposit thickness stabilize around 40 nm right after the n-heptane addition. The density-viscosity profile presents a small positive drift.

#### 4.4 Interpretation of occurring physical phenomena from $\Delta\Gamma_\eta$ , $\Delta F_\eta$ and $\Delta F_m$ data: whole crude oils and extracted asphaltenes in toluene

The analysis of the raw data and the interpretation of the applied model prompted us to formulate a phenomenological theory of the occurring physical processes during asphaltenes destabilization and deposition. The interpretation of different processes occurring in the dilution plus destabilization region is for no means trivial since many parameters are being changed during the experiment. Changes in density, viscosity and flow conditions due to n-heptane injection as well due to asphaltene precipitation are simultaneously occurring<sup>219–221</sup>. With the asphaltenes destabilization aggregation occurs from the angstrom/nanometer scale, with different colloidal states of solvation or different macromolecular states<sup>84,222</sup>, to hundreds of micrometers with deposition simultaneously taking place.

Within the continuous n-heptane injection, asphaltene aggregation is not naturally undergoing as it is the case of a system brought to a constant n-heptane mass fraction. The continuous n-heptane injection results in a forced aggregation. Segregation of micrometer-sized particles arise due to the centrifugal force inherent to the agitation schema. Despite the number of uncontrolled variables the experiments with different oils presented the same patterns of  $\Delta F_n$  and  $\Delta\Gamma_n$ . The presence of patterns and the coherence of the data prompted us to theorize the mechanistic of asphaltene deposition from crude oils. Two characteristics of the experimental apparatus and experimental system makes the interpretation of the occurring phenomena easier: the high concentration of asphaltenes and the area averaged measures of shifts in frequency and energy dissipation which highlights main occurring processes over small heterogeneities.

A schematics of the hypothesized mechanisms of deposit build up during the titration of crude oils with an asphaltene non solvent is shown to the right of Figure 129. Numbers 1 to 5 indicate the discretized regions and sub-regions exposed on Figure 67 which is also added to the left of Figure 129, for convenience.

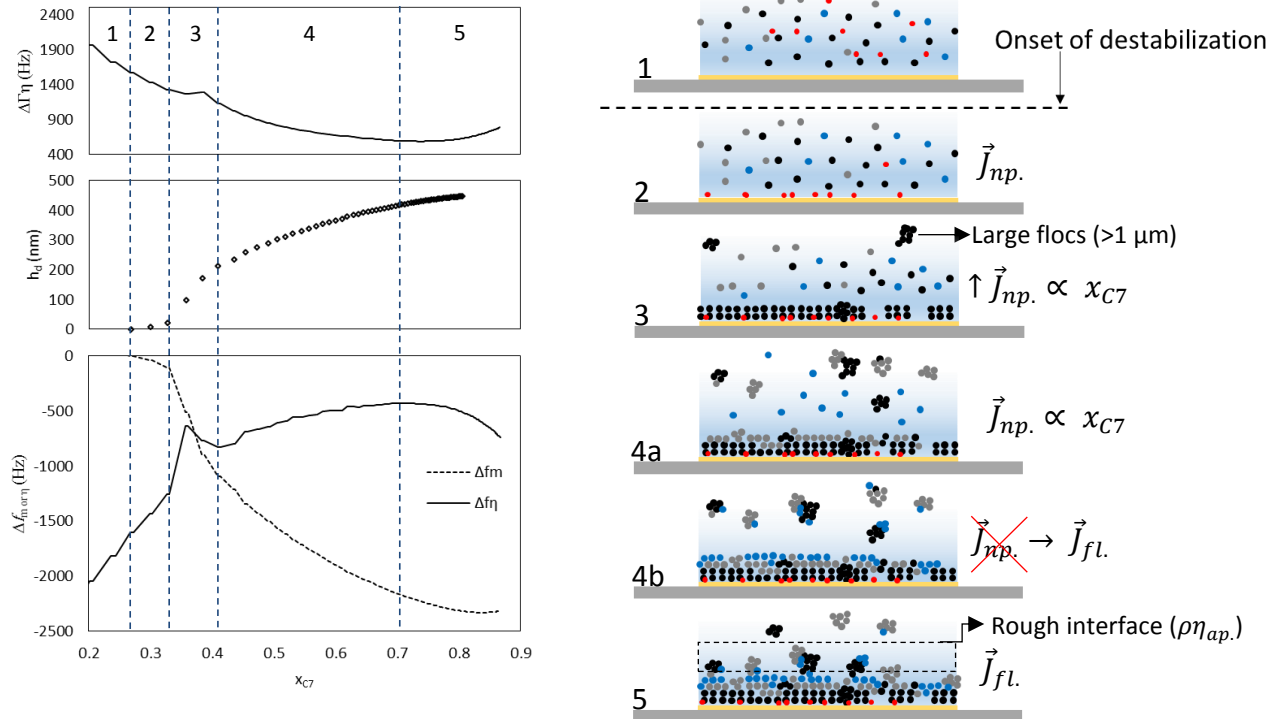


Figure 129. Schematics of the proposed physical processes occurring within the continuous destabilization of asphaltenes by n-heptane injection. Different colors standing for different asphaltenes solubility classes.

The first region or the dilution region is represented by the gold electrode exposed to the crude oil with different solubilized or dispersed asphaltenes (Figure 129-1). Different particle colors stands for different asphaltenes solubility classes. Asphaltene adsorption that may occur once the electrode is dipped in crude oil is neglected due to its small overlayer thickness when compared to thicknesses once asphaltene destabilization is reached and deposition begins. At the onset of destabilization the least soluble asphaltenes starts to deposit on the quartz electrode initiating the flux of nanoparticles ( $\vec{J}_{np.}$ ) particles as observed by the schematics as the second region

(Figure 129-2). The third region (Figure 129-3) is represented by an accentuated increase in deposit thickness within a small solubility window. Such increase may be due to the destabilization of a second intermediary solubility class of asphaltenes. The maximum point in bandwidth and the minimum in frequency (observed for crude oils A, C, D and E) in the third region suggests the occurrence of different interfacial processes which can be the organization of this second layer of deposit. Large flocs ( $>1 \mu\text{m}$ ) may also appear in this region and it is hypothesized that most of the techniques of measurement of asphaltene onset detection would sense onset conditions at this region. Region 4 (Figure 129-4a and 4b) is characterized by a constant asphaltene deposition with the n-heptane mass fraction. The bulk fluid is enriched in micrometer sized asphaltenes flocs (see Figure 134). Asphaltene deposition from sub-regions 2, 3 and 4 are observed to be linearly related to the n-heptane mass fraction and thus solution solubility towards asphaltenes and are hypothesized to occur mainly by nanoaggregates or clusters of a few nanoaggregates building up a rather elastic deposit with roughness and porosity much smaller than the penetration depth of the 7<sup>th</sup> harmonic which is  $\sim 90 \text{ nm}$  in pure heptane. The beginning of the fifth region is found by the minimum in energy dissipation (Figure 129-5). At this region the great majority of asphaltenes on the nanometer size range (nanoaggregates) are already destabilized and depleted from the bulk. The bulk solution is composed of aggregates or flocs from hundreds of nanometers to hundreds of micrometers. The fifth region is then characterized by the deposition of this flocs which are on the same size range of the probing shear wave penetration depths inducing an increase in bandwidth due to the rough interface (dashed rectangle in Figure 129-5). In the fifth region, the measured viscosity is not anymore the bulk density-viscosity product but rather represents an apparent density-viscosity product ( $\rho\eta_{ap}$ ) of

the interface. The analysis of the bandwidth minimum may indicate the solubility of the most soluble asphaltenes.

The crucial aspect of the formation of the weakly dissipative asphaltenic deposit is the great flux of destabilized nanoaggregates ( $J_{na}$ ) and their higher diffusion coefficients compared to the flocs. Diffusion is however not the only factor on the buildup of a smooth and elastic deposit. The high flux of nanometer-sized aggregates may also act as cementing agent smoothing up the surfaces and preventing the bandwidth to increase when bigger aggregates deposit. It is also hypothesized that primary soluble or stable asphaltene particles in crude oil have much higher deposition propensity than the subsequent aggregates of such particles. Particles other than nanoaggregates would stay in the bulk solution undergoing flocculation processes.

The base of the asphaltene deposition phenomena is then the primary asphaltene particle stable or solubilized in crude oil. The deposition phenomenon is a competitive process with bulk aggregation, with deposition being to some extent truncated within the primary stages of asphaltenes aggregation. The extent of deposition being strongly dependent on the solubility gradients inducing a faster or lower aggregation rate. Lower aggregation rates giving rise to much severe asphaltene deposition. The kinetics of asphaltene destabilization, intrinsically related to solubility gradients, is then a crucial parameter on accessing asphaltene deposition, which was clearly stated in a former study<sup>114</sup>. Moreover, the aggregate states yielded after asphaltene destabilization are rather important when detecting deposition. The structure of the asphaltenes aggregates on their propensity to adsorb was already pointed out by Acevedo<sup>223</sup>. Here such a physics is extended to the destabilized particles which will have more or less propensity to deposit according to their destabilization path. This is schematically shown in Figure 130.

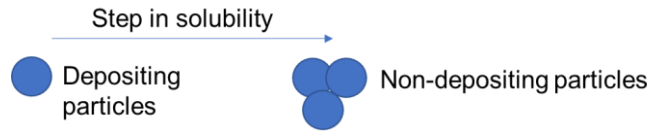


*Figure 130. General perceived effect when asphaltenes are destabilized by a step solubility change. Particles deposition are truncated in a very early stage of asphaltene particle aggregation.*

Figure 130 schematically shows that a step crude oil solubility change may induce the appearance of first aggregates with no depositing propensity. The study of the solubility or stability of aggregation first particles aggregation stages, which are still suspended in solution, related to one or other destabilization mechanism is itself an important parameter on accessing asphaltene deposition. The rather high deposition propensity of primary destabilized particles was shown numerically by Schutte<sup>224</sup> who also pointed out for the importance of the primary particles interaction with the bulk media in the deposition process. However they never took into account the way of asphaltenes destabilization yielding different particles structures presenting different affinity to the surfaces. As an indication of the fast deactivation against deposition, asphaltenes particles suffers, they point out for the accentuated deposition near the region of asphaltenes phase separation. The way the step solubility change yields non-depositing particles may be compared to the way some surfactants acts as asphaltenes aggregation inhibitors as well as wax and hydrates growth, i. e., by steric mechanisms. In this regards, the continuous or step destabilization procedure would yield different particles presenting different affinities towards the depositing surface or towards the bulk media (Figure 131).



Figure 131. (A) Proposed mechanisms of ordered aggregation obtained for the first destabilized particles by a continuous solubility gradient which induce severe deposition by inducing particles aggregation in an ordered way. (B) Disordered aggregation of the first destabilized particles occurring with the step solubility gradient yielding aggregates with low propensity to deposit due to steric hindrances. (1) nanoaggregate (2) asphaltene monomer (3) nanoaggregate (4) paraffin (5) two nanoaggregates orderly aggregated (6 and 7) two nanoaggregates disorderly aggregated.

The mechanisms of deposition in the scale researched within this work also shows that the bulk deposit primary depositing particles has much smaller dimensions as the ones proposed by Vargas<sup>142</sup> in their asphaltene aggregation and deposition mechanisms when analyzing SEM images. Primary depositing particles in the range of 300 – 500 nm, as Vargas proposes, would give rise to a rather porous and rough deposit which would present much higher energy dissipation profile.

The experiments with extracted asphaltenes yielded a bandwidth profile which were more similar to existing reports on the deposition of colloidal particles on the quartz crystal resonators (see section 2.5). The bandwidths profiles in such systems were shown to display a maximum and then decrease with increasing n-heptane addition. Figure 132 brings a schematics of the processes which are hypothesized to be occurring when a solution of extracted asphaltenes in toluene is continuously destabilized by an asphaltene nonsolvent injection.

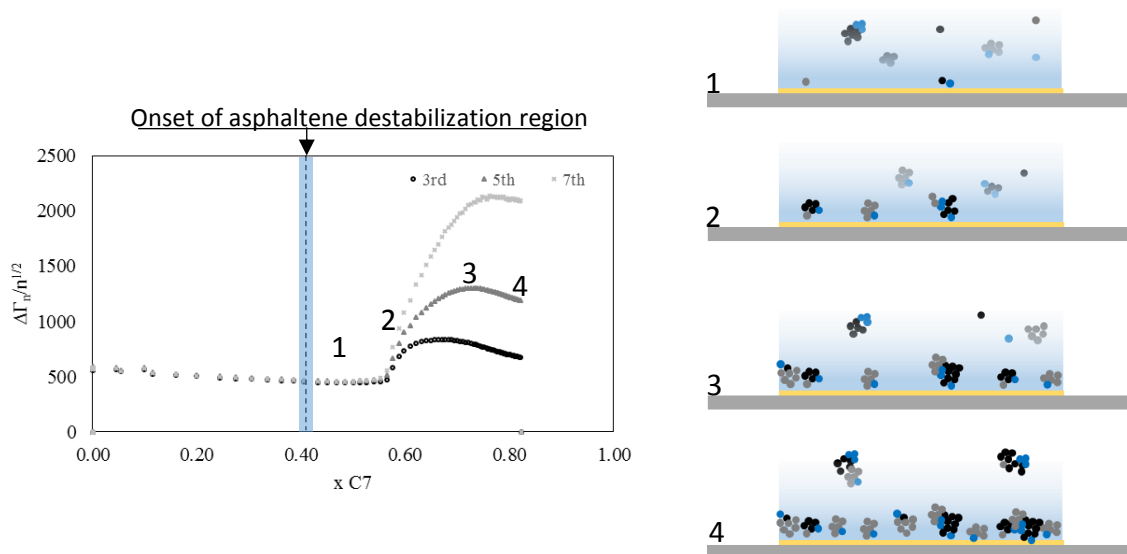


Figure 132. Hypothesis on the occurring processes when extracted asphaltenes in toluene are continuously destabilized by *n*-heptane injection. Different colors standing for different asphaltenes solubility classes.

With the use of extracted asphaltenes in toluene, the high degree of particles size polydispersity (Figure 132-1 and 2) induces the formation of laterally heterogeneous deposits presenting a maximum in bandwidth profile (Figure 132-3). Such maximum is hypothesized to arise when the surface attains its maximum lateral heterogeneity and particles are free to move. Further asphaltene particles deposition induces a decrease in bandwidth profiles as a result of the surface smoothing and particles immobilization (Figure 132-4). The high degree of polydispersity of extracted asphaltenes in toluene as reported on the study by Sheu<sup>225</sup> may not be the only factor promoting the buildup of a highly dissipative asphaltenic deposit: the deposit inter-particle interactions may be playing a key role. Further studies may shed some light on the bulk properties of such colloids and how they are depositing when destabilized.

#### 4.5 Macroscopic and microscopic experimental aspects

Both destabilization mechanisms obtained either by a step or a continuous n-heptane injection, gave different macro and microscopic observations as shown in Figure 133.

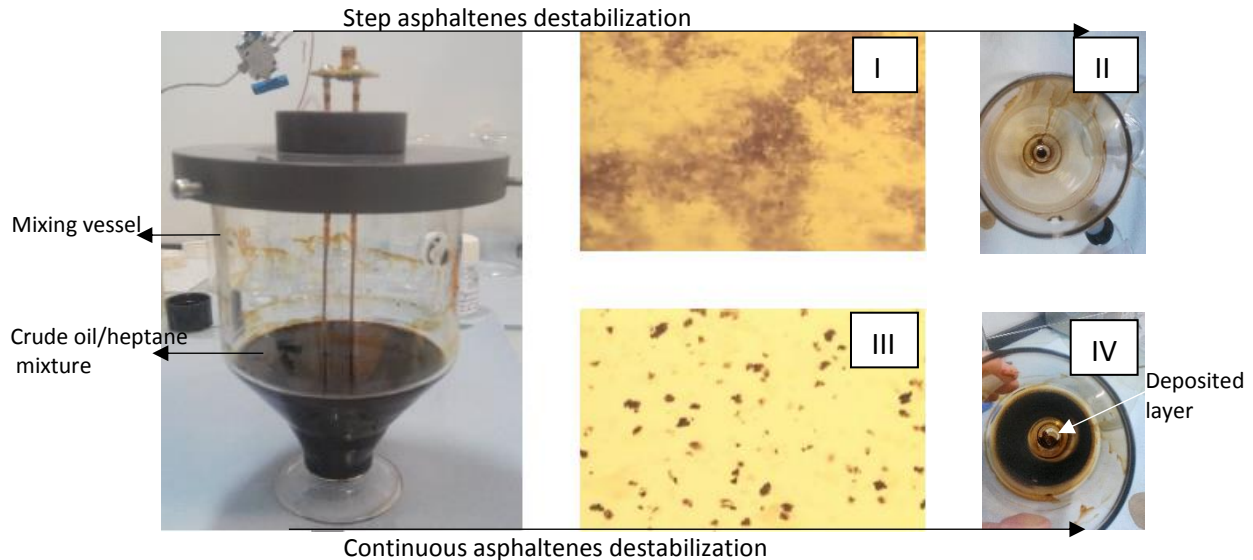
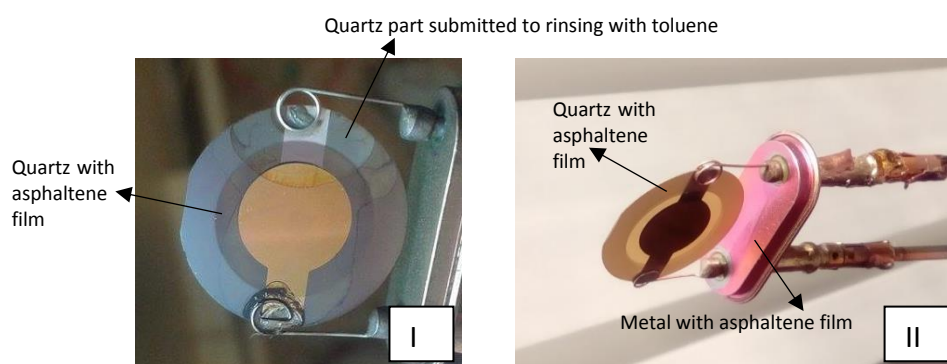


Figure 133. Macroscopic and Microscopic aspects on the precipitated asphaltenes by the step and continuous n-heptane injection. (I) and (III): Optical microscopy images from the asphaltenes flocs, in the bulk media, destabilized by a step or continuous n-heptane injection. (II) and (IV): aspect of the wall of the mixing vessel after a step (II) or continuous (IV) n-heptane injection is performed. A thick deposit layer on the glass surface is observed when the asphaltenes are destabilized continuously. In (IV) it can be observed a thick and easily removable (by agitation) asphaltene deposit and a rigidly attached film on the glass surface. Such film is not observed in the case when the asphaltene destabilization is proceeded at once (step destabilization).

The bulk precipitated asphaltenes obtained from the continuous n-heptane injection gave rise to more compact (Figure 133-III) flocs which had a tendency to stick on the mixing vessel walls (Figure 133-IV). The step change in n-heptane content give rise to smaller, less dense flocs which were kept in the bulk phase (Figure 133-I), and had no tendency to stick to the walls as it is observed (Figure 133-II). The thick deposit formed within the continuous experiment was easily removed by shaking the vessel with the n-heptane/crude oil mixture. Thus, this deposit is mostly

formed by forced sedimentation due to the centrifugal force due to fluid mixing by the magnetic bar. However, in the continuous experiment, after the non-consolidated deposit is removed, a film can be observed to coat the glass which is shown in the bottom of the mixing vessel (Figure 133-IV, white arrow). In the present work the study on the possibly formation of such films, with thicknesses on the nanometer-micrometer range, is analyzed by the use of the quartz crystal resonator. Such a film was also observed to cover the resonator and metal fittings, as it is shown in Figure 134, for two different experiments.



*Figure 134. Quartz crystal resonator after two experiments in which n-heptane was continuously added to crude oil. (I) An asphaltene deposit is observed on the quartz and electrode surfaces. In the top of the image a region which was cleaned with toluene can be observed. (II) Asphaltene film on the metal surface inducing a change in the surface color by birefringence.*

The deposits obtained on the gold electrodes were visualized with the aid of an optical microscopy at a 50x magnification, with a resolution of 0.5  $\mu\text{m}$ . Some images are shown in Figure 135.

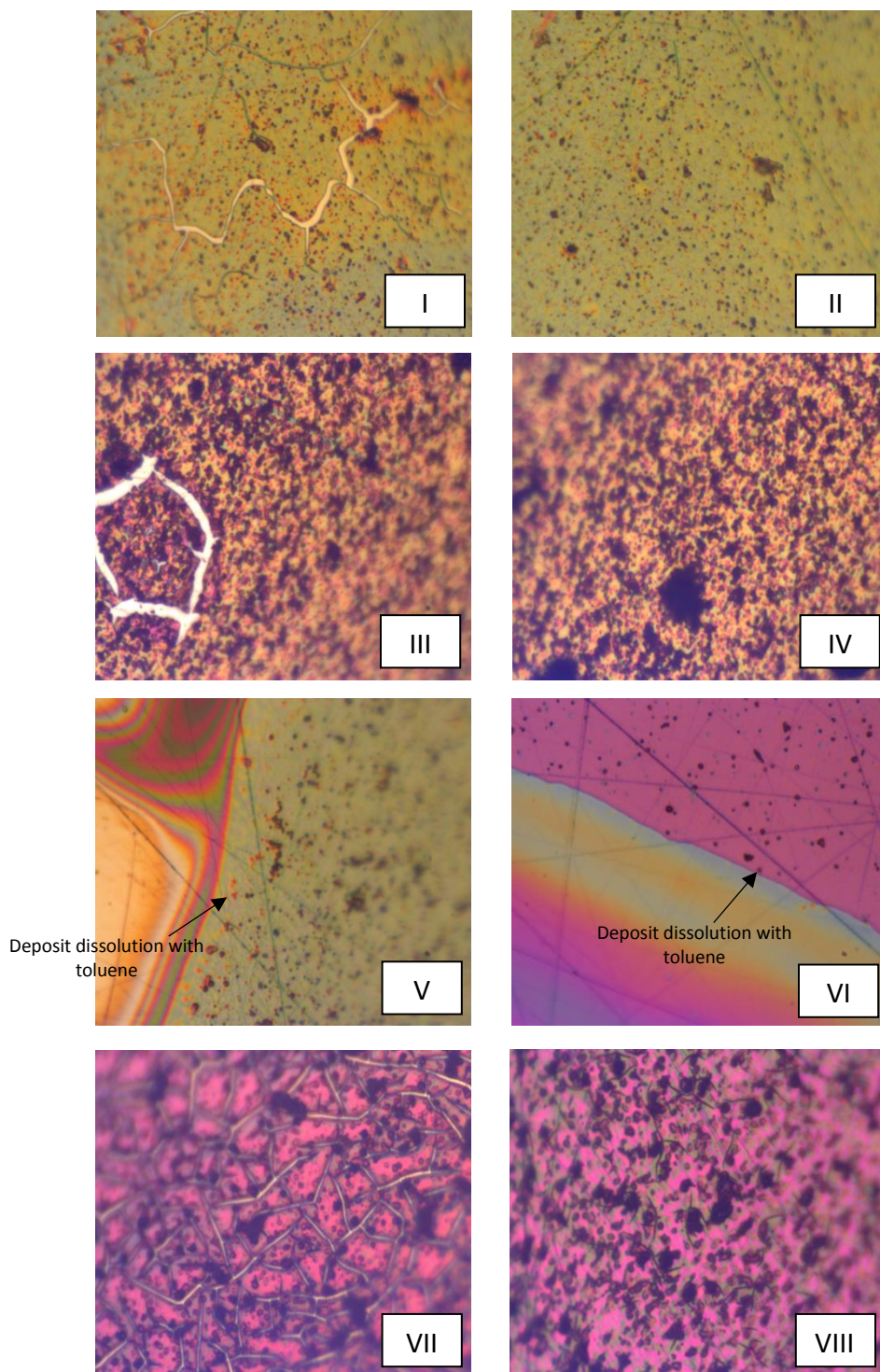


Figure 135. Micrographs of some asphaltene deposits on the gold electrode surface after the continuous destabilization procedure. (I) And (II): deposits obtained after the continuous destabilization of crude oil C at 25 °C; (III) and (IV), deposits obtained after the continuous destabilization of crude oil A with 11.9 wt % asphaltenes at 25 °C; (V), asphaltene deposit from crude oil C (continuous destabilization at 25 °C) dissolved by toluene; (VI) asphaltene deposit formed after the onset of flocculation in a clean gold surface and its frontier with toluene dissolution; (VII), asphaltene deposit formed after the continuous asphaltene destabilization of crude oil D by continuous n-heptane injection at 55 °C; (VIII), asphaltene deposit after continuous destabilization of crude oil D with n-pentane at 25 °C.

A main aspect in the asphaltenic deposit obtained by continuous asphaltene destabilization is the formation of sub-micrometric films which is put in evidence by the cracks in the deposits presented in Figures 135-I and III. The difference in colors also indicates the presence of thin films on the gold electrode surface. Quartz crystal resonator technique senses mostly the characteristics of such films. The Gaussian distribution of the amplitude of shear motion on a quartz crystal plate confers the signal to be coming from areal average effects which is taken as an advantage for capturing the overall depositing mechanisms.

Optical microscopy images (Figure 136) from the bulk fluid during the titration of crude oil C reveals that although the onset of destabilization was detected at  $x_{C7} = 0.4$  by the quartz crystal, optical microscopy, with resolution of  $1 \mu\text{m}$ , do not captures the destabilized particles at  $x_{C7} = 0.50$ . At higher n-heptane concentrations ( $x_{C7} > 0.57$ ) asphaltenes flocs much greater than  $1 \mu\text{m}$  are present in bulk with their aspects changing within the increase in n-heptane mass fraction: around  $x_{C7} = 0.57$  the destabilized asphaltenes are observed to give rise to connected flocs, and with increasing n-heptane mass fraction the destabilized asphaltenes form individual flocs with a denser aspect.

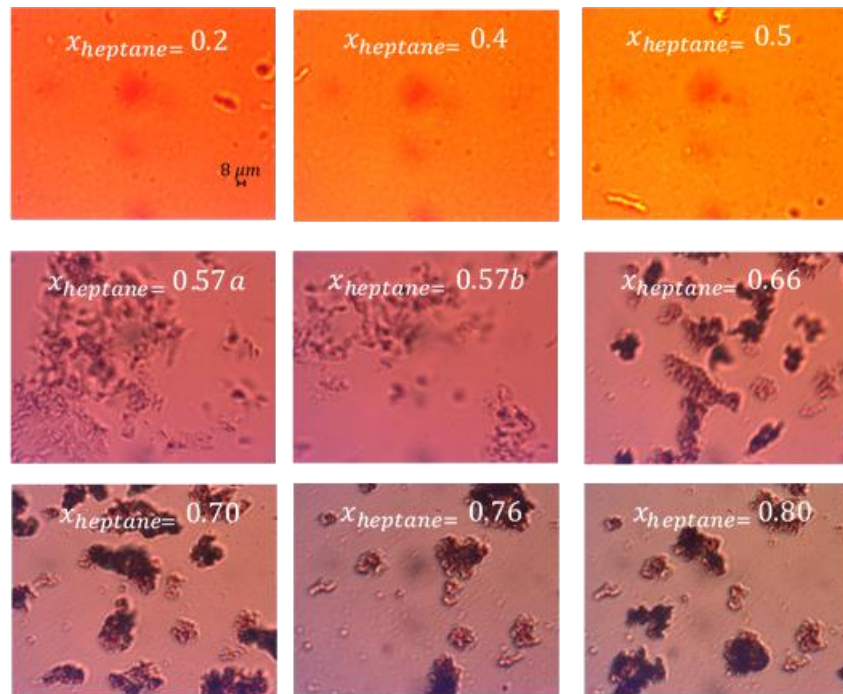


Figure 136. Micrographs from the bulk fluid (crude oil/n-heptane mixture) during the n-heptane injection into crude oil C (25 °C and atmospheric pressure).

The quantification of the precipitated material was performed with by centrifugation and subsequently sample drying. This analysis was performed in order to study the possible role of the destabilization manner on the quantity of precipitated material and its possible relation to asphaltene deposition. The data are shown in Figure 137-I and II. The analysis was done by performing the continuous or step n-heptane injection into an initial crude oil mass of 20 g in all cases. The analysis was performed for crude oils C, D and E.

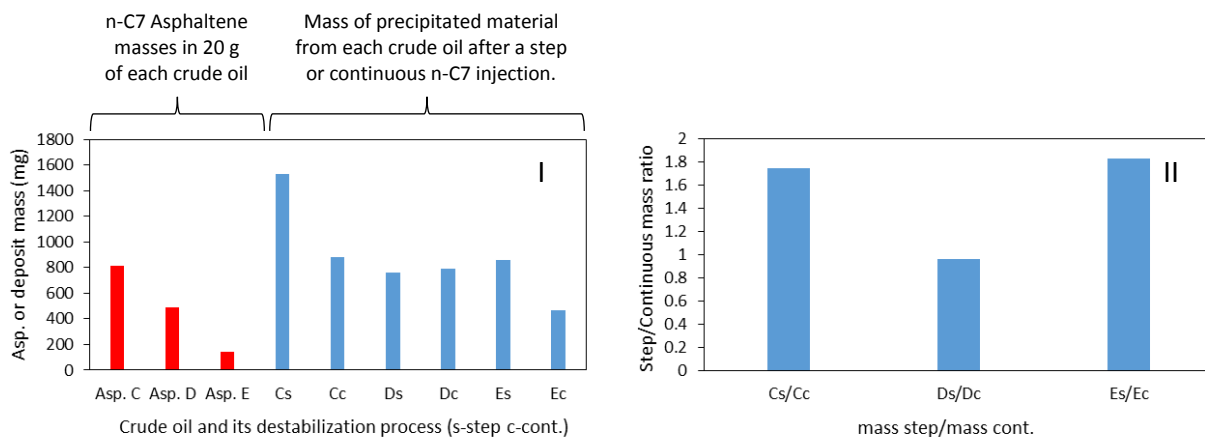


Figure 137. Quantification of the precipitated material by the continuous and step asphaltene destabilization. (I) n-C7 asphaltene masses in each crude oil (red) and the obtained precipitated masses after each destabilization procedure (step-s or continuous-c). (II) Ratio between the mass of precipitated materials obtained in the step n-heptane injection and continuous n-heptane injection.

According to Figure 137, crude oils C and E presented the same propensity on trapping other crude oil components once asphaltene are precipitated. The amount of precipitated material by step n-heptane injection was 1.8 times greater than the amount obtained when the continuous n-heptane injection is performed. Crude oil D, however, yielded about the same amount of precipitated material in both processes (step and continuous n-heptane injection). This analysis may be interesting in order to qualify the oils according to their tendency of yielding significant quantities of asphaltene co-precipitated or trapped materials. It can also be observed from Figure 137-I that the amount of asphaltene obtained on the continuous n-heptane injection into crude oil C and E are about the same amount of asphaltene obtained by the IPT-134 asphaltene extraction method.

#### 4.6 An AFM study of a deposit obtained at asphaltenes continuous destabilization

Atomic Force Microscopy in the contact mode was utilized to research on the structure and thicknesses of the asphaltenic deposits obtained under continuous n-heptane injection into crude oil C. The deposits were prepared on silica coupons which were assembled around the quartz crystal resonator and dipped in the crude oil. The crude oil was then titrated with n-heptane at constant mass flow rate (8 mg/s), at 25 °C and atmospheric pressure. The silica coupons were withdrawn from the mixing vessel at different n-heptane mass fractions, cleaned with excess n-heptane and let submerged in n-heptane at ambient temperature. Figure 138 brings the experimental assembly utilized to collect the asphaltene deposit samples at different n-heptane mass fractions and Figure 139 displays the resonance frequency and bandwidth profile for the performed n-heptane injection into crude oil. The n-heptane mass fractions at the moments of deposits samplings are shown in Figure 139 as dashed vertical lines.

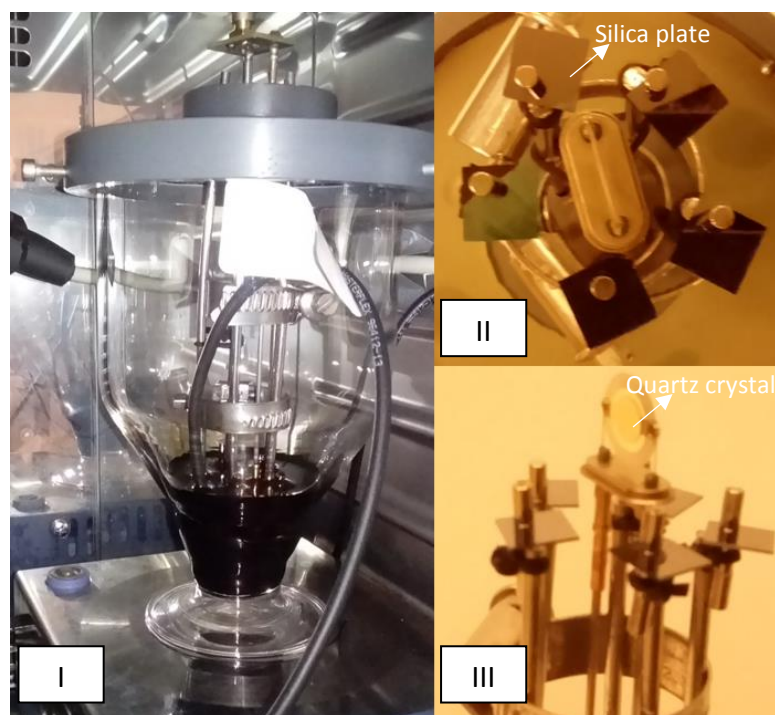


Figure 138. Experimental assembly utilized for collecting asphaltene deposit samples at different *n*-heptane mass fractions. (I) Mixing vessel with the quartz and the silica plates dipped in the crude oil/*n*-heptane mixture. The mixing vessel is inside an oven to maintain constant temperature during the experiment and is posed above a magnetic stirrer. The *n*-heptane injection is performed with the aid of a peristaltic pump subbing inserted in the bulk fluid. (II) and (III) quartz crystal with the surrounding silica coupons for collecting asphaltene deposits.

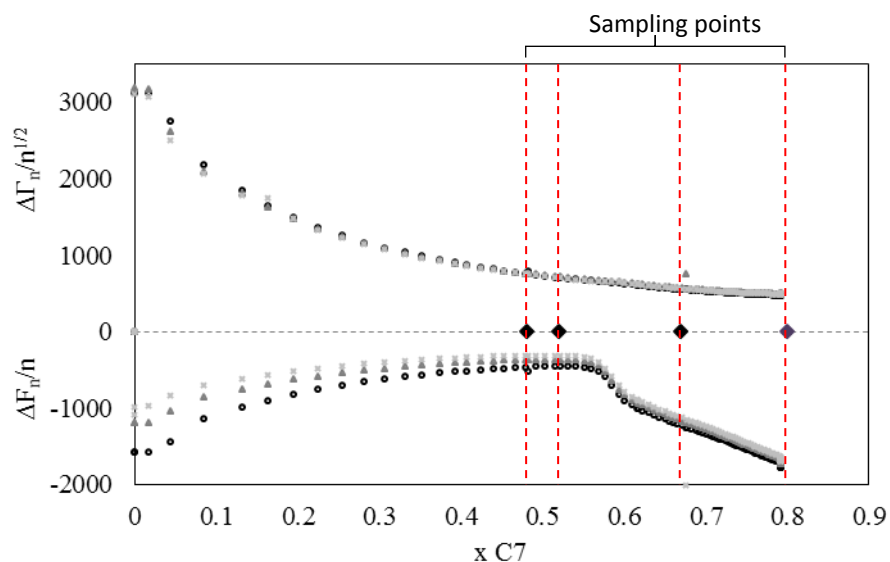


Figure 139. Changes in resonance frequency and bandwidth for the continuous *n*-heptane injection into crude oil C for sampling asphaltenic deposits with the aid of silica coupons. Red vertical dashed lines indicate the system composition in *n*-heptane when the samples were withdrawn from the mixing vessel.

As it is observed on Figure 139, the coupons were withdrawn from the system at four different n-heptane mass fractions,  $x_{C7} = 0.48$ ;  $x_{C7} = 0.52$ ;  $x_{C7} = 0.67$  and  $x_{C7} = 0.79$ . After sampling the deposits were immediately rinsed with pure n-heptane and stored immersed in n-heptane until the AFM analysis was performed. Figure 138 indicates the model calculated density-viscosity product and the deposit thicknesses for the experiment exposed on Figure 140.

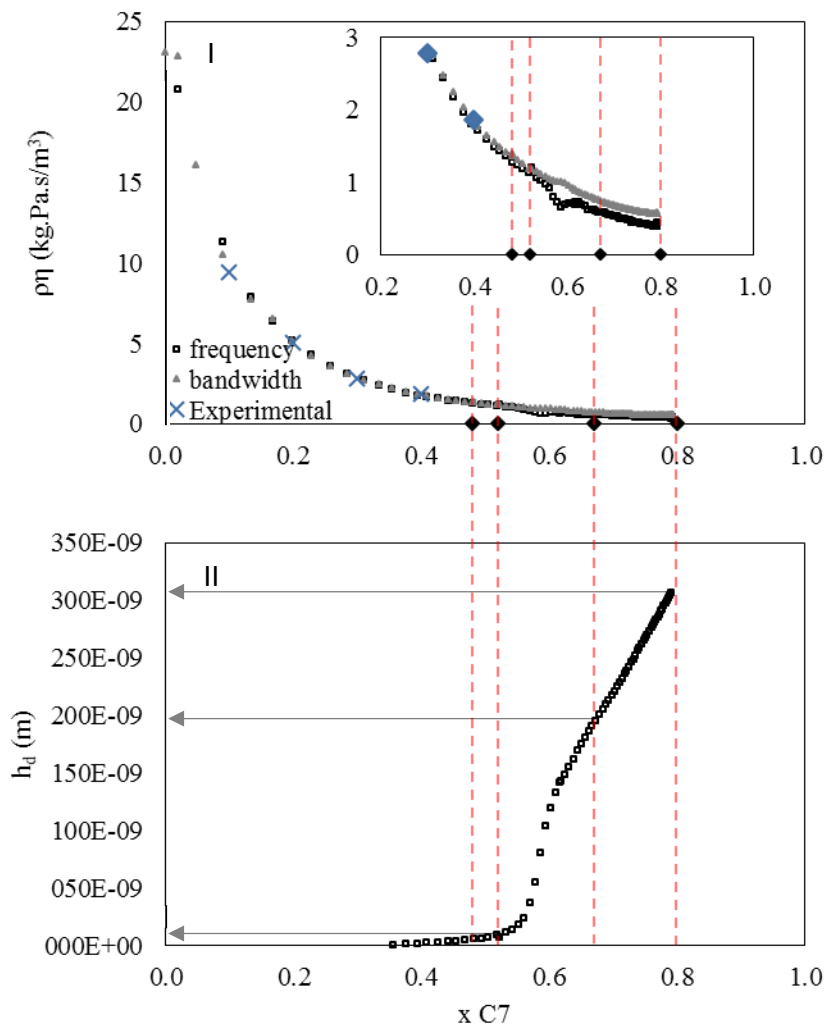


Figure 140. Model calculated crude oil/n-heptane density-viscosity product (I) and asphaltene deposit thicknesses (II) for the experiment shown in Figure 137. Vertical dashed lines indicate the system composition at which the coupons were withdrawn from the system.

The first sample was taken at  $x_{C7} = 0.48$ , above onset conditions, as determined by the derivative method being around  $x_{C7} = 0.40$ . The height profile and the 3D image for the coupon withdrawn at  $x_{C7} = 0.48$  is shown in Figure 141.

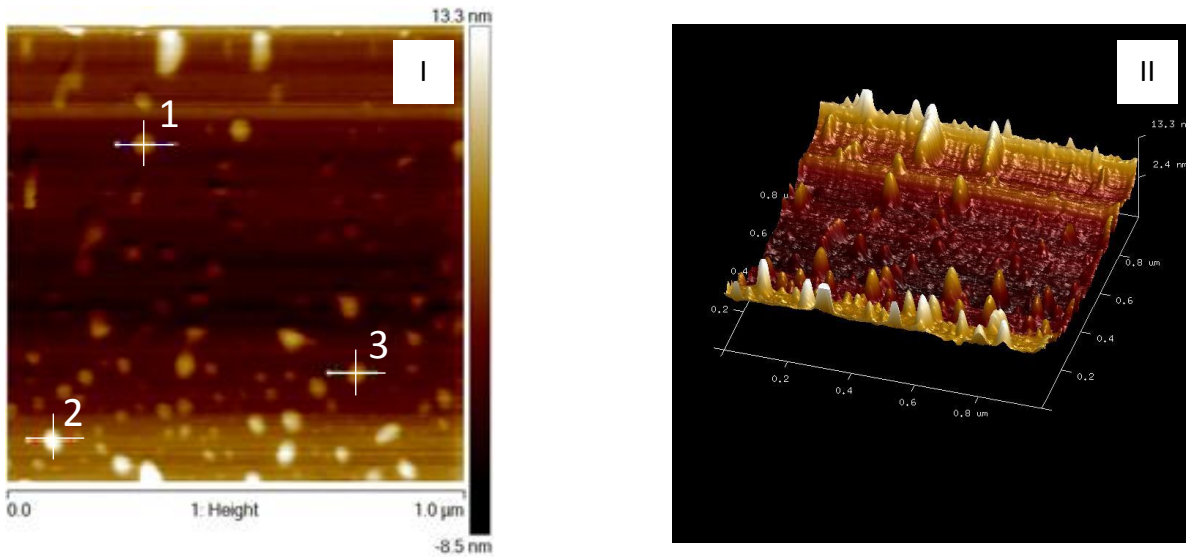


Figure 141. 2D AFM height profile (I) and the 3D representation (II) from the asphaltenic deposit sample taken at  $x_{C7}=0.48$ , above onset conditions and before the deep decrease in resonance frequency arising in region 3 as discretized in Figure 72. The vertical and horizontal cross sections of deposit grains represented by 1, 2 and 3 are shown in Figure 140.

As it can be observed in Figure 141, the deposit withdrawn at  $x_{C7} = 0.48$  is not continuous but constituted of depositing nuclei or grains. The vertical and horizontal height profiles from the deposited nuclei "1", "2" and "3" (Figure 141-I), are shown in Figure 142. The particles present a diameter almost 10 times greater than their height and are round shaped remembering a drop with high affinity to the surface (high contact angle). A highly magnified (200 x 100 nm) 2D height profile and 3D representation from the grain "1" is shown in Figure 143 highlighting the spherical aspect of the first deposited particles.

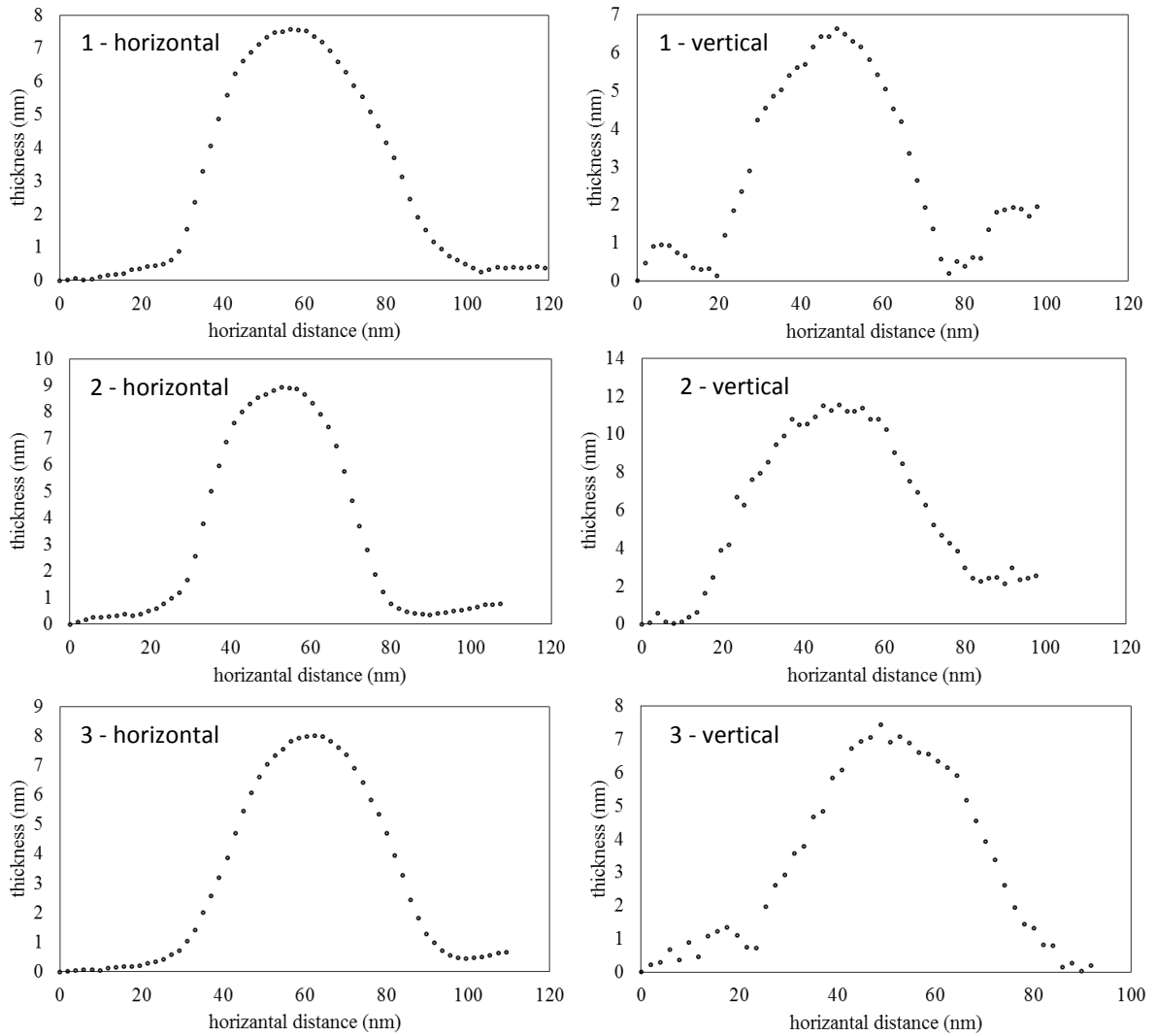


Figure 142. Horizontal and vertical cross sections from three deposit nuclei as shown in Figure 139. The deposit “grains” are observed to be round shaped with diameters much greater than their height.

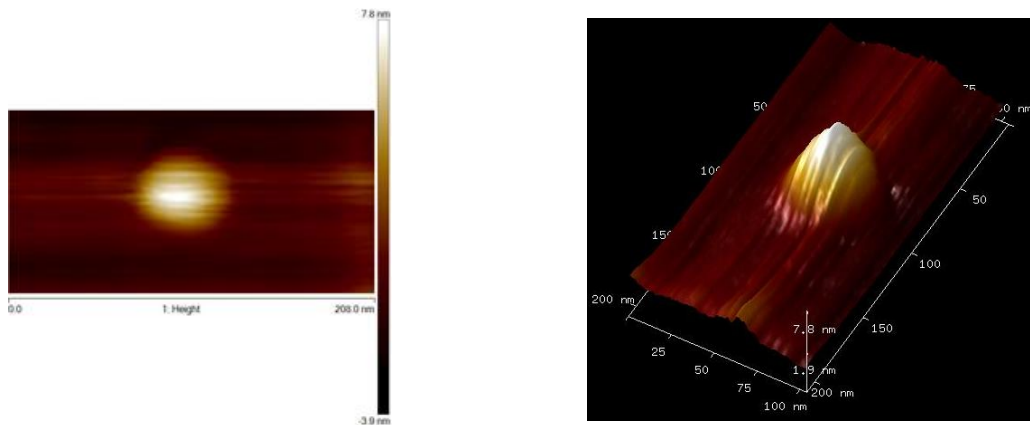
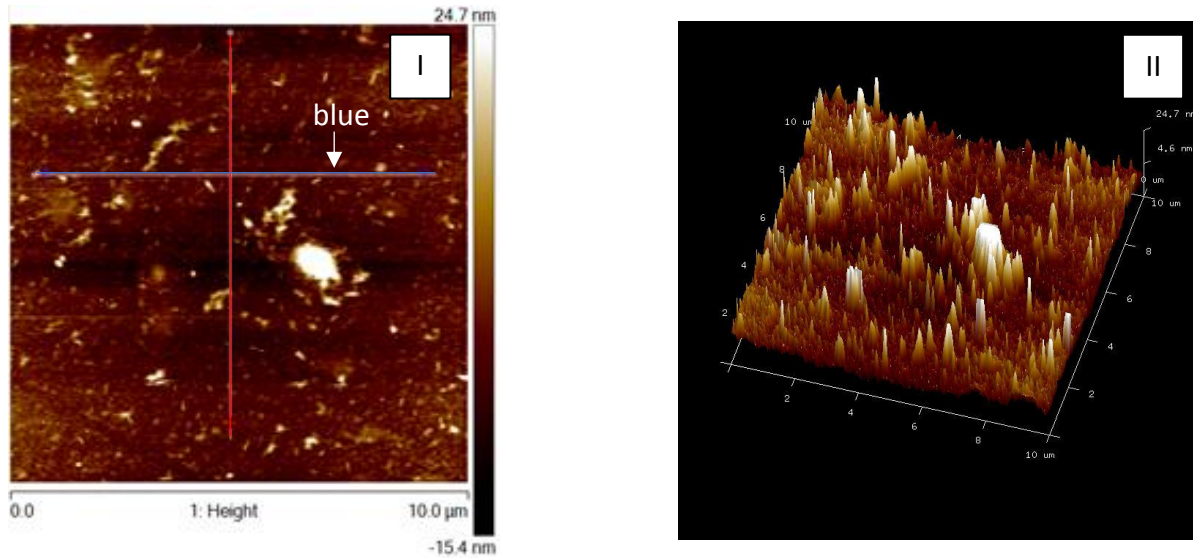


Figure 143. Height profile and the correspondent 3D representation for the nucleus or grain number “1” in Figure 139 at a much greater magnification (200 x 100 nm).

The 2D height profile and the 3D representation for the sample withdrawn at  $x_{C7} = 0.52$  are shown in Figure 144. The deposit mean square roughness ( $R_{ms}$ ) is also added in Figure 144 for two cross sections as shown in Figure 144-I.



	Horizontal Distance ( $\mu\text{m}$ )	$R_{ms}$ (nm)	III
blue	3.443	2.372	
red	5.299	3.835	

Figure 144. 2D height profile (I), 3D representation (II) and mean square roughness (III) for the asphaltenic deposit sample taken at  $x_{C7}=0.52$ .

As it can be observed in Figure 144, contrary to the deposit obtained at  $x_{C7} = 0.48$ , the asphaltenic deposit obtained at  $x_{C7} = 0.52$  covers the totality of the probed silica surface. Deposit mean square roughness is observed to be much smaller than the shear wave penetration depth for the 7<sup>th</sup> overtone at such n-heptane mass fraction ( $\delta_{n=7}^{x_{C7}=0.52} > 100 \text{ nm}$ ). The low deposit roughness and its high elastic nature yield no perceptible bandwidth change (Figure 139). In order to measure the deposit thickness a procedure of scratching the deposit with the AFM tip was employed. Figure 145 brings the obtained 2D height image from the scratched region (Figure

145-I) and also the obtained deposit thickness profile (Figure 145-II). It can be observed that the deposit thickness at  $x_{C7} = 0.52$  is around 5 nm.

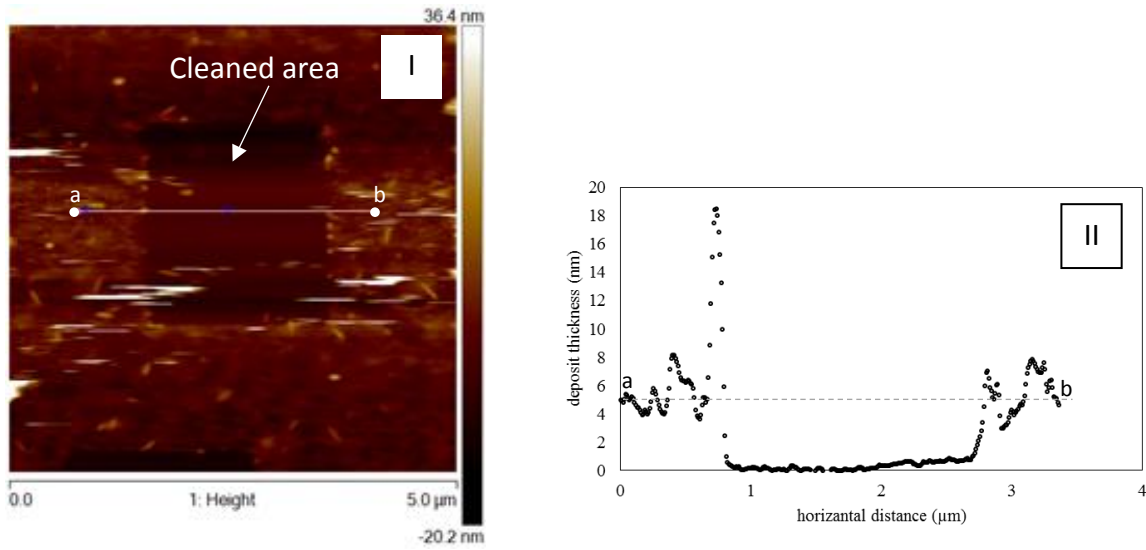
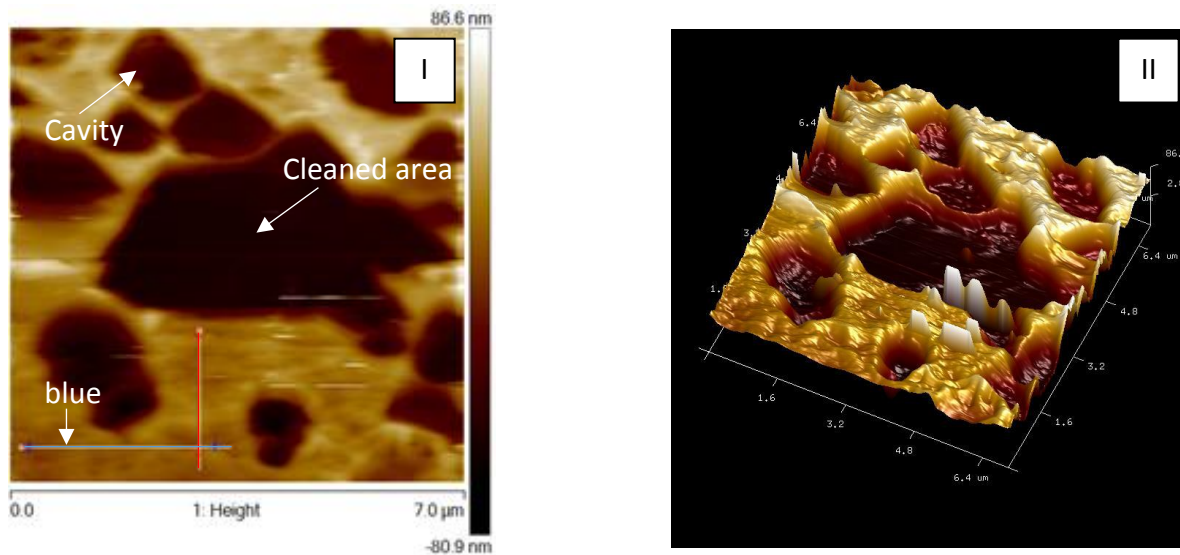


Figure 145. (I) 2D AFM image after the scratching of the deposit and (II) the thickness profile obtained from point “a” to point “b” in the 2D height image. Sample taken at  $x_{C7}=0.52$ . The arrow indicates the area without asphaltenic deposit obtained by scratching the silica surface with the AFM tip.

The 2D height profile, the 3D representation and the deposit mean square roughness for the sample taken at  $x_{C7} = 0.67$  are shown in Figure 146.



	Horizontal Distance ( $\mu\text{m}$ )	$R_{\text{ms}}$ (nm)	III
blue	3.377	4.162	
red	1.836	5.467	

Figure 146. 2D height profile, 3D representation and mean square roughness of one vertical and one horizontal deposit sections. Sample taken at  $x_{C7}=0.67$ . The arrow indicates the presence of cavities within the deposit.

The deposit obtained at  $x_{C7} = 0.67$  is observed to keep its low roughness and to present many cavities in the order of micrometers of diameter. Such cavities may be increasing deposit energy dissipation and contributing to the dissimilarities between thicknesses obtained by the quartz crystal resonator and the observed thicknesses by atomic force microscopy. The deposit thickness was also obtained by scratching the surface with the AFM tip. The scratched (cleaned) area is shown in Figure 146-I and re-printed in Figure 147 which also brings the deposit thickness profile for one vertical cross section.

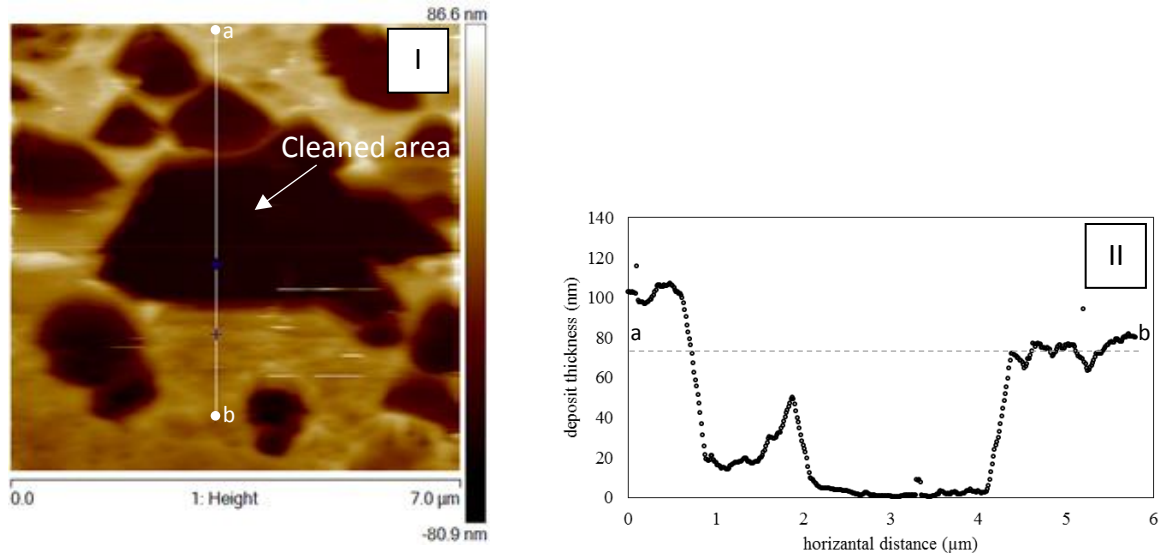
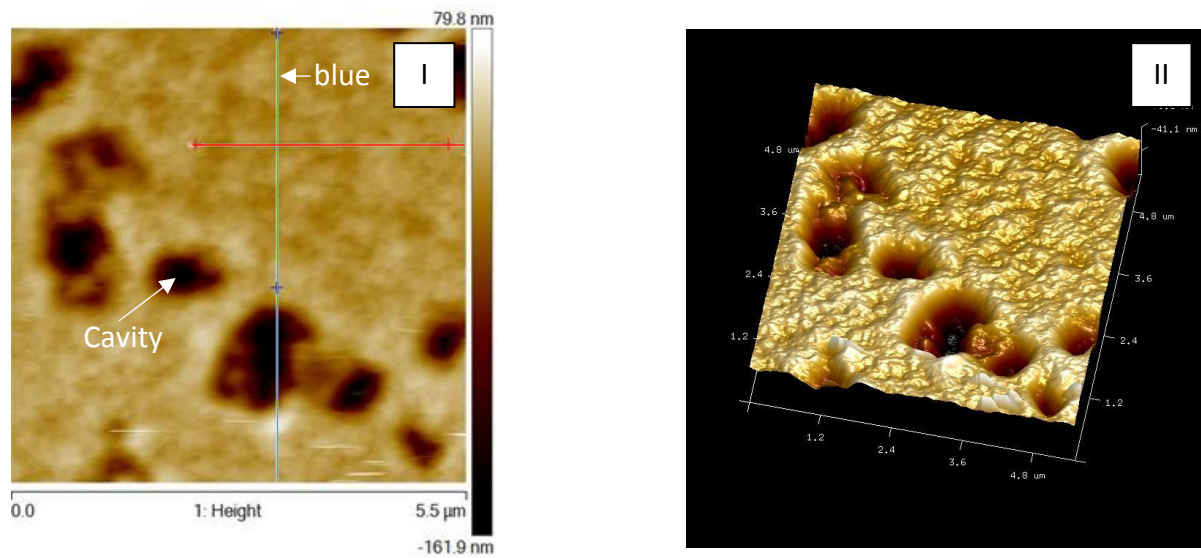


Figure 147. (I) 2D AFM image after the scratching of the deposit and (II) the thickness profile obtained from point “a” to point “b” in the 2D height image. Sample taken at  $x_{C7}=0.67$ . The arrow indicates the area without asphaltenic deposit obtained by scratching the silica surface with the AFM tip.

The 2D height profile, the 3D representation and the deposit mean square roughness for the deposit sample taken at  $x_{C7} = 0.79$  are shown in Figure 148.



	Horizontal Distance (μm)	$R_{ms}$ (nm)	III
blue	3.085	7.13	
red	3.064	6.195	

Figure 148. 2D height profile, 3D representation and mean square roughness of one vertical and one horizontal deposit sections. Sample taken at  $x_{C7}=0.79$ . The arrow indicates the presence of cavities within the deposit.

The asphaltenic deposit obtained at  $x_{C7} = 0.79$  present the cavities found in the deposit sampled at  $x_{C7} = 0.67$ . The roughness of the deposit keeps very low, under 10 nm, which is about nine times smaller than the shear wave penetration depth from the 7<sup>th</sup> overtone of resonance. The deposit thickness for one cross section is shown in Figure 149. The asphaltenic deposit obtained at  $x_{C7} = 0.79$  presents a thickness of about 175 nm.

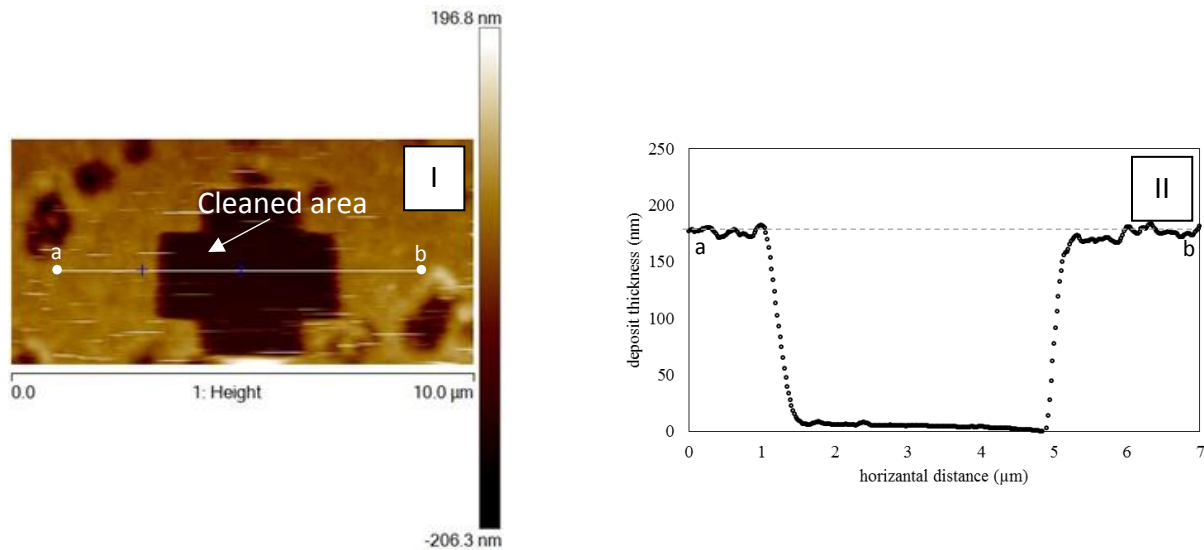


Figure 149. (I) 2D AFM image after the scratching of the deposit and (II) the thickness profile obtained from point “a” to point “b” in the 2D height image. Sample taken at  $x_{C7}=0.79$ . The arrow indicates the area without asphaltenic deposit obtained by scratching the silica surface with the AFM tip.

It can be observed that the deposits become thicker the greater the n-heptane mass fraction without a significant change in deposit surface mean square roughness. The deposits obtained at  $x_{C7} = 0.67$  and  $x_{C7} = 0.79$  presented some cavities as it shown by the arrows in Figure 146 and 148. The comparison between the deposit thicknesses obtained by the quartz crystal resonator and atomic force microscopy is shown in Figure 150.

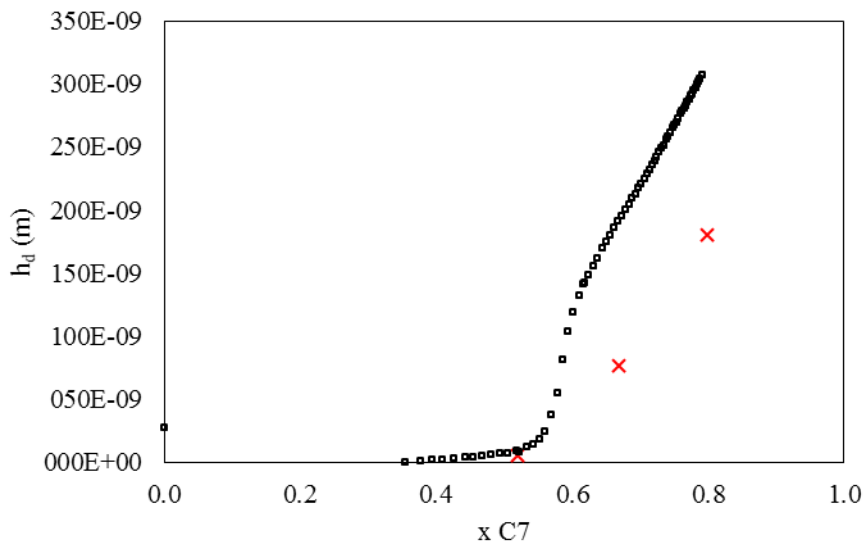


Figure 150. Comparison between the deposit thicknesses obtained by Quartz Crystal Resonator (squares) and Atomic Force Microscopy (crosses).

Deposit thicknesses obtained by QCR is observed to be higher than the deposit thicknesses obtained by AFM although the thicknesses obtained by QCR and AFM are in the same order of magnitude. The differences are 5 nm for the deposit at  $x_{C7} = 0.52$ , 100 nm for the deposit obtained at  $x_{C7} = 0.67$  and 85 nm for the obtained deposit at  $x_{C7} = 0.79$ . Part of the differences may arise from the deposit cleaning procedure, after sampling, by thoroughly rinsing with pure n-heptane. However most of the contributing factors for such differences should mostly be related to the deposit viscoelasticity and the hydrodynamic energy losses due to the observed cavities with size on the order of micrometers. Figure 150 also points out that the strong increase of deposit thickness around  $x_{C7} = 0.52$  as observed by the quartz may be arising from deposit structuration effects as the rate of deposit growth is shown to be steeper from  $x_{C7} = 0.67$  to  $x_{C7} = 0.79$ , when compared to deposit growth from  $x_{C7} = 0.52$  to  $x_{C7} = 0.67$ .

#### 4.7 Crude oil with injected nitrogen and the onset of asphaltene destabilization

The present section is small description of two experiments at high pressure using live oils and injected nitrogen. Further information on the utilized methodology and results can be obtained by both published articles in the context of the present thesis<sup>181,182</sup>.

The possible influence of nitrogen injection into crude oil towards asphaltenes destabilization and deposition was studied. The live crude oils presented in Table 3 were enriched with nitrogen from a 0 to 40 mol%, then, constant mass expansion tests were performed with a parallel recording of changes in bandwidth.

Figures 149 and 150 bring the bandwidth profiles obtained during the isothermal decompression for the experiments with live oil 1 and 2, respectively. The experiments with different nitrogen molar fractions are shown.

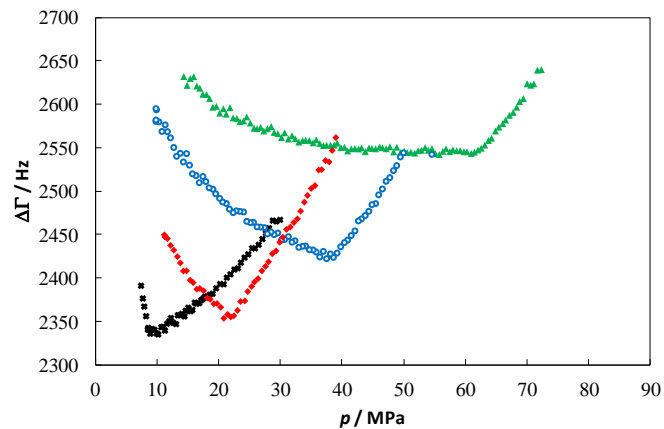


Figure 151. Change in dissipation (half-band-half-width) measured by a quartz crystal resonator immersed in various mixtures of  $N_2$  + live oil 1 during a constant mass expansion experiment at  $T = 347.87$  K. 0% ( $\times$ ); 10% ( $\blacklozenge$ ); 20% ( $\circ$ ) and 30% ( $\blacktriangle$ ) of  $N_2$  in mol%.

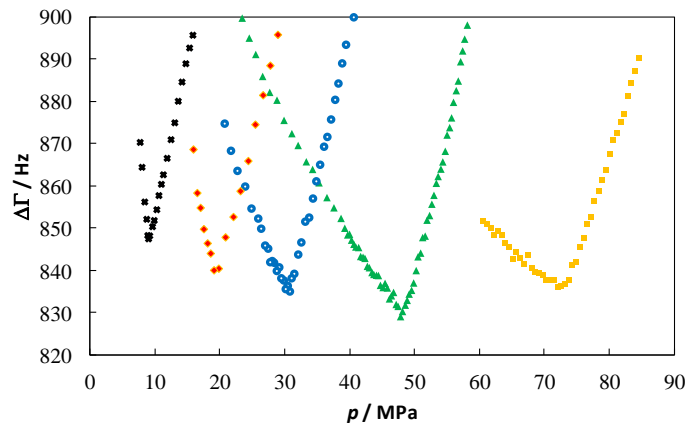


Figure 152. Change in dissipation (half-band-half-width) measured by a Quartz Crystal Resonator immersed in various mixtures of  $N_2$  + live oil 2 during a constant mass expansion experiment at  $T = 367.65$  K. 0% ( $\times$ ); 10% ( $\blacklozenge$ ); 20% ( $\bullet$ ); 30% ( $\blacktriangle$ ) and 40% ( $\blacksquare$ ) of  $N_2$  in mol%.

The bandwidths profiles are observed to monotonically decrease attaining a minima at bubble point conditions as it can be observed by comparing the minima obtained with the PV profile for the constant mass expansions tests (Figure 153). At the bubble point, as gas is released from the live oil there is an increase in the liquid density and viscosity driving an increase in bandwidth.

As the sole effect on bandwidths change is observed of coming from bubble point conditions it is concluded that the nitrogen injection into both live oils never destabilized the asphaltenes in all researched nitrogen concentrations.

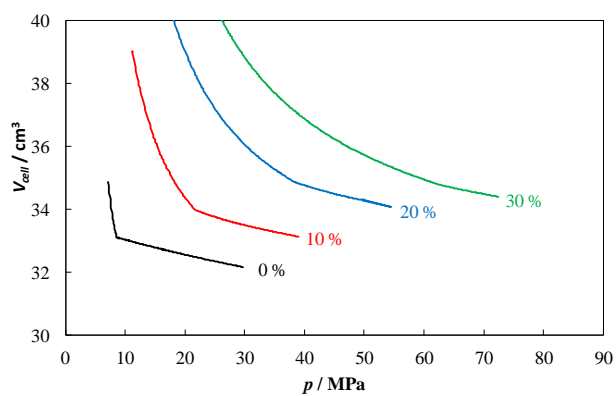


Figure 153. Constant mass expansion test and the PV profile normally used to determine live oil bubble point pressure. Referent to live oil 1 (Figure 151).

## Conclusions

According to the research hitherto presented, quartz crystal resonator technique was utilized totally immersed in crude oils, model oils, diluted oils and live oils to characterize asphaltene destabilization and deposition processes. The character of the study is of cataloging and interpreting phenomena, maintaining a theoretical basis, from the point of view of quartz utilization as well as the physical nature of asphaltenes in crude oils and the other researched systems.

Asphaltenes were destabilized by two mechanisms: a smooth nonsolvent injection and an abrupt nonsolvent injection, mimicking some processes occurring during crude oil production, i. e., depressurization and fluids comingling.

The smooth crude oil solubility change for the 5 probed crude oils gave the same patterns in quartz crystal complex resonance frequency changes. 5 regions were discretized during the process, with their application on the interpretation of production chemicals efficiency on delaying onset of asphaltenes destabilization and also assessing deposition. It was highlighted that the asphaltene deposition is strongly dependent on the manner asphaltenes are destabilized, a subject greatly bypassed among the available literature: the known effect of competition between particles aggregation and deposition. The proposed hypothesized model, explaining the complex resonance frequency changes at smooth crude oil nonsolvent titration was based on the deposition of primary particles present in crude oil, either in molecular state or as nanoaggregates. Such was observed within the AFM study at the imminence of the onset of asphaltene destabilization, with very smooth particles, almost remounting a form of a drop.

Atomic Force Microscope confirmed that the deposit thicknesses calculated by the quartz crystal resonator technique are coherent, with corrections being need to be applied to account for viscoelasticity and cavities that were seen to be present within the deposit. Such cavities raise question on why asphaltenes are not depositing in such regions.

Within the step n-heptane injection above the onset of asphaltene destabilization, an almost instantaneous deposit thickness is maintained over periods of several hours greatly highlighting the rapid deactivation of the particles towards deposition once aggregation is declutched.

Many aspects from the asphaltenes deposit were researched, notably the study of the onset of asphaltene re-dissolution, and deposit aging in n-heptane. An interest aspect on the temperature memory of asphaltenes found, with the complex crude oil structure presenting relaxation profiles when suffering heat treatment. Such characteristics being directly linked to bulk crude oil structure, of outmost importance for understanding complex resonance frequency profiles and having reproducible experimental methods.

Although providing deposition profiles, the quartz crystal technique and the applied model based on Sauerbrey and Kanazawa approaches to the response of complex resonance frequency to mass and liquids, provided first estimations on bulk viscosity, which considering the system complexity, is in good agreement with real values, for instance, for crude oil production conditions. The work was performed always having as objective capture real processes closest as possible from real systems envisaging the development of advanced crude oil production sensors.

The use of extracted asphaltenes was observed to yield high bandwidth data, i. e., deposit energy dissipation. Such characteristics was deemed to come because of the different aggregation states

of asphaltenes in crude oil and in toluene. However, inter-particle and particle surface interactions should also be playing a key role to the observed differences. Diluted crude oils in toluene were observed to yield much smaller deposit energy dissipation.

## Bibliography

- (1) Lei, H.; Yang, S.; Qian, K.; Chen, Y.; Li, Y.; Ma, Q. *Energy & Fuels* **2015**, *29* (11), 6920–6927.
- (2) Tellechea, E.; Johannsmann, D.; Steinmetz, N. F.; Richter, R. P.; Reviakine, I. *Langmuir* **2009**, *25* (9), 5177–5184.
- (3) Olsson, A. L. J.; Quevedo, I. R.; He, D.; Basnet, M.; Tufenkji, N. *ACS Nano* **2013**, *7* (9), 7833–7843.
- (4) Xi, J.; Y. Chen, J. *J. Biochips Tissue Chips* **2013**, *5*, 1–9.
- (5) Lapidot, T.; Sedransk Campbell, K. L.; Heng, J. Y. Y. *Anal. Chem.* **2016**, *88* (9), 4886–4893.
- (6) Shpigel, N.; Levi, M. D.; Sigalov, S.; Girshevitz, O.; Aurbach, D.; Daikhin, L.; Pikma, P.; Marandi, M.; Jänes, A.; Lust, E.; Jäckel, N.; Presser, V. *Nat. Mater.* **2016**, No. February, 1–13.
- (7) Daridon, J.-L.; Carrier, H. *Energy & Fuels* **2017**, *31* (9), 9255–9267.
- (8) James G. Speight. *Fuel Process. Technol.* **1982**, *5* (3–4), 325–326.
- (9) Tissot, B. P.; Welte, D. H. *Petroleum Formation and Occurrence*, Second Edi.; Springer-Verlag Derlin Heidelberg GmbH, 1984.
- (10) Tissot, B. P.; Epitalié, J. *Rev. Inst. Fr. Pét.* **1975**, *30* (5), 743–777.
- (11) Wiehe, I. A.; Liang, K. S. *Fluid Phase Equilib.* **1996**, *117* (1–2 pt 2), 201–210.
- (12) Boduszynski, M. M. *Energy and Fuels* **1987**, *1* (1), 2–11.
- (13) McKenna, A. M.; Marshall, A. G.; Rodgers, R. P. *Energy & Fuels* **2013**, *27* (3), 1257–1267.

- (14) Kruka, V. R.; Cadena, E. R.; Long, T. E. *J. Pet. Technol.* **1995**, *47* (8), 681–687.
- (15) Sanjay, M.; Simanta, B.; Kulwant, S. *SPE Prod. Facil.* **1995**, *10* (1), 50–54.
- (16) Thanh, N. X.; Hsieh, M.; Philp, R. P. *Org. Geochem.* **1999**, *30* (2–3), 119–132.
- (17) Del Carmen García, M.; Carbognani, L. *Energy and Fuels* **2001**, *15* (5), 1021–1027.
- (18) Acevedo, S.; Cordero T, J. M.; Carrier, H.; Bouyssiére, B.; Lobinski, R. *Energy & Fuels* **2009**, *23* (2), 842–848.
- (19) Ariza-Leon, E.; Molina-Velasco, D.; Chaves-Guerrero, A. *Ciencia, Tecnol. y Futur.* **2014**, *5* (5), 39–53.
- (20) Kriz, P.; Andersen, S. I. *Energy and Fuels* **2005**, *19* (3), 948–953.
- (21) Yang, X.; Kilpatrick, P. *Energy Fuels* **2005**, *19* (4), 1360–1375.
- (22) Lei, Y.; Han, S.; Zhang, J.; Bao, Y.; Yao, Z.; Xu, Y. *Energy and Fuels* **2014**, *28*, 2314–2321.
- (23) Asomaning, S. *Pet. Sci. Technol.* **2003**, *21* (3–4), 581–590.
- (24) Loeber, L.; Muller, G.; Morel, J.; Sutton, O. *Fuel* **1998**, *77* (13), 1443–1450.
- (25) Moschopedis, S. E.; Speight, J. G. *Fuel* **1978**, *57*, 25–28.
- (26) Li, T.; Xu, J.; Zou, R.; Feng, H.; Li, L.; Wang, J.; Cohen Stuart, M. A.; Guo, X. *Energy & Fuels* **2018**, *32* (1), 306–313.
- (27) Baugh, T. D.; ConocoPhillips Co; K.V., G.; Mediaas, H.; Vindstad, J. E.; Statoil ASA; Wolf, N. *O. SPE Int. Symp. Oilf.* **2005**, No. August 2004.
- (28) Sjöblom, J.; Simon, S.; Xu, Z. *Adv. Colloid Interface Sci.* **2014**, *205*, 319–338.

- (29) Andersen, S. I.; Speight, J. G. *Pet. Sci. Technol.* **2001**, *19* (September 2012), 1–34.
- (30) Navarro, L.; Álvarez, M.; Grosso, J. L.; Navarro, U. *CT y F - Ciencia, Tecnol. y Futur.* **2004**, *2* (5), 53–67.
- (31) León, O.; Contreras, E.; Rogel, E.; Dambakli, G.; Acevedo, S.; Carbognani, L.; Espidel, J. *Langmuir* **2002**, *18* (15), 5106–5112.
- (32) Koots, J. A.; Speight, J. G. *Fuel* **1975**, *54* (3), 179–184.
- (33) Sedghi, M.; Goual, L. *Energy & Fuels* **2010**, *24* (4), 2275–2280.
- (34) Rogel, E. *Energy and Fuels* **2008**, *22* (6), 3922–3929.
- (35) Hashmi, S. M.; Firoozabadi, A. *J. Colloid Interface Sci.* **2013**, *394*, 115–123.
- (36) Murgich, J.; Rodríguez, J. M.; Aray, Y. *Energy & Fuels* **1996**, *10* (7), 68–76.
- (37) Ellison, B. T.; Gallagher, C. T.; Frostman, L. M.; Lorimer, S. E. In *Offshore Technology Conference*; Society of Petroleum Engineers: Houston, 2000.
- (38) Sjöblom, J.; Aske, N.; Harald, I.; Brandal, Ø.; Erik, T.; Sæther, Ø. *Adv. Colloid Interface Sci.* **2003**, *102*, 399–473.
- (39) Hannisdal, A.; Ese, M.-H.; Hemmingsen, P. V.; Sjöblom, J. *Colloids Surfaces A Physicochem. Eng. Asp.* **2006**, *276* (1–3), 45–58.
- (40) Kralova, I.; Sjöblom, J.; Øye, G.; Simon, S.; Grimes, B. a.; Paso, K. *Adv. Colloid Interface Sci.* **2011**, *169* (2), 106–127.
- (41) Harbottle, D.; Liang, C.; El-Thaher, N.; Liu, Q.; Masliyah, J.; Xu, Z. In *Particle-Stabilized*

- Emulsions and Colloids*; Ngai, T., Bon, S. A. F., Eds.; Royal Society of Chemistry, 2015; pp 283–314.
- (42) Juyal, P.; Mapolelo, M. M.; Yen, A.; Rodgers, R. P.; Allenson, S. J. *Energy & Fuels* **2015**, *29* (4), 2342–2350.
- (43) Varadaraj, R.; Brons, C. *Energy and Fuels* **2007**, *21* (3), 1617–1621.
- (44) Ahmed, N. S.; Nassar, A. M.; Zaki, N. N.; Gharieb, H. K. *Fuel* **1999**, *78* (5), 593–600.
- (45) Langevin, D.; Argillier, J. F. *Adv. Colloid Interface Sci.* **2015**, *233*, 83–93.
- (46) Creek, J. L. *Energy and Fuels* **2005**, *19* (4), 1212–1224.
- (47) Haskett, C. E.; Tartera, M. J. *Pet. Technol.* **1965**, *April*, 388–391.
- (48) Cadena-Nava, R. D.; Cosultchi, a; Ruiz-Garcia, J. *Energy & Fuels* **2007**, *21* (4), 2129–2137.
- (49) Hammami, A.; Ratulowski, J. In *Asphaltenes, Heavy Oils and Petroleomics*; Mullins, O. C., Sheu, E. Y., Hammami, A., Marshall, A. G., Eds.; Springer Netherlands: New York, 2017; pp 617–656.
- (50) Izadi, M.; Khalifeh, M.; Bagherzadeh, H.; Kharrat, R. *Proc. 10th SPE Int. Conf. Exhib. Eur. Form. Damage* **2013**.
- (51) Leontaritis, K. J. *SPE Prod. Oper. Symp.* **1989**, 1–10.
- (52) Zanganeh, P.; Ayatollahi, S.; Alamdari, A.; Zolghadr, A.; Dashti, H.; Kord, S. *Energy & Fuels* **2012**, *26* (2), 1412–1419.
- (53) Jafari Behbahani, T.; Ghotbi, C.; Taghikhani, V.; Shahrabadi, A. *Energy and Fuels* **2012**, *26*

- (8), 5080–5091.
- (54) Ibrahim, H. H.; Idem, R. O. *Energy & Fuels* **2004**, No. 8, 743–754.
- (55) Boussingault, J.-B. *Ann Chim Phys* **1837**, 64, 141–151.
- (56) Nellensteyen, F. Bereiding en constitutie van asphalt, Technische Hogeschool - DELFT, 1923.
- (57) Pfeiffer, J. P.; Saal, R. N. *J. Phys. Chem.* **1940**, 44 (2), 139–149.
- (58) Eilers, H. *J. Phys. Chem.* **1949**, 53 (8), 1195–1211.
- (59) Friberg, S. E. In *Asphaltenes, Heavy Oils and Petroleomics*; Mullins, O. C., Sheu, E. Y., Hammami, A., Marshall, A. G., Eds.; Springer, 2007; pp 189–203.
- (60) Andersen, S. I.; Birdi, K. S. *J. Colloid Interface Sci.* **1991**, 142 (2), 497–502.
- (61) Merino-Garcia, D.; Andersen, S. I. *J. Dispers. Sci. Technol.* **2005**, 26 (2), 217–225.
- (62) Yudin, I. K.; Nikolaenko, G. L.; Gorodetskii, E. E.; Kosov, V. I.; Melikyan, V. R.; Markhashov, E. L.; Frot, D.; Briolant, Y. *J. Pet. Sci. Eng.* **1998**, 20 (3–4), 297–301.
- (63) Andersen, S. I.; Christensen, S. D. *Energy and Fuels* **2000**, 14 (1), 38–42.
- (64) Buenrostro-González, E.; Groenzin, H.; Lira-galeana, C.; Mullins, O. C. *Energy & Fuels* **2001**, 15, 972–978.
- (65) Andreatta, G.; Goncalves, C. C.; Buffin, G.; Bostrom, N.; Quintella, C. M.; Arteaga-larios, F.; Mullins, O. C.; Perez, E. *Energy & Fuels* **2005**, 19 (6), 1282–1289.
- (66) Yen, T. F.; Erdman, J. G.; Pollack, S. S. *Anal. Chem.* **1961**, 33 (11), 1587–1594.

- (67) Dickie, J. P.; Yen, T. F. *Anal. Chem.* **1967**, *39* (14), 1847–1852.
- (68) Mullins, O. C. *Energy & Fuels* **2010**, *24* (4), 2179–2207.
- (69) Goual, L.; Sedghi, M.; Mostowfi, F.; McFarlane, R.; Pomerantz, A. E.; Saraji, S.; Mullins, O. C. *Energy & Fuels* **2014**, *28* (8), 5002–5013.
- (70) Roux, J. N.; Broseta, D.; Demé, B. *Langmuir* **2001**, *17* (16), 5085–5092.
- (71) Barré, L.; Jestin, J.; Morisset, A.; Palermo, T.; Simon, S. *Oil Gas Sci. Technol. - Rev. l'IFP* **2009**, *64* (5), 617–628.
- (72) Eyssautier, J.; Levitz, P.; Espinat, D.; Jestin, J.; Gummel, J.; Grillo, I.; Barré, L. *J. Phys. Chem. B* **2011**, *115* (21), 6827–6837.
- (73) Evdokimov, I. N.; Eliseev, N. Y.; Akhmetov, B. R. *J. Pet. Sci. Eng.* **2003**, *37*, 135–143.
- (74) Evdokimov, I. N.; Fesan, A. A. *Colloids Surfaces A Physicochem. Eng. Asp.* **2016**, *492*, 170–180.
- (75) Evdokimov, I. N.; Fesan, A. A.; Losev, A. P. *Energy & Fuels* **2016**.
- (76) Acevedo, S.; Ranaudo, M. A.; Pereira, J. C.; Castillo, J.; Fernández, A.; Perez, P.; Caetano, M. *Fuel* **1999**, *78* (9), 997–1003.
- (77) Svalova, A.; Parker, N. G.; Povey, M. J. W.; Abbott, G. D. *Sci. Rep.* **2017**, *7* (1), 1–11.
- (78) Betancourt, S. S.; Ventura, G. T.; Pomerantz, A. E.; Vilorio, O.; Dubost, F. X.; Zuo, J.; Monson, G.; Bustamante, D.; Purcell, J. M.; Nelson, R. K.; Rodgers, R. P.; Reddy, C. M.; Marshall, A. G.; Mullins, O. C. *Energy and Fuels* **2009**, *23* (3), 1178–1188.

- (79) Indo, K.; Ratulowski, J.; Dindoruk, B.; Gao, J.; Zuo, J.; Mullins, O. C. *Energy & Fuels* **2009**, *23* (9), 4460–4469.
- (80) Ray, B. R.; Witherspoon, P. a; Grim, R. E. *J. Phys. Chem.* **1957**, *61* (7), 1296–1302.
- (81) Sirota, E. B. *Energy and Fuels* **2005**, *19* (4), 1290–1296.
- (82) Yen, T. F. *Fuel Sci. Technol. Int.* **1992**, *10* (4–6), 723–733.
- (83) Gray, M. R.; Tykwinski, R. R.; Stryker, J. M.; Tan, X. *Energy and Fuels* **2011**, *25* (7), 3125–3134.
- (84) Tukhvatullina, A. Z.; Barskaya, E. E.; Kouryakov, V. N.; Yusupova, T. N.; Romanov, G. V. *J. Pet. Environ. Biotechnol.* **2013**, *4* (4), 1–8.
- (85) Wiehe, I. A.; Kennedy, R. J. *Energy and Fuels* **2000**, *14* (1), 56–59.
- (86) Murgich, J. *Pet. Sci. Technol.* **2002**, *20* (9–10), 983–997.
- (87) Hashmi, S. M.; Zhong, K. X.; Firoozabadi, A. *Soft Matter* **2012**, *8* (33), 8778.
- (88) F. G. Unger; Andreeva, L. N. In *Fundamentals of Oil Chemistry: Nature of Asphaltenes and Resins*; Cambridge International Science, 2003.
- (89) Dolomatov, M. Y.; Petrov, A. M.; Bakhtizin, R. Z.; Dolomatova, M. M.; Khairudinov, I. R.; Shutkova, S. A.; Kovaleva, E. A.; Paymurzina, N. K. *IOP Conf. Ser. Mater. Sci. Eng.* **2017**, *195* (1).
- (90) Taylor, S. E. *Fuel* **1998**, *77* (8), 821–828.
- (91) Khvostichenko, D. S.; Andersen, S. I. *Energy and Fuels* **2009**, *23* (2), 811–819.

- (92) Khvostichenko, D. S.; Andersen, S. I. *Energy & Fuels* **2010**, *24* (4), 2327–2336.
- (93) Siffert, B.; Kuczinski, J.; Papirer, E. J. *Colloid Interface Sci.* **1990**, *135* (1), 107–117.
- (94) Katz, D. L.; Beu, K. E. *Ind. Eng. Chem.* **1945**, *37* (2), 195–200.
- (95) Pfeiffer, J. P.; Doormaal, P. M. *J. Inst. Pet. Tech.* **1936**, *22*, 414.
- (96) Moschopedis, S. E.; Fryer, J. F.; Speight, J. G. *Fuel* **1976**, *55* (3), 227–232.
- (97) Acevedo, S.; Gutierrez, L. B.; Negrin, G.; Pereira, J. C.; Mendez, B.; Delolme, F.; Dessalces, G.; Broseta, D. *Energy and Fuels* **2005**, *19* (15), 1548–1560.
- (98) Akhmetov, B. R.; Evdokimov, I. N.; Eliseev, N. Y. *Chem. Technol. Fuels Oils* **2002**, *38* (4), 266–270.
- (99) Chacón-Patiño, M. L.; Rowland, S. M.; Rodgers, R. P. *Energy and Fuels* **2017**, *31* (12), 13509–13518.
- (100) Schuler, B.; Meyer, G.; Peña, D.; Mullins, O. C.; Gross, L. *J. Am. Chem. Soc.* **2015**, *137* (31), 9870–9876.
- (101) Schuler, B.; Fatayer, S.; Meyer, G.; Rogel, E.; Moir, M.; Zhang, Y.; Harper, M. R.; Pomerantz, A. E.; Bake, K. D.; Witt, M.; Peña, D.; Kushnerick, J. D.; Mullins, O. C.; Ovalles, C.; van den Berg, F. G. A.; Gross, L. *Energy & Fuels* **2017**, *31* (7), 6856–6861.
- (102) Mitchell, D. L.; Speight, J. G. *Fuel* **1973**, *52* (2), 149–152.
- (103) Ganeeva, Y. M.; Yusupova, T. N.; Romanov, G. V.; Bashkirtseva, N. Y. *J. Therm. Anal. Calorim.* **2014**, *115* (2), 1593–1600.

- (104) Kaminski, T. J.; Fogler, H. S.; Wolf, N.; Wattana, P.; Mairal, A. *Energy and Fuels* **2000**, *14* (1), 25–30.
- (105) Gutiérrez, L. B.; Ranaudo, M. A.; Méndez, B.; Acevedo, S. *Energy & Fuels* **2001**, *15* (7), 624–628.
- (106) Marcano, F.; Flores, R.; Chirinos, J.; Ranaudo, M. A. *Energy and Fuels* **2011**, *25* (5), 2137–2141.
- (107) Acevedo, S. *Pet. Petrochemical Eng. J.* **2017**, *1* (3), 1–5.
- (108) Rogel, E.; Ovalles, C.; Moir, M. *Energy & Fuels* **2010**, *24* (8), 4369–4374.
- (109) Rogel, E.; Ovalles, C.; Moir, M. *Energy and Fuels* **2012**, *26* (5), 2655–2662.
- (110) Adams, J. J. *Energy & Fuels* **2014**, *28* (5), 2831–2856.
- (111) Dudášová, D.; Simon, S.; Hemmingsen, P. V.; Sjöblom, J. *Colloids Surfaces A Physicochem. Eng. Asp.* **2008**, *317* (1–3), 1–9.
- (112) Dudášová, D.; Silset, A.; Sjöblom, J. *J. Dispers. Sci. Technol.* **2008**, *29* (1), 139–146.
- (113) Maqbool, T.; Balgoa, A. T.; Fogler, H. S. *Energy and Fuels* **2009**, *23* (7), 3681–3686.
- (114) Hoepfner, M. P.; Limsakoune, V.; Chuenmeechao, V.; Maqbool, T.; Fogler, H. S. *Energy & Fuels* **2013**, *27* (2), 725–735.
- (115) Wiehe, I. A.; Yarranton, H. A.; Akbarzadeh, K.; Rahimi, P. M.; Teclemariam, A. *Energy & Fuels* **2005**, *19* (4), 1261–1267.
- (116) Sieben, V. J.; Tharanivasan, A. K.; Ratulowski, J.; Mostowfi, F. *Lab Chip* **2015**, *15* (20), 4062–

4074.

- (117) Anisimov, M. A.; Yudin, I. K.; Nikitin, V.; Nikolaenko, G.; Chernoutsan, A.; Toulhoat, H.; Frot, D.; Briolant, Y. *J. Phys. Chem.* **1995**, *99* (23), 9576–9580.
- (118) Aske, N.; Kallevik, H.; Johnsen, E. E.; Sjöblom, J. *Energy Fuels* **2002**, *16* (7), 1287–1295.
- (119) Oh, K.; Ring, T. A.; Deo, M. D. *J. Colloid Interface Sci.* **2004**, *271* (1), 212–219.
- (120) Wang, J. X.; Buckley, J. S. *SPE Int. Symp. Oilf. Chem.* **2001**, 1–9.
- (121) Vargas, F. M.; Tavakkoli, M.; Boggara, M. In *15th International Conference on Petroleum Phase Behavior & Fouling*; Galveston, TX, 2014.
- (122) Buckley, J. S. *Fuel Sci. Technol. Int.* **1996**, *14* (1–2), 55–74.
- (123) Mousavi-Dehghani, S. A.; Riazi, M. R.; Vafaie-Sefti, M.; Mansoori, G. A. *J. Pet. Sci. Eng.* **2004**, *42*, 145–156.
- (124) Liu, T.; Wei, H.; Wang, X.; Sun, D.; Ma, Z. *Recent Pat. Mech. Eng.* **2015**, *8* (1), 3–15.
- (125) Shadman, M. M.; Saeedi Dehaghani, A. H.; Badizad, M. H. *Petroleum* **2016**, 1–5.
- (126) Sieben, V. J.; Molla, S.; Mostowfi, F.; Floquet, C. F. A.; Speck, A.; Chau, K. *Energy & Fuels* **2017**, *31* (6), 5891–5901.
- (127) Buckley, J. S.; Wang, J. X.; Creek, J. L. In *Asphaltenes, Heavy Oils and Petroleomics*; Mullins, O. C., Sheu, E. Y., Hammami, A., Marshall, A. G., Eds.; Springer Netherlands: New York, 2007; pp 401–437.
- (128) Khaleel, A.; Abutaqiya, M.; Tavakkoli, M.; Melendez-alvarez, A. A. In *SPE Abu Dhabi*

*International Petroleum Exhibition and Conference, ADIPEC 2015*; Society of Petroleum Engineers: Abu Dhabi, UAE, November 9-12, 2015.

- (129) Buckley, J. S.; Hirasaki, G. J.; Liu, Y.; Von Drasek, S.; Wang, J.-X.; Gill, B. S. *Pet. Sci. Technol.* **1998**, *16* (3–4), 251–285.
- (130) Kurup, A. S.; Wang, J.; Subramani, H. J.; Buckley, J.; Creek, J. L.; Chapman, W. G. *Energy and Fuels* **2012**, *26* (9), 5702–5710.
- (131) Kurup, A. S.; Vargas, F. M.; Wang, J.; Buckley, J.; Creek, J. L.; Subramani, H. J.; Chapman, W. G. *Energy and Fuels* **2011**, *25* (10), 4506–4516.
- (132) Broseta, D.; Robin, M.; Savvidis, T.; Féjean, C.; Durandeau, M.; Zhou, H. In *SPE/DOE Improved Oil Recovery Symposium*; Society of Petroleum Engineers: Tulsa, Oklahoma, 3-5 April, 2000.
- (133) Rodríguez, S.; Ancheyta, J.; Guzmán, R.; Trejo, F. *Energy & Fuels* **2016**, *30* (10), 8216–8225.
- (134) Toth, J. In *SPE International Symposium on Oilfield Chemistry*; Society of Petroleum Engineers: Texas, U.S.A, 5-8 February, 2003; p 12.
- (135) Zougari, M.; Jacobs, S.; Ratulowski, J.; Hammami, A.; Broze, G.; Flannery, M.; Stankiewicz, A.; Karan, K. *Energy Fuel* **2006**, *20* (4), 1656–1663.
- (136) Eskin, D.; Ratulowski, J.; Akbarzadeh, K.; Pan, S. *Can. J. Chem. Eng.* **2011**, *89* (3), 421–441.
- (137) Vilas Bôas Fávero, C.; Hanpan, A.; Phichphimok, P.; Binabdullah, K.; Fogler, H. S. *Energy & Fuels* **2016**, *30* (11), 8915–8921.
- (138) Akbarzadeh, K.; Eskin, D.; Ratulowski, J.; Taylor, S. *Energy & Fuels* **2012**, *26* (1), 495–510.

- (139) Arsalan, N.; Palayangoda, S. S.; Nguyen, Q. P. *J. Pet. Sci. Eng.* **2014**, *121*, 66–77.
- (140) Eskin, D.; Ratulowski, J.; Akbarzadeh, K.; Andersen, S. I. *AIChE J.* **2011**, *58* (9), 2936–2948.
- (141) Eskin, D.; Mohammadzadeh, O.; Taylor, S. D.; Ratulowski, J.; Rosas, A. C.; Jaramillo, E. R. *Can. J. Chem. Eng.* **2016**, *94* (7), 1308–1312.
- (142) Vargas, F. M.; Tavakkoli, M.; Boggara, M. In *Presented at the 15th International Conference on Petroleum Phase Behavior and Fouling*; Galveston, TX, 2014.
- (143) Tanaka, R.; Sato, E.; Hunt, J. E.; Winans, R. E.; Sato, S.; Takanohashi, T. *Energy and Fuels* **2004**, *18* (4), 1118–1125.
- (144) Savvidis, T. G.; Fenistein, D.; Barr, L.; Bhar, E. *AIChE J.* **2001**, *47* (1), 206–211.
- (145) Curie, J.; Curie, P. *Comptes rendus l'Académie des Sci.* **1880**, No. 91, 3–90.
- (146) Curie, P.; Curie, J. *Comptes rendus l'Académie des Sci.* **1881**, No. 93, 1137–1140.
- (147) Sauerbrey, G. *Zeitschrift für Phys.* **1959**, *155*, 206–222.
- (148) Nomura, T.; Hattori, O. *Anal. Chim. Acta* **1980**, *115* (C), 323–326.
- (149) Nomura, T.; Okuhara, M. *Anal. Chim. Acta* **1982**, *142*, 281.
- (150) Bruckenstein, S.; Shay, M. *Electrochim. Acta* **1985**, *30* (10), 1295–1300.
- (151) Kanazawa, K. K.; Gordon, J. G. *Anal. Chem.* **1985**, *57* (8), 1770–1771.
- (152) Muramatsu, H.; Tamiya, E.; Karube, I. *Anal. Chem.* **1988**, *60* (3), 2142–2146.
- (153) Ward, M. D.; Buttry, D. A. *Science (80-. )*. **1990**, *249*, 1000–1007.

- (154) Lu, C. S.; Lewis, O. J. *Appl. Phys.* **1972**, *43* (11), 4385–4390.
- (155) Johannsmann, D. *The Quartz Crystal Microbalance in Soft Matter Research*; Springer: Zurich, Switzerland, 2015.
- (156) Mason, W. P. *Piezoelectric Crystals and Their Application to Ultrasonics*; Van Nostrand: Princeton, 1948.
- (157) Beck, R.; Pittermann, U.; Weil, K. G. *Berichte der Bunsengesellschaft für Phys. Chemie* **1988**, *92* (11), 1363–1368.
- (158) Cassiède, M.; Daridon, J.-L.; Paillol, J. H.; Pauly, J. J. *Appl. Phys.* **2011**, *109* (7), 74501.
- (159) Hillman, A. R.; Jackson, A.; Martin, S. J. *Anal. Chem.* **2001**, *73* (3), 540–549.
- (160) Stockbridge, C. D. *Vac. Microbalance Tech.* **1966**, *5*, 147–178.
- (161) Susse, C. J. *Phys. Radium* **1955**, No. 16, 348–349.
- (162) Cassiède, M.; Daridon, J. L.; Paillol, J. H.; Pauly, J. *Sensors Actuators, A Phys.* **2011**, *167* (2), 317–326.
- (163) Cassiède, M.; Daridon, J.-L.; Paillol, J. H.; Pauly, J. J. *Appl. Phys.* **2010**, *108* (3), 34505.
- (164) Cassiède, M.; Paillol, J. H.; Pauly, J.; Daridon, J.-L. *Sensors Actuators A Phys.* **2010**, *159* (2), 174–183.
- (165) Daridon, J.-L.; Cassiède, M.; Paillol, J. H.; Pauly, J. *Rev. Sci. Instrum.* **2011**, *82* (9), 95114.
- (166) Ekholm, P.; Blomberg, E.; Claesson, P.; Auflem, I. H.; Sjöblom, J.; Kornfeldt, A. J. *Colloid Interface Sci.* **2002**, *247* (2), 342–350.

- (167) Xie, K.; Karan, K. *Energy & Fuels* **2005**, *19* (4), 1252–1260.
- (168) Goual, L.; Horváth-Szabó, G.; Masliyah, J. H.; Xu, Z. *Langmuir* **2005**, *21* (18), 8278–8289.
- (169) Rudrake, A.; Karan, K.; Horton, J. H. *J. Colloid Interface Sci.* **2009**, *332* (1), 22–31.
- (170) Abudu, A.; Goual, L. *Energy & Fuels* **2009**, *23* (3), 1237–1248.
- (171) Farooq, U.; Sjöblom, J.; Øye, G. *J. Dispers. Sci. Technol.* **2011**, *32* (10), 1388–1395.
- (172) Zahabi, a.; Gray, M. R.; Dabros, T. *Energy and Fuels* **2012**, *26* (2), 1009–1018.
- (173) Tavakkoli, M.; Panuganti, S. R.; Vargas, F. M.; Taghikhani, V.; Pishvaie, M. R.; Chapman, W. G. *Energy* **2014**, No. 28, 1617–1628.
- (174) Tavakkoli, M.; Panuganti, S. R.; Taghikhani, V.; Pishvaie, M. R.; Chapman, W. G. *Energy & Fuels* **2014**, *28* (6), 3594–3603.
- (175) Kiasari, H. H.; Rabbani, A. R.; Mousavi-Dehghani, S. A.; Qobadi, A. *J. Dispers. Sci. Technol.* **2014**, 37–41.
- (176) Subramanian, S.; Simon, S.; Gao, B.; Sjöblom, J. *Colloids Surfaces A Physicochem. Eng. Asp.* **2016**, *495*, 136–148.
- (177) Tapio, L.; Subramanian, S.; Simon, S.; Sjöblom, J. *J. Dispers. Sci. Technol.* **2017**, *38* (3), 355–360.
- (178) Daridon, J. L.; Cassiède, M.; Pauly, J.; Nasri, D.; Carrier, H. *Energy & Fuels* **2013**, *27* (8), 4639–4647.
- (179) Rondon-gonzalez, M.; Kane, M.; Quintero, C.; Passade-boupat, N.; Zhou, H. In *Abu Dhabi*

*International Petroleum Exhibition and Conference; Abu Dhabi, UAE, 10-13 November, 2014.*

- (180) Cardoso, F. M. R.; Carrier, H.; Daridon, J.-L.; Pauly, J.; Rosa, P. T. V. *Energy & Fuels* **2014**, *28* (11), 6780–6787.
- (181) Daridon, J. L.; Orlandi, E.; Carrier, H. *Fluid Phase Equilib.* **2016**, *427*, 152–160.
- (182) Orlandi, E.; Daridon, J.-L.; Carrier, H. *Eur. Phys. J. Spec. Top.* **2017**, *226* (5), 1065–1073.
- (183) Pauly, J.; Coutinho, J.; Daridon, J.-L. *Fluid Phase Equilib.* **2007**, *255* (2), 193–199.
- (184) Cassiède, M.; Pauly, J.; Milhet, M.; Rivaletto, M.; Marrucho, I. M.; Coutinho, J. a P.; Daridon, J.-L. *Meas. Sci. Technol.* **2008**, *19* (6), 65704.
- (185) Joonaki, E.; Burgass, R.; Hassanpouryouzband, A.; Tohidi, B. *Energy & Fuels* **2017**, *31* (11).
- (186) Eroini, V.; Anfindsen, H.; Mitchell, A. F. In *SPE International Symposium on Oilfield Chemistry*; Society of Petroleum Engineers: Woodlands, Texas, USA. 13 - 15 April, 2015.
- (187) Wei, D.; Orlandi, E.; Barriet, M.; Simon, S.; Sjöblom, J.; Wei, D.; Barriet, M.; Simon, S.; Sjöblom, J. *J. Therm. Anal. Calorim.* **2015**, *122* (1), 463–471.
- (188) Buckley, J. S. *Energy & Fuels* **2012**, *26* (7), 4086–4090.
- (189) Santos, S. Dos; Poulidakos, L. D.; Partl, M. N. *RSC Adv.* **2016**, *6* (47), 41561–41567.
- (190) Carbognani, L.; Espidel, J.; Morales-Izquierdo, A. In *Asphaltenes and Asphalts, 2*; Yen, T. F., Chilingarian, G. V, Eds.; Elsevier: Amsterdam, 2000; pp 335–359.
- (191) Etchenique, R.; Brudny, V. L. *Langmuir* **2000**, *16* (11), 5064–5071.

- (192) Urbakh, M.; Daikhin, L. *Phys. Rev. B* **1994**, *49* (7), 4866–4870.
- (193) Urbakh, M.; Daikhin, L. *Colloids Surfaces A Physicochem. Eng. Asp.* **1998**, *134* (1–2), 75–84.
- (194) Daikhin, L.; Gileadi, E.; Katz, G.; Tsionsky, V.; Urbakh, M.; Zagidulin, D. *Anal. Chem.* **2002**, *74* (3), 554–561.
- (195) Johannsmann, D. *Macromol. Chem. Phys.* **1999**, *516*, 501–516.
- (196) Yangt, M.; Thompson, M. *Langmuir* **1994**, No. 4, 1990–1994.
- (197) Urbakh, M.; Daikhin, L. *Langmuir* **1994**, *10* (8), 2836–2841.
- (198) Daikhin, L.; Urbakh, M. *Langmuir* **1996**, *12* (26), 6354–6360.
- (199) Rechendorff, K.; Hovgaard, M. B.; Foss, M.; Besenbacher, F. *J. Appl. Phys.* **2007**, *101* (11).
- (200) Olsson, A. L. J.; Van Der Mei, H. C.; Johannsmann, D.; Busscher, H. J.; Sharma, P. K. *Anal. Chem.* **2012**, *84* (10), 4504–4512.
- (201) Pomorska, A.; Shchukin, D.; Hammond, R.; Cooper, M. A.; Grundmeier, G.; Johannsmann, D. *Anal. Chem.* **2010**, *82* (6), 2237–2242.
- (202) Johannsmann, D.; Reviakine, I.; Richter, R. P. *Anal. Chem.* **2009**, *81* (19), 8167–8176.
- (203) Johannsmann, D.; Reviakine, I.; Rojas, E.; Gallego, M. *Anal. Chem.* **2008**, *80* (23), 8891–8899.
- (204) Peschel, A.; Langhoff, A.; Johannsmann, D. *Nanotechnology* **2015**, *26* (48), 484001.
- (205) Reviakine, I.; Johannsmann, D.; Richter, R. P. *Anal. Chem.* **2011**, *83* (23), 8838–8848.
- (206) Martin, S. J.; Granstaff, V. E.; Frye, G. C. *Anal. Chem.* **1991**, *2281* (26), 2272–2281.

- (207) Reviakine, I.; Morozov, A. N.; Rossetti, F. F. *J. Appl. Phys.* **2004**, *95* (12), 7712–7716.
- (208) Amin, J. S.; E.nikooee; Ghatee, M. H.; Ayatollahi, S.; Alamdari, A.; Sedghamiz, T. *Appl. Surf. Sci.* **2011**, *257* (20), 8341–8349.
- (209) Höök, F.; Kasemo, B.; Nylander, T.; Fant, C.; Sott, K.; Elwing, H. *Anal. Chem.* **2001**, *73* (24), 5796–5804.
- (210) Rojas, E.; Gallego, M.; Reviakine, I. *Anal. Chem.* **2008**, *80* (23), 8982–8990.
- (211) Ocanto, O.; Marcano, F.; Castillo, J.; Fernandez, A.; Caetano, M.; Chirinos, J.; Ranaudo, M. *A. Energy & Fuels* **2009**, *23* (6), 3039–3044.
- (212) Rogel, E.; Ovalles, C.; Bake, K. D.; Zuo, J. Y.; Dumont, H.; Pomerantz, A. E.; Mullins, O. C. *Energy and Fuels* **2016**, *30* (11), 9132–9140.
- (213) Torkaman, M.; Bahrami, M.; Dehghani, M. R. *Energy & Fuels* **2017**, *31* (10), 11169–11180.
- (214) Andersen, S. I. *Fuel Sci. Technol. Int.* **1994**, *12* (1), 51–74.
- (215) Goual, L.; Firoozabadi, A. *AIChE J.* **2004**, *50* (2), 470–479.
- (216) Al-Sahhaf, T. A.; Fahim, M. A.; Elkilani, A. S. *Fluid Phase Equilib.* **2002**, *194–197*, 1045–1057.
- (217) Clarke, P. F.; Pruden, B. B. *Pet. Sci. Technol.* **1998**, *16* (3–4), 287–305.
- (218) Wang, J.; Li, C.; Zhang, L.; Que, G.; Li, Z. *Energy and Fuels* **2009**, *23* (7), 3625–3631.
- (219) Escobedo, J.; Mansoori, G. A.; Illinois, U. Society of Petroleum Engineers: Richardson, TX, USA., 1994.
- (220) Ekulu, G.; Magri, P.; Rogalski, M. *J. Dispers. Sci. Technol.* **2004**, *25* (3), 321–331.

- (221) Ekulu, G. .; Sadiki, A. . b; Rogalski, M. . *J. Dispers. Sci. Technol.* **2010**, *31* (11), 1495–1503.
- (222) Ganeeva, Y. M.; Yusupova, T. N.; Romanov, G. V. *Russ. Chem. Rev.* **2011**, *80* (10), 993–1008.
- (223) Acevedo, S.; Castillo, J.; Fernández, A.; Goncalves, S.; Ranaudo, M. a. *Energy & Fuels* **1998**, *12* (2), 386–390.
- (224) Schutte, K. C. J.; Portela, L. M.; Twerda, A.; Henkes, R. a. W. M. *Energy & Fuels* **2015**, *29* (5), 2754–2767.
- (225) Sheu, E. Y.; Liang, K. S.; Sinha, S. K.; Overfield, R. E. *J. Colloid Interface Sci.* **1992**, *153* (2), 399–410.

ECOLE DOCTORALE :  
Doctoral School of Exact Sciences and their Applications (ED 211)

LABORATOIRE :

Laboratoire des Fluides Complexes et leurs Réservoirs  
Université de Pau et de Pays de l'Adour  
BP 1155 – 64 013 PAU Cedex